Springer Proceedings in Physics 186

Ahmet Yavuz Oral
Zehra Banu Bahsi Oral *Editors*

3rd International Multidisciplinary Microscopy and Microanalysis Congress (InterM)

Proceedings, Oludeniz, Turkey, 19–23 October 2015

Springer

Springer Proceedings in Physics

Volume 186

The series Springer Proceedings in Physics, founded in 1984, is devoted to timely reports of state-of-the-art developments in physics and related sciences. Typically based on material presented at conferences, workshops and similar scientific meetings, volumes published in this series will constitute a comprehensive up-to-date source of reference on a field or subfield of relevance in contemporary physics. Proposals must include the following:

- name, place and date of the scientific meeting
- a link to the committees (local organization, international advisors etc.)
- scientific description of the meeting
- list of invited/plenary speakers
- an estimate of the planned proceedings book parameters (number of pages/articles, requested number of bulk copies, submission deadline).

More information about this series at http://www.springer.com/series/361

Ahmet Yavuz Oral · Zehra Banu Bahsi Oral
Editors

3rd International Multidisciplinary Microscopy and Microanalysis Congress (InterM)

Proceedings, Oludeniz, Turkey, 19–23 October 2015

Springer

Editors
Ahmet Yavuz Oral
Department of Materials Science and Engineering
Gebze Technical University
Gebze, Kocaeli
Turkey

Zehra Banu Bahsi Oral
Department of Environmental Engineering
Gebze Technical University
Gebze, Kocaeli
Turkey

ISSN 0930-8989 ISSN 1867-4941 (electronic)
Springer Proceedings in Physics
ISBN 978-3-319-46600-2 ISBN 978-3-319-46601-9 (eBook)
DOI 10.1007/978-3-319-46601-9

Library of Congress Control Number: 2016952505

Printed on acid-free paper

This Springer imprint is published by Springer Nature
The registered company is Springer International Publishing AG
The registered company address is: Gewerbestrasse 11, 6330 Cham, Switzerland

Preface

The 3rd International Multidisciplinary Microscopy Congress (InterM2015) provided all scientists the opportunity to meet, present their work, discuss and mutually interact in order to enhance and promote their research work.

This volume, published by Springer, includes selected papers presented at this congress, held in Oludeniz, Turkey, October 19–23, 2015.

On behalf of the organizing committee we would like to thank all the participants, plenary and invited speakers for their valuable contribution.

We would also like to thank AIGTUR for their support in the organization of the congress as well as the publishers for the quality of this edition.

Gebze, Turkey

Ahmet Yavuz Oral
Zehra Banu Bahsi Oral

Organization

Scientific Committee

George A. Stanciu, University "Politehnica" of Bucharest, Romania
Seong-Ho Kang, Kyung Hee University, Korea
Jonas Fransson, Uppsala University, Sweden
M. Alper Sahiner, Seton Hall University, USA
Mohamed Bououdina, University of Bahrain, Kingdom of Bahrain
Cengiz Ozkan, University of California, Riverside, USA
Kunio Takeyasu, Kyoto University, Japan
Jiri Nemecek, Czech Technical University in Prague, Czech Republic
Junsang Doh, Pohang University of Science and Technology, Korea
Olga Duarte Silva, Universidade de Lisboa, Portuguese
Ying Feng, The University of Alabama, USA
Paul Thomas, Matsudaira National University of Singapore, Singapore
Yoshiaki Uesu, Waseda University, Japan
Kazuo Umemura, Tokyo University of Science, Japan
Peter Guttmann, Helmholtz Zentrum Berlin, Germany
Quanmin Guo, University of Birmingham, UK
Ivan Stich, Slovak Academy of Sciences, Slovakia
Golap Kalita, Nagoya Institute of Technology, Japan
Hideki Kawakatsu, Institute of Industrial Science, the University of Tokyo, Japan
Masashi Arita, Hokkaido University, Japan

Organizing Committee

Ahmet Yavuz Oral, Gebze Technical University, Turkey
Zehra Banu Bahsi Oral, Gebze Technical University, Turkey
M. Alper Sahiner, Seton Hall University, USA

Ersin Kayahan, Kocaeli University, Turkey
Tarik Talib Issa Al-Omran, University of Baghdad, Iraq
Mehmet Sezer, Gebze Technical University, Turkey

Conference Organizing Company

Aig Turizm Seyahat Kongre ve Org. Tic. Ltd. Şti.

Atatürk Cad No:1 Tever Apt. D:11
Sahrayıcedid, Kadıkoy, Istanbul, Turkey
+90 216 330 80 90
http://aigtur.com.tr/

Contents

Contributors

O. Aissaoui Zitoun INATAA, Laboratory of Nutrition and Food S Technologies, University Frères Mentouri Constantine 1, Constantine, Algeria

Hideki Aizaki Virus Division II, National Institute of Infectious Disease, Tokyo, Japan

Nuri Akkaş Department of Metallurgical and Materials Engineering, University of Sakarya, Sakarya, Turkey

A.K. Akurpekova D.V.Sokolsky Institute of Organic Catalysis and Electrochemistry, Almaty, Kazakhstan

Abdulkadir Akyol Department of Metallurgy and Materials Engineering, Engineering Faculty, Esentepe Campus, Sakarya University, Sakarya, Turkey

Masashi Arita Graduate School of Information Science and Technology, Hokkaido University, Kita-ku, Sapporo, Japan

Suguru Asai Laboratory of Plasma Membrane and Nuclear Signaling, Kyoto University Graduate School of Biostudies, Kyoto, Japan

Salim Aslanlar Department of Metallurgical and Materials Engineering, University of Sakarya, Sakarya, Turkey

T. Astruc Theix, QuaPA, INRA de Clermont Ferrand, St Genes Champanelle, France

H. Attia Unité d'Analyses Alimentaires - École Nationale d'Ingénieurs, Sfax, Tunisie

Sunay Ayhan Department of Metallurgy and Materials Engineering, Engineering Faculty, Esentepe Campus, Sakarya University, Sakarya, Turkey

Nacer E. Bacha Lab. of Surface Treatment and Materials, University of Blida, Blida, Algeria

Smrutisikha Bal Department of Metallurgical and Materials Engineering, National Institute of Technology, Rourkela, Odisha, India

T.G. Baluyan Chair of the Solid State Physics, Department of Physics, Moscow State University, Moscow, Russia

S. Becila INATAA, Bothers Mentouri Constantine University, Constantine, Algeria

R. Belachehabe INATAA, Bothers Mentouri Constantine University, Constantine, Algeria

Jan Burke System Technologies and Image Exploitation IOSB, Fraunhofer Institute of Optronics, Karlsruhe, Germany

Jürgen Beyerer System Technologies and Image Exploitation IOSB, Fraunhofer Institute of Optronics, Karlsruhe, Germany; Vision and Fusion Laboratory (IES), Karlsruhe Institute of Technology (KIT), Karlsruhe, Germany

H. Boudchicha INATAA, Bothers Mentouri Constantine University, Constantine, Algeria

Y. Boudida INATAA, Bothers Mentouri Constantine University, Constantine, Algeria

A. Boudjellal INATAA, Bothers Mentouri Constantine University, Constantine, Algeria

S. Carpino CoRFiLaC, Ragusa Mare, Italy

Oleg V. Chertkov Biological Faculty, Lomonosov Moscow State University, Moscow, Russia; Shemyakin-Ovchinnikov Institute of Bioorganic Chemistry, Russian Academy of Sciences, Moscow, Russia

Betül Çıtak Department of Metallurgy and Materials Engineering, Engineering Faculty, Esentepe Campus, Sakarya University, Sakarya, Turkey

Roxana Cojoc Microbiology Department, Institute of Biology Bucharest, Romanian Academy, Bucharest, Romania

M.A.C. Crapez Marine Biology Postgraduate Program, Federal Fluminense University, Angra dos Reis, Brazil

O. Dalelkhanuly D.V.Sokolsky Institute of Organic Catalysis and Electrochemistry, Almaty, Kazakhstan

Katashi Deguchi Laboratory of Plasma Membrane and Nuclear Signaling, Kyoto University Graduate School of Biostudies, Sakyo-ku, Kyoto, Japan

Mădălin Enache Microbiology Department, Institute of Biology Bucharest, Romanian Academy, Bucharest, Romania

Alexey V. Feofanov Biological Faculty, Lomonosov Moscow State University, Moscow, Russia; Shemyakin-Ovchinnikov Institute of Bioorganic Chemistry, Russian Academy of Sciences, Moscow, Russia

Erman Ferik Department of Metallurgical and Materials Engineering, University of Sakarya, Sakarya, Turkey

Peter Frühberger System Technologies and Image Exploitation IOSB, Fraunhofer Institute of Optronics, Karlsruhe, Germany; Vision and Fusion Laboratory (IES), Karlsruhe Institute of Technology (KIT), Karlsruhe, Germany

N. Fucà CoRFiLaC, Ragusa Mare, Italy

Yoshitaka Fujimoto Department of Physics, Tokyo Institute of Technology, Tokyo, Japan

M. Gagaoua INATAA, Bothers Mentouri Constantine University, Constantine, Algeria

Jamie L. Gilmore Laboratory of Plasma Membrane and Nuclear Signaling, Kyoto University Graduate School of Biostudies, Sakyo-ku, Kyoto, Japan

Sergey V. Gnedenkov Institute of Chemistry Far-Eastern Branch Russian Academy of Sciences, Vladivostok, Russia

Uilame Umbelino Gomes Graduate Program in Materials Science and Engineering, Departamento de Fisica, Universidade Federal Do Rio Grande Do Norte, Natal-RN, Brazil

Ioana Gomoiu Conservation and Restoration Department, National University of Arts, Bucharest, Romania

M.V. Gorshenkov National University of Science and Technology "MISIS", Moscow, Russia

K. Hafid INATAA, Bothers Mentouri Constantine University, Constantine, Algeria

N. Haniche Laboratoire de Biologie et Physiologie Des Organismes Equipe de Neurobiologie, USTHB, Bab Ezzouar, Algérie

Ken Hashigata Chemical Engineering Department, Parahyangan Catholic University, Bandung, Indonesia

C.H. Herrera-Mendez Departamento de Ingeniería Agroindustrial, Universidad de Guanajuato, Salvatierra, Mexico

Hammad R. Humud Physics Department, College of Science, University of Baghdad, Jadiriya, Baghdad, Iraq

Kiwamu Hyodo Laboratory of Plant Physiology, Kyoto University Graduate School of Agriculture, Kyoto, Japan

Anastasiya A. Ignatova Biological Faculty, Lomonosov Moscow State University, Moscow, Russia; Shemyakin-Ovchinnikov Institute of Bioorganic Chemistry, Russian Academy of Sciences, Moscow, Russia

Erdinç İlhan Department of Metallurgical and Materials Engineering, University of Sakarya, Sakarya, Turkey

Mohammed E. Ismael Physics Department, College of Science, University of Baghdad, Jadiriya, Baghdad, Iraq

Yaroslav O. Ivanov Biological Faculty, Lomonosov Moscow State University, Moscow, Russia

A.E. Kalmykov Ioffe Institute, St. Petersburg, Russia

V. Yu. Karaulov SERNIA LLC, Moscow, Russia

A.V. Kartavykh National University of Science and Technology "MISIS", Moscow, Russia

K. Kaviyarasu UNESCO-UNISA Africa Chair in Nanosciences/Nanotechnology Laboratories, College of Graduate Studies, University of South Africa (UNISA), Pretoria, South Africa; Nanosciences African Network (NANOAFNET), Materials Research Group (MRG), iThemba LABS-National Research Foundation (NRF), Somerset West, Western Cape Province, South Africa

J. Kennedy UNESCO-UNISA Africa Chair in Nanosciences/Nanotechnology Laboratories, College of Graduate Studies, University of South Africa (UNISA), Pretoria, South Africa; National Isotope Centre, GNS Science, Lower Hutt, New Zealand

D.A. Kirilenko Ioffe Institute, St. Petersburg, Russia

Mikhail P. Kirpichnikov Biological Faculty, Lomonosov Moscow State University, Moscow, Russia; Shemyakin-Ovchinnikov Institute of Bioorganic Chemistry, Russian Academy of Sciences, Moscow, Russia

A.V. Korotitskiy National University of Science and Technology "MISIS", Moscow, Russia

Kseniya S. Kudryashova Biological Faculty, Lomonosov Moscow State University, Moscow, Russia; Shemyakin-Ovchinnikov Institute of Bioorganic Chemistry, Russian Academy of Sciences, Moscow, Russia

Masahiro Kumeta Laboratory of Plasma Membrane and Nuclear Signaling, Kyoto University Graduate School of Biostudies, Kyoto, Japan

Recep Kılıç Sakarya Metropolitan Municipality, Sakarya, Turkey

R. Labas Theix, QuaPA, INRA de Clermont Ferrand, St Genes Champanelle, France

R. Ladchumananandasiivam Department of Textile Engineering and Post Graduate Programme in Mechanical Engineering, Centre of Technology, Federal University of the State of Rio Grande Do Norte, Campus Universitario, Natal-RN, Brazil

R.G. Leitão Nuclear Instrumentation Laboratory, PEN/COPPE/UFRJ, Rio de Janeiro, Brazil

I. Lima Nuclear Instrumentation Laboratory, PEN/COPPE/UFRJ, Rio de Janeiro, RJ, Brazil

R.T. Lopes Nuclear Instrumentation Laboratory, PEN/COPPE/UFRJ, Rio de Janeiro, RJ, Brazil

Irina N. Lyapun Cell Biology and Histopathology Laboratory, Somov Institute of Epidemiology and Microbiology, Vladivostok, Russia

M. Maaza UNESCO-UNISA Africa Chair in Nanosciences/Nanotechnology Laboratories, College of Graduate Studies, University of South Africa (UNISA), Pretoria, South Africa; Nanosciences African Network (NANOAFNET), Materials Research Group (MRG), iThemba LABS-National Research Foundation (NRF), Somerset West, Western Cape Province, South Africa

Biswa Bhusana Mahapatra Department of Life Science, National Institute of Technology Rourkela, Rourkela, Odisha, India

Yu. B. Mandzhieva Chair of the Solid State Physics, Department of Physics, Moscow State University, Moscow, Russia

E. Manikandan UNESCO-UNISA Africa Chair in Nanosciences/Nanotechnology Laboratories, College of Graduate Studies, University of South Africa (UNISA), Pretoria, South Africa

M.L. Mansour Faculté des Sciences de la Nature et de la Vie, Université Ferhat Abbas, Setif, Algeria

Sandhya Marathe Department of Biological Sciences, Birla Institute of Technology and Science, Pilani, Rajasthan, India

Sabera Millan Department of Chemistry, National Institute of Technology, Rourkela, Odisha, India

Monalisa Mishra Department of Life Science, National Institute of Technology Rourkela, Rourkela, Odisha, India

Dan Mohanu Conservation and Restoration Department, National University of Arts, Bucharest, Romania

Ileana Mohanu Binders Materials Research Department, CEPROCIM S.A., Bucharest, Romania

Genene T. Mola School of Chemistry and Physics, University of Kwazulu-Natal, Scottsville, Pietermaritzburg, South Africa

A.V. Myasoedov Ioffe Institute, St. Petersburg, Russia

Oksana V. Nekrasova Biological Faculty, Lomonosov Moscow State University, Moscow, Russia; Shemyakin-Ovchinnikov Institute of Bioorganic Chemistry, Russian Academy of Sciences, Moscow, Russia

D.A. Nielsen Department of Physics and Nanotechnology, Aalborg University, Aalborg, Denmark

Inge W. Noordergraaf Chemical Engineering Department, University of Groningen, Groningen, The Netherlands

A.A. Novakova Chair of the Solid State Physics, Department of Physics, Moscow State University, Moscow, Russia

Sergey A. Novopashin Kutateladze Institute of Thermophysics, Novosibirsk, Russia

Tetsuro Okuno Laboratory of Plant Physiology, Kyoto University Graduate School of Agriculture, Kyoto, Japan

A. Ouali Theix, QuaPA, INRA de Clermont Ferrand, St Genes Champanelle, France

Tuğba Tunç Parlak Department of Metallurgy and Materials Engineering, Engineering Faculty, Esentepe Campus, Sakarya University, Sakarya, Turkey

K. Pedersen Department of Physics and Nanotechnology, Aalborg University, Aalborg, Denmark

S. Pennafirme Marine Biology Postgraduate Program, Federal Fluminense University, Angra dos Reis, Brazil

B. Picard Theix, QuaPA, INRA de Clermont Ferrand, St Genes Champanelle, France

Natalia G. Plekhova Central Scientific Research Laboratory, Pacific State Medical University, Vladivostok, Russia; School of Natural Sciences, School of Biomedical, Far Eastern Federal University, Vladivostok, Russia

V.N. Popok Department of Physics and Nanotechnology, Aalborg University, Aalborg, Denmark

Evgenii V. Pustovalov School of Natural Sciences, School of Biomedical, Far Eastern Federal University, Vladivostok, Russia

Artem V. Puz' Institute of Chemistry Far-Eastern Branch Russian Academy of Sciences, Vladivostok, Russia

O. Saadi-Brenkia Laboratoire de Biologie et Physiologie Des Organismes Equipe de Neurobiologie, USTHB, Bab Ezzouar, Algérie; Departement de Biologie, Université M'hamed Bougara Boumerdes, Boumerdes, Algérie

Debabrat Sabat Department of Life Science, National Institute of Technology, Rourkela, Odisha, India

Harekrushna Sahoo Department of Chemistry, National Institute of Technology, Rourkela, Odisha, India

Sheetal Sahu Department of Life Science, National Institute of Technology Rourkela, Rourkela, Odisha, India

Susumu Saito Department of Physics, Tokyo Institute of Technology, Tokyo, Japan

Herry Santoso Chemical Engineering Department, Parahyangan Catholic University, Bandung, Indonesia

Seetha Seetha Department of Life Science, National Institute of Technology Rourkela, Rourkela, Odisha, India

M.A. Sentandreu Instituto de Agroquimica y Tecnologia de Alimentos, CSIC, Valencia, Spain

Marina A. Serebryakova Kutateladze Institute of Thermophysics, Novosibirsk, Russia

Valentin B. Shumatov Central Scientific Research Laboratory, Pacific State Medical University, Vladivostok, Russia

Sergey L. Sinebryukhov Institute of Chemistry Far-Eastern Branch Russian Academy of Sciences, Vladivostok, Russia

H. Smili INATAA, Bothers Mentouri Constantine University, Constantine, Algeria

L.M. Sorokin Ioffe Institute, St. Petersburg, Russia

Thomas Stephan System Technologies and Image Exploitation IOSB, Fraunhofer Institute of Optronics, Karlsruhe, Germany; Vision and Fusion Laboratory (IES), Karlsruhe Institute of Technology (KIT), Karlsruhe, Germany

Vasily M. Studitsky Cancer Epigenetics Program, Fox Chase Cancer Center, Philadelphia, USA; Biological Faculty, Lomonosov Moscow State University, Moscow, Russia

P. Suchismita Sethy Department of Life Science, National Institute of Technology, Rourkela, Odisha, India

A. Şükran Demirkıran Department of Metallurgy and Materials Engineering, Engineering Faculty, Esentepe Campus, Sakarya University, Sakarya, Turkey

Yasuo Takahashi Graduate School of Information Science and Technology, Hokkaido University, Kita-ku, Sapporo, Japan

Kunio Takeyasu Laboratory of Plasma Membrane and Nuclear Signaling, Kyoto University Graduate School of Biostudies, Sakyo-ku, Kyoto, Japan

A.P. Teles Nuclear Instrumentation Laboratory, PEN/COPPE/UFRJ, Rio de Janeiro, RJ, Brazil

Takaji Wakita Virus Division II, National Institute of Infectious Disease, Tokyo, Japan

Ahmed S. Wasfi Physics Department, College of Science, University of Baghdad, Jadiriya, Baghdad, Iraq

Judy R.B. Witono Chemical Engineering Department, Parahyangan Catholic University, Bandung, Indonesia

Aiko Yoshida Laboratory of Plasma Membrane and Nuclear Signaling, Kyoto University Graduate School of Biostudies, Kyoto, Japan

Alexey V. Zaikovskii Kutateladze Institute of Thermophysics, Novosibirsk, Russia

N.A. Zakarina D.V.Sokolsky Institute of Organic Catalysis and Electrochemistry, Almaty, Kazakhstan

D.A. Zhumadulaev D.V.Sokolsky Institute of Organic Catalysis and Electrochemistry, Almaty, Kazakhstan

M.N. Zidoune INATAA, Laboratory of Nutrition and Food S Technologies, University Frères Mentouri Constantine 1, Constantine, Algeria

Part I
Applications of Microscopy in the Biological Sciences

Structural Analysis of Long Single-Stranded RNA Molecules with Atomic Force Microscopy Imaging

Jamie L. Gilmore, Aiko Yoshida, Katashi Deguchi, Suguru Asai, Hideki Aizaki, Masahiro Kumeta, Kiwamu Hyodo, Tetsuro Okuno, Takaji Wakita and Kunio Takeyasu

Abstract Characterization of the structure of long RNA molecules (>1 kb) is usually a time-consuming and tedious process. In this study, we have developed an imaging procedure for obtaining images of the extended secondary structures of long RNA molecules combined with automated MATLAB-based data processing algorithms for identification of the domain architecture of the molecules in these images. These algorithms include a molecule autoselection procedure based on height and area thresholding, a morphological thinning procedure to generate skeletons of the molecule in order to analyze the branched structure of the molecules, and a procedure to generate local volume profiles along the main chain of the molecule for identification of domains and prediction of the number of nucleotides comprising each domain. The single-molecule nature of this technique also allows for the identification of varying conformations of the molecule and assessment of the conformational flexibility of the identified domain organization.

1 Introduction

Structural characterization of long single-stranded RNA molecules (>1 kb) is a process that often takes many years with each domain identified and studied in independent sets of experiments. In the case the of the Hepatitis C virus (HCV) RNA genome, structural characterization has proceeded gradually, focused mainly

J.L. Gilmore (✉) · A. Yoshida · K. Deguchi · S. Asai · M. Kumeta · K. Takeyasu
Laboratory of Plasma Membrane and Nuclear Signaling, Kyoto University Graduate School of Biostudies, Yoshida-konoe, Sakyo-ku, Kyoto 606-8501, Japan
e-mail: gilmore.jamielynn.3e@kyoto-u.ac.jp

H. Aizaki · T. Wakita
Virus Division II, National Institute of Infectious Disease, Toyama, Shinjuku-ku, Tokyo 162-8640, Japan

K. Hyodo · T. Okuno
Laboratory of Plant Physiology, Kyoto University Graduate School of Agriculture, Yoshida-konoe, Sakyo-ku, Kyoto 606-8501, Japan

A.Y. Oral and Z.B. Bahsi Oral (eds.), *3rd International Multidisciplinary Microscopy and Microanalysis Congress (InterM)*, Springer Proceedings in Physics 186,
DOI 10.1007/978-3-319-46601-9_1

on the 5′ and 3′ untranslated regions (UTRs), with the internal structures remaining largely uncharacterized [1, 2]. Given the tedious nature of these processes, the development of methods to perform high-throughput characterization of RNA structure could greatly advance our ability to recognize the structural features on long RNA molecules such as viral RNA genomes, messenger RNA (mRNA) transcripts, or ribosomal RNA (rRNA).

Towards this goal, we are attempting to develop Atomic Force Microscopy (AFM) imaging as a method to characterize the secondary structure of these molecules [3]. The first step of this process is the development of procedures to reproducibly image extended secondary structures of various RNA molecules. The next step is the development of automated procedures to extract structural information from the molecules in these images. To do this, we have developed MATLAB-based algorithms to autoselect the molecules from the images by height and area thresholding, generate skeletons of the molecule to analyze the branches of the RNA molecules, and generate local volume profiles along the morphological backbone of the molecule to predict the location of domains along the chain and the number of nucleotides in each.

2 Development of AFM Procedures to Image RNA Secondary Structure

Taking advantage of the fact that Mg^{2+} is necessary for RNA tertiary structure but not for secondary structure [4, 5], we have developed a method to reproducibly observe secondary structures of RNA molecules on a spermidine-modified mica surface using AFM imaging by omitting Mg^{2+} from our reactions and briefly heating the RNA to 65 °C (Fig. 1). This technique has proved effective for a variety of RNA molecules, including the 9.7 kb full-length genome of HCV (JFH-1) [6], a 3.9 kb importin β gene transcript, a polyadenylated importin β transcript, a 5.0 kb 28S rRNA, a 1.9 kb 18S rRNA, and the bipartite genome of the Red clover necrotic mosaic virus (RCNMV) [7] comprised of RNA1 and RNA2 (Fig. 1). Due to the hierarchical nature of RNA folding [5], much of this structure is likely to be conserved in the final folded molecule.

3 Analysis and Domain Recognition of RNA

After development of procedures to obtain reproducible images of RNA molecules, the next stage is to develop data analysis procedures that can extract structural information from these images. To do this, we have developed a series of automated MATLAB-based algorithms to analyze RNA molecules. For now, these algorithms have been applied to a 1.1 kb deletion mutant of the JFH-1 HCV genome with

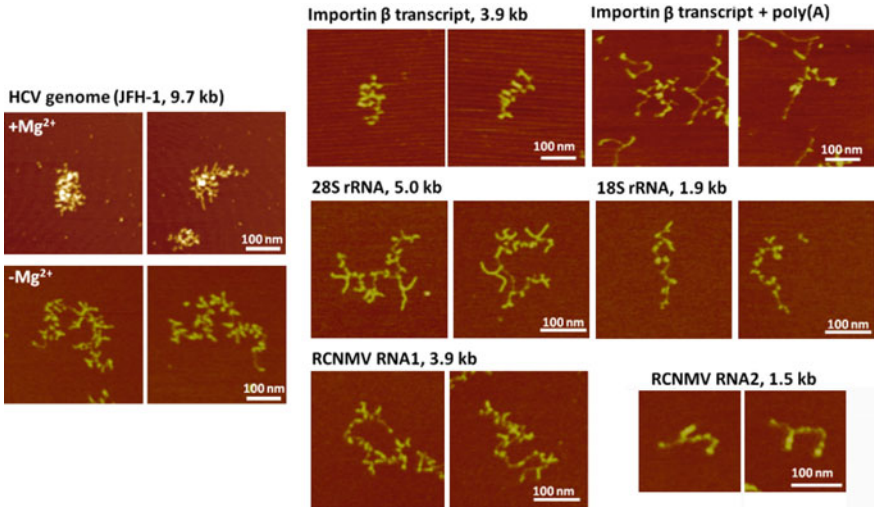

Fig. 1 AFM images of various RNA molecules. Images of the full-length 9.7 kb JFH-1 Hepatitis C Virus (HCV) genome are displayed on the *left* showing the tertiary structure in the presence of 1 mM Mg^{2+} and without the addition of Mg^{2+} (1 mM EDTA). The remaining images all show the secondary structure in Mg^{2+}-free conditions

8.6 kb of the coding region removed (JFH-1dC_5B, Fig. 2a), leaving mainly the 5′ and 3′ UTRs which are important for guiding the viral translation and viral replication processes, respectively. These regions have been reported to be some of the most structurally conserved regions of the genome [8]. Structures in these regions have been well characterized [1, 2], making it ideal to test the validity of our method.

Our algorithms were developed using the MATLAB image processing toolbox [9]. A detailed description of the algorithms will be reported elsewhere. These include autoselection of the molecules through height and area thresholding (Fig. 2b, left), 2D morphological thinning to generate a skeleton of the molecule to analyze its branched structure (Fig. 2b, middle and right), and the generation of 'local' volume profiles along the length of the molecule (Fig. 2c). By plotting the 'local' volume versus the length along the molecule, we can get an idea of the domain structure (Fig. 2c, left). Furthermore, the nucleotide number of each domain structure could be predicted based on the cumulative volume along the chain (Fig. 2c). For the molecule displayed in Fig. 2c, three of the four domains identified corresponded reasonably well to previously reported domains in the HCV genome, including the internal ribosome entry site (IRES) (domain#1), stem loops V-VI (domain #2), and the 3′X RNA (domain #4) located at the end of the genome which is located at the end of a notable single-stranded polyU/UC region (Fig. 2c, right). However, the 5BSL and VSL regions appeared to be contained within a domain structure that encompasses more of the coding region of the genome (domain #4, Fig. 2c, right).

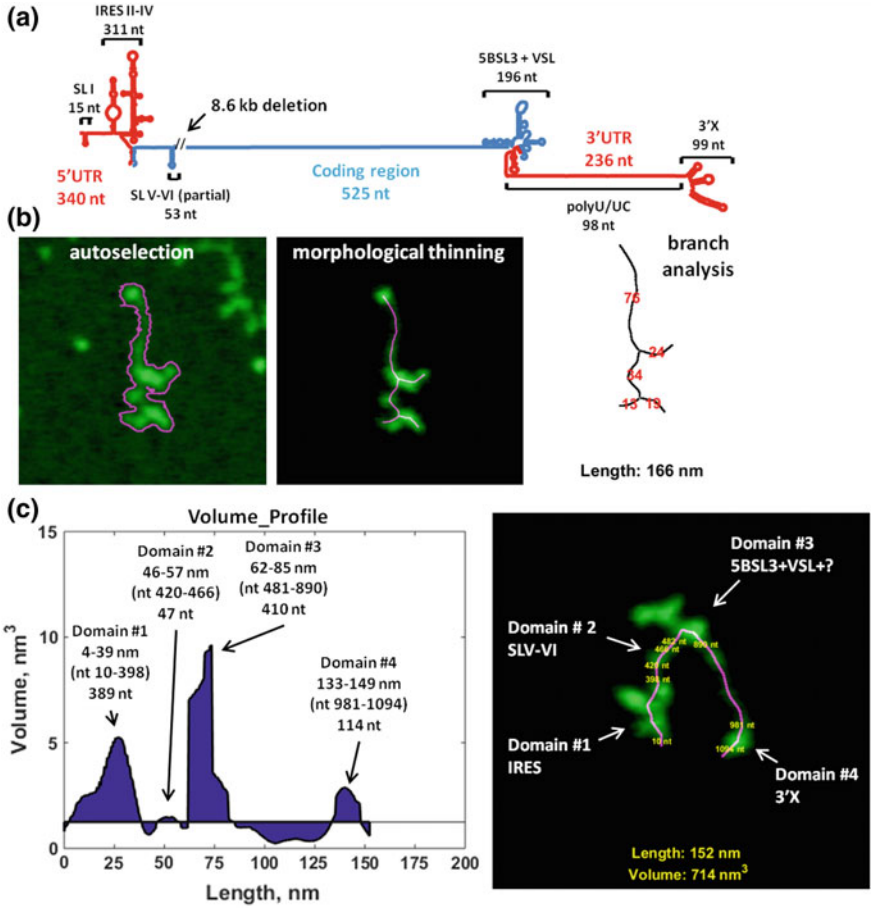

Fig. 2 Automated MATLAB-based algorithms to analyze a 1. 1 kb JFH-1 HCV deletion mutant with 8.6 kb of the coding region deleted. **a** Model of the HCV deletion mutant with well characterized structures labeled. **b** Automated data analysis processes for the deletion mutant include autoselection of the molecule, morphological thinning to produce a skeleton, and branch analysis. The length of each branch in nanometers in displayed in red and the total length is recorded at the bottom of the image. **c** On the *left*, a profile of the 'local' volume along the main chain detects four domains when a threshold of 1.25 nm^3 is used. The profile was generated by identifying the longest end-to-end chain in the skeleton previously generated by morphological thinning. All pixels in the original autoselected region were then assigned to a pixel in the main chain through an image transformation process which iteratively assigns nearby pixels a value corresponding to the value of the line pixel. The volume was then summed for all pixels which were 'local' to the line pixel and the length of the line was determined using a geodesic quasi-Euclidean distance transform and then converted to nanometers according to the image dimensions in order to generate the graph of 'local' volume versus length. The corresponding molecule is shown on the *right* with the predicted domains based on the predicted nucleotide number determined according to the cumulative volume along the main chain. Images are displayed using the MATLAB default falsecolor visualization (*green-magenta*) to overlay the *lines* onto the original image. Image dimensions are 200 × 200 nm^2

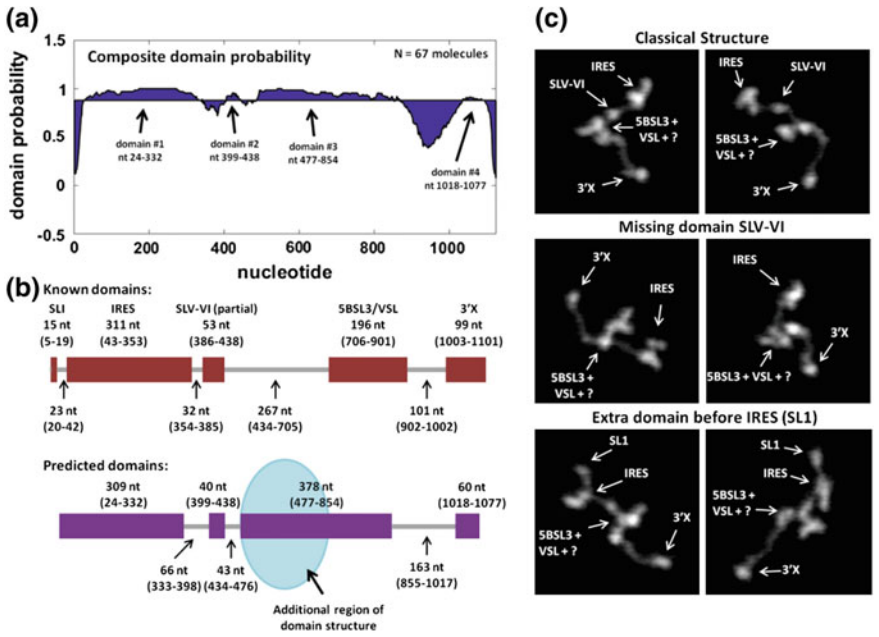

Fig. 3 Composite domain analysis in a JFH-1 HCV deletion mutant for N = 67 molecules. **a** The probability that a domain will be detected at each nucleotide value was calculated and plotted. The edges of the graph falsely have very low probabilities due to low height at the edge of the molecules. **b** Regions of expected structure based on previously described structures are shown on *top* and the predicted regions for each domain based on the domain probability in **a** are displayed below. **c** By sorting the molecules in the dataset, examples of conformational flexibility are observed. Image dimensions are 200 × 200 nm^2

By calculating the composite probability that a domain will be detected at each nucleotide for N = 67 molecules (Fig. 3a), another ~230 nt in addition to the 196 nt reported for the 5BSL and VSL regions (Fig. 3a, b) was predicted by our analysis, although this still remains to be confirmed for the full length HCV genome. Notably, this domain usually had an extended two-lobed structure suggesting that it is composed of 'subdomains'. The predicted nucleotides for each domain often vary from the predicted structures by as much as 50 nt, however there may be variations in the predicted value depending on how the domains may be oriented on the mica surface, and on the threshold used to define the region of domains. Additional sorting of the molecules also allows for alternative conformations of the molecules to be detected (Fig. 3c). For example, although many of the molecules in our dataset had the classical four domain structure, the second small domain (SLV-VI) was sometimes missing from a subset of the molecules. Additionally, in some molecules, the 15 nt SLI domain which precedes the IRES could be detected as a separate domain.

4 Conclusions

The experiments presented in this report demonstrate that AFM can be used as a versatile technique to image the secondary structure of a variety of long RNA molecules; and that a series of algorithms can select the molecule, extract information about the molecular morphology, identify the domain organization, and predict the nucleotides contained in each domain. Using these algorithms allowed for the identification of a larger domain structure than previously reported, and investigation of variations among the single-molecule images allows for the identification of the conformational flexibility of these molecules. This study has characterized the structure of only a small portion of the HCV genome at this time, but refinement of the algorithms to characterize the full genome structure should be possible in the near future.

Through the continued development of the algorithms, additional metrics for the identification of recurring domains can effectively be used for pattern recognition of various RNA molecules observed in our images. Also, assessment of the shape(s) and orientation(s) of each individual domain can also allow us to construct composite models of each domain structure as well as obtain information about the conformational flexibility of each domain. This may aid in the identification of which structures are most conserved amongst the molecules in our images and may help to guide scientists to the regions of RNA molecules which should be the focus of additional study. Combining our method with thermodynamic modeling or techniques with single nucleotide resolution such as SHAPE profiling may help to model the structure of RNA within the domain structures identified in our images.

Once the secondary structure is understood, AFM could also be used to assess how the molecules coalesce to form the compact tertiary structure. These experiments can be performed by imaging samples of RNA with varying Mg^{2+} concentrations, or by imaging dynamics of RNA folding in buffer conditions using high-speed AFM [10, 11]. To accommodate the increased height of folded molecules, the development of 3D algorithms to assess their structures would be beneficial. Finally, to study the role of the identified structures in viral processes, the addition of viral or host proteins known to interact with the RNA genome can aid in understanding the role the RNA genome plays in regulating the viral lifecycle. Additionally, the effects of changing environmental factors such as temperature, pH, or ionic conditions may help to understand changes in the RNA structure depending on differing cellular microenvironments. These studies could eventually have a significant impact on the understanding viral processes such as protein translation, genome replication, or genome packaging into viral particles.

Acknowledgments This work has been supported by a Grant-in-Aid for Scientific Research on Innovative Areas “Molecular basis of host cell competency in virus infection” (#24115003) from MEXT Japan. We also thank Dr. James Hejna for access to the MATLAB software.

References

1. Tellinghuisen, T.L., et al.: Studying hepatitis C virus: making the best of a bad virus. J. Virol. **81**, 8853–8867 (2007). doi:10.1128/JVI.00753-07
2. Sagan, S.M., et al.: cis-Acting RNA elements in the hepatitis C virus RNA genome. Virus Res. **206**, 90–98 (2015). doi:10.1016/j.virusres.2014.12.029
3. Gilmore, J.L., et al.: Nanoimaging of ssRNA: genome architecture of the Hepatitis C Virus revealed. J Nanomed. Nanotechnol. **S5** (2014). doi:10.4172/2157-7439.S5-010
4. Brion, P., Westhof, E.: Hierarchy and dynamics of RNA folding. Ann. Rev. Biophys. Biomol. Struct. **26**, 113–137 (1997). doi:10.1146/annurev.biophys.26.1.113
5. Tinoco Jr., I., Bustamante, C.: How RNA folds. J. Mol. Biol. **293**, 271–281 (1999). doi:10.1006/jmbi.1999.3001
6. Wakita, T., et al.: Production of infectious hepatitis C virus in tissue culture from a cloned viral genome. Nat. Med. **11**, 791–796 (2005). doi:10.1038/nm1268
7. Okuno, T., Hiruki, C.: Molecular biology and epidemiology of dianthoviruses. Adv. Virus Res. **87**, 37–74 (2013). doi:10.1016/B978-0-12-407698-3.00002-8
8. Mauger, D.M., et al.: Functionally conserved architecture of hepatitis C virus RNA genomes. Proc. Nat. Acad. Sci. **112**, 3692–3697 (2015). doi:10.1073/pnas.1416266112
9. MathWorks.: MATLAB and image processing toolbox release R2014b. (2014)
10. Gilmore, J.L., et al.: Single-molecule dynamics of the DNA-EcoRII protein complexes revealed with high-speed atomic force microscopy. Biochemistry **48**, 10492–10498 (2009). doi:10.1021/bi9010368
11. Suzuki, Y., et al.: Visual analysis of concerted cleavage by type IIF restriction enzyme SfiI in subsecond time region. Biophys. J. **101**, 2992–2998 (2011). doi:10.1016/j.bpj.2011.09.064

Recombinant Fluorescent Ligand of Potassium Kv1.1 and Kv1.3 Channels: Design, Properties and Applications

Alexey V. Feofanov, Kseniya S. Kudryashova, Anastasiya A. Ignatova and Oksana V. Nekrasova

Abstract Here we report on the development of the recombinant fluorescent ligand RFP-AgTx2 by fusing tagRFP fluorescent protein through a flexible linker with a peptide blocker of Kv1.x (x = 1, 3) channels, agitoxin 2 (AgTx2). RFP-AgTx2 can be easily produced in *E. coli* cells and purified in the folded functionally active form. The yield of RFP-AgTx2 achieves 100 mg per 1 L of bacterial culture that makes it the cheapest fluorescently labeled ligand of Kv1 channels. It is shown that RFP-AgTx2 binds to chimeric KcsA-Kv1.1 and KcsA-Kv1.3 channels with low nanomolar dissociation constants and is displaced from these complexes with Kv1.x pore blockers such as tetraethylammonium, AgTx2, kaliotoxin and OSK1. RFP-AgTx2 is an advanced fluorescent molecular tool to image Kv1 channels in cells and tissues. We present and discuss the distribution of Kv1 channels highlighted with RFP-AgTx2 in living rat glioma C6 and pheochromocytoma PC12 cells.

1 Introduction

Potassium ion channels constitute one of the most widespread superfamily and are present in all organism from bacteria to mammals [1]. K^+-channel modulators include metal ions, small organic molecules, venom-derived peptides and antibodies [2]. Peptide blockers from venomous animals (snakes, sea anemones, scorpions and others) are increasingly used in neurobiology due to their high affinity and selectivity. In particular, fluorescently labeled peptide blockers are widely applied for K^+-channel imaging in cells and tissues.

A.V. Feofanov (✉) · K.S. Kudryashova · A.A. Ignatova · O.V. Nekrasova
Biological Faculty, Lomonosov Moscow State University,
Leninskie Gory 1, 119992 Moscow, Russia
e-mail: avfeofanov@yandex.ru

A.V. Feofanov · K.S. Kudryashova · A.A. Ignatova · O.V. Nekrasova
Shemyakin-Ovchinnikov Institute of Bioorganic Chemistry, Russian Academy of Sciences,
ul. Miklukho-Maklaya 16/10, 117997 Moscow, Russia

A.Y. Oral and Z.B. Bahsi Oral (eds.), *3rd International Multidisciplinary Microscopy and Microanalysis Congress (InterM)*, Springer Proceedings in Physics 186,
DOI 10.1007/978-3-319-46601-9_2

Three basic approaches are currently used for fluorescent labeling of peptide blockers. A fluorophore can be attached to the N-terminal NH_2-group of the peptide at the last step of a solid phase peptide synthesis. Alternatively, peptide can be conjugated with an amino-reactive organic label in solution via any free NH_2-group (including N-terminal group, amino-groups of Lys and Arg side chains). Pre-modified peptides bearing additional Cys residue or a biotinylated amino acid can be labeled with a thiol-reactive dye or a (strept)avidin-conjugated fluorophore, respectively. Main limitations of these approaches relate to the high cost of a commercial synthesis of a labeled peptide as well as to low reaction yields in the case of labeling in solution. Last limitation becomes a big problem when multiple sites of labeling are present in the peptide, and separation of different variants of labeled peptide is required.

Here we report on the development of a new type of fluorescent probes for the studies of voltage-gated potassium Kv1-channels. The new probe consists of the peptide blocker of Kv1-channels fused by a flexible linker with a fluorescent protein. In our bioengineering construct RFP-AgTx2, a red fluorescent protein TagRFP (RFP) and agitoxin 2 (AgTx2) are used as a fluorophore and a channel blocker, respectively. This recombinant chimeric protein is produced with a high yield in *E. coli* cells, preserves high affinity and specificity to target channels and has a wide spectrum of applications.

2 Materials and Methods

Chimeric RFP-AgTx2 protein was expressed in *E. coli* Rosetta-gami (DE3) pLysS strain transformed with pET23-RFP-AgTx2 plasmid. Recombinant protein was purified from soluble cytoplasmic fraction by Ni-affinity chromatography and further by gel-filtration on a Superdex 75 10/300 GL column.

E. coli BL21 (DE3) cells that express KcsA-Kv1.1 or KcsA-Kv1.3 hybrid channels in the inner membrane were obtained as described earlier [3, 4]. Protocols of cell cultivation and preparation of spheroplasts can be found elsewhere [3, 4]. Spheroplasts staining with RFP-AgTx2 and competitive binding with Kv1.x pore blockers was performed in the buffer: 10 mM Tris-HCl (pH 7.5), 0.1 % bovine serum albumin, 0.25 M sucrose, 10 mM MgCl2, 4 mM KCl, 0.3 mM EDTA. Recombinant agitoxin-2 (AgTx2), kaliotoxin (KTX) and OSK1 were produced by us and purified as described earlier [5, 6].

Rat pheochromocytoma PC-12 cells was cultured in Roswell Park Memorial Institute (RPMI) 1640 medium with 10 mM HEPES, whereas rat glioma C6 cells were grown in a Dulbecco's minimum essential medium at 5 % CO_2, 37 °C in a humidified atmosphere (95 %). Both growth media were supplemented with 8 % fetal calf serum (FCS) and 2 mM L-glutamine. The day before microscopic experiments C6 and PC-12 cells were transferred into corresponding culture medium with 2 % FCS but without phenol red (to reduce background fluorescence).

Cells were thoroughly washed with a Hank's balanced salt solution, incubated with RFP-AgTx2, rinsed again and analyzed with confocal laser scanning microscopy (CLSM).

CLSM measurements of spheroplasts were performed with the LSM 710 microscope (Zeiss, Germany) using the αPlan-Apochromat objective (NA 1.46 × 63) and the 543.5 nm excitation wavelength. Fluorescence of RFP-AgTx2 was registered within the 560–760 nm range. In CLSM of eukaryotic cells, fluorescence of RFP-AgTx2 was excited with the 561 nm wavelength and detected within the 570–650 nm region.

3 Results and Discussion

AgTx2 from *Leiurus quinquestriatus* scorpion venoms is a well known high-affinity pore blocker of Kv1.1 and Kv1.3 channels that acts at subnanomolar concentrations. It can be produced as a recombinant molecule in *E. coli* [7]. To obtain recombinant fluorescent AgTx2, the peptide was fused to TagRFP via 50 a.a. linker, which included 6xHis-Tag. TagRFP is a widely used tag for cellular and animal fluorescent microscopy imaging, but it was never fused with peptide pore blockers of K^+-channels. N-terminal location of TagRFP in the RFP-AgTx2 was dictated by the known structural organization of a blocker-channel complex, in which N-terminus of a peptide is exposed to solvent and not involved in interactions with a channel [7]. Long flexible linker was introduced between TagRFP and AgTx2 to avoid considerable disturbance of blocker-channel interactions.

After careful optimization of cell growth and protein expression, the high yield of recombinant RFP-AgTx2 was achieved (ca. 100 mg per 1 L of a bacterial culture). Fluorescence excitation and emission spectra of RFP-AgTx2 and TagRFP were found to be very similar (not shown) indicating correct folding of a fluorescent protein in RFP-AgTx2. Peptide portion of RFP-AgTx2 was cleaved off with TEV protease, isolated by reverse-phase HPLC and analyzed by MALDI MS. The measured molecular mass of the peptide corresponded to that of native AgTx2, in which three disulfide bonds were formed indicating that the peptide blocker adopted a correctly folded conformation in RFP-AgTx2.

To characterize affinity of RFP-AgTx2 to Kv1-channels, the spheroplasts were used, which expressed KcsA-Kv1.1 or KcsA-Kv1.3 hybrid channels in plasma membrane. As shown with the CLSM-based approach earlier [3–5, 7, 8], such hybrid channels bind specifically with pore blockers of Kv1-channels, and dissociation constants of these complexes correspond to the constants estimated with electrophysiological techniques on native Kv1-channels. As revealed with CLSM, RFP-AgTx2 but not TagRFP binds to KcsA-Kv1.x (x = 1, 3) channels on spheroplast membrane (Fig. 1) and demonstrates concentration-dependent saturation of binding in a low nanomolar range of concentrations (data not shown). RFP-AgTx2 binds very weakly to spheroplasts expressing KcsA and to

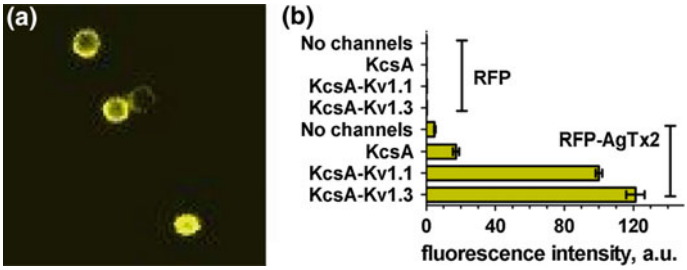

Fig. 1 **a** An example of CLSM images of KcsA-Kv1.3-bearing spheroplasts stained with RFP-AgTx2. Bar is 2 μm. **b** Comparison of binding of RFP-AgTx2 (10 nM) and TagRFP (10 nM) to KcsA-Kv1.1-, KcsA-Kv1.3- and KcsA-bearing spheroplasts as well as to spheroplasts without recombinant channels (no channels)

spheroplasts without hybrid channels (Fig. 1b). RFP-AgTx2 is replaced from complexes with hybrid channels by Kv1 pore blockers such as tetraethylammonium, AgTx2, KTX and OSK1 (data not shown) that confirms additionally the specific type of interactions between RFP-AgTx2 and KcsA-Kv1.x (x = 1, 3). Evidently, RFP-AgTx2 is a reliable alternative to rhodamine labeled AgTx2, which is an essential component of our cellular systems for search and study of Kv1 pore blockers in animal venoms [5, 6, 8, 9].

High affinity of RFP-AgTx2 to Kv1.1 and Kv1.3 opens a possibility to apply fluorescent chimeric proteins for investigation of distribution of Kv1-channels in eukaryotic cells. In cells expressing Kv1-channels endogenously, amount of these channels can be rather low, and analysis of their localization and distribution in situ is a challenging task with any molecular instrument, either fluorescently labeled peptide blockers or antibodies.

C6 cells are known to express Kv1.1 channels [10]. RFP-AgTx2 accumulated in cytoplasm of C6 cells in granular structures (Fig. 2a). No membrane staining with

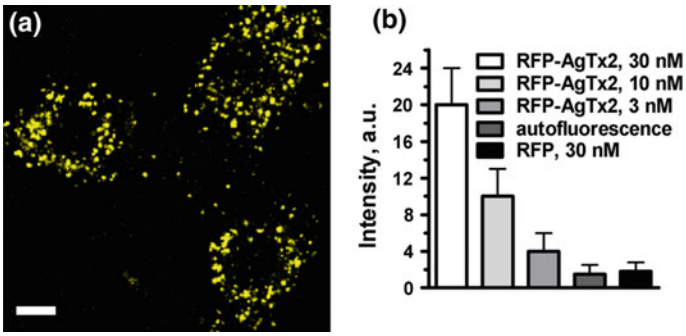

Fig. 2 **a** CLSM analysis of RFP-AgTx2 distribution in living C6 cells. Cells were stained with 30 nM RFP-AgTx2 for 1 h. Bar is 5 μm. **b** Average fluorescence intensities of RFP-AgTx2 and TagRFP in C6 cells (1 h incubation) as compared to cellular autofluorescence intensity

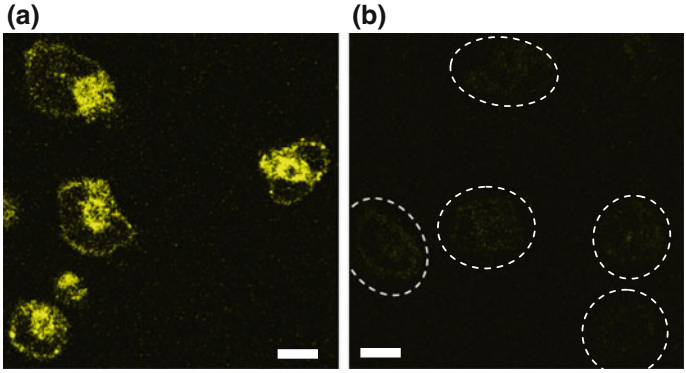

Fig. 3 CLSM analysis of distribution of RFP-AgTx2 (**a**) and TagRFP (**b**) in living PC12 cells. Cells were stained with 30 nM RFP-AgTx2 (**a**) or TagRFP (**b**) for 1 h. Bar is 10 μm. *Dashed ovals* in panel **b** mark locations of cells

RFP-AgTx2 was detected. This pattern is reproduced at different concentrations of RFP-AgTx2. Intracellular accumulation of RFP-AgTx2 varies as a function of its extracellular concentration (Fig. 1b). One can suppose that RFP-AgTx2 binding to Kv1.1 on membrane of C6 cells is accompanied with fast internalization of complexes, intracellular release of the blocker and recycling of Kv1.1 channels to membrane.

In contrast to C6 cells, complexes of RFP-AgTx2 with Kv1.3 channels in PC12 cells are observed on plasma membrane, and only restricted fraction of RFP-AgTx2 is internalized (Fig. 3a). Distribution of RFP-AgTx2 on plasma membrane is non-uniform: particular bright clusters are distinctly observed. TagRFP does not bind to PC12 cells, and a level of autofluorescence was much lower than the RFP-AgTx2 signal in cells (Fig. 3b). These control measurements as well as data on endogenous expression of Kv1.3 (along with other Kv channels) [11] confirm that RFP-AgTx2 binding to PC12 cells is specific.

4 Conclusions

A novel RFP-tagged peptide blocker of Kv1-channel was obtained by simple protein engineering technique avoiding any chemical modifications. Using membrane-embedded hybrid KcsA-Kv1.1 and KcsA-Kv1.3 channels we confirmed that RFP-AgTx2 retained nanomolar affinity to Kv1 channels. We have demonstrated an applicability of RFP-AgTx2 for optical microscopy investigation of cellular distribution and trafficking of Kv1-channels in different cells as well as for CLSM-based analytical test-systems. We argue that tagged Kv1 pore blockers such as RFP-AgTx2 can be used for localization and imaging of their targets and can efficiently substitute peptide ligands labeled with organic fluorophores in most neurobiology applications.

Acknowledgments This work was supported by the Russian Science Foundation (grant no. 14-14-00239). We thank A. Kuzmenkov and Dr. A.Vassilevskiy (Shemyakin-Ovchinnikov Institute of Bioorganic Chemistry) for collaboration in the pioneering development of recombinant fluorescent ligands of Kv1 channels.

References

1. Tian, C., Zhu, R., Zhu, L., Qiu, T., Cao, Z., Kang, T.: Potassium channels: structures, diseases, and modulators. Chem. Biol. Drug Des. **83**, 1–26 (2014). doi:10.1111/cbdd.12237
2. Wulff, H., Castle, N.A., Pardo, L.A.: Voltage-gated potassium channels as therapeutic targets. Nat. Rev. Drug Discov. **8**, 982–1001 (2009). doi:10.1038/nrd2983
3. Nekrasova, O.V., Ignatova, A.A., Nazarova, A.I., Feofanov, A.V., Korolkova, Y.V., Boldyreva, E.F., Tagvei, A.I., Grishin, E.V., Arseniev, A.S., Kirpichnikov, M.P.: Recombinant Kv channels at the membrane of *Escherichia coli* bind specifically agitoxin2. J. Neuroimmune Pharmacol. **4**, 83–91 (2009). doi:10.1007/s11481-008-9116-4
4. Nekrasova, O., Tagway, A., Ignatova, A., Feofanov, A., Kirpichnikov, M.: Studying of membrane localization of recombinant potassium channels in *E. coli*. Acta Naturae **1**, 91–95 (2009)
5. Kudryashova, K.S., Nekrasova, O.V., Kuzmenkov, A.I., Vassilevski, A.A., Ignatova, A.A., Korolkova, Y.V., Grishin, E.V., Kirpichnikov, M.P., Feofanov, A.V.: Fluorescent system based on bacterial expression of hybrid KcsA channels designed for Kv1.3 ligand screening and study. Anal. Bioanal. Chem. **405**, 2379–2389 (2013). doi:10.1007/s00216-012-6655-6
6. Kuzmenkov, A.I., Vassilevski, A.A., Kudryashova, K.S., Nekrasova, O.V., Peigneur, S., Tytgat, J., Feofanov, A.V., Kirpichnikov, M.P., Grishin, E.V.: Variability of potassium channel blockers in Mesobuthus eupeus scorpion venom with focus on Kv1.1: an integrated transcriptomic and proteomic study. J. Biol. Chem. **290**, 12195–12209 (2015). doi:10.1074/jbc.M115.637611
7. Yu, L., Sun, C., Song, D., Shen, J., Xu, N., Gunasekera, A., Hajduk, P.J., Olejniczak, E.T.: Nuclear magnetic resonance structural studies of a potassium channel—charybdotoxin complex. Biochemistry **44**, 15834–15841 (2005). doi:10.1021/bi051656d
8. Hoang, A.N., Vo, H.D., Vo, N.P., Kudryashova, K.S., Nekrasova, O.V., Feofanov, A.V., Kirpichnikov, M.P., Andreeva, T.V., Serebryakova, M.V., Tsetlin, V.I., Utkin, Y.N.: Vietnamese Heterometrus laoticus scorpion venom: evidence for analgesic and anti-inflammatory activity and isolation of new polypeptide toxin acting on Kv1.3 potassium channel. Toxicon **77**, 40–48 (2014). doi:10.1016/j.toxicon.2013.10.027
9. Anh, H.N., Hoang, M., Do, V., Kudryashova, K.S., Nekrasova, O.V., Feofanov, A.V., Andreeva, T.V., Tsetlin, V.I., Utkin, Y.N.: Hetlaxin, a new toxin from the Heterometrus laoticus scorpion venom, interacts with voltage-gated potassium channel Kv1.3. Dokl. Biochem. Biophys. **449**, 109–111 (2013). doi:10.1134/S1607672913020142
10. Zhu, J., Yan, J., Thornhill, W.B.: The Kv1.3 potassium channel is localized to the cis-Golgi and Kv1.6 is localized to the endoplasmic reticulum in rat astrocytes. FEBS J. **281**, 3433–3445 (2014). doi:10.1111/febs.12871
11. Conforti, L., Millhorn, D.E.: Regulation of shaker-type potassium channels by hypoxia. Adv. Exp. Med. Biol. **475**, 265–274 (2000)

Single-Particle FRET Microscopy of Immobilized Nucleosomes: Technique Development

Alexey V. Feofanov, Oleg V. Chertkov, Kseniya S. Kudryashova, Yaroslav O. Ivanov, Vasily M. Studitsky and Mikhail P. Kirpichnikov

Abstract Mononucleosomes formed by histone octamer and short DNA is an advanced model system for investigation of RNA polymerase (RNAP) transcription and its modulation with various transcription factors. Recent achievements of fluorescent microscopy allow one to complement these studies with single-particle Forster resonance energy transfer (spFRET) analysis. FRET efficiency between Cy3 and Cy5 dyes introduced in the neighboring coils of nucleosomal DNA is a sensor of structural changes caused by DNA unwrapping or looping, or restoration of DNA-histone interactions. Here we report on experimental setup and protocols for spFRET microscopy of immobilized nucleosomes. Using confocal laser scanning and total internal reflection fluorescence microscopy we demonstrated preservation of the nucleosome structure during immobilization and long-term (>100 s, ca. 140 ms/frame) spFRET kinetic measurements. The effect of ionic strength on nucleosome structure was studied. Applications of spFRET microscopy of immobilized nucleosomes include analysis of their structural dynamics (DNA "breathing"), kinetics of formation/dissociation of DNA-protein complexes, formation and structure of stalled elongation complexes with RNAP, as well as conformational transitions in nucleosome structure in the course of transcription.

A.V. Feofanov (✉) · O.V. Chertkov · K.S. Kudryashova · Y.O. Ivanov
V.M. Studitsky · M.P. Kirpichnikov
Biological Faculty, Lomonosov Moscow State University,
Leninskie Gory 1, 119992 Moscow, Russia
e-mail: avfeofanov@yandex.ru

A.V. Feofanov · O.V. Chertkov · K.S. Kudryashova · M.P. Kirpichnikov
Shemyakin-Ovchinnikov Institute of Bioorganic Chemistry, Russian Academy of Sciences,
ul. Miklukho-Maklaya 16/10, 117997 Moscow, Russia

V.M. Studitsky
Cancer Epigenetics Program, Fox Chase Cancer Center, Philadelphia, USA
e-mail: Vasily.Studitsky@fccc.edu

A.Y. Oral and Z.B. Bahsi Oral (eds.), *3rd International Multidisciplinary Microscopy and Microanalysis Congress (InterM)*, Springer Proceedings in Physics 186,
DOI 10.1007/978-3-319-46601-9_3

1 Introduction

Precisely positioned mononucleosomes formed on a short (~250–500-bp) DNA fragment containing the T7A1 promoter are widely and successfully used in analyses of important aspects of RNA polymerase (RNAP) transcription and its modulation by different protein factors using modern biochemical and molecular biology approaches [1, 2]. The progress in the development of advanced fluorescent microscopy techniques allows one to complement and extend these studies with single-particle Forster resonance energy transfer (spFRET) analysis. Adaptation of mononucleosomes for spFRET microscopy was achieved by precise covalent labeling of non-transcribed DNA strand in the neighboring coils of nucleosomal DNA with Cy3 and Cy5 fluorophores [3–5]. Analysis of transcripts by DNA polyacrylamide gel electrophoresis confirmed that the introduction of fluorescent labels in the nucleosome had no significant impact on the transcription. FRET efficiency between Cy3 and Cy5 was shown to be a reliable sensor of structural changes caused by DNA unwrapping from the octamer or DNA looping, or restoration of the DNA-histone interactions. Our previous spFRET studies were performed in diluted solutions by measuring FRET from freely diffusing single nucleosomes [3–5]. According to our experience, spFRET microscopy is indispensable for analysis of complex heterogeneous systems and characterization of structurally different subpopulations of nucleosomes and their complexes. However, experiments with freely diffusing nucleosomes do not allow one to follow structural dynamics at the level of single complexes. This restriction can be overcome by nucleosome immobilization. In the present work we report on the development of an experimental setup and approaches for spFRET microscopy of immobilized nucleosomes.

2 Materials and Methods

Template 603 DNA labeled with Cy3 and Cy5 dyes and containing T7A1 promoter was obtained as described in [3, 5]. Mononucleosomes were prepared on the basis of the H1-depleted donor chromatin from chicken erythrocytes as described in [1]. Nucleosomes were ligated through *Tsp*RI site to an additional DNA fragment (178 base pairs) having biotinylated 5′-terminal cytosine (Fig. 1a).

Cleaned cover glasses and microscope slides were treated with an ethanol solution of silane-polyethyleneglycol (silane-PEG, 2 kDa), and silane-PEG-biotin (2 or 5 kDa, Nanocs, USA) mixed in the proportion of 100:1 by weight. After washing and drying, a microfluidic cell was assembled from a cover glass and a microscope slide (treated sides in) using a double-sided Skotch® tape. To immobilize nucleosomes, streptavidin (10 ng/ml) was pre-bound to biotin-PEG-silane on the walls of a microfluidic cell, and nucleosomes (0.5 nM, 30 μl) were added to the

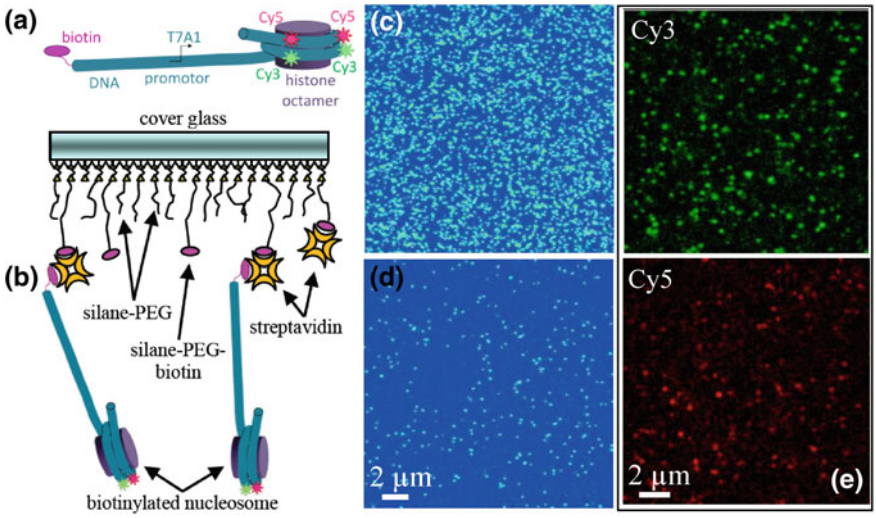

Fig. 1 Immobilization of mononucleosomes on glass. **a** Schematic structure of a fluorescently labeled mononucleosome ligated with biotinylated DNA fragment. Two alternatively positioned pairs of Cy3 and Cy5 labels on adjacent coils of nucleosomal DNA are shown. **b** Scheme of immobilization of biotinylated nucleosomes via high-affinity streptavidin-biotin complexes. **c**, **d** Confocal laser scanning microscopy (CLSM) images of distribution of single molecules of Cy3-avidin immobilized with silane-PEG-biotin at the concentration of Cy3-avidin of 100 ng/ml (**c**) and 10 ng/ml (**d**). **e** Typical images of Cy3 and Cy5 fluorescence from single immobilized nucleosomes measured with CLSM

cell for 5 min in the buffer 20 mM Tris–HCl (pH 8.0), 5 mM $MgCl_2$, 2 mM 2-mercaptoethanol, 150 mM KCl, 0.1 % poly(ethylene glycol) (ca. 400 Da). Non-bound nucleosomes were washed out with the buffer before measurements.

spFRET measurements were performed with either the SP2 laser scanning confocal microscope (Leica, Germany) using avalanche photodiode (APD) detectors and the HCX PL APO objective (100×, 1.46 NA), or a total internal reflection fluorescence (TIRF) microscopy setup described below. Fluorescence was excited with the 514.5 nm laser line of an Ar^+-ion laser (2 and 240 µW at a specimen in confocal laser scanning microscopy (CLSM) and TIRF microscopy measurements, respectively). Laboratory assembled experimental setup for spFRET TIRF microscopy (Fig. 2a, b) includes Ar^+-ion laser (Lasertechnik GmbH, Germany), inverted microscope AxioObserver (Zeiss, Germany) with TIRF module and αPlan-Apochromat objective (100×, 1.46 NA), OptoSplit II module (Cairn Research, UK) and EMCCD iXon Ultra 897 (Andor, UK). Fluorescence of Cy3 and Cy5 was recorded in the 535–607 and 635–800 nm ranges, respectively.

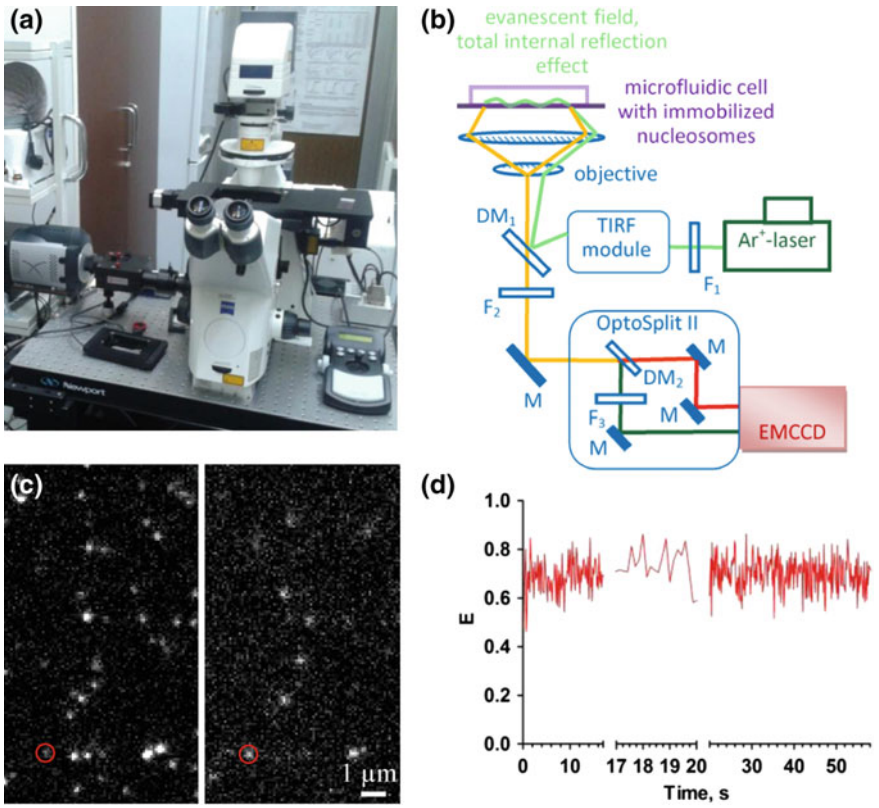

Fig. 2 An experimental setup for spFRET TIRF microscopy (**a**) and its block-scheme (**b**). F_1 is the BP514/10 narrow band filter (Zeiss, Germany). DM_1 and DM_2 are the Di01-R532 and FF635-Di01 dichroic mirrors, respectively (SemRock, USA). F_2 is the ET525LP long-pass barrier filter (Chroma Technology, USA). F_3 is the FF01-571/72 band filter (SemRock). M is a mirror. **c** Typical images of Cy3 (*left*) and Cy5 (*right*) fluorescence from single immobilized nucleosomes measured with the experimental setup for spFRET TIRF microscopy. **d** Time dependence (140 ms/frame) of the *E* value for a nucleosome marked with a *red circle* in panel **c**

Fluorescence intensities of Cy3 (I_3) and Cy5 (I_5) of single immobilized nucleosomes were recalculated into FRET efficiencies (E) using equation

$$E = (I_5 - 0.14 \times I_3)/(I_5 + 0.86 \times I_3), \quad (1)$$

where factors 0.14 and 0.86 provided correction for the contribution of Cy3 fluorescence in the Cy5 detection channel (spectral cross-talk). FRET efficiencies calculated for nucleosome samplings were presented as frequency distribution histograms or as time dependences.

3 Results and Discussion

Fluorescent mononucleosomes, which were developed earlier [3–5], were ligated with a biotinylated DNA fragment (Fig. 1a) and immobilized on a glass surface of a microfluidic cell modified with a mixture of silane-PEG and silane-PEG-biotin (100:1 by weight) (Fig. 1b).

Studies of modified glass surfaces using CLSM and Cy3-labeled avidin (eukaryotic analog of streptavidin) revealed the high density of a silane-PEG-biotin distribution (Fig. 1c). For spFRET microscopy, distances between immobilized nucleosomes should exceed several times a microscope resolution. Accordingly, surface density of immobilized nucleosomes was adjusted by optimizing a streptavidin concentration (Fig. 1d).

CLSM with APD detectors was found to be sufficiently sensitive to perform spFRET measurements of immobilized nucleosomes (Fig. 1e) but restricted in the speed of measurements. One-two seconds were required to record nucleosome images with a high signal-to-noise ratio using the point-by-point scanning algorithm of CLSM.

Increased temporal resolution was achieved with TIRF microscopy, which is based on the wide field simultaneous excitation and detection of immobilized molecules. An experimental setup for spFRET TIRF microscopy was assembled with a careful selection of filters and dichroic mirrors having high throughput for Cy3 and Cy5 fluorescence and manifold increased suppression at the excitation wavelength (514.5 nm, Fig. 2a, b). Extremely sensitive EMCCD camera is another key element of this setup. Exposure time to image immobilized nucleosomes with our TIRF microscopy setup can be as low as 100 ms (plus 40 ms for EMCCD reading, Fig. 2c).

Immobilization on the glass modified with 2 kDa silane-PEG-biotin and 2 kDa silane-PEG was accompanied by structural destabilization even in the central part of a nucleosome, which was detected as an essential decrease in E value (not shown). Addition of bovine serum albumin (1 mg/ml) or 1 % PEG in the buffer did not stabilize a nucleosome structure (not shown). The problem was solved by using 5 kDa silane-PEG-biotin in a combination with 2 kDa silane-PEG (Fig. 3a). It seems that the increased length of 5 kDa silane-PEG-biotin molecules reduced a probability of destabilizing interactions of nucleosomes with a surface.

A nucleosome structure was found to be stable during at least 40 min after immobilization and was not perturbed during buffer changes in a microfluidic cell. It was demonstrated that a time lapse for a continuous measurement of immobilized nucleosomes without fluorophore photobleaching could be 100 s or even longer.

Using spFRET TIRF microscopy we have studied the effect of ionic strength on the structure of immobilized nucleosomes. It was found that an increase in KCl concentration from 150 to 600 mM induced rather moderate changes in DNA packing on a histone core and only for small fraction of nucleosomes (Fig. 3a), although a loss of the H2A-H2B histone dimer could occur at 600 mM KCl. However kinetic analysis of single nucleosomes revealed a considerable increase in

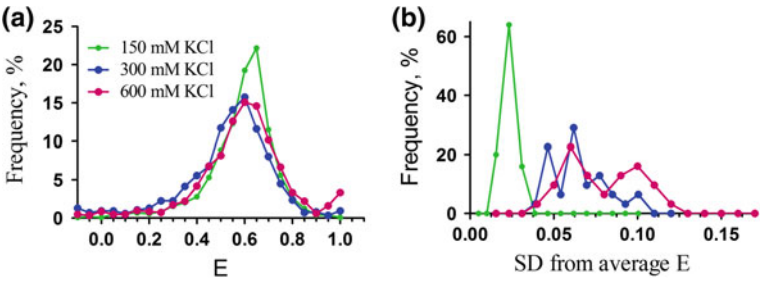

Fig. 3 Effect of ionic strength on a nucleosome structure studied with spFRET TIRF microscopy. **a** Frequency histograms of FRET efficiency (*E*) for immobilized nucleosomes at different KCl concentrations in the buffer. Cy3 and Cy5 labels were placed in the central region of nucleosomal DNA [5]. **b** Frequency histograms of standard deviations from average *E* values measured for single nucleosomes in kinetics at different KCl concentrations

the amplitude of temporal fluctuations of E value (estimated as a standard deviation from an average E value for each measured nucleosome) at the increase in KCl concentration (Fig. 3b). Thus high ionic strength likely induces and facilitates periodic unwrapping of DNA from histone core, so called DNA breathing.

The developed experimental setup and protocols for time-resolved spFRET microscopy of immobilized nucleosomes provide us with new possibilities for analysis of structural dynamics of nucleosomes (DNA "breathing"), kinetics of formation/dissociation of various DNA-protein complexes, formation and structure of an extensive set of stalled elongation complexes with RNAP, as well as conformational transitions in nucleosome structure in the course of transcription.

Acknowledgments This work was supported by Russian Science Foundation (grant 14-24-00031).

References

1. Gaykalova, D.A., Kulaeva, O.I., Bondarenko, V.A., Studitsky, V.M.: Preparation and analysis of uniquely positioned mononucleosomes. Methods Mol. Biol. **523**, 109–123 (2009). doi:10.1007/978-1-59745-190-1_8
2. Gaykalova, D.A., Kulaeva, O.I., Pestov, N.A., Hsieh, F.K., Studitsky, V.M.: Experimental analysis of the mechanism of chromatin remodeling by RNA polymerase II. Methods Enzymol. **512**, 293–314 (2012). doi:10.1016/B978-0-12-391940-3.00013-5
3. Kudryashova, K.S., Chertkov, O.V., Nikitin, D.V., Pestov, N.A., Kulaeva, O.I., Efremenko, A.V., Solonin, A.S., Kirpichnikov, M.P., Studitsky, V.M., Feofanov, A.V.: Preparation of mononucleosomal templates for analysis of transcription with RNA polymerase using spFRET. Methods Mol. Biol. **1288**, 395–412 (2015). doi:10.1007/978-1-4939-2474-5_23
4. Feofanov, A.V., Kudryashova, K.S., Chertkov, O.V., Nikitin, D.V., Pestov, N.A., Kulaeva, O.I., Studitsky, V.M., Kirpichnikov, M.P.: Analysis of nucleosome transcription using single-particle FRET. Springer Proc. Phys. **164**, 255–260 (2015). doi:10.1007/978-3-319-16919-4_33

5. Kudryashova, K.S., Nikitin, D.V., Chertkov, O.V., Gerasimova, N.S., Valieva, M.E., Studitsky, V.M., Feofanov, A.V.: Development of fluorescently labelled mononucleosomes to study transcription mechanisms by method of microscopy of single complexes. Moscow Univ. Biol. Sci. Bull. **70**, 189–193 (2015). doi:10.3103/S0096392515040069

Post Embryonic Changes in the Eye of an Economic Mango Plant Pest *Amritodus atkinsoni* Leth. (Hemiptera: Membracoidea: Cicadellidae)

Seetha Seetha, Sheetal Sahu, Biswa Bhusana Mahapatra and Monalisa Mishra

Abstract Mango hopper, *Amritodus atkinsoni* is a serious pest of mango, which may cause up to 50 % crop loss in cases of severe infestation. It leads to large economic loss, as mango is of great economic importance. *Amritodus atkinsoni* possess two compound eye on either side of the head. Eye plays an important role in the growth and development of the organism. It helps in locating of food as well as partner for mating. Compound eye is known as matching eye to the environment, which undergoes modification with habitat. During the time of development from nymph to adult, remarkable changes are seen in the pattern of food intake and habitat. Young ones of this species prefer feeding on sap of leaves and fruits compared to the adults, which are seen on the barks. Taking this idea we checked for changes in the eye at various developmental stages. The pattern of structural change was examined under scanning electron microscope (SEM). Under SEM the eye possesses numerous functional units called ommatidia and occasionally corneal hairs are present in the eye. At higher magnification the cornea appears rough. More importantly with the increase of age the body length increases which is correlated with the eye size. The functional units, or the ommatidia also change with the size of the animal. With the change in eye size probably the sensitivity changes and thus make the animal more sensitive towards light resulting the change of habitat with age.

1 Introduction

Many crustaceans and hemimetabolous insects grow throughout its lifespan. Along with the body size eye size changes and so is it's functionality [1, 2]. In comparison to the other aspects of compound eye the post embryonic change is least studied. Only a handful of literature is available on post-embryonic growth of insect's

S. Seetha · S. Sahu · B.B. Mahapatra · M. Mishra (✉)
Department of Life Science, National Institute of Technology Rourkela, Rourkela, Odisha, India
e-mail: mishramo@nitrkal.ac.in

A.Y. Oral and Z.B. Bahsi Oral (eds.), *3rd International Multidisciplinary Microscopy and Microanalysis Congress (InterM)*, Springer Proceedings in Physics 186,
DOI 10.1007/978-3-319-46601-9_4

compound eye. Change of eye size and structure with age of stick insect *Carausius morosus* is reported by Meyer-Rochow and Keskinen [1]. Another post embryonic age dependent eye ultrastructure study is described from spittle bug *Philaenus spumarius* [2]. In this study how the eye ultrastructure changes to cope with age and environment is demonstrated. Later the post embryonic change of the same insect was reinvestigated by Forlove et al. [3]. Forlove et al., pronounced the change of biophysical property of the eye with age. Additional post embryonic study from *Cimex lectularius* reported change in facet size and number with the increase of body size of the animal [4]. All the age dependent study concluded that with the change of eye reflects the change in behaviour of animal life either by switching the habitat or from diurnal to nocturnal life style.

Hemiptera are the sap sucking insects causes enormous harm to many economic plants. Hemiptera are hemimetabolous insects in which the nymph resemblance with adult and it grows to many developmental stages in it's life span. Along with the body size eye size also changes with each stage of development. Change in eye size affects the behaviour of the animal to certain extend [2, 3]. In comparison to other insects the eye of Hemipteran is least studied. Settembrini, reported that less information is known in terms of post embryonic change in number and size of the functional units of the eye for Hemipteran [5]. Later Fischer et al. describe the compound eye of Hemipterans [6]. Doring and Sapthe calculated the eye size and the acuity of a Hemipetera *Acanthisiphon pisum* [7]. Recently Baker et al. correlated the eye size with body size in bed bugs, *Cimex lectularius* [4]. The current study aims to investigate the post embryonic change of another economic important mango pest *Amritodus atkinsoni* Leth not described in earlier studies.

2 Experimental

A. atkinsoni Leth causes major damage to mango trees in India [8, 9] were collected from May to June 2015 from NIT Rourkela, Rourkela Campus, Odisha, India (latitude and longitude of 22.25 N and 84.90 E respectively) for this study. The *A. atkinsoni* was characterized and confirmed as per the description of Anufriev [10]. The adult ones are generally found on the barks of the mango tree during midday only and they were collected by means of sticky tape from mango tree barks. The nymphs are collected at night by using light bulbs as they are flying it is difficult to catch them during the day. Various insects were staged as per their length of the body. Live samples were collected and the whole body was fixed for scanning electron microscopy. Although air drying is used for the preparation of many insect eyes air drying method it did not work well for *A. atkinsoni* (Nayak et al., in preparation). Samples were fixed with 2.5 % glutaraldehyde and 2 % paraformaldehyde diluted in PBS at 4 °C. Next day samples were dehydrated in gradual dehydration method with series of ethanol. The dried samples were mounted on a stub with double adhesive carbon sticky tape. Samples were coated with platinum in a sputter coater (JEOL-JFC-1600 auto fine coater) for 45 s. The

samples were placed under scanning electron microscopy (JSM-M6480-LV) and imaged from appropriate regions. All the measurements of SEM were done by using ImageJ 1.48v software.

3 Results and Discussion

Mango hoppers *A. Atkinsoni* used in the current study was characterised by its broad round head, with extending a little between both the eyes (Fig. 1). The adults are 4.2–5 mm in size with dark grey in color with two distinct spot on abdomen as well as scutellum as reported earlier Anufriev [10]. The nymphs are green in color and the length of the flying nymphs varies from 2.8 to 3.5 mm. Debnath reported the differential distribution of *A. atkinsoni* pest in different parts of the mango tree [11]. In this paper highest amount of *A. atkinsoni were* found on the primary branch near the trunk whereas tertiary branches have lowest amount of insects. We also observed the adults prefer the bark of trunk whereas the nymphs are flying around in the tertiary branches. Debnath et al., advocated the differential distribution of the *A. atkinsoni* in different parts of the tree help the mango hopper to provide better survivability. What brings the variation in terms of the distribution of these insects in different parts of the tree was not mentioned in that paper. Study of various insect eyes reported the change in the niche occupation is often scaled with the change in eye size and structure of the pest to provide better survivability.

To know the relationship of the eye with shift of habitat various stages of *A. atkinsoni*, were observed under Scanning electron microscope. Like other insects *A. atkinsoni*, possess two compound eyes on either side of the head (Fig. 2). Although

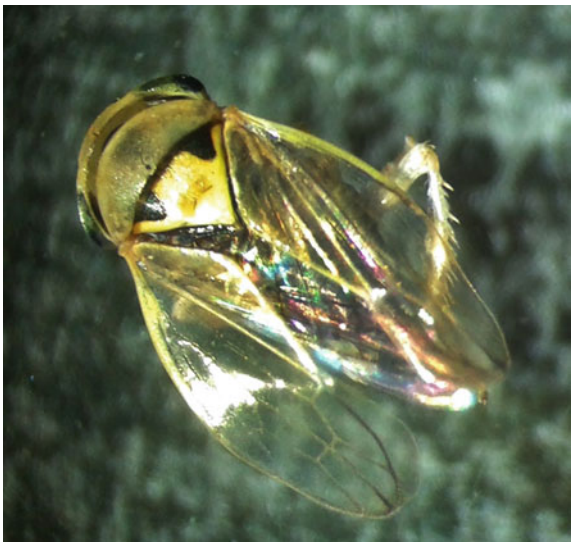

Fig. 1 Light micrograph of *A. Atkinsoni* taken under stereo microscope. Note the black convex eyes present on either side of the head. Note the two dark patches on the anterior part of the abdomen

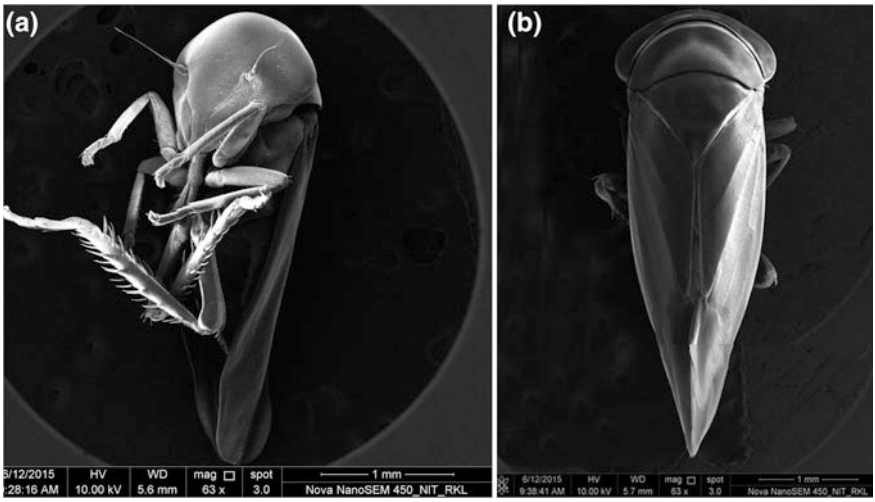

Fig. 2 Scanning electron micrograph of nymph and adult of *A. Atkinsoni*. **a** Nymph. **b** adult. Note the size and shape difference between both the eyes

there are two distinct black spot on the abdomen and scutellum in adults under light microscope such structures are hard to distinguish under scanning electron microscope. (Fig. 2a, b). In nymphs the curvature of the eye matches with the curvature of the head whereas the eyes are bulging in adults (Fig. 2a, b). In nymphs the eye appears circular whereas in adults the eyes are oval in shape (Fig. 3a). Each eye is composed on numerous functional units called ommatidia (Fig. 3b, c). The ommatidia are hexagonal in shape and tightly packed with each other (Fig. 3c). The lose arrangement of the facets depict poor vision whereas with tight hexagonal facets, the resolution of the eye expected to be high. Irregular ommatidia as reported in other species are not found for *A. atkinsoni.* At higher magnification corneal hairs are found. In nymphs corneal hairs are –present only at the central part of the eye. The length of the corneal hair is $\sim$2.5 µm (Fig. 3d). In adults corneal hairs present throughout the eye except the marginal region. The corneal hairs are reported in some Hemiptera like *C. versicolor* [12] and absent from *A. pisum* [13]. The role of corneal hair is to protect the eye from strong sunlight by forming shadow and it also has cleaning action [14–16]. The presence of corneal hair in the central part of the eye in nymphs is probably to protect the eye from strong light as reported from pollen eating beetle *Xanthochroa luteipennis* [15]. Since the adults live inside the bark of the tree probably more cleaning action is required resulting more corneal hair throughout the eye. At very high magnification the cornea appears rough. A similar rough eye is reported from *Scaphidium japonum* beetle [17] and hemiptera *C. versicolor* [12].

The size of the eye increases with the body size (Fig. 4a). The base of the eye and the distance between the eye also increases with the increase of body length. The lowest diameter of the facet is found to be 12 µm. The diameter of the facet size

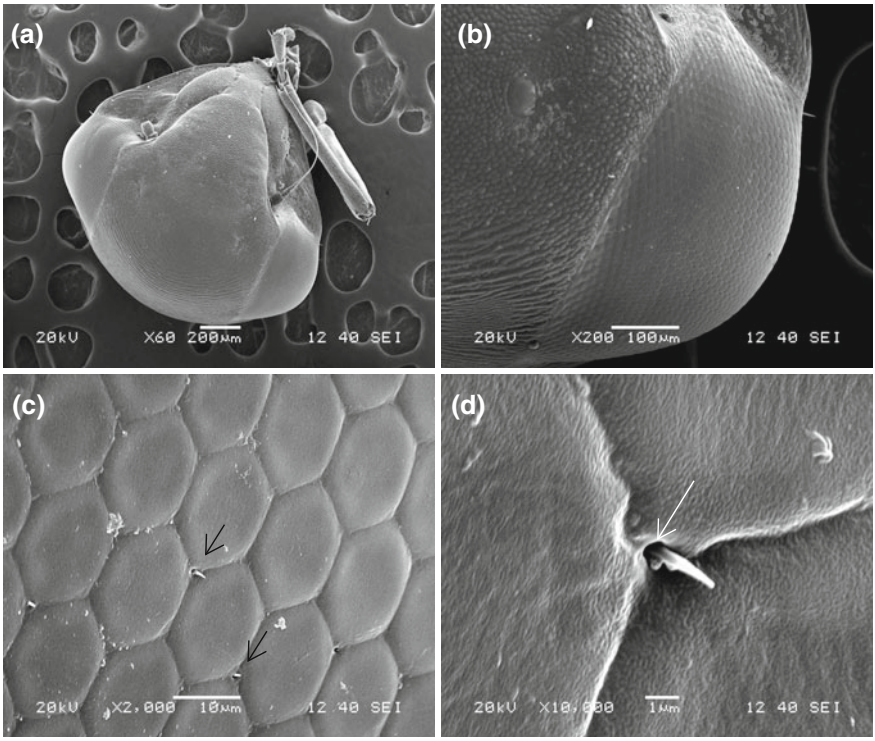

Fig. 3 Scanning electron micrographs of the compound eye of *A. Atkinsoni*. **a**. Whole head depicting compound eyes on either side of the head. Eyes are not easily distinguishable from its peripheral region. **b**. An individual compound eye demonstrating hexagonal array of numerous compact functional units or ommatidia. **c**. Central part of the eye showing tight arrangement of hexagonal ommatidia with occasional corneal hairs (pointed with *arrows*). **d**. Corneal hair at the centre of ommatidia

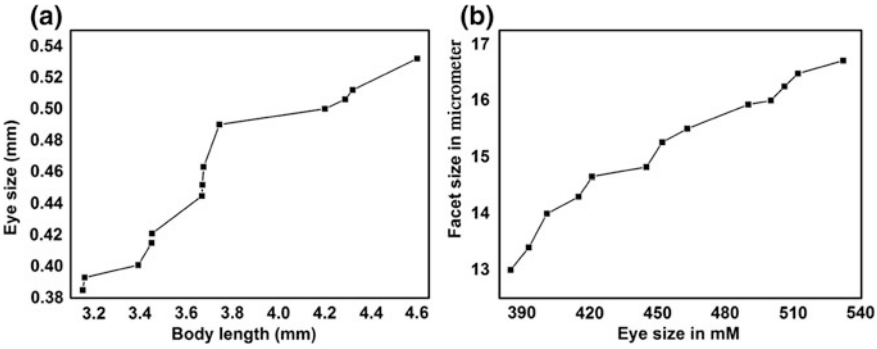

Fig. 4 Graphical representation of post embryonic development of *A. Atkinsoni*. **a** Eye size with body size. **b** Facet size with eye size

satisfies the calculation of Barlow 1950 to perform the function of the eye [18]. With the increase of the eye the facet size increases (Fig. 4b). Large facets capture more light than the smaller one. A similar eye to facet size relationship is also reported from hemiptera *Cimex lectularius* [4]. Larger facet and large eye probably makes the animal more sensitive towards light. Insect eyes are more susceptible towards light damage [19, 20]. To protect the eye from photic damage probably the larger insects move to the bark region. Light/dark adaptation is more conspicuous in various Hemipteran. It would be interesting to see such changes in *A. atkinsoni*. Future study of an eye internal structure will answer how the various parts of the eye undergoes changes with light and dark. Such kind of study will further cast light into the adaptation of insects with light and dark and so is the change of habitat.

4 Conclusion

The above results proved our assumption that the eye size increased with the increase in body length in *A. Atkinsoni*. These modifications in the eye structure of the mango hopper as they grow into adults play a very important role in their change in habitat and food. This change in eye size in-turn affects probably the internal arrangement of the eye. As the pest grows into adults they are mostly found to be present on the barks of the mango tree whereas the younger ones are present on the leaves and fruits. This change of habitat helps us to conclude that the eyes of the nymph are resistant towards bright light of the sun as compared to the adult ones. The adults are more sensitive towards light thus they tend to stay on the barks where the light intensity is less.

Acknowledgments The authors wish to thank Ms. Sabera Millan for her help in preparation of both the graphs used in this study.

References

1. Meyer-Rochow, V.B., Keskinen, E.: Post-embryonic photoreceptor development and dark/light adaptation in the stick insect *Carausius morosus* (Phasmida, Phasmatidae). Appl. Entomol. Zool. **38**(3), 281–291 (2003)
2. Keskinen, E., Meyer-Rochow, V.B.: Post-embryonic photoreceptor development and dark/light adaptation in the spittle bug *Philaenus spumarius* (L.) (Homoptera, Cercopidae). Arthropod Struct. Dev. **33**(4), 405–417 (2004)
3. Frolov, R., Immonen, E.-V., Vähäsöyrinki, M., Weckström, M.: Postembryonic developmental changes in photoreceptors of the stick insect *Carausius morosus* enhance the shift to an adult nocturnal life-style. J. Neurosci. **32**(47), 16821–16831 (2012)
4. Baker, G.T., Lawrence, A., Kuklinski, R., Goddard, J.: Post-embryonic development of the compound eye of bed bugs, *Cimex lectularius* L.(Hemiptera: Cimicidae). Proc. Entomol. Soc. Washington **117**(1), 1–6 (2015)

5. Settembrini, B.P.: The compound eyes of *Triatoma infestans* and *Rhodnius prolixus* (Hemiptera: Reduviidae). J. Med. Entomol. **21**(4), 477–479 (1984)
6. Fischer, C., Mahner, M., Wachmann, E.: The rhabdom structure in the ommatidia of the Heteroptera (Insecta), and its phylogenetic significance. Zoomorphology **120**(1), 1–13 (2000)
7. Döring, T.F., Spaethe, J.: Measurements of eye size and acuity in aphids (Hemiptera: Aphididae). Entomol. Gen. **32**, 77–84 (2009)
8. Sharma, B., Sharma, S.: Seasonal abundance of mango hopper, *Amritodus atkinsoni* (Leth.) (Jassidae: Homoptera) in different environmental conditions of Jammu region. J. Environ. Biol. Sci. **25**(1), 81–83 (2011)
9. Gundappa, P., Kamala, J., Abraham, V.: Migratory behaviour of mango hoppers, idioscopus spp. in relation to host plant flowering phenology: a synchronous shift. The Bioscan. **9**(2), 639–641 (2014)
10. Anufriev, G.: Description of a new genus Amritodus for *Idiocerus atkinsoni* Leth. from India [Hemiptera: Cicadellidae]. J. Nat. Hist.. **4**(3), 375–376 (1970)
11. Debnath, M.K.: Fitting of non-linear and parametric model for the incidence of mango hopper, *Amritodus atkinsoni* Leth. J. Plant Pest Sci. **2**(2), 48–56 (2015)
12. Jia, L.-P., Liang, A.-P.: Fine structure of the compound eyes of *Callitettix versicolor* (Insecta: Hemiptera). Ann. Entomol. Soc. Am. **108**(3), 316–324 (2015)
13. Mishra, M.: An eye ultrastructure investigation of a plant pest *Acyrthosiphon pisum* (harris) (Insecta: hemiptera: Aphididae). Open Access Insect Physiology. **5**, 41–46 (2015)
14. Mishra, M., Meyer-Rochow, V.B.: Fine structure of the compound eye of the fungus beetle *Neotriplax lewisi* (Coleoptera, Cucujiformia, Erotylidae). Invertebr. Biol. **125**(3), 265–278 (2006)
15. Mishra, M., Meyer-Rochow, V.B.: Eye ultrastructure in the pollen-feeding beetle, *Xanthochroa luteipennis* (Coleoptera: Cucujiformia: Oedemeridae). J. Electron Microsc. **55** (6), 289–300 (2006)
16. Mishra, M., Meyer-Rochow, V.B.: Fine structural description of the compound eye of the Madagascar 'hissing cockroach' *Gromphadorhina portentosa* (Dictyoptera: Blaberidae). Insect Sci. **15**(2), 179–192 (2008)
17. Mishra, M.: Eye Ultrastructure Investigation of *Scaphidium japonum* Reitter (Coleoptera: Staphylinidae: Scaphidiidae). J. Entmol. Zool. **1**(2), 8–16 (2013)
18. Barlow, H.: The size of ommatidia in apposition eyes. J. Exp. Biol. **29**(4), 667–674 (1952)
19. Meyer-Rochow, V.B., Mishra, M.: Structure and putative function of dark-and light-adapted as well as UV-exposed eyes of the food store pest *Psyllipsocus ramburi* Sélys-longchamps (Insecta: Psocoptera: Psyllipsocidae). J. Insect Physiol. **53**(2), 157–169 (2007)
20. Mishra, M., Meyer-Rochow, V.B.: Eyes of male and female *Orgyia antiqua* (Lepidoptera; Lymantriidae) react differently to an exposure with UV-A. Micron. **39**(4), 471–480 (2008)

Elemental Analysis of Various Feathers of Indian Rose Ringed Parakeet *Psittacula krameri*

Debabrat Sabat, Sabera Millan, P. Suchismita Sethy, Sandhya Marathe, Harekrushna Sahoo and Monalisa Mishra

Abstract The plumage coloration is a costly phenomenon adapted by birds. In birds, coloration can occur either by pigmentation or structural variation. The feather coloration helps to find partner and protect from predators. A few birds adapted cosmetic coloration, to protect themselves from the predators either by gland secretion or by accumulating certain metals in feathers. Besides protection, what could be the role of metals in feathers has never been identified. The current study investigates the metal composition in different parts of the feathers of Indian parakeet (*Psittacula krameri)* which shows variation in coloration throughout the body. The male shows sexual dimorphism by wearing a red ring in the neck collar region. Here, we have analysed the metal composition in various feathers present in different parts of the body by XRD. The possible role of various metals in different parts of the Indian rose-ringed parakeet is also described in this study.

1 Introduction

In birds, colorful plumage helps in signal communication for recognizing its partner and to avoid the predators by camouflage. Bright coloration also indicates the social status, agility, aggressiveness and most importantly attracting the partner. Thus, plumage is a part of intra-sexual competition within the species and evolution as proposed by Darwin in 1871. The development of color appears gradually with

D. Sabat · P. Suchismita Sethy · M. Mishra (✉)
Department of Life Science, National Institute of Technology, Rourkela, Odisha 769008, India
e-mail: mishramo@nitrkl.ac.in

S. Millan · H. Sahoo
Department of Chemistry, National Institute of Technology, Rourkela, Odisha 769008, India

S. Marathe
Department of Biological Sciences, Birla Institute of Technology and Science, Pilani, Rajasthan 333031, India

A.Y. Oral and Z.B. Bahsi Oral (eds.), *3rd International Multidisciplinary Microscopy and Microanalysis Congress (InterM)*, Springer Proceedings in Physics 186,
DOI 10.1007/978-3-319-46601-9_5

various stages starting from simple to most complex pattern in feathers [1] after molting stage. The feather coloration is also influenced by microbial activity, ectoparasite, accumulation of dirt or UV exposure. The feather having structural coloration follows principle of physics like film interference, diffraction grating, scattering and photonic interference for coloration [2, 3]. The scattering occurs due to the micro and nano structures in barbs and barbules present in feather [4]. The ultrastructure of barbules which contains air, melanin/keratin contributes for coloration by changing internal arrangement of all these layers [5, 6].

Colors produced in birds can be due to pigmentation or structural coloration. Another concept that had emerged is "cosmetic coloration" [7, 8] that helps to protect the bird from accidental staining from environment [9]. Two types of cosmetics are applied to birds, one is secretory product of different gland of birds and the other which the birds acquire from the environment [7]. Besides this metals like iron oxide from the soil is also known to change the feather coloration [7, 10]. Such change in coloration is adapted by the birds either for camouflage and or for extra protection. Similar to iron oxide metals like calcium, zinc and copper are involved in feather coloration by forming eumelanin and phaeomelanin pigment [11, 12]. Metals like calcium is involved in cell signaling and bone development [13] while zinc, copper and iron serves as enzymatic cofactors [14]. Although metal have some role in birds, higher accumulation of these metals leads to their mortality [15]. Birds adapt an innate mechanism to resist the toxic effect by producing proteins or molecules that can bind with these metals. A similar mechanism is reported in diatoms which produce domoic acid to detoxify Iron and Copper [16, 17]. Such process provides an advantage for the bird by helping them in getting the color variations produced by various metal presence. As more of the energy is spent by the bird in producing these molecules so it is an expensive physiological phenomenon for the birds.

Recently different metals were reported from feathers having different colors from sunbird *Nectarinia asiatica* [18]. Indian rose ringed parakeet possesses color variation in different parts of their body. The current study aims to check the presence of various metals in different feathers of *Psittacula krameri* not described in earlier studies.

2 Experimental

2.1 Sample Collection

The Indian Parakeet *P. krameri* feathers were collected from the BITS-Pilani, Pilani campus, Rajasthan, India during 2012–2014. The feathers were cleaned from dust and kept sealed in air tight envelopes until further analysis. The feathers were checked carefully and categorized into tail feathers, side tail feathers, wing feathers, shoulder, head nape, collar feather and stored in separate zip-lock bag for future analysis. At least 30 feathers from each type were used for the analysis.

2.2 X-Ray Diffraction

For X-Ray diffraction (XRD) analysis, the portions of interest was cut from the feathers and put onto the sample holder. The sample holder was placed in a XRD machine (Rigaku Japan/Ultima-IV) and the samples were scanned with an angle rotation of 5–90° with a rate of 5° per minute and with 0.05 step size to obtain the XRD readings. Then the graphs were plotted using Origin8 software and elemental analysis was done by Xpert Highscore Softwere.

3 Results and Discussion

The BITS Pilani campus of Rajasthan is far situated from the industrial region and so the air is quite clean, even the water analysis report confirms presence of all elements in permissible level [19]. Collected feathers from the bird (Fig. 1) were subjected for XRD analyses. The XRD analysis reveals the presence of various metals in different feathers. The metals found in XRD study of different feathers were plotted in Table 1. Why different parts of the body feather have different metals in it? Does the presence of metal in different feathers add advantage to the bird is an open question at this moment. We have analyzed the function of these metals in the light of available literature.

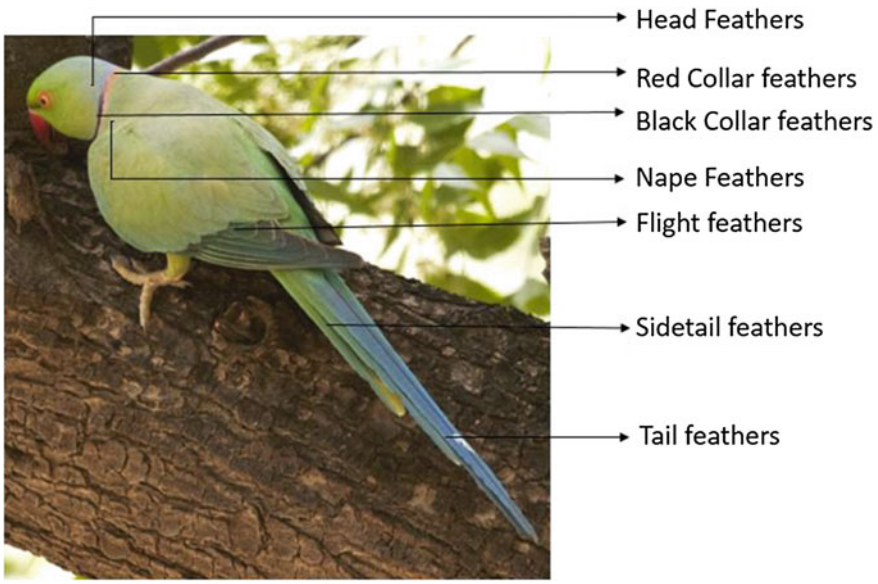

Fig. 1 *Psittacula krameri* (male) labelled with different parts of the body feathers

Table 1 XRD analysis of the feathers from *P. krameri*

Feather types	Color	Metals present
Head feather	Greenish	Copper chloride, manganese dioxide, titanium (traces)
Black collar	Blackish	Copper, nickel, tin sulphide
Red collar	Red-orange color	Lead, zirconium, copper hafnium, titanium dioxide and silver phenyl phosphide
Nape feather	Light green with bluish ting	Copper, zinc, cobalt, titanium
Shoulder feather	Light green	Iron, cobalt, zinc, copper
Flight feather	Dark green	Copper, tin, molybdenum, cobalt, lead
Flight feather	Blackish	Copper chloride, molybdenum oxide, zinc
Flight feather	Yellowish	Titanium, molybdenum
Side tail feather	Yellowish	Copper, titanium, tin telluride
Tail feather	Sky blue color	Copper, tin, zirconium, molybdenum

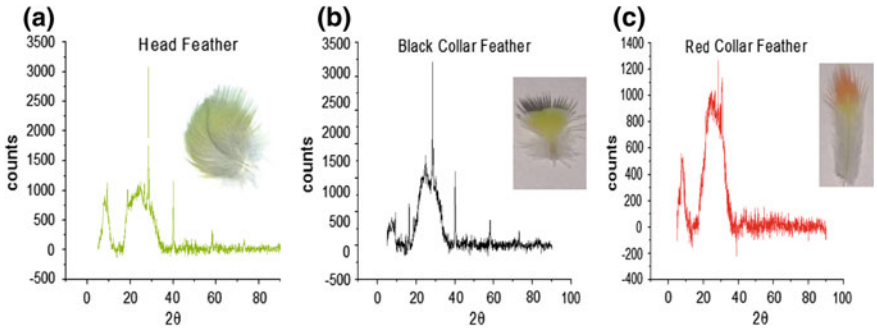

Fig. 2 XRD graph for the feathers from the head region: **a** Head feathers, **b** Black collar feather (in Male) and **c** Red collar feather (in Male)

Metal analysis of feather from an older study report the metals in feathers have antimicrobial activity [20]. The current study discloses metals like copper, manganese, nickel, tin, silver found in the head and collar region (Fig. 2). Zinc and iron in the feather of neck and shoulder region probably help in its light green coloration (Fig. 3). The flight feathers are of three different types primary, secondary and tertials. Along with metals like copper, tin, zinc mentioned above, flight feathers also showed molybdenum, cobalt and lead (Fig. 4). Lastly the tail feathers had an addition of zirconium metal along with copper, tin, molybdenum (Fig. 5).

Zinc and Iron metals are commonly known to be involved in the melanin synthesis and pigment formation respectively [21]. Besides, these metals give anti-bacterial protection to birds as these metals damage the bacterial cell by

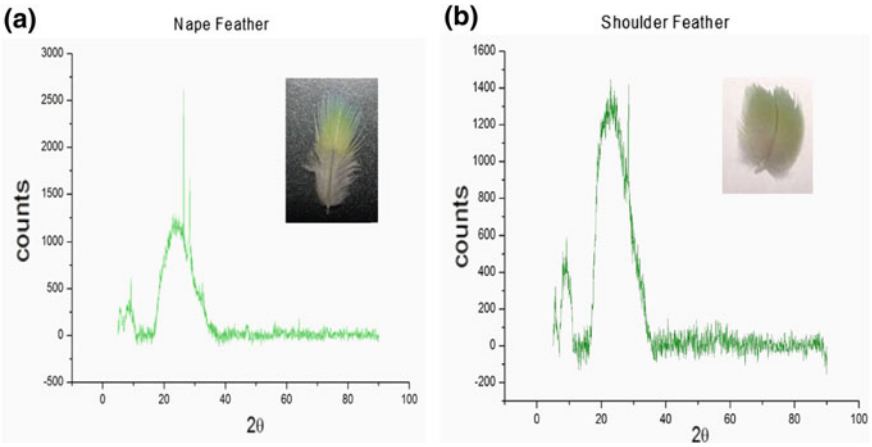

Fig. 3 XRD graph of feathers from the nape and the shoulder region: **a** Nape feathers and **b** Shoulder feather

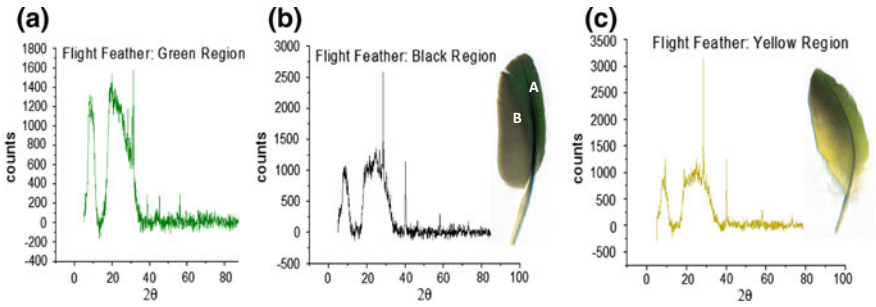

Fig. 4 XRD graph of flight feathers: **a** Green region. **b** Black region from flight feathers (secondary). **c** Yellow region from secondary and tertials feathers

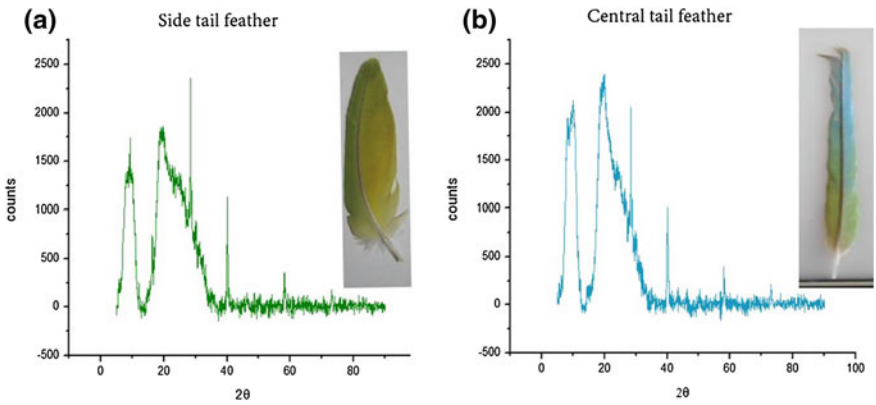

Fig. 5 XRD graph of tail feathers: **a** Side tail feather. **b** Central tail feather

producing reactive oxygen species (ROS) or oxidative stress [22]. Various other metals like titania, nickel and tin also demonstrate antibacterial property, a similar oxidative stress mechanisms is also anticipated from these metals. Titania is found in the nape feather, side tail feather which are lighter in color (Figs. 3a and 5a). Titania itself produces whitish pigmentation and the presence of titania probably help to produce lighter coloration in few feathers [23]. Titania nanoparticles are commercially used in sunscreen to protect from UV light. Mostly, the bird is protected from strong UV because of the presence of titania. Nickel was found in the black part of the neck collar feathers (Fig. 2b). Nickel is known to possess bacteriostatic activity against gram negative bacteria and also has anti-cancerous property [24]. Similarly, tin is found to be in black collar, flight feather, side tail feather and tail feather. Tin can protect the birds against *Staphylococcus aureus*, *Escherichia coli* and many broad strains by undertaking dehydrogenation via respiration process that occurs in the cell membrane of bacteria [25].

Other heavy metals like cobalt, lead, copper and silver that are found in nape feather, black collar, red collar (in male) (Figs. 2b, c and 3a). Cobalt have antitumor, anti-proliferative, antimicrobial, antifungal and antiviral activity acting as hydrolytic agents for DNA damage [26]. Cobalt is also at the active center of vitamin B12 and widely used in medicines forming a complex of CTC96, which is effective in treatment of herpetic keratitis, inhibits membrane fusion then prevents the entry of virus [27, 28]. It can obstruct formation of plaques by VZV (varicella-zoster virus), VSV (vesicular stomatitis virus) and adenovirus. Role of harmful toxic lead in feather is difficult to predict but previous reports states lead can discolor carotenoid. It also take part in bird coloration but is found to be produced in dark green coloration of flight feathers. Copper presence helps in green coloration in of birds like *Knysna turaco* and the *Schalow's turaco*. In those birds "turacoverdin" a pigment is responsible for imparting green coloration. The spectral analyses of those pigments revealed high amount of copper content than iron [29, 30]. Silver traces are also found in feathers present in red collar region in the form of silver phenyl phosphide. Although the complex form of this silver is not known, but silver possess antimicrobial property [31]. Zirconium is an element from the transition metal series and is found in traces from the feathers of red collar and tail feather region. The presence of zirconium in feather is yet unknown but zirconium nanostructures possess antimicrobial activity against *Micrococcus luteus*, *Staphylococcus aureus*, *Pseudomonas fluorescens*, *Bacillus subtilis* and *Escherichia coli* [32] (Figs. 2c and 5b). Similarly, the molybdenum found in the flight feathers and tail feathers also acts as an antimicrobial agent by forming acidic surface which inhibits cell growth and proliferation. The acidic mechanism is explained with the hydronium ions diffusion along the cell membrane. This creates an imbalance of pH, that can affect both enzymes and the cell transport system of cell [33]. Most of the metals described in this paper are in compound form. Although the direct role of these compounds are not known in biological system. It would be interesting to check the function of these compounds in bird's physiology.

4 Conclusion

Cosmetic coloration adapted by birds is an important, necessary and physiological phenomenon which needs more understanding with respect to metal exposure. The presence of various metals in feathers is somehow involved in giving a contrasting variation in the coloration. Besides providing attractive look these metals also possess property of antimicrobial, bacteriostatic, antifungal and antiviral activity. Metals like titania has the capacity to protect these feathers from harmful UV radiation damage. More studies needs to be performed on its interaction basis with the feathers and to learn the significance of its presence in the composite form. The various forms of natural phenomenon adapted by the animals needs to be understood and harnessed in order to utilize them optimally for human benefit.

References

1. Mishra, M.: Transformation of colourful pattern of eyespot in peacock wing. Current Sci. **107** (2), 186 (2014)
2. Zi, J., et al.: Coloration strategies in peacock feathers. Proc. Natl. Acad. Sci. USA **100**(22), 12576–12578 (2003)
3. Fitzpatrick, S.: Colour schemes for birds: structural coloration and signals of quality in feathers. Annales Zoologici Fennici **35**, 67–77 (1998)
4. Prum, R.O.: Anatomy, physics, and evolution of structural colors. Bird Color. **1**, 295–353 (2006)
5. Stavenga, D.G., et al.: Dramatic colour changes in a bird of paradise caused by uniquely structured breast feather barbules. Proc. R. Soc. Lond. B: Biol. Sci. **278**(1715), 2098–2104 (2011)
6. Sun, J., Bhushan, B., Tong, J.: Structural coloration in nature. RSC Adv. **3**(35), 14862–14889 (2013)
7. Delhey, K., Peters, A., Kempenaers, B.: Cosmetic coloration in birds: occurrence, function, and evolution. Am. Nat. **169**(S1), S145–S158 (2007)
8. López-Rull, I., Pagán, I., Garcia, C.M.: Cosmetic enhancement of signal coloration: experimental evidence in the house finch. Behav. Ecol. 781–787 (2010)
9. Moyer, B., et al.: Experimental test of the importance of preen oil in rock doves (*Columba livia*). Auk **120**(2), 490–496 (2003)
10. Montgomerie, R.: Cosmetic and adventitious colors. Bird Color. **1**, 399–427 (2006)
11. Prota, G.: Progress in the chemistry of melanins and related metabolites. Med. Res. Rev. **8**(4), 525–556 (1988)
12. Jawor, J.M., Breitwisch, R.: Melanin ornaments, honesty, and sexual selection. Auk **120**(2), 249–265 (2003)
13. Berridge, M.J.: Calcium signalling and cell proliferation. BioEssays **17**(6), 491–500 (1995)
14. Hänsch, R., Mendel, R.R.: Physiological functions of mineral micronutrients (Cu, Zn, Mn, Fe, Ni, Mo, B, Cl). Curr. Opin. Plant Biol. **12**(3), 259–266 (2009)
15. Hernández, L.M., et al.: Accumulation of heavy metals and As in wetland birds in the area around Donana National Park affected by the Aznalcollar toxic spill. Sci. Total Environ. **242** (1), 293–308 (1999)
16. Wells, M.L., et al.: Domoic acid: the synergy of iron, copper, and the toxicity of diatoms. Limnol. Oceanogr. **50**(6), 1908–1917 (2005)
17. McGraw, K.J.: Melanins, metals, and mate quality. Oikos 402–406 (2003)

18. Mahapatra, B.B., et al.: A closer look at the feather coloration in the male purple sunbird, *Nectarinia asiatica*. Micron **85**, 44–50 (2016)
19. Mitharwal, S., Yadav, R., Angasaria, R.: Water Quality analysis in Pilani of Jhunjhunu District (Rajasthan)-The place of Birla's Origin. Rasayan J. Chem. **2**(4), 920–923 (2009)
20. Krinsky, N.I.: Mechanism of action of biological antioxidants. Exp. Biol. Med. **200**(2), 248–254 (1992)
21. Bowness, J., Morton, R.: The association of zinc and other metals with melanin and a melanin-protein complex. Biochem. J. **53**(4), 620–626 (1953)
22. Wilson, M.R., et al.: Nanoparticle interactions with zinc and iron: implications for toxicology and inflammation. Toxicol. Appl. Pharmacol. **225**(1), 80–89 (2007)
23. Shi, L., et al.: Macroporous oxide structures with short-range order and bright structural coloration: a replication from parrot feather barbs. J. Mater. Chem. **20**(1), 90–93 (2010)
24. Tang, H.A., Wang, L.F., Yang, R.D.: Synthesis, characterization and antibacterial activities of manganese (II), cobalt (II), nickel (II), copper (II) and zinc (II) complexes with soluble vitamin K3 thiosemicarbazone. Trans. Met. Chem. **28**(4), 395–398 (2003)
25. Asadishad, B., Ghoshal, S., Tufenkji, N.: Short-term inactivation rates of selected gram-positive and gram-negative bacteria attached to metal oxide mineral surfaces: role of solution and surface chemistry. Environ. Sci. Technol. **47**(11), 5729–5737 (2013)
26. Hodnett, E.M., Dunn III, W.J.: Cobalt derivatives of Schiff bases of aliphatic amines as antitumor agents. J. Med. Chem. **15**(3), 339 (1972)
27. Schwartz, J.A., Lium, E.K., Silverstein, S.J.: Herpes simplex virus type 1 entry is inhibited by the cobalt chelate complex CTC-96. J. Virol. **75**(9), 4117–4128 (2001)
28. Kobayashi, M., Shimizu, S.: Cobalt proteins. Eur. J. Biochem. **261**(1), 1–9 (1999)
29. McGRAW, K.J.: Mechanics of uncommon colors: pterins, porphyrins, and psittacofulvins. Bird Color. **1**, 354–398 (2006)
30. Brush, A.H., Brush, A.: Avian pigmentation. Chem. Zool. **10**, 141–161 (1978)
31. Rai, M., Yadav, A., Gade, A.: Silver nanoparticles as a new generation of antimicrobials. Biotechnol. Adv. **27**(1), 76–83 (2009)
32. Bajju, G.D., et al.: Synthesis, spectroscopic, and biological studies on new zirconium (IV) porphyrins with axial ligand. Bioinorg. Chem. Appl. (2013). doi:10.1155/2013/903616
33. Plumridge, A., et al.: The weak acid preservative sorbic acid inhibits conidial germination and mycelial growth of *Aspergillus niger* through intracellular acidification. Appl. Environ. Microbiol. **70**(6), 3506–3511 (2004)

PNIPA Microgel and Alcian Blue Dye Aqueous Solution Interaction (Microscopic Investigation)

T.G. Baluyan, A.A. Novakova, Yu. B. Mandzhieva and V. Yu. Karaulov

Abstract The interaction of Poly(N-isopropylacrylamide) (PNIPA) gel and Alcian blue dye (AB) aqueous solution was studied in this work by means of optical and electron microscopy. During the PNIPA synthesis sodium metacrylate (MaNa) monomers were added to the chains to increase the gel charge activity. Optical microscopy was used to observe the results of dye and gel interaction. Scanning electron microscopy was performed in ESEM mode to observe the detailed structure of samples' initial state and state after PNIPA and dye interaction. It was found that Alcian blue dye forms threads that combine microgel particles which leads to complex conglomerates formation. In the macrogel case, alcian blue dye follows the polymer threads that may be used to visualize the gel structure.

1 Introduction

Alcian blue dye is widely used in histology and tomography, but the mechanism of it's interaction with biological tissues is not well known. It is interesting to observe the results of this interaction by means of electron microscopy, especially using ESEM mode.

PNIPA + AB system is a suitable model for the interaction of this dye with biological tissues, because the temperature of phase transition in this polymer is close to the temperatures of the proteins folding.

T.G. Baluyan (✉) · A.A. Novakova · Yu.B. Mandzhieva
Chair of the Solid State Physics, Department of Physics, Moscow State University, Moscow, Russia
e-mail: Tarinax@yandex.ru

A.A. Novakova
e-mail: Novakova.alla@gmail.com

Yu.B. Mandzhieva
e-mail: manjieva@gmail.com

V.Yu. Karaulov
SERNIA LLC, Moscow, Russia

A.Y. Oral and Z.B. Bahsi Oral (eds.), *3rd International Multidisciplinary Microscopy and Microanalysis Congress (InterM)*, Springer Proceedings in Physics 186,
DOI 10.1007/978-3-319-46601-9_6

In this work, we observed PNIPA microgel particles and PNIPA macrogel mixed with various concentrations of alcian blue dye solutions by means of optical and scanning electron microscopy.

2 Experimental

Alcian blue dye is a synthetical phtalocyanine stain. It has a copper atom in the middle of the molecule, that's why it's blue. It's coloring properties may vary with the varying of the medium pH [1]. The coloring is performed through the nitrogen atom in the dye molecule radical Fig. 1 [2].

PNIPA is a polyelectrolyte gel. Our samples under investigation were obtained by radical polymerization method. Sodium metacrylate (MaNa) monomers were added during the radical polymerization to increase the gel charge activity [3]. Two different samples were synthesized: microgel with 5 % MaNa and macrogel with 10 % MaNa. N,N′-ethylene-bis-acrilamyde was used as a cross-linking agent. The gels were washed after the polymerization. The initial sizes of the microgel particles were defined by means of light scattering [3]. Their sizes were in the interval of 160–180 nm. Macrogels were synthesized in the same way using more NIPA and MaNa monomers. Gels were then incubated in the alcian blue dye aqueous solution. The temperature during the whole process was never more than 32 °C—the temperature of PNIPA collapse [4].

Samples under investigation:

1. Alcian blue dye aqueous solution
2. PNIPA microgel (5 % MaNa), incubated in the AB aqueous solution, concentration of AB was 0.038×10^{-3} mol/l
3. PNIPA macrogel (10 % MaNa) incubated in the AB aqueous solution, concentration of AB was 0.02×10^{-3} mol/l
4. PNIPA macrogel (10 % MaNa) incubated in the AB aqueous solution, concentration of AB was 0.4×10^{-3} mol/l
5. PNIPA microgel without MaNa без MNa, incubated in the AB aqueous solution, concentration of AB was 0.02×10^{-3} mol/l.

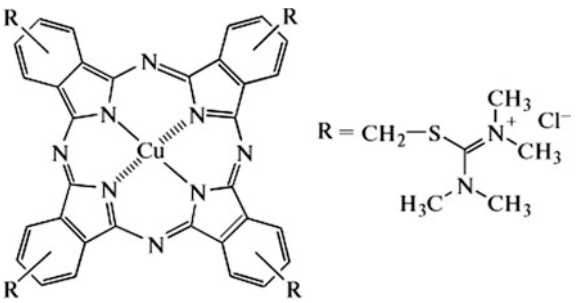

Fig. 1 Alcian blue dye structural formula

Fig. 2 Optical microscope Keyence VHX-5000

Optical microscopy was performed on the Keyence VHX-5000 optical microscope with high-speed camera, which is important for oscillating liquid samples, Fig. 2. Electron microcopy was performed in the Quanta 3D FEG FEI electron microscop, Fig. 3. Environment Simulation Electron Microscopy (ESEM) unit with sample table cooling and aqueous atmosphere creating was used in order to obtain the best quality pictures, which is not available for such samples in high vacuum mode, because they evaporate and burn under the high energy electron beam.

3 Results and Discussion

Alcian blue aqueous solution; Electron microscopy of AB aqueous solution was performed to find out whether any special aggregates form during the AB dissolving. It was found that AB forms 3–12 μm spherical conglomerates without any regular structure and ordering, Fig. 4.

PNIPA microgel (5 % MaNa), incubated in the AB aqueous solution; Optical microscopy of this sample showed that the size of microgel particles significantly increased from 160 nm, Figs. 5 and 6.

Fig. 3 Electron microscope Quanta 3D FEG FEI

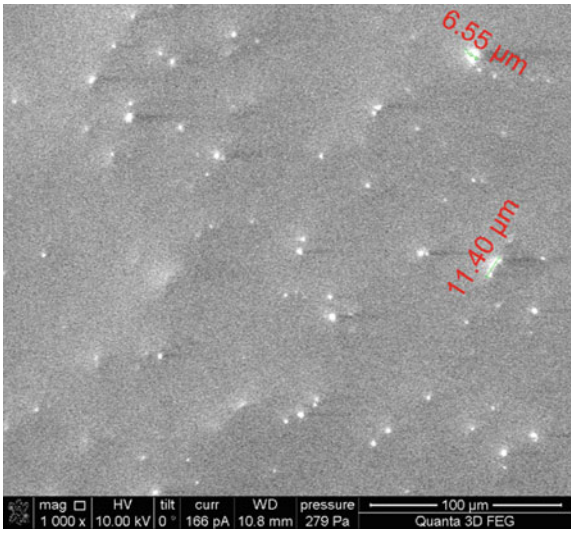

Fig. 4 Alcian blue dye aqueous solution eletron microscopy

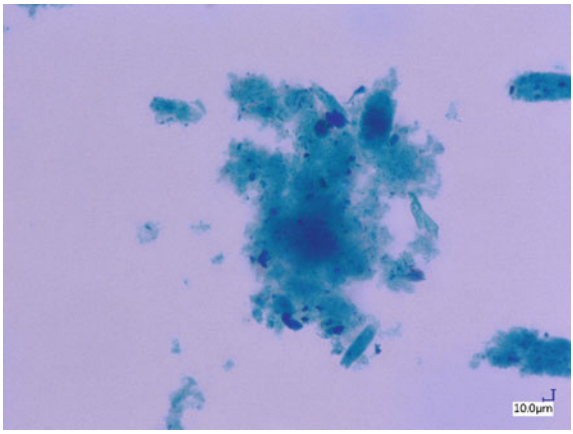

Fig. 5 Incubated PNIPA microgel optical microscopy, dye distribution

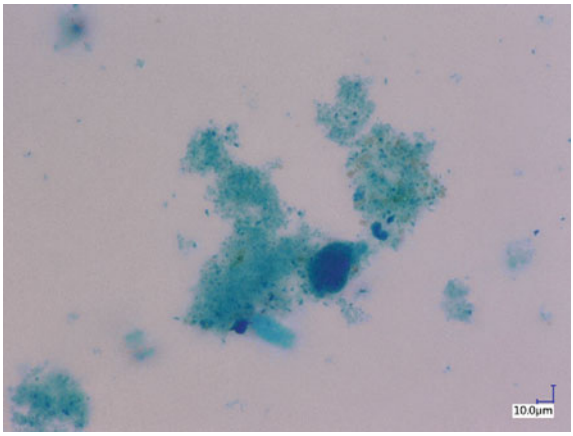

Fig. 6 Incubated PNIPA microgel optical microscop, different particles

Microgel particle size rose up to 200 µm, Figs. 7 and 8. They were colored evenly with some small parts of more intensive color. However, optical microscopy gave no information about the particles' structure that is why electron microscopy was performed.

It was found that AB aqueous solution incubated PNIPA microgel forms 1–200 µm particles with the specific structure—microgel basis and long parallel threads. Electron beam was focused on these threads and they melted with coloring the surrounding medium that is why we can declare that these threads are formed by alcian blue dye. The threads width was estimated 0.8–1 µm and the distances between them were 7–8 µm. The interesting fact it that these threads are parallel to each other.

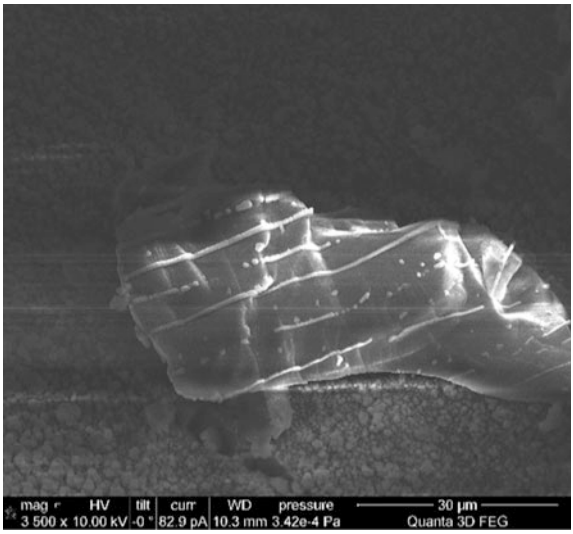

Fig. 7 Incubated PNIPA microgel electron microscopy, microgel particle

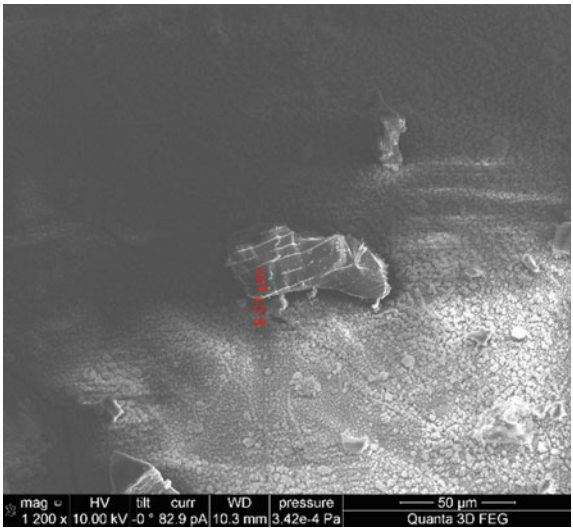

Fig. 8 Incubated PNIPA microgel electron microscopy, microgel particle

The structure of these aggregates is thready due to the alcian blue dye molecule structure—it has many aromatic elements and therefore can act in stacking, or π-π interaction [5]. This interaction leads to thread aggregates forming, as it is observed in the liquid crystals [6].

PNIPA microgel (without MaNa), incubated in the AB aqueous solution; Electron microscopy of this sample showed spongy structure made of polymer, but no alcian blue threads were observed. It occurred because of the lack of charged monomers in

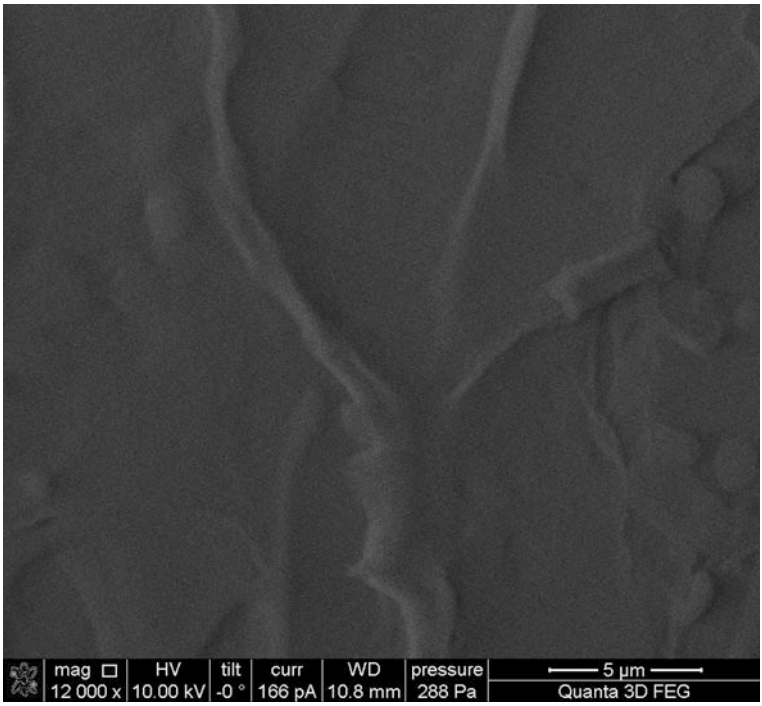

Fig. 9 Incubated PNIPA microgel (no MaNa) electronl microscopy, estimated wisp width

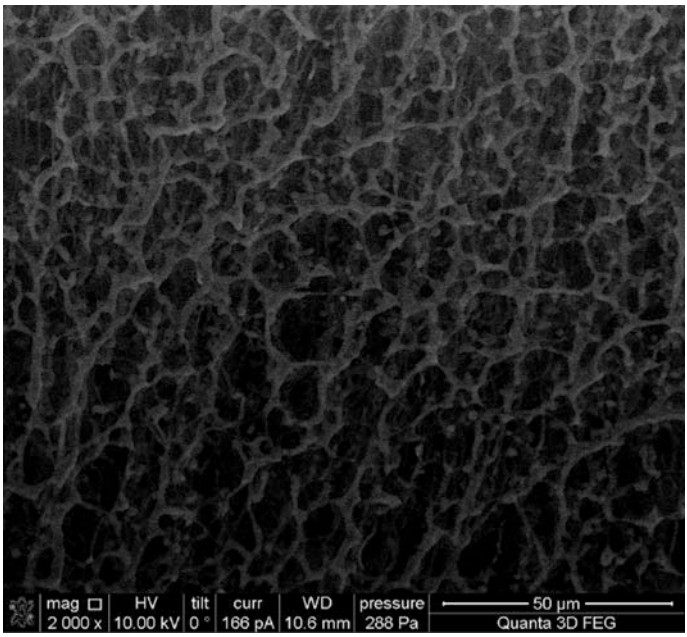

Fig. 10 Incubated PNIPA microgel (no MaNa) electronl microscopy, panoramic view

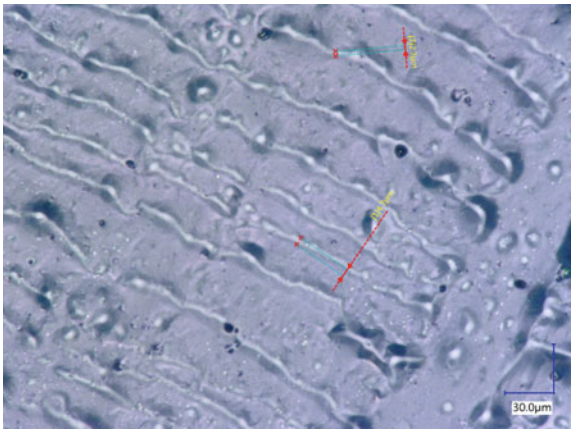

Fig. 11 Optical microscopy of PNIPA macrogel, AB concentration is 0.02×10^{-3} mol/l in the reflected light

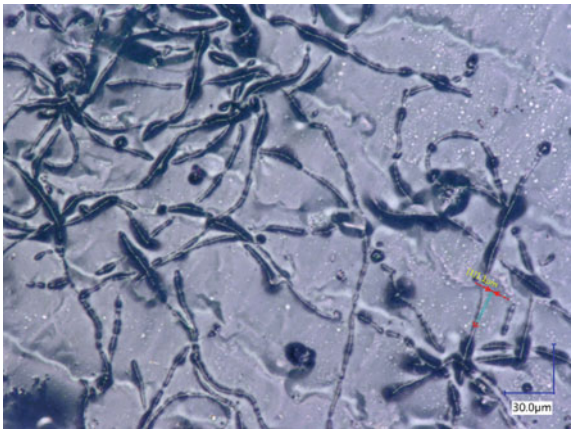

Fig. 12 Optical microscopy of PNIPA macrogel, AB concentration is 0.02×10^{-3} mol/l in the passed light (*right picture*)

the gel structure. Insufficient amount of charged monomers gave AB molecules no chance to get close enough to activate stacking interaction, so these molecules acted like an additional cross-linking agent. The additional cross-linking formed the structure of gel that looks like thick wisps, as it is shown on Figs. 9 and 10.

PNIPA macrogel (10 % MaNa), incubated in the AB aqueous solution; In order to perform a more detailed investigation of AB theads in the gel structures, macrogel was synthesized. Significantly more MaNa (10 % instead of 5 %) was added during the synthesis. Two concentrations of AB were used: 0.02×10^{-3} and 0.4×10^{-3} mol/l. Optical and Electron microscopy of these samples are shown on Figs. 11, 12, 13, 14, 15, 16 and 17.

The pictures shown on Figs. 11 and 12 were obtained from the different parts of the macrogel bulk. Figure 12 was taken from the more colored part. Doubling the MaNa amount lead to the increase of threads' with for two times. These threads were also observed in the optical microscope. These threads were not parallel, as it

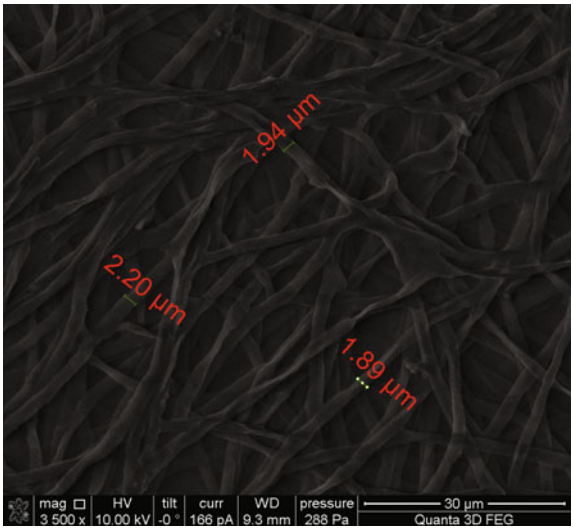

Fig. 13 Electron microscopy of PNIPA macrogel, AB concentration is 0.02×10^{-3} mol/l, threads conglomerate

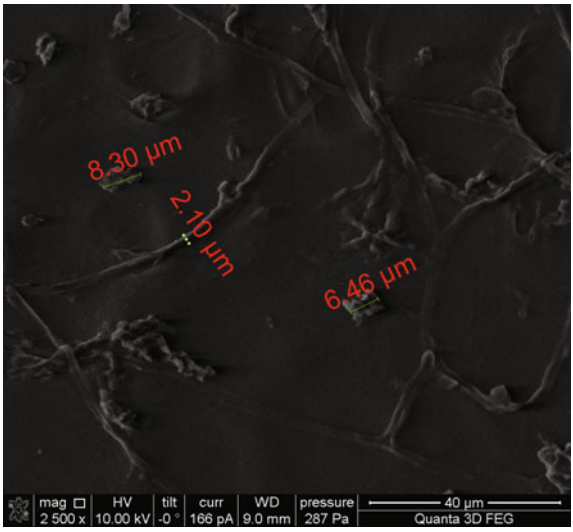

Fig. 14 Electron microscopy of PNIPA macrogel, AB concentration is 0.02×10^{-3} mol/l, smooth part of the gel surface

was observed in the microgel sample. This fact is explained by decreasing of structure-forming function of alcian blue dye when coloring the macrogel. When coloring the microgel, alcian blue dye forms the structure of microgel particles and during the coloring of macrogel the dye attaches to the polymer threads and just repeats their curves.

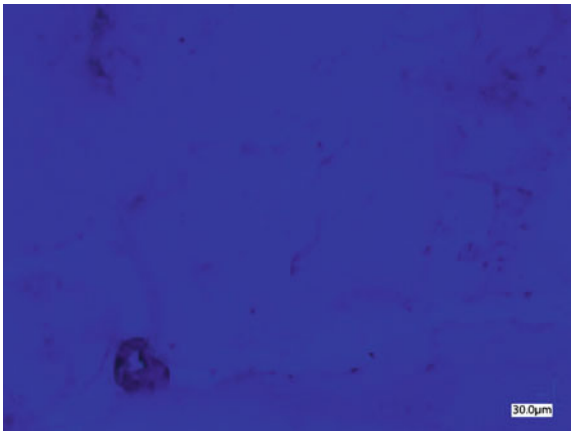

Fig. 15 Optical microscopy of PNIPA macrogel, AB concentration is 0.4×10^{-3} mol/l

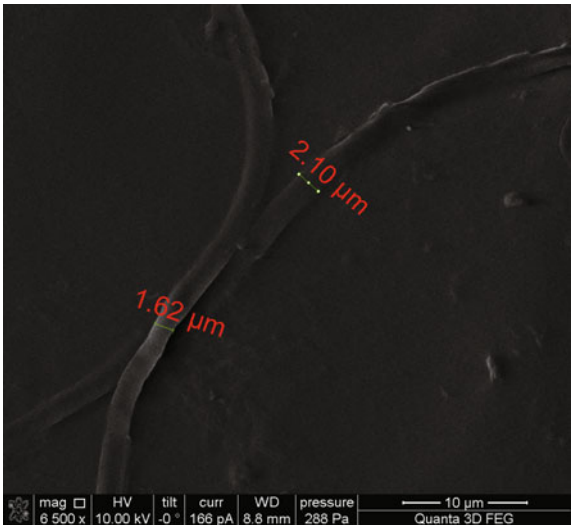

Fig. 16 Electron microscopy of PNIPA macrogel, AB concentration is 0.4×10^{-3} mol/l, estimated thread width

Increasing of AB concentrations 20 times lead to more even coloring, which is seen on Fig. 15. Electron microscopy showed the significant decrease of dye threads amount without any changes in their width. That means that thread width depends only on the charged monomers amount in the gel structure. These threads are not parallel as well which corresponds well with the AB curving of polymer threads.

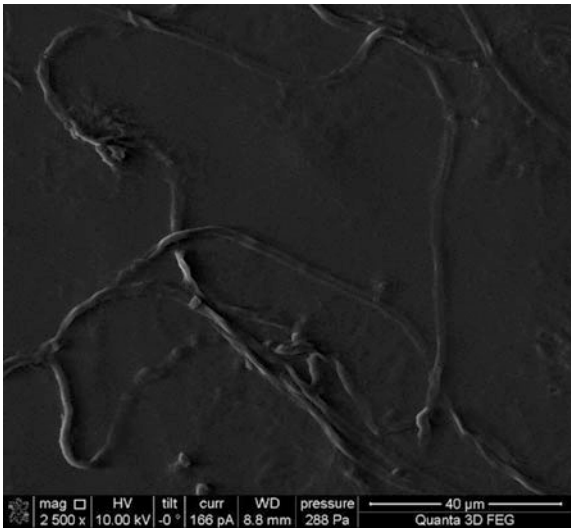

Fig. 17 Electron microscopy of PNIPA macrogel, AB concentration is 0.4×10^{-3} mol/l

4 Conclusion

As a result of this work it was found that alcian blue dye interacts with PNIPA gel in a specific way. It acts as a stain only if the gel is doped with additional charged monomers, otherwise it acts like an additional cross-linking agent. If charged monomers are added, alcian blue forms threads in the gel structures, the width of this threads increases with the increasing of charged monomers amount. When interacting with microgel, alcian blue dye threads form the structure of conglomerates, while interacting with macrogel, alcian blue molecules follow the polymer threads and therefore visualize the structure of gel.

Some problems, though, still left. It is not well understood why the alcian blue thread width is independent on the alcian blue concentration as well it is unclear why increasing of charged monomers amount leads to increasing of thread width. It is also unclear why increasing the amount of alcian blue makes threads almost disappear, so there is much work to be done in this research.

Acknowledgments We want to pay our sincere gratitude to prof. Makhaeva Elena E. and Ph.D. student Bogdashkina Daria for sample preparations and useful consultations. We also thank Kobylin Stanislav and Khakhalin Andrey for their contribution to this work. The work was supported in part by M.V. Lomonosov Moscow State University Program of Development.

References

1. Green, M.R., Pastewka, J.V.: Simultaneous differential staining by a cationic carbocyanine dye of nucleic acids proteins and conjugated proteins II. Carbohydrate and sulfated carbohydrate-containing proteins. J. Histochem. Cytochem. **22**, 774 (1974)

2. Beletskaya, I., Tyurin, V.S., Tsivadze, A.Y., Guilard, R., Stern, C.: Supramolecular chemistry of metalloporphyrins. Chem. Rev. **109**, 1659–1713 (2009)
3. Bogdashkina, D.V., Makhaeva, E.E., Khokhlov, A.R.: Behavior of thermosensitive N-Isopropylacrylamide polyelectrolyte hydrogels n aqueous solutions of alcian blue. Polym. Sci. **57**(6), 773 (2015)
4. Woodward, N.C., Chowdrhy, B.Z., Snowde, M.J., Leharne, S.A., Griffiths, P.C., Winnington, A.L.: Calorimetric investigation of the influence of cross-linker concentration on the volume phase transition of poly(N-isopropylacrylamide) colloidal microgels. Langmuir **19**, 3202–3211 (2003)
5. Steed, J.W., Atwood, J.L.: Supramolecular Chemistry, pp. 55–57. Wiley, New York (2009). ISBN 978-0-470-51234-0
6. Laschat, S., Baro, A., Steinke, N., Giesselmann, F., Hägele, C., Scalia, G., Judele, R., Kapatsina, E., Sauer, S., Schreivogel, A., Tosoni, M.: Angew. Chem. Int. Ed. **46**, 4832–4887 (2007)

Cells Shrinkage and Phosphatidylserine Externalization in Post Mortem Muscle by Fluorescence Microscopy

S. Becila, Y. Boudida, M. Gagaoua, K. Hafid, H. Boudchicha, H. Smili, R. Belachehabe, C.H. Herrera-Mendez, M.A. Sentandreu, R. Labas, T. Astruc, A. Boudjellal, B. Picard and A. Ouali

Abstract *Postmortem* (PM) meat tenderization is a complex biochemical process that involves multiple endogenous proteolytic enzymes and that is not completely understood. Cell death by apoptosis is recently proposed as a novel mechanism in this process. The signification of the caspases implication in muscle proteins degradation is that the cells are dying through apoptosis, a major cell death programme. Our purpose was therefore to verify this statement using different well known hallmarks of the apoptotic process including cell shrinkage, phosphatidylserine (PS) externalization. Cells start to shrink few minutes after animal death and reach a maximum shrinkage about 24 h postmortem while they showed the typical rounding appearance of apoptotic cells. Externalization of PS is detectable within 1 h postmortem and increased gradually with time. The present work is therefore the first to provide direct evidence supporting the onset of apoptosis in post-mortem muscle. The present findings should lead us to reconsider as a whole, the mechanisms contributing of the development of meat qualities (tenderness, flavor, juiciness …) by a detailed analysis of the apoptosis associated biochemical and physiological modifications taking place within the cells.

S. Becila (✉) · Y. Boudida · M. Gagaoua · K. Hafid · H. Boudchicha · H. Smili · R. Belachehabe · A. Boudjellal
INATAA, Bothers Mentouri Constantine University, Aïn El Bey Road, 25000 Constantine, Algeria
e-mail: becila2002@yahoo.fr

R. Labas · T. Astruc · B. Picard · A. Ouali
Theix, QuaPA, INRA de Clermont Ferrand, 63122 St Genes Champanelle, France

C.H. Herrera-Mendez
Departamento de Ingeniería Agroindustrial, Universidad de Guanajuato, 38900 Salvatierra, Mexico

M.A. Sentandreu
Instituto de Agroquimica y Tecnologia de Alimentos, CSIC, Avenida Agustín 7, 46980 Valencia, Spain

A.Y. Oral and Z.B. Bahsi Oral (eds.), *3rd International Multidisciplinary Microscopy and Microanalysis Congress (InterM)*, Springer Proceedings in Physics 186,
DOI 10.1007/978-3-319-46601-9_7

Abbreviations

FITC Fluorescein isothiocyanate
IgG Immunoglobulin
PS Phosphatidylserine

1 Introduction

Over the last years, several reports suggested a contribution of caspases, especially caspase 3, to the overall proteolysis taking place in *postmortem* muscle. After perfusion with the caspase inhibitor Z-VAD-fmk, a reduction in tilapia muscle toughness was thus reported by Ishida et al. [1]. Similarly, a significant reduction of proteolysis in chicken skeletal muscle was observed upon treatment with a specific caspase 3 inhibitor whereas calpain activity was unchanged over the whole treatment length [2]. On the other hand, Kemp and Parr [3] demonstrated the high sensitivity of myofibrils to the action of caspase 3. These findings are in good agreement with the conclusion of Camou et al. [4] who reconsidered the role of calpains in *postmortem* muscle and concluded their investigations by stressing that other proteolytic systems than calpains are involved in *postmortem* proteolysis and pore specially caspases. Hence, caspases contribute very likely to *postmortem* proteolysis. The activation of effector caspases requires the preliminary initiation apoptotic process by specific stimulus. Upon initiation of the apoptotic process, one or several initiator caspases are activated and these will in turn activate, through limited proteolysis, the effector caspases. The effector caspases will then degrade cellular proteins up to total cell dismantling [5].

After animal bleeding, the dynamic regulation of the biological processes existing in the living cells will not be efficient anymore and if the apoptotic process is set up *postmortem*, it will be very probably never fully completed. There is two major reasons supporting this assumption: (a) the physicochemical conditions (pH, osmotic pressure, …) which will change unfavorably and (b) because of the lower efficiency of the supplying energy pathways, the energy needs for a full completion of the process will probably not be fully covered.

Although several sets of evidence suggested the contribution of caspases to *postmortem* proteolysis, especially of caspase 3, the onset of the apoptotic process in *postmortem* muscle has never been clearly established. The purpose of the present work is to fill in this gap and provide experimental data demonstrating that apoptosis is set up in *postmortem* muscle. To achieve this goal two major changes characterizing the apoptotic process (reviewed in [6]). Have been selected and tested in *postmortem* rat muscles: (a) cell shrinkage and rounding; (b) phosphatidylserine externalization and. The whole set of findings reported in this paper led us to conclude that the apoptotic process starts to be set up in the first few minutes postmortem and progresses then during time.

2 Experimental

2.1 Animals and Muscle Sampling

Five 10–12 weeks old Wistar rats provided by the research center rat breeding group were used in the present work. Animals were anesthetized by intra-peritoneal injection of sodium pentobarbital (0.1 ml/100 g of rat weight) and then killed by decapitation. For each animal, *Gastrocnemius* (red muscle) and *Plantaris* (white muscle) muscles were excised from the left hind leg within 1 h postexsanguination. The muscle from the right hind leg was maintained on place and excised 24 h postmortem after storage of the carcass at 10 °C for 5 h and then at 4 °C up to 1 day postmortem. These two muscles were used to study the extent of cell shrinkage and rounding together with the phosphatidylserine externalization. Because more samples were needed for DNA fragmentation studies, this experiment was performed on a larger muscle, namely rat *Longissimus* muscle, from which samples were taken at each predefined times postmortem from the left side and then from the right side of the carcass.

2.2 Muscle Cells Shrinkage

Muscle strips from Gastrocnemius and Plantaris muscles were immersed in 4 % paraformaldehyde and 0.1 % E were cut and observed without any additional staining or treatment with an Axioplan 2E Zeiss light microscope (Zeiss, Lyon, France).

2.3 Estimation of the Extent of Shrinkage

The estimation was carried out on samples excised just after bleeding from rat Longissimus muscle, a larger muscle enabling analysis of a greater number of samples. Samples were prepared for microscopy examination as described above for cells shrinkage. The contrast of the image was adjusted in order to identify clearly the cell limits using Corel Paint Shop Pro X application from Macromedia (Paris). After printing the image presented in Fig. 1, cells were cut out with or without the associated extracellular space and pieces of paper corresponding to the cell alone (grey (G) area in Fig. 1) and to the cell plus the extracellular space (grey (G) + black (B) area in Fig. 1) were weighted. The extent of shrinkage was calculated using the following equation:

$$\text{Shrink} = (1 - (\text{G}/(\text{G} + \text{B}))) * 100$$

where "Shrink" is the extent of shrinkage (%), "G", the weight of the cell alone and (G + B), the weight of the cell plus the associated extracellular space.

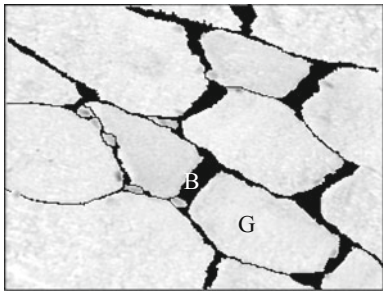

Fig. 1 Estimation of the extent of shrinkage on samples excised just after bleeding from rat *Longissimus* muscle

Measurements were carried out on 1–3 cells per cut and 5 cuts were analyzed for each animal. A total of 52 fibers were analyzed on samples prepared within the first 10 min after animal decapitation. As a reference we used the cell volume for a negligible extracellular space (B = 0 and cell weight = B + G).

2.4 Phosphatidylserine Externalization and Laminin Labelling

Phosphatidylserine externalization was investigated using 2.5 × 6 mm strips from Gastrocnemius and Plantaris muscles. These samples were stretched and fixed with needles on cork plates before immersion in 1 % (v/v) paraformaldehyde, 0.1 % (v/v) glutaraldehyde, 0.1 M sucrose in 0.1 M sodium phosphate buffer, pH 7.2, for 15 min at room temperature. FITC-Annexin V Conjugate (Sigma-Aldrich A9210, Saint-Quentin Fallavier, France) was used for Phosphatidylserine detection. After three washes with PBS buffer for 5 min, muscle strips were incubated in PBS buffer containing FITC labeled Annexin V (1.8 µg/ml) for 24 h at 4 °C and kept overnight in the dark upon mild stirring. One strip was used as a control and similarly incubated in the same buffer but in the absence of Annexin V. After three washes with PBS buffer for 5 min, muscles were cut into small pieces (1 × 3 mm) parallel to the fibre axis. These small cuts were frozen at −160 °C in isopentane immersed in liquid nitrogen and subsequently kept at −80 °C until use. Transversal sections (10 µm) were then cut using a Reichert Frigocut 2800 (Leika) and dried in the dark at room temperature before fixation in PBS buffer containing 2 % formol. Thin Annexin V labeled cuts were then treated for Laminin labeling as previously described [7], using a rabbit anti-Laminin (Sigma-Aldrich) primary antibody (dilution: 1/100) followed by the addition of a cyanine 3 conjugated goat anti-rabbit IgG (dilution: 1/150) as the secondary antibody (Santa Cruz SC-5879, Santa Cruz Biotechnology Inc., Heidelberg, Germany). Finally, sections were mounted on glass slides in Mowiol and observed by using an Axioplan 2E Zeiss light microscope. FITC-Annexin V conjugate was revealed using ʎexc 488 nm and ʎemm 530 nm whereas for cyanine.

2.5 Preparation of Samples for Electron Microscopy

For routine ultrastructural studies, rat muscle samples were treated as previously described [8].

3 Results and Discussion

3.1 Muscle Cells Shrinkage

Cell shrinkage which is one of the first steps of the cell death program [9], has been investigated on both rat Gastrocnemius and Plantaris muscles. Similar findings were obtained for both muscles. Thus only those corresponding to Gastrocnemius muscle are presented hereafter. As shown in Fig. 2a, after1 h postmortem, some cells are shrunk (left part of the white line) whereas some other are not (right part of the white line). It is worthy to remember here that each cell can decide by itself,

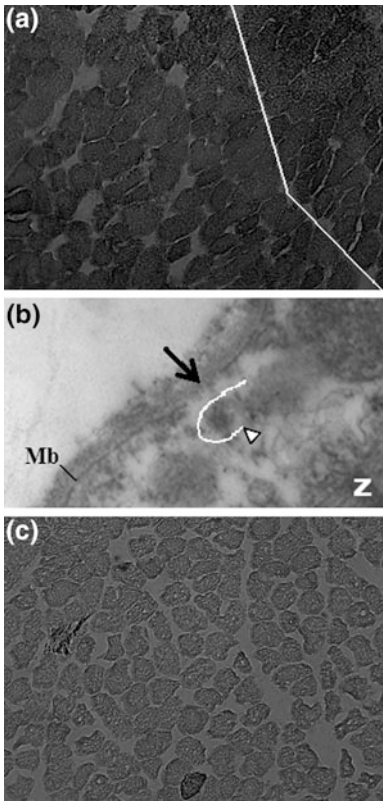

Fig. 2 Cell shrinkage and related structural damage of the membrane. **a** Transversal section of rat *Gastrocnemius* muscle excised 1 h *postmortem* (×1000). The *white line* delimited the left region of the section where shrinkage is more important than in the *right* one. **b** Membrane disruption at the costamere level observed by electron microscopy examination of a 2 h *postmortem* sample (magnification: ×100,000). The *black arrow* indicate the position of the hole in the membrane and the *white open arrowheads* shows the released portion of the membrane still bound to the costamere/Z-line (Z) transversal filaments. **c** Transversal section of rat *Gastrocnemius* muscle excised 24 h (×1000). For more details see the materials and methods section

independently from the others, to commit suicide by engaging into the cell death program at the right time. This explains why, within the same cut, the behaviour of each cell can be different. The extra-cellular space is thus minimal and more regular in the right part of the plate as compared to the left part, where this space is abnormally large and variable from one area to another.

An estimation of the extent of shrinkage has been performed as described in the Materials and Methods section on rat Longissimus samples excised just after bleeding. For each sell examined, the reference is the same cell before shrinkage meaning that shrink = 0 and total cell weight = G + B. On average, cell volume decreased by about 20 % (20 ± 6 %). age This shrinkage results very likely from the cytoskeletal induced traction forces on the cell membrane with a concomitant water out flux towards the extracellular space.

The intensity of the forces concerned at the time of the cellular retraction is sufficiently important to cause wrenching of anchorage structures (costameres, integrins, …) from the membrane. They also cause a retraction of all intracellular organelles contributing, at least partly, to their dysfunctions. This feature is illustrated in Fig. 2b for a 2 h postmortem sample from Gastrocnemius muscle showing a clear release (black arrow) of part of the membrane corresponding to the costamere region, the membrane fragment being still anchored to the transversal intermediate filaments emanating from the Z-line (open arrowhead).

Figure 2c presents a cut from the same Gastrocnemius muscle at time 24 h postmortem. After 24 h, all cells are shrunk and extra-cellular space increased significantly, suggesting a time-dependent progress of the cell death process. Another interesting feature is that, in the 24 h postmortem sample, almost all fibres showed the typical rounding appearance of cells dying by apoptosis [9].

3.2 Phosphatidylserine Externalisation

Analysis of phosphatidylserine externalisation was performed on both rat Gastrocnemius and Plantaris muscles and, as no difference was observed, only results of the former muscle are presented herein. Besides cell shrinkage, another characteristic feature of apoptosis is the externalization of phosphatidylserine (PS), a class of acidic phospholipids normally located on the internal leaflet of the lipid bilayer. However, in some physiologic conditions, the internal PS is exposed to the external surface especially in dying cells [10, 11]. Phosphatidylserine (PS) externalization is thus regarded as one of the earliest hallmarks of cells undergoing programmed cell death [12]. In living organisms, macrophages recognize the PS externalized cells through a specific PS receptor, resulting in a possible contribution of macrophages to the target cell dismantling [13].

To comfort the idea that the onset of the cell death program takes place immediately after bleeding, an assumption supported by the intense cell shrinkage observed as soon as 1 h postmortem, redistribution of PS has been investigated on small muscle fibers bundles using a FITC labeled specific PS-binding protein,

Annexin V, as a specific probe. To attest the extracellular location of PS, we referred to Laminin, a major component of the basal lamina. In living cells, the primary function of the Laminin protein family is the anchorage of the plasma membrane to the extracellular matrix. Hence, these proteins are located in the vicinity of the external leaflet of the plasma membrane [14] and constitute an interesting internal control to verify that the PS labeling is extracellular and not intracellular.

Small muscle fiber bundles taken at 1 h (Fig. 3a) and 24 h (Fig. 3b) postmortem were incubated with FITC-labeled annexin V for 24 h and then frozen. Frozen cuts obtained from the Annexin V labeled samples (Fig. 3a1) were then treated with a primary rabbit Laminin antibody, revealed with a FITC-labeled goat anti-rabbit secondary antibody (Fig. 3a2) and examined under the light microscope for Annexin V and Laminin fluorescence. Note that serial thin cuts were obtained from the central part of the frozen sample avoiding the peripheral fibers which can be damaged during preparation of the sample.

As depicted in Fig. 3a1 (1 h postmortem sample) and Fig. 3b1 (24 h postmortem sample) analysis of the Annexin V distribution in transversal muscle thin cuts led to a specific green fluorescent labeling of the periphery of the fibers. In addition, the labeling intensity appeared to be greater in the 24 h postmortem sample suggesting a time course progress in the PS externalization during the first 24 h post-exsanguination. No fluorescence was detected in fibers treated with the same buffer in which Annexin V was omitted (Fig. 3a4). Immunostaining of rat muscle fibers prepared 1 h (Fig. 3a2) or 24 h (Fig. 3b2) postmortem with a Laminin rabbit polyclonal antibody revealed with a cyanin 3 conjugated goat anti-rabbit IgG led to specific fluorescent red labeling of the periphery of the fibers. When the first antibody was omitted, no fluorescence was detected (Fig. 3b4).

Merging images corresponding Laminin and PS labeling led to a yellow color, a result indicative of a co-localization of Laminin and PS-bound Annexin V. Such color change was observed both at 1 h (Fig. 3a3) and 24 h (Fig. 3b3) postmortem samples. The co-localization of both antigens confirms that Annexin V is bound to extracellular PS and not to intracellular acidic phospholipids. It is noteworthy that the yellow color is more intense in the 24 h sample, suggesting an increase in the number of externalized PS between 1 and 24 h postmortem. The present results clearly indicate that PS groups are externalized in postmortem muscle as soon as 1 h postmortem and that the extent of PS externalization increased between 1 and 24 h postmortem. By contrast, Laminin labeling tends to decrease between 1 h (Fig. 3a2) and 24 h (Fig. 3b2), a feature indicative of a probable degradation of this protein soon after death.

Since the beginning of the present decade, several reports suggested a contribution of caspases, especially caspase 3, to the postmortem proteolysis [1, 2, 4]. On the other hand, caspases are the driven motor of the programmed cell death by apoptosis development. The present work intended therefore to obtain evidence supporting the onset of the apoptotic process in postmortem muscle.

The concept of apoptosis was introduced by Kerr et al. 4 [15] to indicate a form of cellular death totally different from necrosis, from both the morphological and

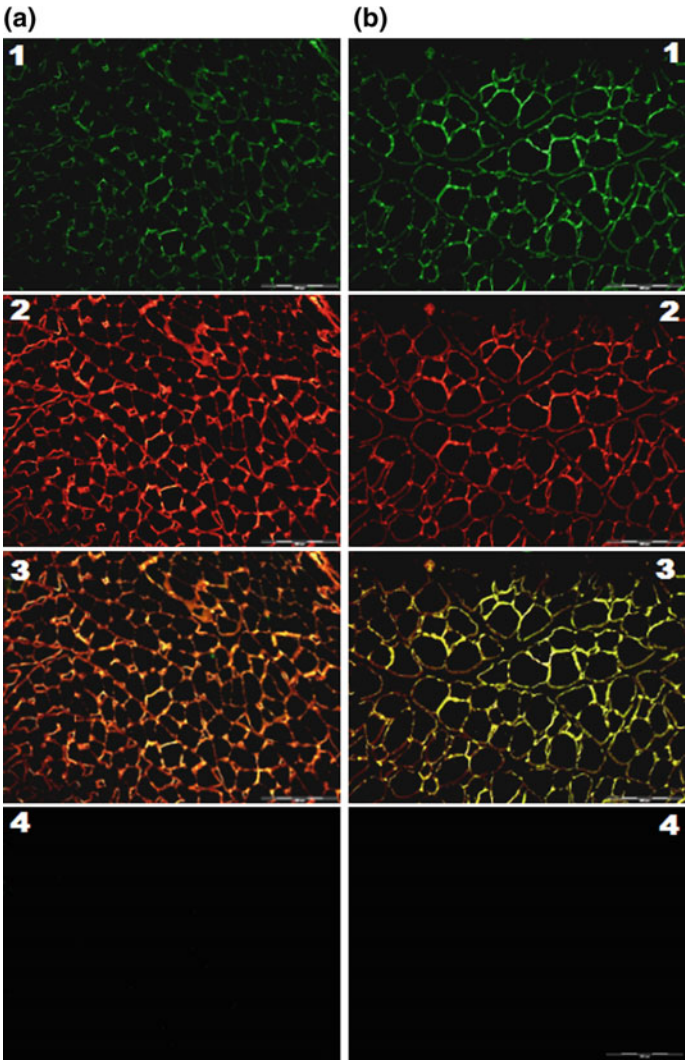

Fig. 3 Phosphatidylserine externalization and Laminin labeling. **a** Samples from rat *Gastrocnemius* muscle excised 1 h *postmortem*. **b** Samples from rat *Gastrocnemius* muscle excised from the second leg 24 h *postmortem*. **1** Samples labeled with a FITC-Annexin V conjugate at 1 h (**a**) and 24 h (**b**) postmortem. Note the greater fluorescent labeling of the 24 h sample as compared to 1 h (λexc 488 nm; λemm 530 nm). **2** Samples labeled with a rabbit specific Laminin antibody revealed with a cyanine 3 goat anti-rabbit IgG conjugate at 1 h (**a**) and 24 h postmortem. Note the lower fluorescent labeling of the 24 h sample as compared to 1 h probably indicative of the degradation of the Laminin (λexc 554 nm; λemm 568 nm). **3** Merged image from 1 and 2. **4** Control samples for annexin V (**a4**) and Laminin (**b4**) labeling in which the FITC Annexin V conjugate and the primary anti-Laminin antibody respectively were omitted

biochemical points of view. In muscle tissue, chronological events conducting to apoptosis are the same than in mononucleated cells which are usual models for such studies [16]. As previously reviewed [6], in contrast to necrosis often considered as a "disordered" cellular death, apoptosis is regarded as an "ordered" cellular death proceeding through a series of chronological and strictly regulated events: Dying cells lose their contact with neighboring cells and signal their status by externalization of phosphatidylserine which are normally located on the inner leaflet of the membrane. Concomitantly, the general condensation affecting the dying cells and their organelles led to an intense shrinkage and a significant reduction in the cell volume together with an increase in the extracellular space. Mitochondria undergo several major modifications leading to a release of pro-apoptotic proteins including cytochrome c. After condensation of the nucleus, chromatin is cleaved in regular fragments of approximately 180 pairs of bases.

According to Green programmed cell death is a rapid process taking place within few minutes to few hours. Hence, if apoptosis [17]. Set up in postmortem muscle, the first characteristic changes induced by process would be detectable soon after animal death. Four of the above hallmarks of apoptosis, including cell shrinkage, phosphatidylserine externalization, DNA fragmentation and actin degradation, were therefore investigated.

It was shown that cell shrinkage is detectable few minutes after exsanguination and that this change progress over time to reach its maximum about 24 h postmortem. For samples excised within 1 h postmortem, the cell volume decreased by about 20 % but all cells are not concerned at the same time, comforting the idea that each cell decides when it will commit to suicide and engages into the cell death programme. After 24 h, all cells are shrunk and all have the rounding shape characterizing apoptosis. Cell shrinkage led to an important increase in the extracellular space. This increase in the extracellular space was generally ascribed to a decrease in the capacity of myofibrillar protein to bind water during the acidification of muscle and the consequent pH drop [18, 19]. The causes of the large raise of the extracellular space in postmortem muscle would have to be reconsidered in the light of the present findings.

One of the major consequences of cell shrinkage is the strong constraints supported by the anchorage structures associated to the plasma membrane (costameres, integrins, …) which can be strongly altered. As illustrated in the present work, costameres are sometimes wrenched from the membrane while they are still attached to the transversal intermediate filaments emanating from the Z-line. This limited opening of the membrane will facilitate water flux towards the extracellular space.

The second hallmark of apoptosis considered was the externalization of phosphatidylserine (PS) which move from the inner to the outer leaflet of the plasma membrane. Using FITC-labeled Annexin V as a specific probe of these acidic phospholipids, it was shown that a strong green labeling was noted in the vicinity of the membrane. To attest the extracellular location of PS, we referred to Laminin, a major component of the basal lamina located in the vicinity of the external membrane leaflet, which ensures the connection of the extracellular matrix to the cell membrane. Laminin was labeled with a specific antiserum and revealed using a

cyan 3-conjugate secondary antibody (red color). When the fluorescent images were merged the color changed to yellow indicative of a co-localization of the proteins, i.e. Annexin V and Laminin. In addition, we noted a decrease in the Laminin labeling intensity probably suggesting a probable alteration of this protein over the first 24 h postmortem. In contrast, intensity of PS labeling seemed to increase over this time laps suggesting a time dependent raise in the number of PS group transferred on the outer leaflet.

Recently Huang et al. [20] demonstration thereby strengthened the hypothesis that in post mortem muscle, oxygen deprivation-induced apoptosis is dependent on the mitochondrial pathway. On the other hand, proteins involved in the regulation of the apoptotic process whether released from mitochondria (AIF, Endo G, Cytochrome c, …) or expressed in muscle cells (IAPs, caspase inhibiting serpin, …) have never been revealed by 2D gel electrophoresis proteome analysis and thus they would merit to be selectively targeted using alternative more specific approaches [21].

4 Conclusion

In conclusion, the present work provides, for the first time, indisputable evidence supporting the set up of apoptosis in muscle immediately after animal death. It has been further proven that this process affects cell metabolism, oxidative processes affecting proteins, lipids and meat color, cytoskeletal network degradation. These different events contributing the development of different meat qualities (tenderness, color, flavor and juiciness) must be reconsidered in relation with the complex apoptotic induced modifications of cell metabolism and physiology.

Acknowledgments Many thanks to Christine Barboiron, Arnaud Delavaud and Jean-Luc Montel (URH unit, C2M team) for their invaluable assistance in light microscopy studies. This work is part of one of the QUAPA transversal project funded by INRA. The visit of S. Becila in our institute was funded by a grant from the Algerian Ministry of Education. Many thanks for this support.

References

1. Ishida, N., Yamashita, M., Koizumi, N., Terayama, M., Ineno, T., Minami, T.: Inhibition of post mortem muscle softening following in situ perfusion of protease inhibitors in tilapia. Fish. Sci. **69**, 632–638 (2003)
2. Huang, M., Huang, F., Xu, X., Zhou, G.: Influence of caspase 3 selective inhibitor on proteolysis of chicken skeletal muscle proteins during post mortem aging. Food Chem. **115**, 181–186 (2009)
3. Kemp, C.M., Parr, T.: The effect of recombinant caspase 3 on myofibrillar proteins in porcine skeletal muscle. Animal **2**, 1254–1264 (2008)

4. Camou, J.P., Marchello, J.A., Thompson, V.F., Mares, S.W., Goll, D.E.: Effect of postmortem storage on activity of μ- and m-calpain in five bovine muscles. J. Anim. Sci. **85**, 2670–2681 (2007)
5. Gagaoua, M., Boudida, Y., Becila, S., Picard, B., Boudjellal, A., Sentandreu, M.A., Ouali, A.: New caspases' inhibitors belonging to the serpin superfamily: a novel key control point of apoptosis in mammalian tissues. Adv. Biosci. Biotechnol. **3**, 740–750 (2012)
6. Ouali, A., Herrera-Mendez, C.H., Coulis, G., Becila, S., Boudjellal, A., Aubry, L., Sentandreu, M.A.: Revisiting the conversion of muscle into meat and the underlying mechanisms. Meat Sci. **74**, 44–58 (2006)
7. Raynaud, F., Fernandez, E., Coulis, G., Aubry, L., Vignon, X., Bleimling, N., Gautel, M., Benyamin, Y., Ouali, A.: Calpain 1-titin interactions concentrate calpain 1 in the Z-band edges and in the N2-line region within the skeletal myofibril. FEBS J. **272**, 2578–2590 (2005)
8. Vignon, X., Beaulaton, J., Ouali, A.: Ultrastructural localization of calcium in postmortem bovine muscles: a cytochemical and X-ray microanalytical study. Histochem. J. **21**, 403–411 (1989)
9. Taylor, R.C., Cullen, S.P., Martin, S.J.: Apoptosis: controlled demolition at the cellular level. Nat. Rev. Mol. Cell Biol. **9**, 231–241 (2008)
10. Op den Kamp, J.A.F.: Lipid asymmetry in membranes. Annu. Rev. Biochem. **48**, 47–71 (1979)
11. Williamson, P., Schlegel, R.A.: Back and forth: the regulation and function of transbilayer phospholipid movement in eukaryotic cells. Mol. Membr. Biol. **11**, 199–216 (1994)
12. Martin, S.J., Reutelingsperger, C.P., McGahon, A.J., Rader, J.A., Van Schie, R.C., LaFace, D. M., Green, D.R.: Early redistribution of plasma membrane phosphatidylserine is a general feature of apoptosis regardless of the initiating stimulus: inhibition by overexpression of Bcl-2 and Abl. J. Exp. Med. **182**, 1545–1556 (1995)
13. Fadok, V.A., Savill, J.S., Haslett, C., Bratton, D.L., Doherty, D.E., Campbell, P.A., Henson, P.M.: Exposure of phosphatidylserine on the surface of apoptotic lymphocytes triggers specific recognition and removal by macrophages. J. Immunol. **148**, 2207–2216 (1992)
14. Colognato, H., Yurchenco, P.D.: Form and function: the laminin family of heterotrimers. Dev. Dynam. **218**, 213–234 (2000)
15. Kerr, J.F., Wyllie, A.H., Currie, A.R.: Apoptosis: a basic biological phenomenon with wide-ranging implications in tissue kinetics. Br. J. Cancer **26**, 239–257 (1972)
16. Fidzianska, A., Kaminska, A., Glinka, Z.: Muscle cell death. Ultrastructural differences between muscle cell necrosis and apoptosis. Neuropat. Polska **29**, 19–28 (1991)
17. Green, D.R.: Apoptotic pathways: ten minutes to dead. Cell **121**, 671–674 (2005)
18. Offer, G., Trinick, J.: On the mechanism of water holding in meat: The swelling and shrinking of myofibrils. Meat Sci. **8**, 245–281 (1983)
19. Boudjellal, A., Becila, S., Coulis, G., Herrera-Mendez, C.H., Aubry, L., Lepetit, J., Harhoura, K., Sentandreu, M.A., Ait-Amar, H., Ouali, A.: Is the pH drop profile curvilinear and either monophasic or polyphasic? Consequences on the ultimate bovine meat texture. Afr. J. Agric. Res. **3**(3), 195–204 (2008)
20. Huang, F, Huang, M, Zhang, H, Zhang, C, Zhang, D, Zhou, G.: Changes in apoptotic factors and caspase activation pathways during the postmortem aging of beef muscle. Food Chem. **190**, 110–114 (2016)
21. Ouali, A., Gagaoua, M., Boudida, Y., Becila, S., Boudjellal, A., Sentandreu, M.A.: Biomarkers of meat tenderness: present knowledge and perspectives in regards to our current understanding of the mechanisms involved. Meat Sci. (2013)

Part II
Applications of Microscopy in the Physical/Chemical Sciences, at all Dimensional Scales

Synthesis of Nanostructure Carbon Thin Films by Microwave Plasma-Enhanced Chemical Vapor Deposition

Ahmed S. Wasfi, Hammad R. Humud and Mohammed E. Ismael

Abstract In this work, hydrogenated amorphous carbon (a-C:H) thin films were prepared from methane gas using microwave plasma enhanced chemical vapor deposition (MPECVD). The microwave plasma system was built in our laboratory with maximum attained plasma electron temperature and density of (0.65 eV) and (1.45×10^{18} cm^{-3}), respectively. The effect of argon/methane mixing ratio on the optical and structural properties of the films were investigated. X-ray diffraction results indicated a broad peak ranging from 15 to 35 in 2θ angle confirm the amorphous nature of the deposited carbon films. While, FTIR measurements revealed the existence of (a-C:H) through its absorption peak. AFM was used to study the morphological characteristics and to monitor the nanostructure under the influence of different mixing ratios of argon with methane. The distribution of granularity ranged from 30 to 140 nm, and the particles average diameter were 94.39–81.92 nm, also the root mean square roughness was increased with the increasing of the argon/methane mixing ratio. The optical energy gap (E_g) decreased from 2.76 to 2.40 eV with increasing deposition pressure from 0.5 to 1.5 mbar and varying the argon/methane mixing ratio.

1 Introduction

In the last four decades, a huge number of researchers have worked on the microwave induced plasma and microwave plasma enhanced chemical vapor deposition [1, 2]. This technology is extremely promising because of its high

A.S. Wasfi (✉) · H.R. Humud · M.E. Ismael
Physics Department, College of Science, University of Baghdad,
Jadiriya, Baghdad, Iraq
e-mail: a.wasfi@scbaghdad.edu.iq

H.R. Humud
e-mail: dr.hammad6000@yahoo.com

M.E. Ismael
e-mail: mohamad_physics2011@yahoo.com

A.Y. Oral and Z.B. Bahsi Oral (eds.), *3rd International Multidisciplinary Microscopy and Microanalysis Congress (InterM)*, Springer Proceedings in Physics 186,
DOI 10.1007/978-3-319-46601-9_8

control of film quality, low cost, high efficiency and reproducibility. Moreover, the subject of amorphous carbon deposition occupied the interest of researchers as a coating material which has unique properties such as a wide range of optical energy gap and other features [3].

These films are produced by ionizing a hydrocarbon compound, which is possibly dissociated and accelerated in an electric field towards the substrate where the film is grown at a moderately low pressure. Amorphous carbon (a-C) is a non-crystalline form of carbon that only has a short range structural order. The term (a-C:H) is also used to include hydrogen-containing (hydrogenated) forms of non-crystalline carbon. The two main crystalline forms of carbon exhibit either 100 % sp^3 bonding (in the case of diamond) or 100 % sp^2 bonding (in the case of graphite), while a-C films contain a mixture of sp^3 and sp^2 bonding. It is the ability to control the ratio of sp^3 to sp^2 bonds through growth conditions that allows the development of a-C films to exhibit astonishingly different mechanical, electrical and optical properties [4]. In addition to bonding hybridization, a second parameter like hydrogen content, plays an important role in determining the film properties. Such films have found applications as dielectrics in the electronics industry and as a protective coating for metals and other surfaces such as silicon and silicon devices [5].

In this work, deposition of carbon films by microwave plasma enhanced chemical vapor deposition was achieved, using methane as a hydrocarbon precursor gas. Furthermore, the structural and optical properties of these films with different deposition parameters were investigated.

2 Experimental

Our home-built microwave plasma system consisted of cylindrical stainless steel vacuum chamber of 10 cm inner diameter and 30 cm length. The cylindrical chamber has many ports, one port is coupled with vacuum pump system (double stage rotary vane pump, pumping speed 25 m^3/h with zeolite trap), to maintain a vacuum of about 10^{-4} mbar in the chamber. The other port is used to introduce the gases, which are fed through highly precision (±2.5 %) flowmeters (glass rotameters) from Shanghai Cixi Instrument. Furthermore, there is a borosilicate glass view window fixed at the side port which is used to monitor the plasma spectrum of the reacting species by an optical spectrometer. The viewport is employed also as a quick access door which can be used to feed the samples into the plasma reaction chamber. The two axial end ports of the cylindrical chamber are closed with two flanges that have circular holes at their centres where a quartz glass tube is passed through along the cylindrical chamber axis.

The inside of the glass tube was at atmospheric pressure whereas the outside was at low pressure. After proper evacuation time, Argon was fed to the chamber, as a working plasma gas, through a needle valve that controls the gas flow precisely. The filling pressure in the chamber was monitored using Pirani gauge. To avoid

heating due to the plasma in the chamber, air blower was fixed at one end of the quartz tube.

Microwave was generated by means of 750 W magnetron, working at frequency of 2.45 GHz, and was transmitted to the plasma chamber through a rectangular waveguide which hold a TE_{10} transmission mode.

A copper pipe of diameter (6 mm) was inserted at the other end of the glass tube through the waveguide at a certain position that represents a maximum of the standing wave oscillating in it. This copper pipe acts as an antenna that conducts the microwave radiation from the waveguide to the vacuum chamber. A cylindrical plasma column obtained as a result of the propagation of electromagnetic surface wave plasma (SWP). In fact, this configuration can be considered as a coaxial cable transmission line where the copper pipe represents the central conductor of the cable, the glass tube represents its outer insulator and the generated plasma, which is a conductive medium, replaces the missing outer conductor of the coaxial cable. When the electric field strength, which is transmitted through the copper antenna, exceeds the breakdown field strength of the argon gas, discharge ignites at the low pressure regime inside the chamber. Increasing the microwave power, the plasma grows along the quartz tube and radially homogeneous plasma is formed. The space occupied by the plasma is proportional to many factors such as microwave power and working gas pressure.

The glass substrate after proper cleaning procedure was fixed at certain position just below the plasma; this was done using a linear motion feedthrough adjusting the position of the substrate holder. Schematic diagram and a photograph of the experimental arrangement are shown in Fig. 1.

Diagnostic of the microwave argon plasma was done in an earlier work [6], in order to optimize our system and ensuring that the MPECVD system is capable of producing a good quality and reproducible a-C:H films. Optical emission spectroscopy was used as a plasma diagnostic method; it gives very interesting information on the plasma parameters such as plasma electron temperature and density,

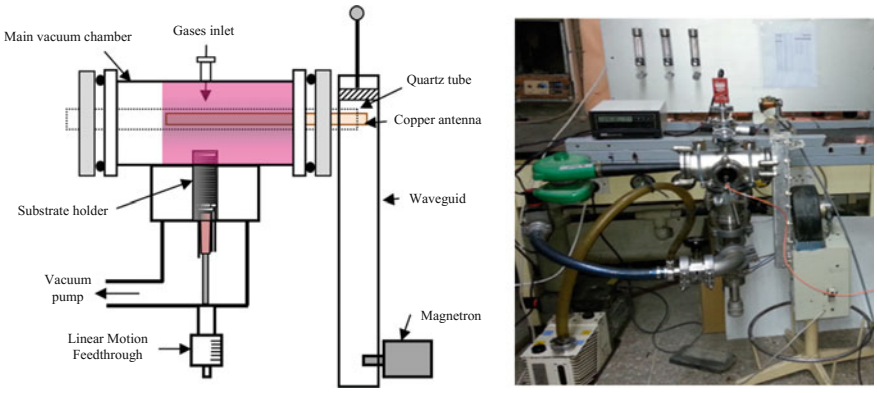

Fig. 1 A schematic diagram and a photograph of the microwave plasma system

moreover, on the influence of process parameters. Electron temperature was determined using the ratio of two argon plasma spectral lines' intensity method. The maximum attainable plasma electron temperature and density were 0.65 eV and 1.45×10^{18} cm^{-3}, respectively.

3 Results and Discussion

Three sets (A, B and C) of amorphous carbon films were deposited on glass substrates, from pure methane gas and methane diluted with argon, at three different working pressures using microwave plasma. The deposition pressure was varied from 0.5 to 1.5 mbar. Whereas, the methane flow rate was fixed at 24 sccm for all sets, the deposition time was fixed at 90 min and the substrate temperature was at room temperature for all deposited films. Table 1 shows the methane, argon and their mixing flow rates, thickness and deposition rate of carbon films at different working pressures.

Thicknesses of carbon thin films were measured using StellarNet (EPP2000) system. Figure 2 shows the variation of a-C:H film thickness with working pressure and at different argon dilution ratios (0, 25 and 40 %). It is found that the highest thickness and deposition rate of a-C:H films was achieved at the lowest working pressure of 0.5 mbar. Furthermore, the thickness of a-C:H films decreased when the percentage of argon gas increased.

The formed CH radicals are favourable in the development of the a-C:H films [7]. Therefore, decreasing of methane concentration (adding more argon gas) reduces C_2 and CH radicals, which contributed in the growth of the a-C:H films through the deposition process. Also, when the pressure decreases the plasma electron temperature (T_e) increases and consequently more dissociation of the methane molecules occurs, hence the growth rate increases as shown in Fig. 2. The

Table 1 Flow rate of methane and argon at different working pressures, film thickness and deposition rate

Working pressure (mbar)	Sample	CH_4 flow (sccm)	Ar flow (sccm)	Total flow (sccm)	CH_4 (%)	Ar (%)	Film thickness (nm)	Deposition rate (nm/min)
0.5	A1	24	0	24	100	0	293.1	3.25
	A2	24	8	32	75	25	180.8	2.01
	A3	24	16	40	60	40	152.3	1.69
1.0	B1	24	0	24	100	0	241.5	2.68
	B2	24	8	32	75	25	161.2	1.79
	B3	24	16	40	60	40	144.7	1.61
1.5	C1	24	0	24	100	0	142.4	1.58
	C2	24	8	32	75	25	109.2	1.21
	C3	24	16	40	60	40	89.3	0.99

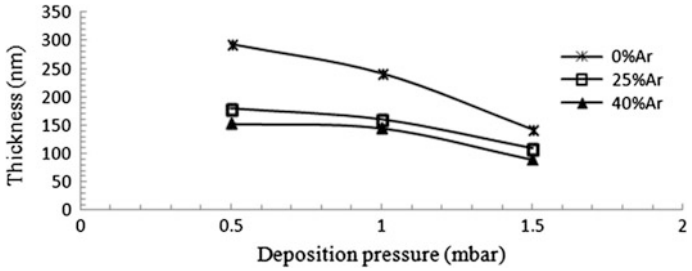

Fig. 2 Thickness of a-C:H films as a function of deposition pressure at different argon dilation ratios (0, 25 and 40 %)

simultaneous effects of argon ion sputtering at the film surface and the reduction of carbon radicals due to the increasing of argon gas percentage, reduce the film thickness and the deposition rate of a-C:H films.

X-ray diffraction (XRD) is a common non-destructive experimental method to structurally characterize materials. The X-ray diffraction patterns of three samples A1, A2 and A3 were investigated using Shimadzu diffractometer unit (LabX XRD —6000). The three samples have similar patterns as they are shown in Fig. 3, the broad peak ranging from 15 to 35 in 2θ angle confirms the amorphous structure of the carbon films.

FTIR measurements were made using SHIMADZU FTIR-8400S with spectral range 400–4000 cm^{-1} and a maximum resolution of 0.85 cm^{-1}. Figure 4 represents infrared transmission curves of samples (A1, A2 and A3) obtained using the FTIR spectrometer. The absorption band 2800–3000 cm^{-1} can be attributed to hydrogen-carbon stretching modes. This absorption band is related to the presence of H bonds in the form of sp-CH and sp^3-CH_2 groups in the a-C:H films [8].

The morphological characteristics of the amorphous carbon films were studied by Atomic Force Microscope (AFM) to monitor the nanostructure of the films under the influence of different mixing ratios of argon with methane. Figure 5 illustrates the surface morphology of sample A1 that scanned by AFM. It can be seen that the particles grown on the surface of the deposited films are comparatively uniform with few large particles protruding on the surface. The AFM results of the distributions of granularities are approximately from 30 to 140 nm and the average

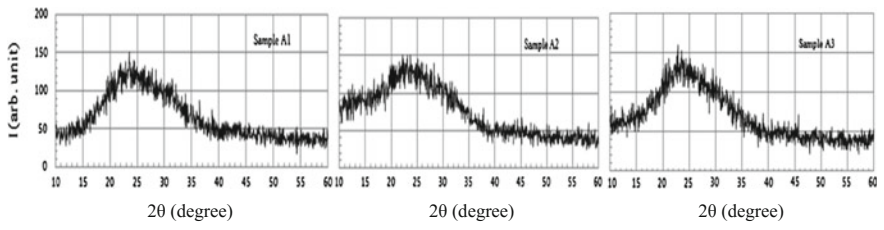

Fig. 3 XRD patterns for A1, A2 and A3 samples

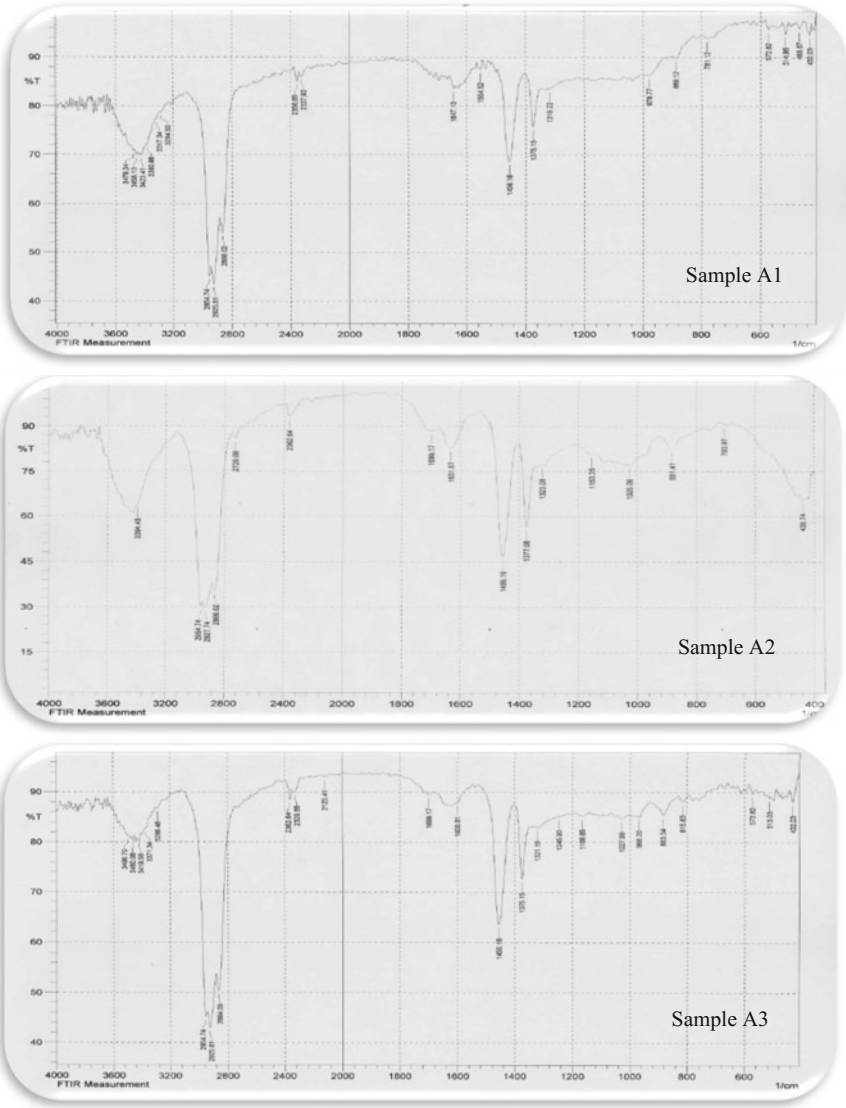

Fig. 4 FTIR spectrum of samples A1, A2 and A3

diameter of particles is 94.39, 85.59 and 81.92 nm for samples A1, A2 and A3, respectively. Table 2 lists the particles average diameter, root mean square roughness and roughness average of the samples that have obtained from AFM.

Figure 6 shows the particles average diameter in samples A1, A2 and A3 as a function of argon concentration. It is clear, once the mixing ratio of argon to methane increases the particles average diameter is decreased. Figure 7 represents

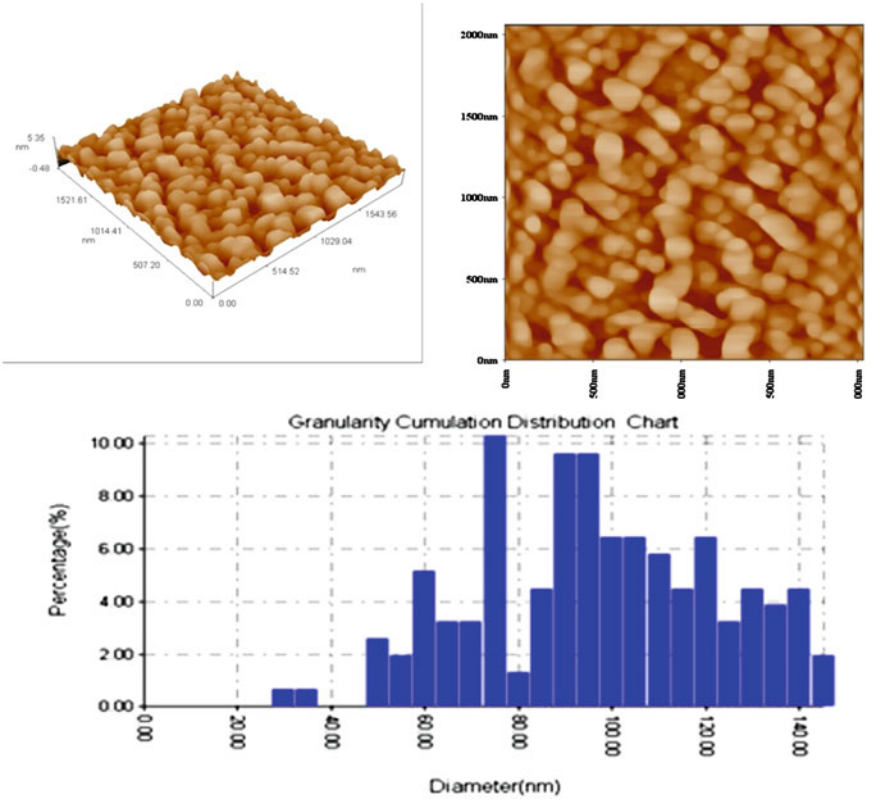

Fig. 5 AFM topography and granularity cumulation distribution charts for sample A1

Table 2 Particles average diameter, root mean square roughness and roughness average of samples A1, A2 and A3 that were obtained from AFM

Sample	Particles average diameter (nm)	Root mean square roughness (nm)	Roughness average (nm)
A1	94.39	0.759	0.626
A2	85.59	2.17	1.9
A3	81.92	3.38	2.88

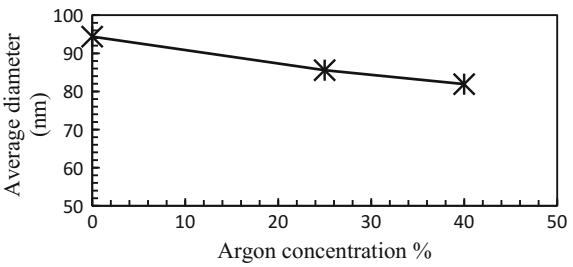

Fig. 6 Particles average diameter in samples as a function of argon concentration

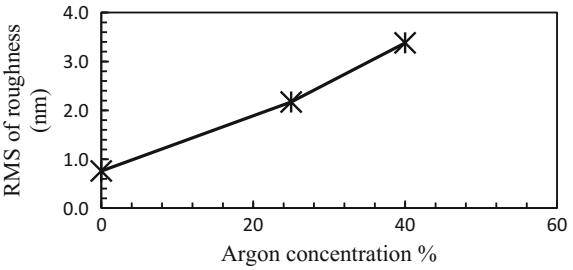

Fig. 7 Variation of root mean square roughness in samples with argon concentration

the variation of root mean square (RMS) of roughness with argon concentration in samples A1, A2 and A3, which increased with the increasing of argon/methane mixing ratio.

The optical properties of the a-C:H films deposited by MPECVD technique on glass substrates, at different methane concentrations and different pressures have been investigated using the UV-VIS-IR spectrophotometer (Metertech SP-800, wavelength range: 190–1100 nm, bandwidth: 2 nm, wavelength accuracy: 0.5 nm).

After obtaining the optical absorbance spectra and calculating the absorption coefficient α of a-C:H films in the wavelength range 300–700 nm, the optical band gap can be obtained from the extrapolation of the asymptotic at the linear part of the curve that is drawn between $(\alpha h\upsilon)^2$ and photon energy (hυ), its intersection with the photon energy axis represents the optical band gap E_g. Figure 8 illustrates E_g values of the samples at different working pressures (0.5, 1.0 and 1.5 mbar) and different methane/argon mixing ratios.

The variation of the optical energy gap (E_g) with methane concentration at different pressures is illustrated in Fig. 9, it can be seen that the optical energy gap increases when the methane concentration is increased and decreases as the

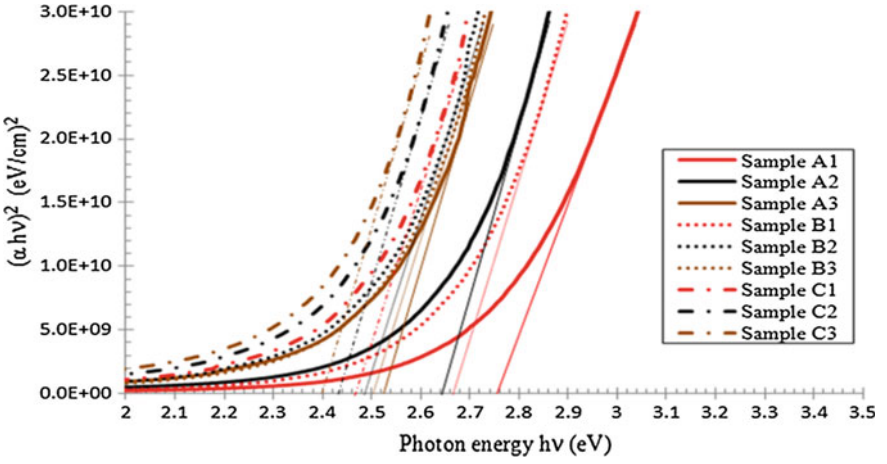

Fig. 8 Variation of $(\alpha h\upsilon)^2$ with photon energy (hυ) of a-C:H films

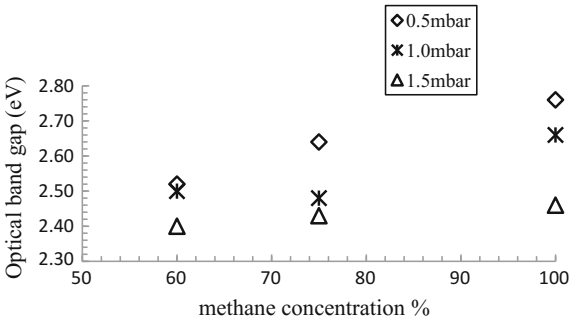

Fig. 9 Optical energy gap E_g versus methane concentration percentage at different working pressures

deposition pressure is increased, a decrease in the E_g can be attributed to: (1) an increase in sp^2 fraction, (2) a decrease in H content, (3) an increase in sp^2 cluster size in the a-C films, this result has a good agreement with the results of Silva [9].

4 Conclusion

Nanostructured amorphous carbon films were successfully deposited via microwave plasma enhanced chemical vapor deposition (MPECVD). The outcomes of this work showed that highest deposition rates were obtained for the films deposited at lowest flow rate or lowest deposition pressure. Argon addition to the CH_4 plasmas decreases the growth rate due to the sputtering effect of Ar ions. The reported experimental results of the optical and structural properties of the films suggested the possibility to control the film growth rate and the optical energy gap and consequently the improvement of the photoconductivity by proper selection of the deposition parameters. It is obvious that mixing ratio of argon to methane has an important effect on the topography of the amorphous carbon film surface.

References

1. Lebedev, Y.: Microwave discharges: generation and diagnostics. J. Phys. Conf. Ser. **257**, 012016 (2010). http://iopscience.iop.org/1742-6596/257/1/012016
2. Hinkov, I., Farhat, S., Lungu, C., Gicquel, A., Silva, F., Mesbahi, A., Brinza, O., Porosnicu, C., Anghel, A.: Microwave plasma enhanced chemical vapor deposition of carbon nanotubes. J. Surf. Eng. Mater. Adv. Technol. **4**(4), 196–209 (2014). doi:10.4236/jsemat.2014.44023
3. Tachibana, K., Nishida, M., Harima, H., Urano, Y.: Diagnostics and modelling of a methane plasma used in the chemical vapour deposition of amorphous carbon films. J. Phys. D Appl. Phys. **17**(8), 1727–1742 (1984)
4. Mutsukura, N., lnoue, S., Machi, Y.: Deposition mechanism of hydrogenated hard-carbon films in a CH_4 discharge plasma. J. Appl. Phys. **72**(43), 43–53 (1992)
5. Adhikari, S., Kayastha, M., Ghimire, D., Aryal, H., Adhikary, S., Takeuchi, T., Murakami, K., Kawashimo, Y., Uchida, H., Umeno, M.: Improved photovoltaic properties of heterojunction

carbon based solar cell. J. Surf. Eng. Mater. Adv. Technol. **3**, 178–183 (2013). doi:10.4236/jsemat.2013.33024
6. Wasfi, A.S., Humud, H.R., Ismael, M.E.: Spectroscopic measurements of the electron temperature in low pressure microwave 2.45 GHz argon plasma. Iraqi J. Phys. **13**(27), 23–34 (2015)
7. Cicala, G., Bruno, P., Losacco, A.: PECVD of hydrogenated diamond like carbon films from CH_4-Ar mixtures: growth chemistry and material characteristics. Diam. Relat. Mater. **13**, 1361–1365 (2004)
8. Lazar, G., Zellama, K., Vascan, I., Rusu, I.: Infrared absorption properties of amorphous carbon films. J. Optoelectron. Adv. Mater. **7**(2), 647–652 (2005)
9. Silva, S., Forrest, R., Burden, A., Anguita, J., Shannon, J., Sealy, B., Okano, K.: Amorphous carbon: state of the art. In: Proceeding of the 1st International Specialist Meeting on Amorphous Carbon, pp. 1–374. World Scientific Press (1997)

Microstructural Investigation of SPA-C Steel Sheets Used in Railway Vehicles in Resistance Spot Welding

Nuri Akkaş, Erman Ferik, Recep Kılıç, Erdinç İlhan and Salim Aslanlar

Abstract This paper presents an experimental study on resistance spot welding of SPA-C steel sheets used in side wall and roof in rail vehicles. SPA-C steel sheets having 2.3 mm thicknesses were joined by using resistance spot welding as lap joint. A timer and current controlled resistance spot welding machine having 120 kVA capacity and a pneumatic application mechanism with a single lever was used to prepare the specimens. Welding periods were chosen as 5, 10, 15, 20, 25 and 30 cycles and also welding currents were increased from 6 kA up to 14 kA by rise of 0.5 kA. The electrode force was kept constant at 6 kN. The micro and macro-structures of prepared welding specimens were investigated by means of an optical microscope and scanning electron microscope (SEM) in order to see the joinability of SPA-C steel sheets by resistance spot welding.

N. Akkaş (✉) · E. Ferik · E. İlhan · S. Aslanlar
Department of Metallurgical and Materials Engineering,
University of Sakarya, Sakarya, Turkey
e-mail: akkas.nuri@gmail.com

E. Ferik
e-mail: ermanferik@gmail.com

E. İlhan
e-mail: ozsarac@sakarya.edu.tr

S. Aslanlar
e-mail: aslanlar@sakarya.edu.tr

R. Kılıç
Sakarya Metropolitan Municipality, Sakarya, Turkey
e-mail: recep.kilic@sakarya-saski.gov.tr

A.Y. Oral and Z.B. Bahsi Oral (eds.), *3rd International Multidisciplinary Microscopy and Microanalysis Congress (InterM)*, Springer Proceedings in Physics 186,
DOI 10.1007/978-3-319-46601-9_9

1 Introduction

Resistance spot welding (RSW) is one of the oldest of the electric welding processes in use by industry today. The weld is made by a combination of heat, pressure and time. As the name implies, it is the resistance of the material to be welded to current flow that causes a localized heating in the part [1].

The RSW is a complex process which involves electrical, thermal, mechanical and metallurgical phenomenon. These complicated phenomenon have a major influence on the formation of a welded joint, including the nugget and the heat-affected zone (HAZ) [2]. In order to appropriate weld nuggets, understanding these complicated factors and evaluating the role of the major metallurgical factors and processing parameters are necessary.

The weld microstructure is the most complete measure of weld quality and is therefore the best way to define process requirements [3]. However, RSW produces more complex microstructures than other welding processes, because it involves rapid heating and cooling. Microstructural changes during RSW dramatically affect mechanical properties by transforming the base metal microstructure [4]. The result of this usually weld nugget with significantly different microstructure than the base metal. A coarse granular structure is susceptible to hot cracking. A finer structure, distorted columnar structure, or equiaxed structure is more resistant. The structure and crystallographic orientation of grains in the heat affected zone generally continue to the fusion zone [5]. This complex microstructure development can impact the failure behavior of RSW and should be taken into account.

To date, the microstructures and failure mechanisms of RSW SPA-C steel sheets have not been examined in sufficient detail. So, the objective of the present study is to characterize the microstructure of SPA-C steel sheets after RSW, as a basis for understanding the relationship between the microstructure and the failure behavior.

2 Experimental Work

2.1 Materials

The materials studied are SPA-C steel sheets having 2.3 mm thicknesses, which are used in rail vehicle bodies. The chemical composition and the mechanical properties of the sheet are, respectively, shown in Tables 1 and 2.

Table 1 Chemical composition of steel sheets used in experiments

Chemical composition	C	Si	Mn	P	S	Cr	Ni	Cu
wt%	0.097	0.397	0.433	0.0913	0.0016	0.605	0.257	0.331

Table 2 Mechanical properties of the sheet steel

Yield strength (MPa)	430
Tensile strength (MPa)	550
Total elongation (%)	45

2.2 Welding Process

A timer and current controlled RSW machine having 120 kVA capacity and pneumatic application mechanism with a single lever was used in the experiments.

The electrode force was continuously measured and controlled during the experiments. Weld time, hold time and clamping time were adjusted automatically by electronic devices of machine. Welding was carried out by using water cooled conical Cu–Cr electrodes having a contact surface of same diameter (7 mm) in accordance with EN ISO 5182 [6].

The prepared specimens were overlapped with 30 mm. spacing and welded. For joining, 5, 10, 15, 20, 25 and 30 cycles weld time were applied while other welding parameters such as applied electrode pressure (6 kN) and clamping and hold times of electrode (25 cycles) were kept constant. The welding current was increased from 6 to 14 kA by 0.5 kA increments.

The cross-sections of the weld joints were polished mechanically and etched with Nital. The specimens were then examined with an optical microscope (Nikon SMZ800) and a scanning electron microscope (SEM; JEOL JSM-6060LV).

3 Results and Discussion

The spot weld joint of SPA-C steel sheets contains three microstructural zones of primary interest that will be described based on the proximity to the weld. Figure 1 displays the three zones of interest:

(i) Fusion Zone (FZ) or weld nugget contains the sections of the material that becomes molten and resolidifies during the welding and subsequent cooling.
(ii) Heat Affected Zone (HAZ) which is experienced solid state microstructural alterations during thermal cycle of welding. This section of the weld has not been melted; however, significant thermal affects are evident. Several microstructural changes can occur in the HAZ. The HAZ of a spot weld can be subdivided into three main regions which include the coarse grain (CG), fine grain (FG) and intercritical (IC) HAZ [4].
(iii) The final zone is the base material (BM). This zone is adjacent to the HAZ and represents the portion of the spot weld joint that has not been affected by the welding process and is comprised of the parent material used to produce the weld [7].

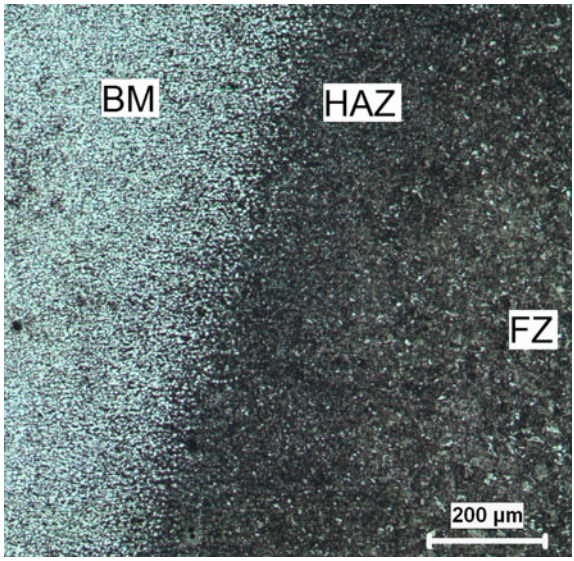

Fig. 1 Metallurgical zones of the spot weld joint of SPA-C steel

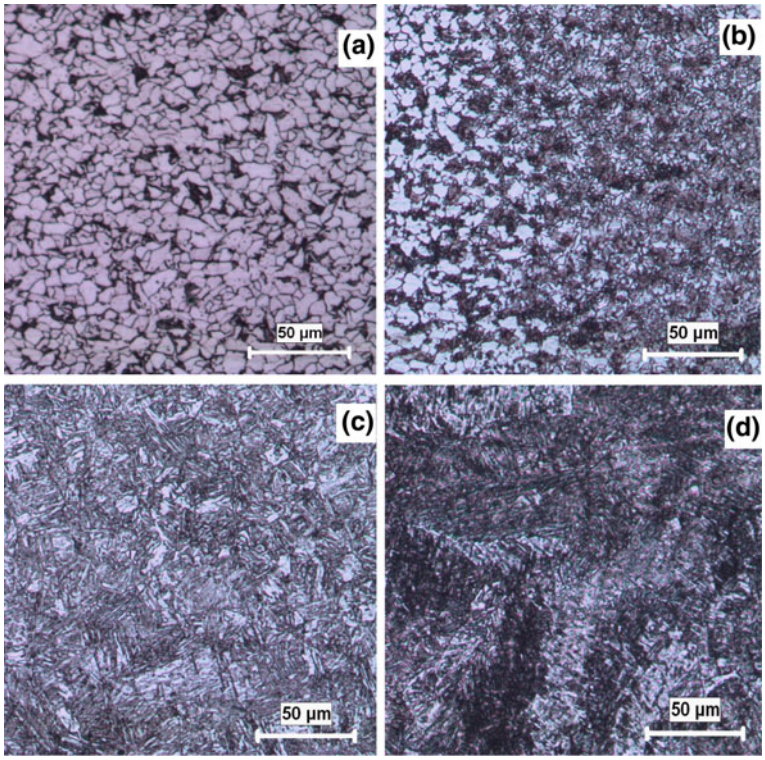

Fig. 2 Microstructures of spot welded SPA-C samples **a** base metal, **b** IC-FG HAZ, **c** CG HAZ, and **d** fusion zone or weld nugget

Figure 2 shows the weld microstructure for SPA-C steel. The BM microstructure consists of ferrite grains (grey) with carbides (dark colored) situated at grain boundaries (Fig. 2a).

The IC HAZ consists mainly of ferrite and some pearlite (Fig. 2b). The FG HAZ consists mainly of pearlite and some ferrite (Fig. 2b). The CG HAZ shown in Fig. 2c has a needle like structure. The needle like structure consists of island and side plate ferrite with stripes of grain boundary ferrite. The FZ consists of a columnar structure composed mainly of martensite, which is shown in Fig. 2d. In this region which experience grain coarsening during thermal cycle of the welding process, both high cooling rate and large grain size promote the formation of martensite.

Several researchers have noted the presence of martensite in the RSW nugget and HAZ. Martensite will create altered mechanical properties (i.e., increased strength, reduced ductility) in comparison to the original material properties [8].

Figure 3 shows the SEM micrograph of (a) BM, (b) IC HAZ, (c) CG HAZ and (d) FZ. As shown in Fig. 3a, the microstructure of base metal used in this investigation is ferritic with a small amount of Fe_3C. EDS analysis of point (1) were given in Table 3. SEM images of FZ (Fig. 3d) reveal that there exist needle-like microstructures within the martensite laths.

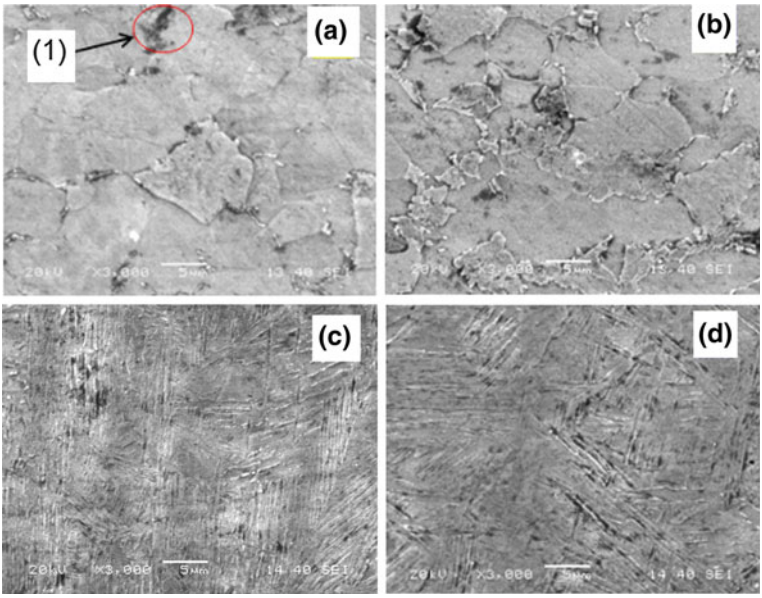

Fig. 3 SEM micrograph of spot welded SPA-C samples **a** base metal, **b** IC HAZ, **c** CG HAZ, and **d** fusion zone or weld nugget

Table 3 EDS analysis of point (1)

Elt.	Line	Intensity (c/s)	Error 2-sig	Conc	Units	
C	Ka	3.85	1.240	3.744	wt%	
O	Ka	14.04	2.370	5.043	wt%	
Fe	Ka	338.99	11.644	91.213	wt%	
				100.000	wt%	Total

4 Conclusion

The microstructures in the fusion zone of SPA-C steel sheets after RSW were characterized by means of optical microscopy and SEM. The main conclusions are summarized as follows.

- The microstructure of base metal used in this investigation is ferritic with a small amount of Fe_3C.
- The microstructure of weld nugget, which mainly consists of martensite. Despite the low carbon content of the base metal, martensite phase was formed due to high cooling rate involved in RSW process.
- Several microstructural changes can occur in the HAZ. The HAZ can be sub-divided into three main regions which include the coarse grain (CG), fine grain (FG) and intercritical (IC) HAZ. The IC HAZ consists mainly of ferrite and some pearlite. The FG HAZ consists mainly of pearlite and some ferrite. The CG HAZ has a needle like structure. In HAZ, the grain coarsening occurred owing to thermal cycle of the welding process.

References

1. American Welding Society: Safety and Health Fact Sheet no: 21. Florida, Miami (1999)
2. Zhang, H., Senkara, J.: Resistance Welding-Fundamentals and Applications. Florida, Boca Raton (2006)
3. Karagoulis, M.J.: Control of materials processing variables in production resistance spot welding. Dissertation, University of Michigan State (1991)
4. Khan, M.I.: Spot welding of advanced high strength steels. Dissertation, University of Waterloo (2007)
5. Miller, K.W.: Impact strength and failure mechanisms of spot welds in automotive materials. Dissertation, University of South Carolina (2000)
6. Turkish Standards Institution: Resistance welding—materials for electrodes and ancillary equipment, TS EN ISO 5182. Ankara (2010)
7. Weishaupt, E.R.: Effect of weld schedule variation on the weldability and durability of AHSS spot weld joints. Dissertation, University of Alabama (2012)
8. Vogler, M.M.B.: Investigation of resistance spot weld formation. Dissertation, University of Stanford (1993)

Microstructure/Properties Relationship of Advanced Heat-Resistant Intermetallics TiAl(Nb,Cr,Zr) After Casting and Float Zone Processing

A.V. Kartavykh, M.V. Gorshenkov and A.V. Korotitskiy

Abstract New Ti-44Al-5Nb-3Cr-1.5Zr (at.%) β-stabilized intermetallic alloy was synthesized by the electron beam casting and afterwards re-solidified by the high-gradient (300 °C cm^{-1}) induction float zone (FZ) technique. FZ-processing led to the ordered microstructure creation consisting of volumetrically prevailing ($\gamma + \alpha_2$) lamellar colonies separated by minor seam-like γ-granular interlayers, and the least intergranular quota of β(Ti)/B2 phase. The optimum phase balance, sub-micron interlamellar spacing and preferable alignment of lamellae along the thermal gradient were controlled by FZ-conditions. Unique microstructural adjustment enhances drastically the high-temperature yield strength, Young modulus and creep resistance. Thus the thermal limit of γ-TiAl(Nb,Cr,Zr) structural applicability could be extended from 750–800 °C towards 900–950 °C.

1 Introduction

γ-TiAl based intermetallics are attractive candidates for applications in aircraft turbine engines for their low density and specific strength [1]. Recently General Electric has reported the application of GE48-2-2 (Ti-48Al-2Nb-2Cr at.%) alloy in its newest engine, *GEnx-1B* for the *Boeing-787 Dreamliner* that best illustrates the cutting edge of TiAl technology. Low pressure turbine (LPT) firstly incorporates the last two stages made of γ-TiAl blades that save 180 kg per engine when compared to its precursor. The *GEnx* offers up to 15 % better fuel consumption, which translates to 15 % less CO_2 emission [2]. However, heat-resistant potential of GE48-2-2 alloy is seemingly near to be limited by the final LPT stages operating at the "softest" thermal modes. Many investigations are targeted to improve strength and ductility of γ-TiAl within the temperature range expanded towards 800–850 °C. In the last years, novel γ-TiAl based alloys family, so-called TNM alloys, have been developed which define the upper strength limit of titanium aluminides [3–5].

A.V. Kartavykh (✉) · M.V. Gorshenkov · A.V. Korotitskiy
National University of Science and Technology "MISIS",
Leninsky Pr. 4, 119049 Moscow, Russia
e-mail: karta@korolev-net.ru

A.Y. Oral and Z.B. Bahsi Oral (eds.), *3rd International Multidisciplinary Microscopy and Microanalysis Congress (InterM)*, Springer Proceedings in Physics 186,
DOI 10.1007/978-3-319-46601-9_10

These Al-lean alloys contain a high level of β-stabilizing elements Nb, Mo, Cr, W et al. That lead to the existing of a significant amount of β(Ti) phase with disordered *bcc* structure, or its ordered B2 counterpart within technologically important domains of phase diagram. Being especially ductile at the elevated temperatures, stabilized β(Ti)/B2 phase plays the positive role in an improvement of workability and applicability of TNM alloys.

Present paper reports the results of advanced structural properties development of Ti-44Al-5Nb-3Cr-1.5Zr (at.%) alloy belonging to the TNM family. Aiming its microstructure control and thus enhancement of heat resistance and deformability on the basis of purely thermodynamic approach, we applied the high-gradient float zone processing, offering additionally the advantage of a crucibleless technique.

2 Experimental Design, Materials and Methods

The synthesis of raw alloy has been performed by the electron beam semi-continuous casting. As-cast billet had 165 mm in diameter being 15 kg of mass; the casting details could be found in [6]. The rod-shaped blanks (Ø10 × 120 mm) of cast alloy with uncontrolled microstructure were directionally re-solidified by the vertical FZ technique in argon of 4 N grade purity. Zone melting is ensured by narrow inductor loop that is powered by AC current of 400 kHz frequency. The inductor power of 700 V A caused the axial temperature gradient value 300 °C cm^{-1} at solid/melt interface. Re-solidification proceeds at the upward inductor movement with the rate of 150 mm h^{-1}, that ensured the cooling rate of 5.5 °C s^{-1} of processed material. The facility is represented in Fig. 1a, and the details of FZ process could be found in [7]. Figure 1b shows the exterior of FZ-processed ingot.

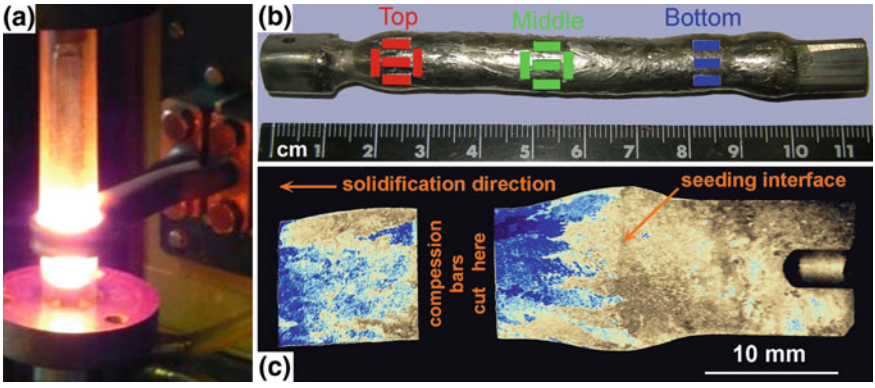

Fig. 1 **a** Induction FZ-resolidification of γ-TiAl(Nb,Cr,Zr) cast blank in the laboratory facility; **b** FZ-processed ingot with labeled positions where the specimens were cut for the compression testing; **c** appearance of the aligned lamellar microstructure (*blue areas*) within axial bottom section of FZ-ingot

As-cast and FZ-alloys were comparatively analyzed in SEM and TEM modes using the *JEOL JSM6610* electron microscope also equipped with *AZtecSynergy* EBSD system. The revealing of ordered structure appearance at the initial stage of FZ-process was implemented by optical polarized light microscopy (Fig. 1c).

Mechanical properties of alloys at 750–1050 °C were examined under 10^{-7} bar vacuum using quenching-deformation dilatometer *DIL 805A/D* by Bähr Thermoanalyse GmbH. The device has operated under the static loads varying from 1 to 700 MPa to obtain the temperature-stress dependences of creep rate, and to plot the stress/strain curves using the test bars of Ø2.5 × 5 mm dimensions.

3 Results and Discussion

SEM micrograph of as-cast alloy (Fig. 2a) displays the coarse three-phase microstructure. Basic intermetallic phase γ-TiAl (D 0.19 type) is imaged here by grey, α_2-Ti_3Al (L 1.0 type)—by black and stabilized B2—as bright phase. Although XRD revealed the same phases in FZ-ingots [7], their microstructure has refined drastically (Fig. 2b). The continuous cooling transformation diagrams, both calculated and experimental [8, 9] predict the formation of duplex microstructure consisting of ($\gamma + \alpha_2$) lamellae regions and massive γ grains, and what's more the lamellar fraction should exceed 90 % at the applied cooling rate of 5.5 °C·s^{-1}.

Really in our β-stabilized alloy the lamellae occupy about 80 % of volume. This structural constituent is shown in Fig. 2c, d representing the magnified framed areas in Fig. 2b. Fine design of such area (Fig. 2d) is composed of the alternating γ-TiAl (grey) and α_2-Ti_3Al (black) lamellae. γ-TiAl lamellae of 400–800 nm thickness are volumetrically prevailing. α_2-Ti_3Al phase contains in FZ-alloy as lamellae of 100–200 nm thickness. γ-granular fraction (Fig. 2b, c) is estimated as 15 %, and the remaining 5 % falls at the B2 fraction that is seen in Fig. 2b, c as bright phase.

Within the state diagram the phase transformation path of cooling Ti-44Al-5Nb-3Cr-1.5Zr alloy can be simplified as the follow:

$$\beta(\mathrm{Ti}) \longrightarrow (\mathrm{a})\mathrm{B2} + \alpha \longrightarrow (\mathrm{b})\mathrm{B2} + \alpha_2\text{-}\mathrm{Ti_3Al} + \gamma\text{-}\mathrm{TiAl} \quad (1)$$

where the stage (b) is splintered in turn into two kinetic mechanisms really proceeding in non-equilibrium mode:

$$\alpha \rightarrow (\alpha_2\text{-}\mathrm{Ti_3Al} + \gamma\text{-}\mathrm{TiAl})\text{-lamellar} \quad (2)$$

$$\mathrm{B2} \rightarrow \gamma\text{-}\mathrm{TiAl}\text{-granular} \quad (3)$$

They explain the joint formation of γ-granular and ($\gamma + \alpha_2$)-lamellar fractions co-existing with the retained B2 phase. The reaction (2) begins inside α-grains leading to basic lamellar colonies formation within the boundaries of each transformed α-grain (Fig. 2b, d). Since B2 is disposed along these boundaries, the partial

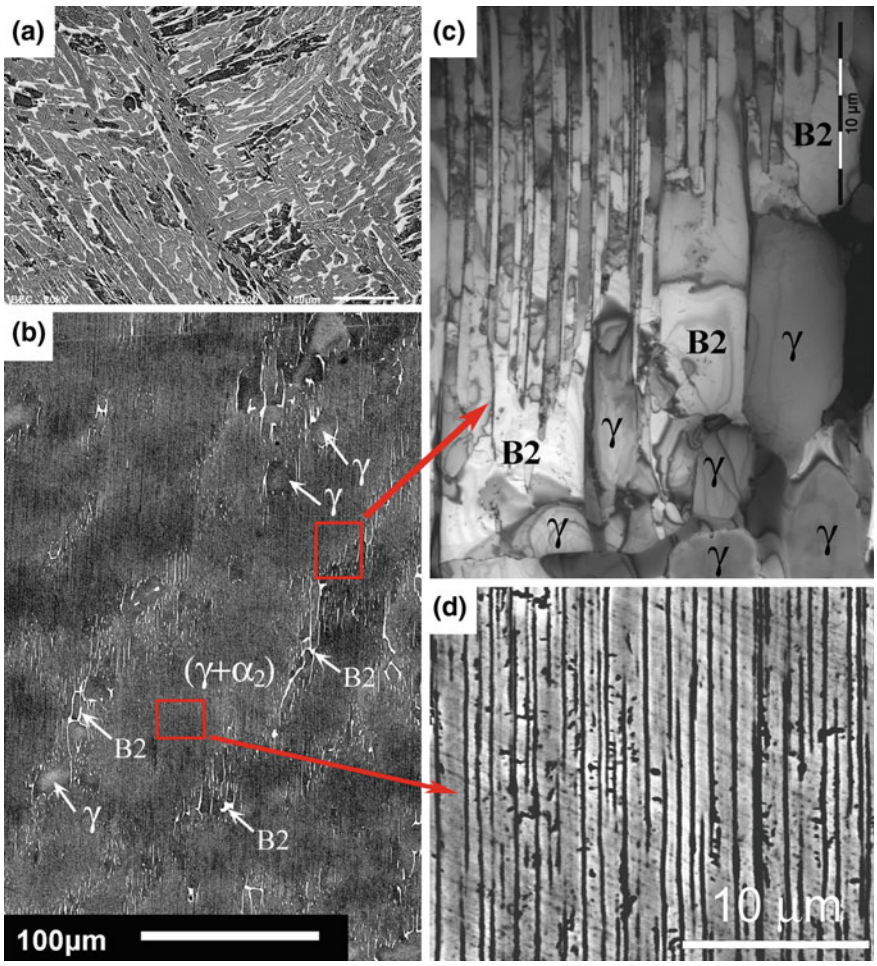

Fig. 2 **a** Irregular microstructure of cast Ti-44Al-5Nb-3Cr-1.5Zr; **b** ordered microstructure of FZ-processed alloy; **c** magnified transition between the lamellar area and (γ + B2) interlayer; **d** magnified axially-aligned (γ + α_2) lamellae. **a**, **b**, **d** SEM, and **c** TEM micrographs

proceeding of reaction (3) results to the formation of (B2 + γ) seam-like interlayers between (γ + α_2) colonies (Fig. 2c). The ratio of transformation (3) can be controlled kinetically by the cooling rate and thus by the related zone melting rate. Therefore, the phase content ratio (γ + α_2)/γ/B2 can be controlled within some limits.

The effect of ultra-high directional thermal gradient is extremely important for ordering of resulted micro-structural system. Owing to this thermodynamic spatially anisotropic "pulling" impact in the course of FZ-processing, the aligned lamellar microstructure is formed throughout the sample, where direction of (γ + α_2) lamellae is preferably parallel to the ingot's axis. As revealed from Fig. 1c, the new

ordered structure appears shortly after the initial seeding interface. In Fig. 1c this structure is given in blue, thus reflecting the axially aligned lamellar fraction.

For detailed analysis of lamellae orientation the selected area of 2×3 mm^2 dimension that disposed in ingot's longitudinal section was examined by EBSD. Colored orientation map of this area is shown in Fig. 3a. Figure 3b, c display the inverse pole figures (IPF) derived from Y (axial) and X (diametrical) directions of ingot's section, respectively. Because of much smaller α_2-lamellae thickness, the γ-phase solely was revealed in *Kikuchi* pattern. Although SEM images in Fig. 2b–d demonstrate at the first glance well-aligned lamellar colonies, it is clear from Fig. 3a that the domains of different γ-lamellae orientations still occur inside the former β-grains. The IPF of axial ingot's direction (Fig. 3b) indicates the lamellae

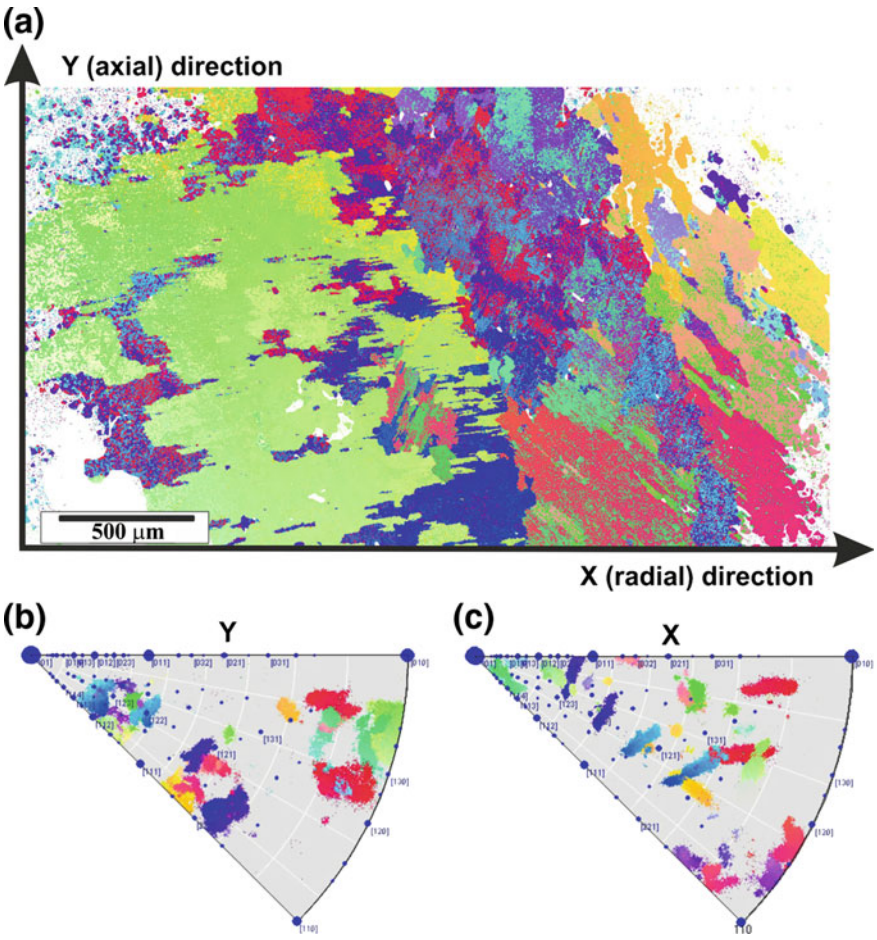

Fig. 3 **a** EBSD colored orientation map in the longitudinal ingot's section along with the inverse pole figures derived from Y-axial (**b**) and X-diametrical (**c**) directions of the ingot

tendency to be oriented along three selected directional zones with low (of few degrees order) angle deviations around each. This selective growth conditioned by the high-gradient thermal impact and results in the axially-ordered substructure formation. Only three *Blackburn* orientation relationships between the parent α and born γ-lamellar phases can survive within the directional seedless solid-phase transformation. In contrast, Fig. 3c shows a multiple orientations of γ-lamellae and does not reflect any preferable growth along an ingot radius.

The ordered microstructure depicted in Fig. 2b possesses more balanced properties compared to the cast material. Fine lamellar constituent (Fig. 2d) is responsible for the improved strength and creep under axial loading. The heat resistance and plasticity get enhanced thanks to the incorporated interlayers composed of γ- and ductile B2-phases (Fig. 2c). At the expense of limited elastic mobility of γ-grains within the medium of B2-phase, such interlayers promote relaxation of stresses in lamellar structure, thus raising the high-temperature threshold of its destruction.

The results of high-temperature compression tests are given in Fig. 4a–d. FZ-processing led to substantial improvement of deformability (Fig. 4a), increase of yield strength (Fig. 4b) and Young modulus (Fig. 4c) at the same temperatures. At the same loads the creep resistance rises. Exemplarily, under the load of

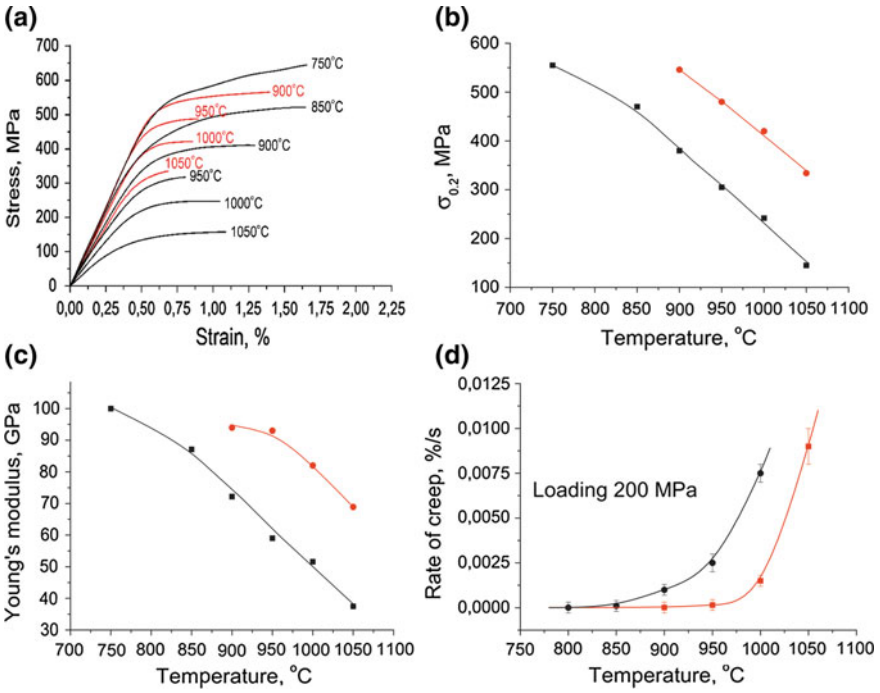

Fig. 4 Plots of physical-mechanical properties of cast (in *black*) and FZ-processed (in *red*) alloys versus temperature: **a** axial deformation curves; **b** yield strength; **c** Young's modulus; **d** creep rate

200 MPa the first signs of creep of FZ-alloy appear only at 950 °C (Fig. 4d). In other words, FZ-alloy possesses the identical level of deformability parameters at the temperatures by 100–150 °C higher when compared to cast material. Thus the upper temperature limit of γ-TiAl(Nb,Cr,Zr) applicability could be extended from 750–800 °C towards 900–950 °C.

4 Conclusions

1. The applicability of high-gradient induction float zone (FZ) processing is demonstrated for microstructure engineering and enhancement of mechanical properties of β-stabilized γ-TiAl intermetallics.
2. FZ processing led to specific microstructure creation of Ti-44Al-5Nb-3Cr-1.5Zr (at.%) alloy consisting of ($\gamma + \alpha_2$) lamellar colonies separated by minor interlayers of (B2 + γ) phases. The ($\gamma + \alpha_2$)/γ/B2 phase balance, submicron lamellar thickness and preferable alignment of lamellae along the applied thermal gradient were controlled by FZ conditions.
3. Microstructural adjustment enhances the high-temperature deformability parameters: yield compressive strength, Young modulus and creep resistance.
4. As a result the upper temperature limit of γ-TiAl(Nb,Cr,Zr) structural applicability could be extended from 750–800 °C towards 900–950 °C.

ACKNOWLEDGMENTS Authors acknowledge the Russian Ministry of Education and Science grant 11.951.2014/K, and Russian Foundation for Basic Research grant 16-03-00757-a.

References

1. Appel, F., Paul, J.D.H., Oering, M.: Gamma Titanium Aluminide Alloys: Science And Technology. WILEY-VCH, Weinheim (2011)
2. http://www.geaviation.com/commercial/engines/genx
3. Clemens, H., Mayer, S.: Adv. Eng. Mater. **15**, 191 (2013)
4. Schwaighofer, E., Clemens, H., Mayer, S., et al.: Intermetallics **44**, 128 (2014)
5. Erdely, P., Werner, R., Schwaighofer, E., et al.: Intermetallics **57**, 17 (2015)
6. Kartavykh, A.V., Asnis, E.A., Piskun, N.V., et al.: J. Alloy. Compd. **588**, 122 (2014)
7. Kartavykh, A.V., Asnis, E.A., Piskun, N.V., et al.: J. Alloy. Compd. **643**, S182 (2015)
8. Rostamian, A., Jacot, A.: Intermetallics **16**, 1227 (2008)
9. Hu, D., Huang, A.J., Wu, X.: Intermetallics **15**, 327 (2007)

Micro Graphical Analysis and Comparison of MWNT and CNF Reinforced Polymer Composite

Smrutisikha Bal

Abstract Numerous research efforts have been undertaken regarding the mechanical and electrical behavior of epoxy matrix by the introduction of carbon nanofillers like multiwall carbon nanotube (MWNT) and carbon nanofiber (CNF). In the present work, a simple but novel route regarding preparation of nanocomposites has been reported in terms of curing them at low temperature. The purpose is to investigate the effect of reinforcing strategies on properties of prepared composites using different nanomaterials that are again supplemented by microscopic investigations. Flexural properties, hardness and electrical conductivity of nanocomposites improved significantly than epoxy. Among the two nanocomposites, MWNT composite demonstrated enhanced results that were again confirmed from micro graphical analysis. CNF composite exhibited comparatively lower mechanical result but almost equivalent electrical result with CNT composite.

1 Introduction

Polymer matrix composites with carbon nanotube (CNT)/Carbon nanofibres (CNF) reinforcement have become popular in structural applications because of their unique atomic structure, very high aspect ratio and extraordinary mechanical and physical properties like strength and flexibility [1–3]. CNTs are crystalline carbon nanostructures consisting of single or multiple concentric graphene cylinders. The high bond strength of the constituent carbon–carbon bonds of multi-walled carbon nanotubes (MWNTs) are the reason behind its outstanding mechanical properties. Carbon nanofibres (CNF) are hollow cylinders with diameters typically in the range 50–500 nm and lengths of a few tens of microns giving high aspect ratios (length/diameter > 100) with parallel and homogeneous alignment of nanoscopic graphene layers along the axis. In the polymer field, epoxy resins are well

S. Bal (✉)
Department of Metallurgical and Materials Engineering,
National Institute of Technology, Rourkela, Odisha, India
e-mail: balss@nitrkl.ac.in

A.Y. Oral and Z.B. Bahsi Oral (eds.), *3rd International Multidisciplinary Microscopy and Microanalysis Congress (InterM)*, Springer Proceedings in Physics 186,
DOI 10.1007/978-3-319-46601-9_11

established thermosetting matrices of advanced composites, displaying a series of interesting characteristics, which can be adjusted within broad boundaries [4–7]. They are used as high grade synthetic resins, for example, in the electronics, aeronautics, and astronautics industries. Several studies related to the enhancement of the mechanical and electrical properties of epoxy matrix by the introduction of CNT/CNF have been conducted [6, 8–14].

In this work, the nanocomposites have been prepared using sonication method with very low content (0.75 wt%) of MWNTs and of CNFs in the epoxy matrix. Additionally, the nanocomposites were prepared for the first time at low temperature in refrigeration process. Flexural modulus and strength, hardness and electrical conductivity of resin as well as nanocomposite samples were examined and variations in different properties between the respective cases were observed. The purpose of this study is to optimize the conventional method of manufacturing composites and examine their effect on mechanical and electrical which were again supplemented by electron microscopy.

2 Materials and Methods

Multiwall carbon nanotubes (MWNTs) used for this experiment are of 95 % purity, 10–50 μm length and 20–70 nm diameter (Fig. 1a). Carbon nanofibers (CNFs) are 200–500 nm in diameter (Fig. 1b), 10–50 μm long and >95 % purity. Transmission and scanning electron microscope (TEM and SEM morphology) of these products (Fig. 2) reveals that they are randomly oriented, curved and entangled as well as multiwall in nature. Epoxy polymer matrix was prepared by mixing epoxy resin (Ciba-Geigy, araldite LY-556 based on Bisphenol A) and hardener HY-951 (aliphatic primary amine) in wt. ratio 100/12. Epoxy resin (5.3–5.4 equiv/kg) was of low processing viscosity and good overall mechanical properties.

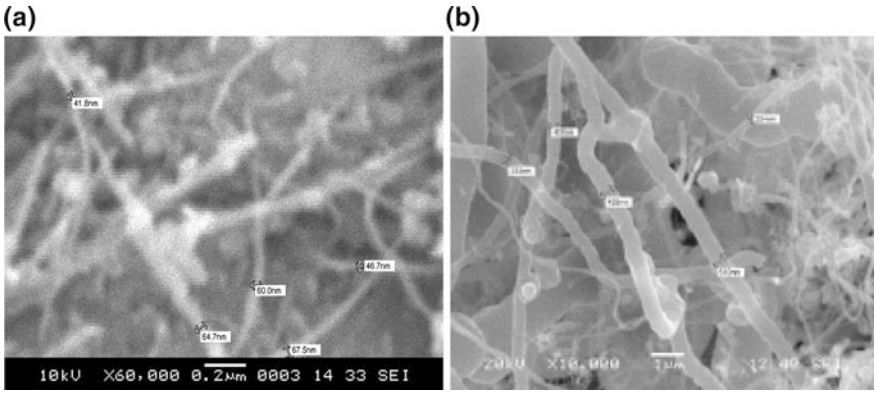

Fig. 1 SEM of **a** MWNTs and **b** CNFs; showing their diameter

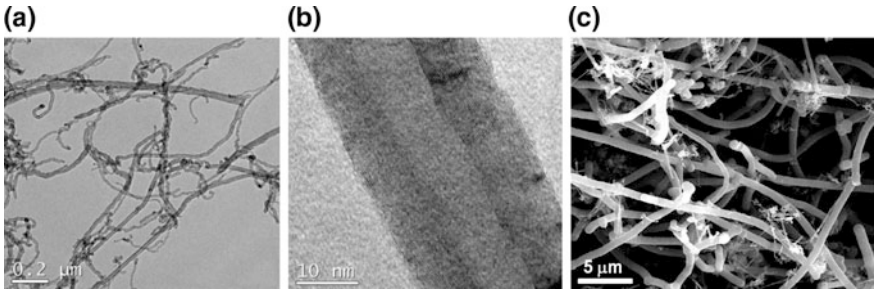

Fig. 2 **a** TEM of MWNTs, **b** TEM of MWNTs showing multiwall nature, and **c** SEM of CNFs

Nanocomposites were prepared by dispersing MWNTs and CNFs in the epoxy resin kinetically by ultrasonication. Then the mixture was cured under vacuum at 90 °C followed by hardener addition by manual stirring. One part of sample was allowed to set at room temperature and another part under refrigeration. Flexural tests were accompanied according to ASTM D790–00 on an Instron 5967 testing machine. The hardness of all composite specimens was measured using a micro-hardness tester by the Vickers hardness test method. The electrical properties of the neat and nanophased epoxy were measured by using a Keithley electrometer with sample dimension (8 mm × 5 mm × 4 mm). All the results obtained by mechanical and electrical studies were supplemented and complimented by microscopic investigation through scanning electron microscope (SEM: Jeol JSM 6480 LV), Field emission scanning electron microscope (FESEM: Nova NANOSEM 450) and Transmission Electron Microscope (TEM: FEI, TECHNAI G2).

3 Results and Discussion

3.1 Morphological Analysis

The fracture surfaces of composites give first information about fracture mechanisms and the influence of particle modification on the fracture behaviour. To investigate the failure mechanism of CNF/epoxy as well as MWNT/epoxy composites, the fracture surfaces of failed specimens were examined. The fracture mechanism was different for neat epoxy resin and reinforced composites. While the surface of epoxy resin was very smooth (Fig.3a), the fracture surfaces of composites contained some deep cleavages with deviation of crack propagation plane (Fig. 3b, c). The nano-reinforcements, here carbon nanofillers may act as obstacles, change of the propagation rate that justified the higher mechanical strength of composites. Low magnification surface image of failure nanocomposite samples were compared to obtain some remarkable information. CNF composite surface (Fig. 3b) demonstrates a typical feature of brittle fracture behaviour, thus accounting for the low fracture

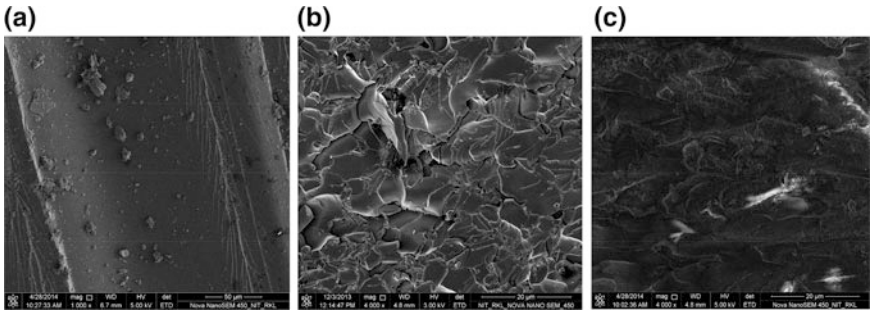

Fig. 3 Fracture surface of **a** neat epoxy, **b** CNF/epoxy, and **c** MWNT/epoxy composites

toughness. However, the fracture surfaces of MWNT composites in Fig. 3c seem to be comparatively rougher. The surface with very non-directional deformation lines thus interrupting the crack propagation. In other words, since the segments of primary crack front had to bend between the nanotubes, more energy must be necessary for such local deviation which leads to an increase in mechanical properties [15].

3.2 Dispersion Behaviour

The final properties of a composite primarily depend on the dispersion of the fillers inside the matrix. Hence a micrographical comparison of dispersion behavior is necessary between CNF and MWNT composites in the present work. It was found that dispersion was better in MWNT composite (Fig. 4a) where nanotubes were seen to be uniformly distributed. Aggregated phases were found in CNF composite (Fig. 4b) that may be the reason behind poor mechanical properties mentioned in the following section. Reported study reveals that CNFs are more prone to agglomeration that ultimately affects the modulus [16].

3.3 Mechanical Properties

Increase in flexural properties was found in the order Epoxy < CNF/epoxy < MWNT/epoxy (Table 1). This may be attributed to the high mechanical strength of MWNT. Further, low temperature treatment results relatively better curing of epoxy resin, which allows more interaction with hardener by delaying the settling time [17, 18]. This facilitates improvement in dispersion in nanocomposites. Stronger bonding between matrix and nanofillers is expected from these nanocomposites whose microscopic verification was elaborated afterwards.

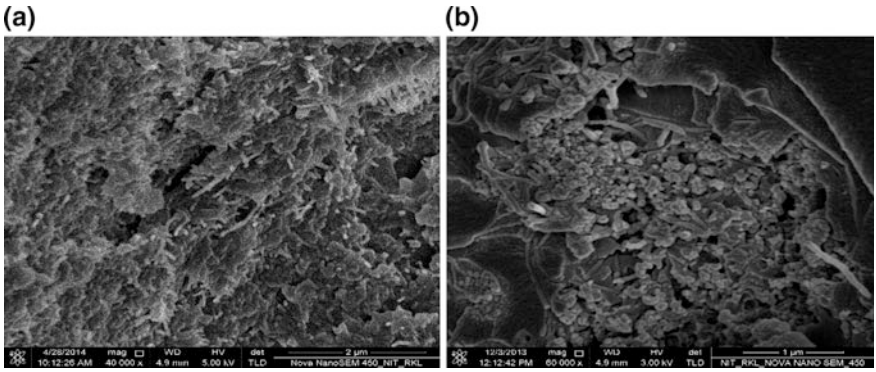

Fig. 4 Dispersion of nanofillers in **a** MWNT/epoxy and **b** CNF/epoxy composites

Table 1 Flexural properties and hardness of specimens

Sample	Epoxy	CNF/epoxy	MWNT/epoxy
Flexural modulus (MPa)	1998	2835	3673
Flexural strength (MPa)	45	62	79
Hardness (MPa)	12	19	22

Hardness results agreed well with flexural test results with the confirmation that MWNT composite samples had improved mechanical properties than CNF composite samples with the same wt% of nanofiller.

4 Microscopic Analysis

Comparative analysis of high magnification fracture images of MWNT and CNF composites highlighted some vital evidences. Bridging of nanotube inside the crack region is observed in MWNT that facilitates mechanical properties (Fig. 5a). In these composites, the cracks were spanned by the nanotubes causing enhanced resistance to the crack propagation process. The bridging of the nanotubes as a mechanism of inhibiting the crack initiation in polymer and ceramic based nanocomposites has been well illustrated in literature [19]. On the other hand, Carbon nanofibers are debonded from the epoxy matrix that creates a weak interfacial bonding (Fig. 5b). Few CNFs are pulled out depicting lesser mechanical properties.

4.1 Electrical Conductivity

Demonstrable improvement in electrical conductivity was found in CNF/MWNT reinforced composites. Conductivity of these nanocomposite samples are 6 orders

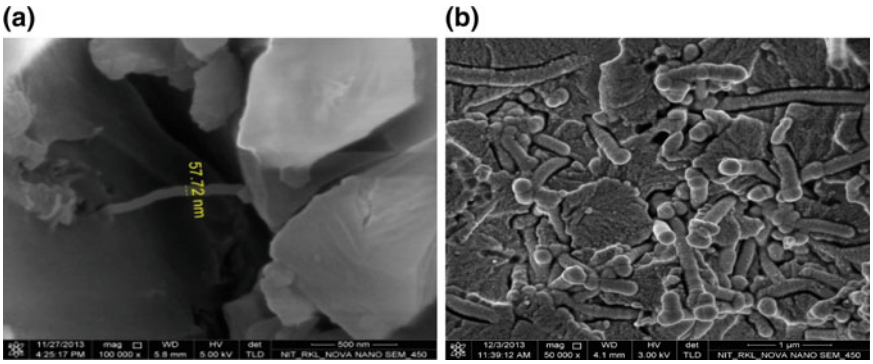

Fig. 5 Bridging in **a** MWNT/epoxy; **b** debonding in CNF/epoxy composites

Table 2 Electrical conductivity of specimens

Sample	Conductivity in S/cm
Epoxy	2.8×10^{-9}
MWNT	5.4×10^{-3}
CNF	2.7×10^{-3}

higher to that of resin sample (Table 2). MWNTs are generally conducting and typically have aspect ratio of around 1000. Even if the CNFs do not touch each other directly, conductivity of the nanocomposites is achieved as long as the distances between them are lower than the hopping distances of the conducting electrons. As the materials with electrical conductivity between 10^{-6} and 10^{-2} S/cm are treated as semiconductors, the nanocomposites presented in this work can be utilized for electrostatic discharge and electromagnetic interference shielding applications [16].

4.2 Network Formation

SEM of fracture surface of one direction of MWNT composites shows limited agglomerates of nanotubes near the fracture area (Fig. 6a). Improvement of electrical conductivity in this case was due to the fact that aggregated phases form a conductive three-dimensional network throughout the whole sample (Fig. 6b). This agglomeration promoted CNT-to-CNT interactions through surface contact (or tunnelling) and hence facilitates the electrons flow through the formed CNT network [20]. Furthermore, formation of network inside the epoxy matrix by the

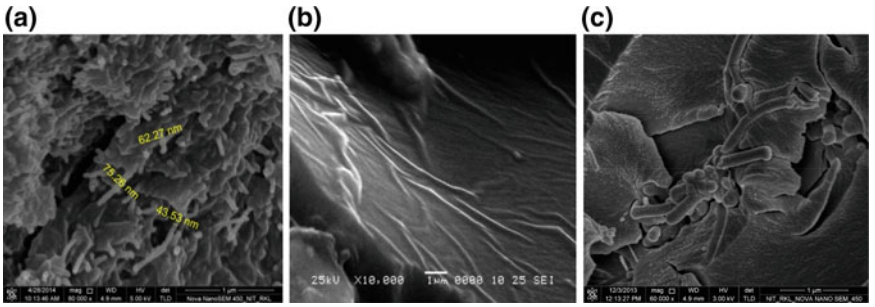

Fig. 6 Network formation in **a** MWNT/epoxy, **b** MWNT/epoxy, and **c** CNF/epoxy composites

aggregate phases of carbon nanofibers in CNF composite is shown in Fig. 6c. Although the network formation feature by nanofillers here is different from MWNT composite but the result in both is enhancement in electrical conductivity.

5 Conclusions

- Although flexural and hardness values of MWNT/epoxy sample are much higher than CNF/epoxy sample, electrical conductivity in those samples offer little variation.
- Uniform dispersion of nanofillers inside epoxy matrix of MWNT composites facilitates higher flexural modulus and hardness.
- Agglomerates and debonding of nanofibers in CNF composites are the reason for lower value of mechanical properties.
- Network formation of nanoparticle inside the matrix of both nanocomposites is observed in micrographs that confirms electrical conductivity.
- The results obtained from mechanical and electrical studies in this work are well supported by microscopic demonstration.

Acknowledgments The authors would like to thank Naval Research Board (DRDO), Govt. of India for the financial support to carry the research work.

References

1. Wagner, H.D., Lourie, O., Feldman, Y., Tenne, R.: Stress-induced fragmentation of multiwall carbon nanotubes in polymer matrix. Appl. Phys. Lett. **72**, 188–190 (1998). doi:10.1063/1.120680
2. Dagani, R.: Nanocomposites. Chem. Eng. News **77**(23), 25–37 (1999)

3. Maruyama, B., Alam, K.: Carbon nanotubes and nanofibers in composite materials, Sampe J, **38**(3), 59–70 (2002) (ISSN 0091-1062)
4. Peyser, P., Bascom, W.D.: Effect of filler and cooling rate on the glass transition of polymers. J. Macromol. Sci. Phys. B **13**, 597–610 (1977). doi:10.1080/00222347708212211
5. Schadler, L.S., Giannaris, S.C., Ajayan, P.M.: Load transfer in carbon nanotube 0060 composite. Appl. Phys. Lett. **73**, 3842–3844 (1998). doi:10.1063/1.122911
6. Sandler, J., Shaffer, M.S.P., Prasse, T., Bauhofer, W., Schutle, K., Windle, A.H.: Development of a dispersion process for carbon nanotubes in an epoxy matrix and the resulting electrical properties. Polymer **40**, 5967–5971 (1999). doi:10.1016/S0032-3861(99)00166-4
7. Cooper, C.A., Young, R.J., Halsall, M.: Investigation into the deformation of carbon nanotubes and their composites through the use of Raman spectroscopy. Compos. A **32**, 401–411 (2001). doi:10.1016/S1359-835X(00)00107-X
8. Lau, K.T., Hui, D.: Effectiveness of using carbon nanotubes as nano-reinforcements for advanced composite structures. Carbon **40**, 1605–1606 (2002)
9. Penumadu, D., Dutta, A., Pharr, G.M., Files, B.: Mechanical properties of blended singlewall carbon nanotube composites. J Mater Res **18**, 1849–1853 (2003). doi:10.1557/JMR.2003.0258
10. Gojny, F.H., Wichmann, M.H.G., Köpke, U., Fiedler, B., Schulte, K.: Functionalisation effect on thermo-mechanical behavior of multi-wall carbon nanotube/epoxy-composite. Compos. Sci. Technol. **64**, 2303–2308 (2004). doi:10.1016/j.compscitech.2004.01.024
11. Kotaki, M., Wang, K., Toh, M.L., Chen, L., Wong, S.Y., He, C.: Electrically conductive epoxy/clay/vapor grown carbon fiber hybrids. Macromolecules **39**(3), 908–911 (2006). doi:10.1021/ma0522561
12. Lee, H., Mall, S., He, P., Shi, D.L., Narasimhadevara, S., Yeo-Heung Y.: Shanov V., Schulz, M.J.: Characterization of carbon nanotube/nanofiber-reinforced polymer composites using an instrumented indentation technique. Compos. Part B. **38**(1), 58–65 (2007). doi:10.1016/j.compositesb.2006.04.002
13. Xu, L.R., Bhamidipati, V., Zhong, W.H., Li, J., Lukehart, C.M., Lara-Curzio, E., Liu, K.C., Lance, M.J.: Mechanical property characterization of a polymeric nanocomposite reinforced by graphitic nanofibers with reactive linkers. J. Compos. Mater. **38**(18), 1563–1582 (2004). doi:10.1177/0021998304043758
14. Choi, Y.K., Sugimoto, K., Song, S., Gotoh, Y., Ohkoshi, Y., Endo, M.: Mechanical and physical properties of epoxy composites reinforced by vapor grown carbon nanofibers. Carbon **43**, 2199–2208 (2005). doi:10.1016/j.carbon.2005.03.036
15. Ayatollahi, M.R., Shadlou, S., Shokrieh, M.M.: Mixed mode brittle fracture in epoxy/multiwalled carbon nanotube nanocomposites. Eng. Fract. Mech. **78**, 2620–2632 (2011). doi:10.1016/j.engfracmech.2011.06.021
16. Xu, L.R., Rosakis, A.J.: Impact failure characteristics of sandwich structures; part II: effects of impact speeds and interfacial bonding strengths. Int. J. Solids Struct. **39**(16), 4237–4248 (2002). doi:10.1016/S0020-7683(02)00245-7
17. Bal, S.: Experimental study of mechanical and electrical properties of carbon nanofiber/epoxy composites. Mater. Des. **31**, 2406–2413 (2010). doi:10.1016/j.matdes.2009.11.058
18. Bal, S., Saha, S.: Comparison and analysis of physical properties of carbon nanomaterial doped polymer composites. High Perform. Polym. **26**, 953–960 (2014). doi:10.1177/0954008314535823
19. Ma, P.C., Kim, J.K., Tang, B.Z.: Effects of silane functionalization on the properties of carbon nanotube/epoxy nanocomposites. Compos. Sci. Technol. **67**, 2965–2972 (2007). doi:10.1016/j.compscitech.2007.05.006
20. Xiao, G., Tao, Y., Lu, J., Zhang, Z.: Highly conductive and transparent carbon nanotube composite thin films deposited on polyethylene terephthalate solution dipping. Thin Solid Films **518**, 2822–2824 (2010). doi:10.1016/j.tsf.2009.11.021

The Effect of ZrO_2 Addition on Sintering and Microstructural Properties of Cordierite Produced from Zeolite

Betül Çitak, Sunay Ayhan, Abdulkadir Akyol, Tuğba Tunç Parlak and A. Şükran Demirkıran

Abstract Cordierite ($2MgO.2Al_2O_3.5SiO_2$) that is known as a high technology ceramics was produced from mechanically activated powder mixture with the intention of increasing the reactivity of substance. The powder mixture consisted of zeolite that was used as a source of silica, pure MgO, Al_2O_3 and ZrO_2. During powder preparation, mechanical activation duration, speed of main disc and ball to mass ratio was kept constant at 60 min, 600 rpm and 20:1, respectively. After compacting of the mechanically activated powder mixture, the samples were sintered at 1250 °C for 1 h. The sintered samples were analyzed by means of X-ray diffraction (XRD) and scanning electron microscopy (SEM). The sintering behavior of the samples was determined by measuring the linear shrinkage, water absorption, density and apparent porosity. The hardness measurements were performed by using a Vickers microhardness tester under the load of 500 gf for 10 s. The density of samples ranged between 2.554 and 2.777 g/cm^3 depending on ZrO_2 additive. The hardness values of the undoped sample, the sample containing 10 % Zirconia and the sample containing 20 % Zirconia were found as 8.63, 9.60 and 11.9 GPa, respectively.

1 Introduction

Cordierite ($2MgO.2Al_2O_3.5SiO_2$) is a technically important ceramic due to combination of properties such as its excellent thermal shock resistance resulting from its low thermal expansion coefficient, high thermal and chemical stability, high refractoriness and mechanical strength [1–5]. Until now, many raw materials, such as clay, kaolinite, talc, andalusite, stevensite, diatomite, steatite, gibbsite, sepiolite, and forsterite, were used as raw materials in the production of cordierite. However, there is no sufficient knowledge about cordierite ceramic produced from zeolite [6].

B. Çitak · S. Ayhan · A. Akyol · T.T. Parlak · A. Şükran Demirkıran (✉)
Department of Metallurgy and Materials Engineering, Engineering Faculty, Esentepe Campus, Sakarya University, 54187 Sakarya, Turkey
e-mail: dkiran@sakarya.edu.tr

A.Y. Oral and Z.B. Bahsi Oral (eds.), *3rd International Multidisciplinary Microscopy and Microanalysis Congress (InterM)*, Springer Proceedings in Physics 186,
DOI 10.1007/978-3-319-46601-9_12

Zeolites are hydrate aluminosilicate minerals with a structure based on a three-dimensional network of aluminium and silicon tetrahedra linked by sharing oxygen atoms [7]. Low-cost natural zeolites are abundantly found as raw materials in many countries; they are very easily crushed and milled; and they facilitate sintering in the production of ceramic bodies [8, 9]. Recently, attention has been given to studies involved the addition of suitable dopants such as zirconia, ceria, titania, yttria and silicon carbide to improve properties of ceramics.

The aim of this study is to investigate the effect of ZrO_2 addition on sintering and microstructural properties of cordierite produced from zeolite.

2 Experimental Procedures

In this study, natural zeolite (90–95 % clinoptilolite, cristobalite), MgO (99 %, Alfa Aesar), Al_2O_3 (99.9 %, Alfa Aesar) and ZrO_2 (99 %, Alfa Aesar) were used as raw materials. The natural zeolite used as a silica source was supplied from the ETI Holding Company located in Turkey. The chemical composition of zeolite used as raw material is presented in Table 1. Firstly, the mixture of $MgO/Al_2O_3/SiO_2$ in the ratios of 2:2:5 adjusted according to the cordierite stoichiometry was prepared. Then, ZrO_2 (10 and 20 wt%) to this mixture was added and mechanically activated for 1 h using a planetary high-energy ball mill (Fristch Mono Mill Pulverisette 6) with tungsten carbide (WC) balls of 10-mm diameter. The milling was performed in dry conditions at 600 rpm, and the ball to mass ratio was 20:1.

The mechanically activated powders were shaped by uniaxial dry pressing under a pressure of 2 tones. The compact samples were dried at 110 °C for 24 h in a drying oven and sintered in an electrical furnace with a heating rate of 10 °C/min at 1250 °C for 1 h in air atmosphere. The samples were cooled to room temperature in the furnace.

The sintering behaviour of the samples was evaluated by measuring the linear shrinkage, water absorption, density and apparent porosity. The density of the sintered specimens was determined by the Archimedes principle. The phase analyses of the samples were realised using X-ray diffraction analysis with a Rigaku D/MAX 220 PC diffractometer operating with Cu-K_α (λ = 1.54056 Å) radiation. The microstructures of the metallographically prepared samples were examined by scanning electron microscopy (JEOL JSM 6060 LV). The hardness measurements were performed on the polished surface of the samples by using a Vickers microhardness tester (FutureTech FM 700) under the load of 500 gf for 10 s.

Table 1 The chemical compositions of zeolite used as raw material

Components (wt%)										
SiO_2	Al_2O_3	Na_2O	K_2O	Fe_2O_3	CaO	MgO	TiO_2	SrO	Rb_2O	ZnO
79.28	11.22	0.15	4.22	1.20	2.52	1.22	0.08	0.06	0.03	0.02

3 Results and Discussion

The XRD patterns of three compositions (without ZrO_2 addition, with 10 and 20 wt% ZrO_2 addition) sintered at 1250 °C for 1 h are presented in Fig. 1. The XRD pattern of undoped sample consists of cordierite and spinel peaks. In addition to these phases, some glassy phase is present. In case of ZrO_2 present in the samples, ZrO_2 reacts with silica present in the mixture and forms $ZrSiO_4$ [10]. As shown in Fig. 1, the intensity of cordierite peaks decreases with increasing ZrO_2 addition, while the intensity of zircon peaks rises with increasing ZrO_2 addition.

To see the effect of ZrO_2 additive on the microstructure, examination with SEM was performed. Generally, microstructural investigation of this sample revealed various features, including blocky and nodular grains and porosity. The SEM micrograph of the samples produced without ZrO_2 and EDS analysis at three different points are observed in Fig. 2a. EDS analysis taken from three different points indicated a composition dominated Al, Si, Mg and O. Thus, the presence of cordierite phase determined by XRD analysis was supported by the results of EDS analysis. The same EDS analysis results at the every three points were obtained. Therefore, it is seen that dominant phase of this sample is cordierite. As seen in Fig. 2b, white forms and blocky forms takes attention in the sample containing 10 % ZrO_2. EDS analysis shown that while white forms contain Zr, Si and O as dominant, blocky forms contain Al, Si, Mg and O. Therefore, it is thought that while white forms are zircon, blocky forms are cordierite. The amount of white forms increases in the sample containing 20 % ZrO_2 (Fig. 2c). When it was considered together with the XRD analysis, it appears that the opinion is true.

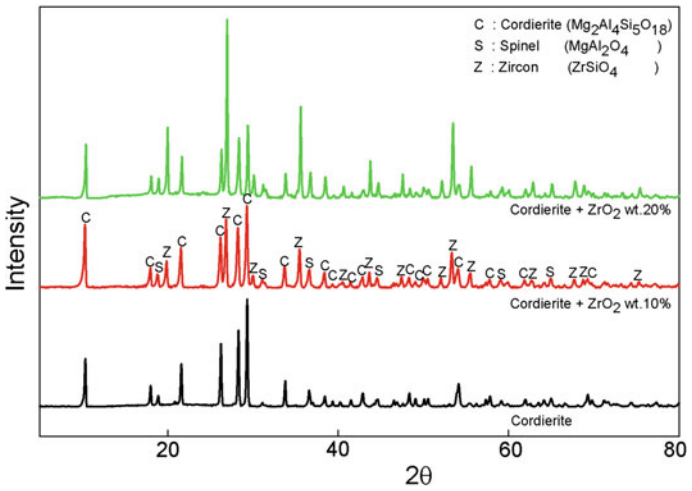

Fig. 1 XRD patterns of the sintered samples

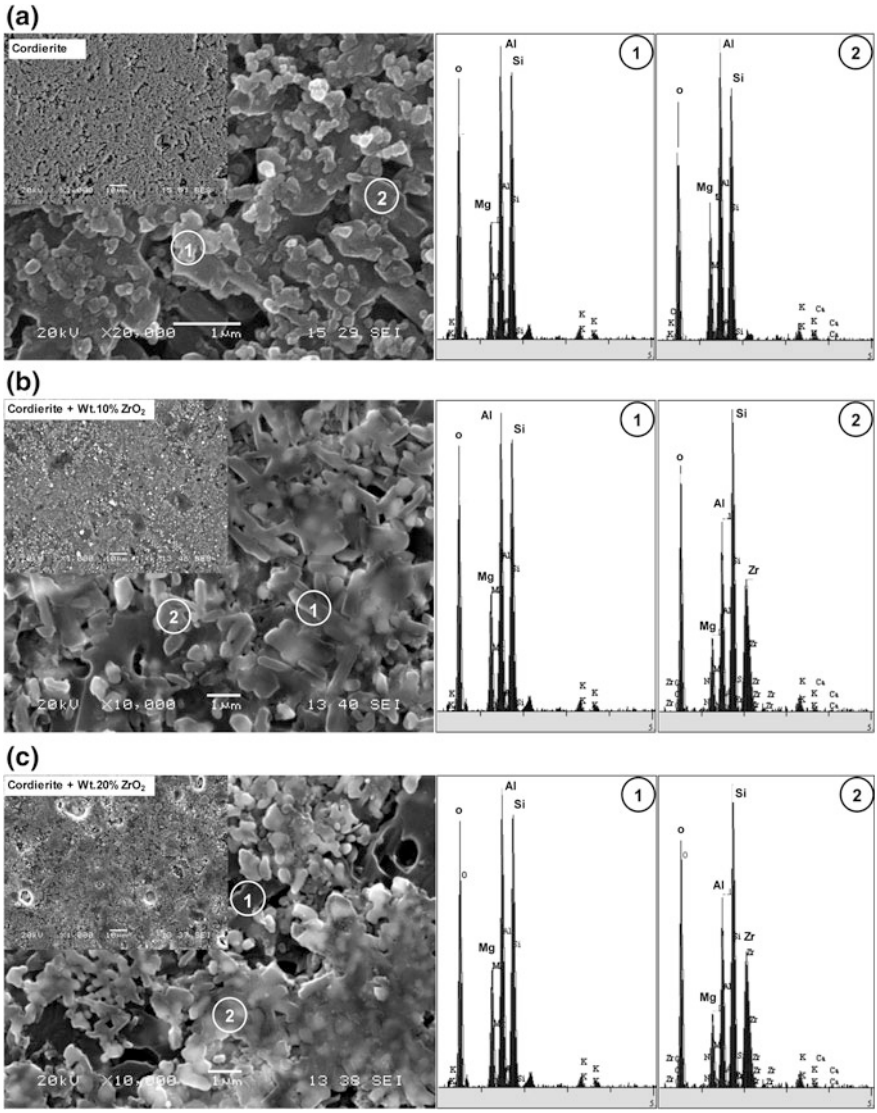

Fig. 2 The SEM micrographs and EDS analysis of the samples **a** without ZrO_2, **b** containing wt.10 % ZrO_2, **c** containing wt.20 % ZrO_2

The sintering behaviour of the samples was evaluated by the determination of density, apparent porosity, water absorption and linear shrinkage as a function of ZrO_2 addition. The obtained results are presented in Fig. 3a–d. The density, apparent porosity, water absorption and linear shrinkage values increased with increasing ZrO_2 addition, as observed from the graphics. While the density of samples without zirconia is 2.554 g/cm^3, the density value of samples containing

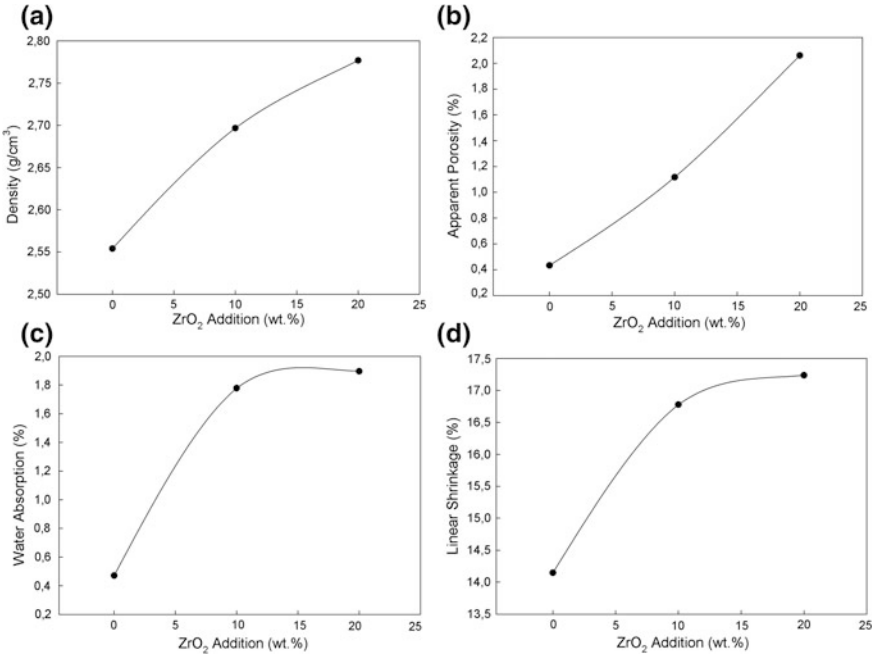

Fig. 3 **a** Density, **b** apparent porosity, **c** water absorption and **d** linear shrinkage of sintered samples as function of the ZrO_2 addition

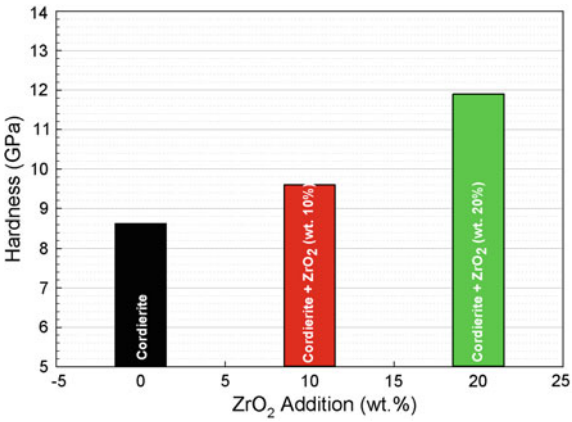

Fig. 4 The hardness variation of the samples as a function of ZrO_2 addition

20 % ZrO_2 additive is 2.777 g/cm^3. As is known, the water absorption is an important parameter of densification or sintering. The water absorption values are between 0.47 and 1.90 %. The shrinkage values of the samples changes between 14.15 and 17.23 % as depending ZrO_2 addition.

The hardness change graphic of the samples as a function of zirconia addition was plotted and presented in Fig. 4. The hardness values of the undoped samples, the samples containing 10 % Zirconia and the samples containing 20 % Zirconia were found as 8.63, 9.60 and 11.9 GPa, respectively. As shown in Fig. 4, the hardness of the samples increased with increasing zirconia additive.

4 Conclusions

The XRD patterns of the samples containing ZrO_2 consist of cordierite, spinel and zircon peaks, while the XRD pattern of undoped sample consists of cordierite and spinel peaks. In addition to these phases, some glassy phase is present. The intensity of zircon peaks rises with increasing ZrO_2 addition.

Generally, microstructural investigation of this sample revealed various features, including blocky and nodular grains and porosity. While white forms are zircon, blocky forms are cordierite and white forms increase with increasing ZrO_2 addition.

While the density of samples without zirconia is 2.554 g/cm^3, the density value of samples containing 20 % ZrO_2 additive is 2.777 g/cm^3. The hardness values of the samples undoped, the samples containing 10 % Zirconia and the samples containing 20 % Zirconia were found as 8.63, 9.60 and 11.9 GPa, respectively.

Acknowledgments This research was performed within the project 2010-01-08-014. We thank the Commission for Scientific Research Projects of Sakarya University for funding this project.

References

1. Fotoohi, B., Blackburn, S.: Effects of mechanochemical processing and doping of functional oxides on phase development in synthesis of cordierite. J. Eur. Ceram. Soc. **32**, 2267–2272 (2012)
2. Kurama, S., Kurama, H.: The reaction kinetics of rice husk based cordierite ceramics. Ceram. Int. **34**, 269–272 (2008)
3. Sandoval, M.L., Talou, M.H., de Souto, P.M., Kiminami, R.H.G.A., Camerucci, M.A.: Microwave sintering of cordierite precursor gren bodies prepared by starch consolidation. Ceram. Int. **37**, 1237–1243 (2011)
4. Bejjaoui, R., Benhammou, A., Nibou, L., Tanouti, B., Bonnet, J.P., Yaacoubi, A., Ammar, A.: Synthesis and characterization of cordierite ceramic from Moroccan stevensite and andalusite. Appl. Clay Sci. **49**, 336–340 (2010)
5. Gökçe, H., Ağaoğulları, D., Öveçoğlu, M.L., Duman, İ., Boyraz, T.: Characterization of microstructural and thermal properties of steatite/cordierite ceramics prepared by using natural raw materials. J. Eur. Ceram. Soc. **31**, 2741–2747 (2011)
6. Tunç, T., Demirkıran, A.Ş.: The effects of mechanical activation on the sintering and microstructural properties of cordierite produced from natural zeolite. Powder Technol. **260**, 7–14 (2014)
7. Wajima, T., Ikegami, Y.: Synthesis of zeolitic materials from waste porcelain at low temperature via a two-step alkali conversion. Ceram. Int. **33**, 1269–1274 (2007)

8. Demirkiran, A.Ş., Artir, R., Avci, E.: Electrical resistivity of porcelain bodies with natural zeolite addition. Ceram. Int. **36**, 917–921 (2010)
9. Demirkiran, A.Ş., Artir, R., Avci, E.: Effect of natural zeolite addition on sintering kinetics of porcelain bodies. J. Mater. Process. Technol. **203**, 465–470 (2008)
10. Costa Oliveira, F.A., Cruz Fernandes, J.: Mechanical and thermal behaviour of cordierite–zirconia composites. Ceram. Inter. **28**, 79–91 (2002)

Energetics and Scanning Tunneling Microscopy Images of B and N Defects in Graphene Bilayer

Yoshitaka Fujimoto and Susumu Saito

Abstract We report energetics and scanning tunneling microscopy (STM) images of boron and nitrogen defects in bilayer graphene using a first-principles density-functional study. It is found that the formation energies of N-doped *AB*-stacked bilayer graphene depend on the substitution sites, while those of B-doped one possess almost the same values without depending on the substitution sites. The STM images of B and N defects in not only *AB*-stacked but also *AA*-stacked bilayer graphene are calculated. The STM images near B and N defects in upper layers of *AA*- as well as *AB*-stacked bilayer graphenes are found to be similar to each other, whereas those of undoped lower layers show different images.

1 Introduction

Graphene, atomic monolayer consisting of hexagonal arrangements of carbon atoms, possesses unique properties such as ballistic transport at room temperature, anomalous quantum Hall effect and extremely high charge mobility [1–3]. A few atomic layered materials of graphene have also received much attention from nanoscience and nanotechnology since the electronic structure of multi-layered graphene is different from that of graphene monolayer. Thereby, graphene-based materials become promising candidates for future nanoelectronics and optoelectronics materials [4].

One of the effective ways to tune the electronic properties of graphene-based materials is to dope them with foreign atoms. The substitutional doping with B and N atoms can often modify the electronic properties and the chemical reactivity of

Y. Fujimoto (✉) · S. Saito
Department of Physics, Tokyo Institute of Technology,
Meguro-Ku, Tokyo 152-8551, Japan
e-mail: fujimoto@stat.phys.titech.ac.jp

S. Saito
e-mail: saito@stat.phys.titech.ac.jp

A.Y. Oral and Z.B. Bahsi Oral (eds.), *3rd International Multidisciplinary Microscopy and Microanalysis Congress (InterM)*, Springer Proceedings in Physics 186,
DOI 10.1007/978-3-319-46601-9_13

graphene, leading to developments of nanoelectronics, sensors, storages and so on [5–10].

In this work, we study energetics and scanning tunneling microscopy (STM) images of B-doped and N-doped graphene bilayers with *AA* and *AB* stackings based on the first-principles density-functional calculations [11]. It is found that the formation energies for N-doped *AB* stacking bilayer graphene vary depending on N-doped sites, whereas B-doped ones show almost the same values. It is also found that doped upper layers and undoped lower layers of bilayer graphenes with *AA* and *AB* stacking patterns show the similar and different STM images, respectively for both B-doped and N-doped cases.

2 Theoretical Methods

We here examine graphene bilayers with *AA* and *AB* stackings as shown in Fig. 1. It is reported that *AB* stacking as well as *AA* stacking patterns of undoped bilayer graphenes are observed experimentally [12]. In the case of *AB* stacking pattern, there are two substitution sites of B(N)-doped bilayer graphene: *AB1* and *AB2* stackings (see Fig. 1). One is that the C atom on top of the C atom of the adjacent graphene layer is replaced with a dopant (*AB1* stacking) and the other is that the C atom on top of the center of a hexagon of the adjacent graphene layer is replaced with a dopant (*AB2* stacking). For the calculations of the energetics and the STM images, the 4×4 supercell along the directions parallel to the graphene sheet is used.

First-principles total-energy calculations are performed within the framework of the density-functional theory (DFT) [13]. The interactions between the ions and the valence electrons are described by the norm-conserving Troullier–Martins pseudo potentials [14], and exchange-correlation effects are treated using the local density approximation (LDA) parameterized by Perdew and Zunger [15–17]. Wave functions in the Kohn–Sham equations are expanded in terms of the plane-wave basis set with the cutoff energy of 50 Ry [18]. The vacuum region of the supercell along

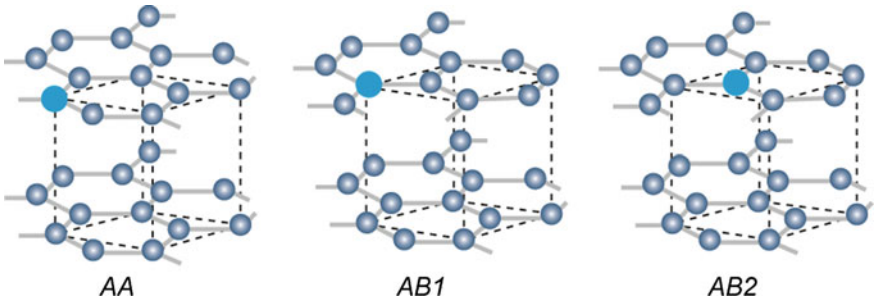

Fig. 1 Schematic views of bilayer graphene with *AA* and *AB* stackings. The *dotted line* denotes the two-dimensional unit cell. *Large circles* denote the substitution sites of dopants

the direction perpendicular to bilayer graphene is set to be 16 Å. The Brillouin-zone integration (BZ) is performed with $6 \times 6 \times 1$ k-points sampling. Upon the geometry optimization, atomic configurations are updated until Hellmann–Feynman forces on all atoms are less than 0.05 eV/Å. The formation energy is defined by

$$E_f = E_{tot} - m_C \mu_C - m_{BorN} \mu_{BorN}, \tag{1}$$

where E_{tot} are the total energies of the B- or N-doped bilayer graphenes with *AA*, *AB1* and *AB2* stacking patterns, m_C is the number of C atoms in a supercell, and μ_C, μ_B and μ_N are the chemical potentials of pristine bilayer graphene with corresponding *AA* or *AB* staking pattern, α-boron crystal, and N_2 molecule, respectively.

The STM images of B- and N-doped bilayer graphenes are calculated based on the Tersoff–Hamann (TH) approximation [19–23]. In the TH approximation, the STM images are obtained from the isosurface of the spatial distribution of local density of states $\rho(\boldsymbol{r}, \epsilon)$ with energy ϵ over the energy range from E_F to $E_F + eV$:

$$I(r) \sim \int_{E_F}^{E_F + eV} \rho(r, \varepsilon) d\varepsilon, \tag{2}$$

where E_F is the Fermi energy and V is the bias voltage. The negative and positive V values reflect the occupied and unoccupied electronic states, respectively.

3 Results and Discussion

We study the energetics of B and N-doped bilayer graphenes. Table 1 shows the formation energies calculated by Eq. (1). Irrespective of the stacking patterns, the B and N dopings into bilayer graphene are found to become energetically favorable rather than those into monolayer graphene. The *AB1*- and *AB2*-stacked graphenes take almost the same formation energies for B-doped cases since their energy difference is only 6 meV. On the other hand, in the case of the N-doped graphene, the formation energy of the *AB1*-stacked graphene is considerably larger by 28 meV than that of *AB2*-stacked one, indicating that the substitution with N atom on top of the center of a hexagon becomes energetically favorable rather than that

Table 1 Calculated formation energies of B and N-doped graphene monolayer and bilayer

Formation energy (eV)			
		B-doped	N-doped
Monolayer		1.42	0.32
Bilayer	*AA*	1.355	0.240
	AB1	1.372	0.284
	AB2	1.366	0.256

See Fig. 1 for stacking patterns of bilayer graphene

on top of C atom. Thus, the formation energy for the substitution with N atom depends on the substitution site, whereas that for B atom does not depend on it.

We next study the STM images of doped upper layers and undoped lower layers of B-doped and N-doped bilayer graphenes.Figure 2a–c show the STM images of upper layers of B- and N-doped bilayer graphenes with *AA*, *AB1* and *AB2* stacking patterns, respectively. It is seen that there is a triangular bright area in the STM images of the B-doped graphene. Interestingly, irrespective of the stacking patterns for *AA*, *AB1*, and *AB2* stackings, the STM images are almost similar to one another. Furthermore, the triangle-shaped bright area in these simulated STM images is also observed experimentally in the B-doped monolayer graphene [24]. In the case of the N-doped cases, there exist in the STM images three bright spots at three C atoms around the N atom and the dark area appears above the N atom as if the N site is vacant. This variation of contrast in the STM image is also observed in the case of the substitutional N defect in monolayer graphene theoretically and experimentally [25, 26]. In addition, the STM images of bilayers with the three stacking patterns for the N-doped cases also are similar to one another as in the case of the B-doped bilayers.

Figure 3a–c show the STM images of undoped lower layers of B- and N-doped bilayer graphenes with *AA*, *AB1* and *AB2* stacking patterns, respectively. The B-doped graphene with *AA* stacking has also triangular bright but small area, compared with the case of the doped upper layer. The STM images of B-doped graphenes with *AA* and *AB* stacking patterns are found to be considerably different from each other. In the N-doped case, the STM image of *AA* stacking patter has a bright spot above the C atom on top of the N atom in the lower layer. The STM

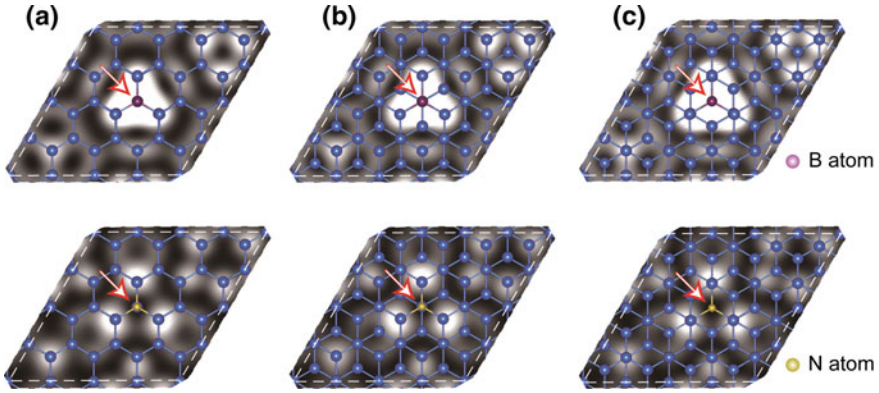

Fig. 2 Simulated STM images of doped upper layers of **a** *AA*, **b** *AB1* and **c** *AB2*-stacked bilayer graphenes doped with B atom (*upper panel*) and N atom (*lower panel*). The STM images for B-doped and N-doped cases are shown at the applied bias voltages of +0.5 eV and −0.5 eV, respectively. The *arrows* denote the dopant sites of the upper layers

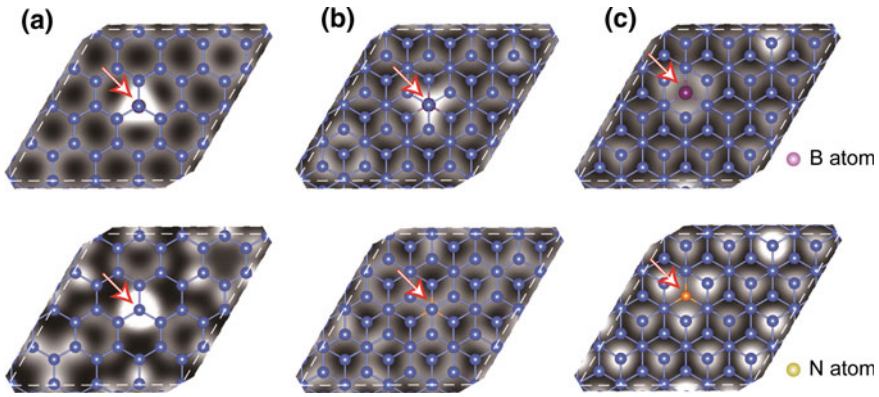

Fig. 3 Simulated STM images of **a** *AA*, **b** *AB1* and **c** *AB2*-stacked bilayer graphenes doped into the lower layers with B atom (*upper panel*) and N atom (*lower panel*). The STM images for B-doped and N-doped cases are shown at the applied bias voltages of +0.5 eV and −0.5 eV, respectively. The *arrows* denote the dopant sites of the lower layers

images of N-doped graphenes with *AA* and *AB* stacking patterns also show different images.

4 Summary

We have studied the energetics and the STM images of B-doped and N-doped bilayer graphenes using first-principles density-functional calculations. It is found that the formation energies of N-doped *AB*-stacked bilayers vary depending on the substitution sites. On the other hand, two *AB*-stacked bilayers for the B-doped case have similar formation energies without depending on the substitution sites. The STM images of B- and N-doped bilayers have triangular bright area and three bright spots, respectively. The STM images near B and N defects in the upper layers for three stackings are found to be similar to one another, whereas those of lower layers are different.

Acknowledgments This work was supported by MEXT Elements Strategy Initiative to Form Core Research Center through Tokodai Institute for Element Strategy, JSPS KAKENHI Grant Numbers JP26390062 and JP25107005. Computations were partly done at Institute for Solid State Physics, the University of Tokyo, at Cybermedia Center of Osaka University, and at Global Scientific Information and Computing Center of the Tokyo Institute of Technology.

References

1. Novoselov, K.S., et al.: Electric field effect in atomically thin carbon films. Science **306**, 666–669 (2004)
2. Berger, C., et al.: Electronic confinement and coherence in patterned epitaxial graphene. Science **312**, 1191–1196 (2006)
3. Zhang, Y., et al.: Experimental observation of the quantum Hall effect and Berry's phase in graphene. Nature **438**, 201–204 (2005)
4. Castro, E.V., et al.: Biased bilayer graphene: semiconductor with a gap tunable by the electric field effect. Phys. Rev. Lett. **99**, 216802 (2007)
5. Williams, J.R., et al.: Quantum Hall Effect in a gate-controlled *p-n* junction of graphene. Science **317**, 638–641 (2007)
6. Young, A.F., Kim, P.: Quantum interference and Klein tunnelling in graphene heterojunctions. Nat. Phys. **5**, 222–226 (2009)
7. Fujimoto, Y., Saito, S.: Structure and stability of hydrogen atom adsorbed on nitrogen-doped carbon nanotubes. J. Phys: Conf. Ser. **302**, 012006 (2011)
8. Jeong, H.M., et al.: Nitrogen-doped graphene for high-performance ultracapacitors and the importance of nitrogen-doped sites at basal planes. Nano Lett. **11**, 2472–2477 (2011)
9. Fujimoto, Y., Saito, S.: Hydrogen adsorption and anomalous electronic properties of nitrogen-doped graphene. J. Appl. Phys. **115**, 153701 (2014)
10. Fujimoto, Y.: Formation, energetics, and electronic properties of graphene monolayer and bilayer doped with heteroatoms. Adv. Condens. Matter Phys. **2015**, 571490 (2015)
11. Fujimoto, Y., Saito, S.: Electronic structures and stabilities of bilayer graphene doped with boron and nitrogen. Surf. Sci. **634**, 57–61 (2015)
12. Liu, Z., et al.: Open and closed edges of graphene layers. Phys. Rev. Lett. **102**, 015501 (2009)
13. Hohenberg, P., Kohn, W.: Inhomogeneous electron gas. Phys. Rev. **136**, B864 (1964)
14. Troullier, N., Martins, J.L.: Efficient pseudopotentials for plane-wave calculations. Phys. Rev. B **43**, 1993 (1991)
15. Kohn, W., Sham, L.J.: Self-consistent equations including exchange and correlation effects. Phys. Rev. **140**, A1133 (1965)
16. Ceperley, D.M., Alder, B.J.: Ground state of the electron gas by a stochastic method. Phys. Rev. Lett. **45**, 566 (1980)
17. Perdew, J.P., Zunger, A.: Self-interaction correction to density-functional approximations for many-electron systems. Phys. Rev. B **23**, 5048 (1981)
18. Yamauchi, J., et al.: Efficient iterative schemes for *ab initio* total-energy calculations using a plane-wave basis set. Phys. Rev. B **54**, 5586 (1996)
19. Tersoff, J., Hamann, D.R.: Theory of the scanning tunneling microscope. Phys. Rev. B **31**, 805 (1985)
20. Okada, H., et al.: Detailed analysis of scanning tunneling microscopy images of the Si(001) reconstructed surface with buckled dimers. Phys. Rev. B **63**, 195324 (2001)
21. Fujimoto, Y., et al.: Theoretical study on the scanning tunneling microscopy image of Cl-adsorbed Si(001). Jpn. J. Appl. Phys. **42**, 5267–5268 (2003)
22. Fujimoto, Y., et al.: Images of scanning tunneling microscopy on the Si(001)-p(2×2) reconstructed surface. Mater. Trans. **42**, 2247–2252 (2001)
23. Fujimoto, Y., Oshiyama, A.: Atomic structures and energetics of 90° dislocation cores in Ge films on Si(001). Phys. Rev. B **81**, 205309 (2010)
24. Zhao, L., et al.: Local atomic and electronic structure of boron chemical doping in monolayer graphene. Nano Lett. **13**, 4659 (2013)
25. Fujimoto, Y., Saito, S.: Formation, stabilities and electronic properties of nitrogen defects in graphene. Phys. Rev. B **84**, 245446 (2011)
26. Zhao, L., et al.: Visualizing individual nitrogen dopants in monolayer graphene. Science **324**, 999–1003 (2011)

Improved, Photon Conversion Efficiency of (SnO_2) Doped Cesium Oxide (Cs) Nanofibers for Photocatalytic Application Under Solar Irradiation

K. Kaviyarasu, E. Manikandan, J. Kennedy, R. Ladchumananandasiivam, Uilame Umbelino Gomes, M. Maaza and Genene T. Mola

Abstract We report the synthesis of high quality Tin Oxide (SnO_2) doped Cesium Oxide (Cs) nanofibers by hydrothermal method at room temperature. Composition, structure and morphology of the nanofibers were analyzed by X-ray diffraction (XRD) and high resolution transmission electron microscopy (HRTEM). XRD assessed the crystal structure of the nanoplatelets which identified peaks associated with (110), (101) and (200) planes of hexagonal wurtzite-type SnO_2 with lattice constants of a = b = 3.249 Å and c = 5.219 Å. XRD results also indicated that the

K. Kaviyarasu (✉) · E. Manikandan · J. Kennedy · M. Maaza
UNESCO-UNISA Africa Chair in Nanosciences/Nanotechnology Laboratories, College of Graduate Studies, University of South Africa (UNISA), Muckleneuk Ridge, PO Box 392, Pretoria, South Africa
e-mail: kaviyarasuloyolacollege@gmail.com; kavi@tlabs.ac.za

K. Kaviyarasu · M. Maaza
Nanosciences African Network (NANOAFNET), Materials Research Group (MRG), iThemba LABS-National Research Foundation (NRF), 1 Old Faure Road, 7129, PO Box 722, Somerset West, Western Cape Province, South Africa

G.T. Mola
School of Chemistry and Physics, University of Kwazulu-Natal, Private Bag X01, Scottsville, Pietermaritzburg 3209, South Africa

J. Kennedy
National Isotope Centre, GNS Science, PO Box 31312 Lower Hutt 5010, New Zealand

R. Ladchumananandasiivam
Department of Textile Engineering and Post Graduate Programme in Mechanical Engineering, Centre of Technology, Federal University of the State of Rio Grande Do Norte, Campus Universitario, Natal-RN 59078-970, Brazil

U.U. Gomes
Graduate Program in Materials Science and Engineering, Departamento de Fisica, Universidade Federal Do Rio Grande Do Norte, Natal-RN 59.072, Brazil

A.Y. Oral and Z.B. Bahsi Oral (eds.), *3rd International Multidisciplinary Microscopy and Microanalysis Congress (InterM)*, Springer Proceedings in Physics 186,
DOI 10.1007/978-3-319-46601-9_14

crystalline properties of the doped samples were improved without affecting the parent lattice. The morphological and optical properties (SnO_2) doped (Cs) nanosamples were characterized by HRTEM and UV-vis spectroscopy. The IR results showed high purity of products and indicated that the nanoplatelets are made up of Sn-O_2 and Cs bonds. Absorption spectra exhibited an upward shift in characteristic peaks caused by the doping material, suggesting that crystallinity of both doped compounds is improved due to specific doping level. The Photoluminescence (PL) spectra are dominated by a strong narrow band edge emission tunable in the blue region of the visible spectra indicating a narrow size distribution of SnO_2/Cs nanofibers.

1 Introduction

Over the past few decades, researchers have turn into increasingly absorbed in the study of metal-oxides [1]. Metal oxides (SnO_2:Cs) are ionic compounds that are through up of positive metallic and negative oxygen ions. The electrostatic exchanges between the positive metallic and negative oxygen ions consequence in firm and solid ionic bonds [2–4]. The s-shells of metal-oxides are entirely filled; hence mainly of the metal oxides have good thermal and chemical constancy [5]. On the other hand, their d-shells may not be completely filled, giving them a assortment of unique properties [6]. These exceptional properties include wide bandgaps [7], soaring dielectric constants [8], hasty electronic transitions and good electrical [9], optical and electrochromic devices [10] as well as superconductivity [11]. Therefore, rapid developments in the field of nanoscience and nanotechnology have very much motivated the scientific community and industry to explore new features of both emblematic and novel materials at the nanoscale level [12]. Materials with dimensions at a nanoscale level are known as nanomaterials. In general, nanomaterials can be categorized as having three different morphologies or nanostructures: 0D, 1D and 2D nanostructures. It should be renowned that when the size and dimensionality are abridged, the electronic structures of the nanomaterials are dissimilar from individuals of the bulk materials [13]. These differences in the electronic structures can source an assortment of changes in both chemical and physical properties. The intrinsic n-type semiconductor with dipole forbidden direct bandgap energy of 3.6 eV at room temperature (RT), crystallizes in the tetragonal rutile structure [14]. At the same time as doped with cesium the transparent oxide the distribution of the energetic level of the trivalent exciting cesium ions, construction them suitable for developing cesium based optical emitters. Tin oxide has been functional in many forms such as in the form of powders, thin films or more lately as nanostructures [15, 16]. Even though well established knowledge on the structural and electrical properties of tin oxide, the material's optically active defects have not been deliberate to a large amount either in their pure or undoped forms. Also, the morphology, shape, size, crystalline structure and chemical composition of the 1D (SnO_2)/(Cs:SnO_2) nanostructures remains a challenge in the

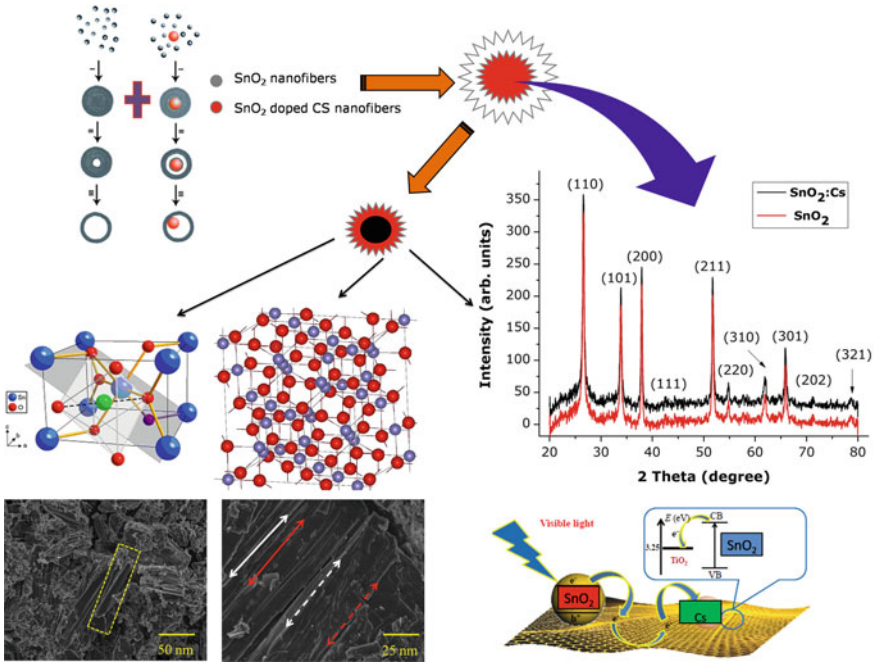

Fig. 1 Schematic mechanism of SnO_2 doped Cs nanofibers

development of 1D convenient synthesis methods [17–19]. The schematic Mechanism of SnO_2 doped Cs nano fibers is shown in Fig. 1.

2 Experimental Details

2.1 Typical Synthesis of Tin Oxide Nanofibers

All the reagents and solvents were analytical grade and were used without any further purification. Tin oxide (SnO_2), Cesium oxide (Cs), ammonium hydroxide and ethanol were purchased from E-Merck Company (99.99 %). In a typical synthesis, 100 ml of 1 M Tin oxide aqueous solution was mixed with 25 ml of 1 M Cesium oxide and the resulting mixture was stirred thoroughly using a magnetic stirrer. The precursor of yellow precipitate was obtained. The as-obtained yellow precipitate was collected and washed with double distilled water twice. For hydrothermal synthesis nearly 0.5 g of precursor was added to 50 ml of 0.5 M concentration of ammonium hydroxide, to get a precipitated liquid. Then the above solution was transferred to Teflon lined autoclave at 700 °C in an oven for 24 h. After 24 h white crystalline product was collected and thoroughly washed with ethanol twice. Finally, the obtained nanofibers of tin oxide were used for

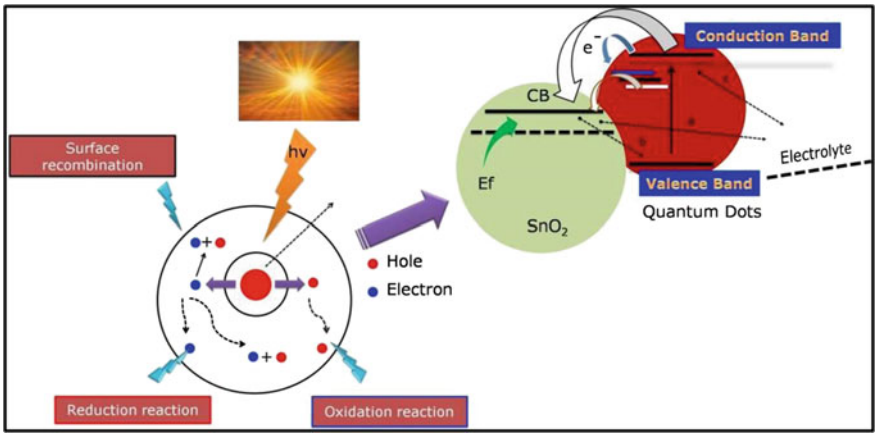

Fig. 2 Mechanism part of photocatalytic activity under SnO_2 doped Cs nanofibers

characterization studies. The mechanism part of Photocatalytic activity under SnO_2 doped Cs nanofibers is shown in Fig. 2.

2.2 *Characterization Studies*

The X-ray powder diffraction (XRD) experiments were measured on a RigaKu D/max-RB diffractometer with Ni-filtered graphite monochromatized Cuk_α radiation (λ = 1.54056 Å) under 40 kV, 30 mA with scanning between 10° to 80° (2θ). UV-vis diffuse reflectance spectra of SnO_2:Cs nanofibers were recorded by a UV-vis-NIR, spectrophotometer (JASCO V-550, Japan). A Renishaw micro-Raman spectrometer RM 2000 with IR (440 nm) and UV (325 nm) excitation lasers was employed to measure the nonresonant and resonant Raman spectra of Sno_2:Cs nanosamples correspondingly. The number of gratings in the Raman spectrometer was 1800 for visible laser and 3000 for IR laser. All spectra were taken in the backscattering configuration at room temperature (RT). Photoluminescence (PL) measurements of the as synthesized products were carried out using an F-4500 KIMON Fluorescence spectrophotometer at room temperature, with a Xe lamp as the excitation light source. The electrochemical responses were measured using single compartment three electrode cell setup CHI-760C, USA Potentiostat workstation. The Pt wire and $Hg/HgCl_2$ (calomel electrode) were used as counter and reference electrode, and glassy carbon electrode (GCE) as working electrode and all the potentials were measured vs GCE. The cyclic voltammetry is the most sensitive technique; to detect the trace level impurities in the measurement. The *I-V* characterization properties were measured by Hioki LCR Hitester 3532. The morphology of pure and doped samples was detected by scanning electron microscopy (JSM-5600 LV, JEOL). The stoichiometries of SnO_2:Cs nanosamples were investigated by energy dispersive spectroscopy. The morphology and microstructure

were examined using high resolution electron microscopy (HRTEM) performed with a Philips CM12 at an acceleration voltage of 200 kV. The selected area electron diffraction (SAED) (IH-300X) analysis was performed at several points in the HRTEM arrangement.

3 Results and Discussion

3.1 XRD Analysis

The X-ray diffraction pattern was calm to identify the crystal structure, phase and purity of the samples. The spectra of SnO_2 and SnO_2:Cs are shown in Fig. 3. All samples show wide diffraction peaks, which could be indexed to the tetragonal rutile structure of SnO_2 (JCPDS card No. 41-1445) with lattice constants of $a = b = 0.4743$ nm and $c = 0.3198$ nm. Furthermore, no other characteristic peaks of impurities such as metallic tin or other tin oxides were pragmatic [20–22]. These indicate that the level of impurity in the sample is low. The crystalline size dimensions were carried out using Debye-Scherrer equation $D_{hkl} = 0.98\lambda/\beta\cos\theta$, where D is the crystallite size, λ is the wavelength of X-ray radiation, β is the line width and θ is the angle of diffraction. The mean grain sizes of as-synthesized SnO_2 and cesium doped SnO_2 were found to be 35 and 40 nm, respectively. By comparing the relative intensity of the diffraction peaks, it can be seen that the relative intensity ratio of (110) to (101) of the diffraction peaks of SnO_2 and cesium doped SnO_2 were found to be 1.145 and 1.149, respectively, which is quite significant with the worth obtained from the standard card (JCPDS card No. 41-1445). An interesting point to mention is, the increase in the relative intensity ratio of the diffraction peaks of cesium doped nanocrystals (i.e., 1.145 to 1.149), which could be attributed to the anisotropic growth of SnO_2 nanopowder by solvothermal

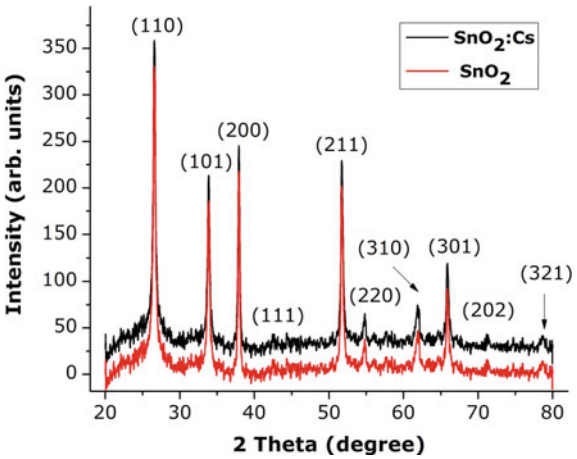

Fig. 3 XRD pattern of Cs: SnO_2 nanofibers calcinated at 700 °C

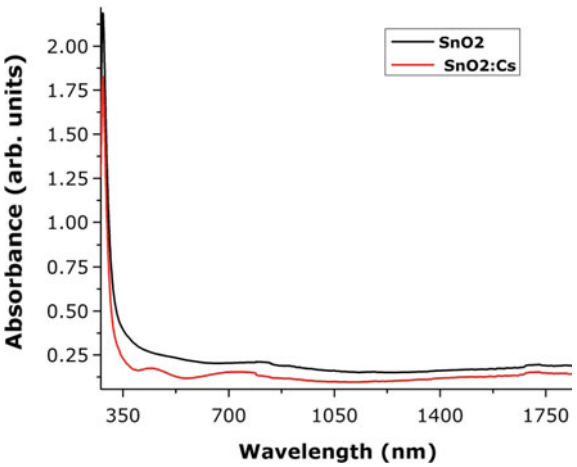

Fig. 4 Absorption spectrum of Cs:SnO_2 nanofibers calcinated at 700 °C

method. The X-ray diffractogram of the undoped SnO_2 displayed only the cassiterite structure for all the nanoparticles treated at 700 °C. These results are in good agreement with the other works. But in the case of cesium doped SnO_2 samples expansion on Raman peaks was found. The research proves that cesium chloride dopant has been incorporated into SnO_2 nanostructures remains a challenge in the development of opto-electronic devices [23].

3.2 UV-Visible Absorption Studies

The UV-visible absorption spectrum which has been comprehensively studied is one of the majority significant methods to reveal the energy structures in addition to optical properties of semiconductor nanostructures. The subsequent band gap spectrum of SnO_2 and SnO_2:Cs are shown in Fig. 4, respectively. The fascination values are at 352 nm and 361 nm. The band gap energy (E_g) for SnO_2 and SnO_2:Cs nanocrystallites be able to exist obtained through extrapolation of the mounting dimension of the combine in the direction of the *x*-axis [24, 25]. The consequential band gap vigor is originated to be 3.53 and 3.62 eV. The reduce in band gap, confirms with the purpose of the conductivity is elevated intended for cesium doped tin oxide than so as to of pure tin oxide nanocrystals [26].

3.3 Raman Measurements

The Raman spectrum of the untainted SnO_2 along with SnO_2:Cs nanocrystals in the 100–1000 cm^{-1} region was deliberate by RENISHAW which is a condescending concert Raman microscope spectrometer by a 442 nm diode lasers. The

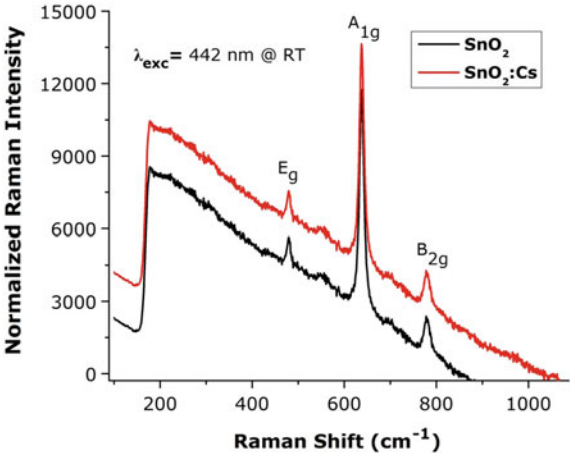

Fig. 5 μ-Raman spectrum of Cs:SnO_2 nanofibers calcinated at 700 °C

arrangement of the tetragonal rutile construction crystalline peak was corroborated by the μ-Raman spectra while shown in Fig. 5. Raman spectra of SnO_2 along with SnO_2:Cs nanocrystals bare the split peaks at room temperature (RT). First sharp peak appears at 475 cm^{-1} which does not subsist within pure SnO_2 nanocrystals, other than after cesium is additional, it happening to exist empirical. During distinctive spectrum of the fashioned samples by means of two molecules for each unit cell, eighteen standard vibrational modes are unsurprising secure to the Γ (q = 0) crest of the primary Brillouin region intended for the substance crystallizing during the tetragonal rutile structure [27–29]. At the same time, while during the case of the single crystals, each and every one three energetic Raman modes having E_g, A_{1g} and B_{2g} symmetries were accredited into the high occurrence array at 475 cm^{-1}(E_g), 663 cm^{-1} (A_{1g}) and 774 cm^{-1} (B_{2g}) correspondingly [30]. In addition, occupied widths on the partially greatest (FWHM) magnification of $A1_g$ peak 4 cm^{-1} seeing that glowing while decreases 3 cm^{-1} red dangle of the vibrational modes were observed in the doped image to be expected outstanding to the lattice distortions [31–33]. Disorder activated resonances (q ≠ 0) depending going on the component volume along with nanosamples assortment temperatures be present in addition experimental within the 475–775 cm^{-1} constituency while reported [34].

3.4 PL Measurements

Although the consideration of the substance intended for a quantity of optoelectronic applications the enlargement of the optically active defects within tin oxide deserves an thoroughly revise. Figure 6a, b shows the PL spectra of wholesome SnO_2 and SnO_2:Cs nanocrystals on extent temperature by means of a 30 W laser power. While aforementioned, such a PL behavior is illustrative of overlapped optical emitting modes throughout distinct de-excitation gateways [35–38]. With

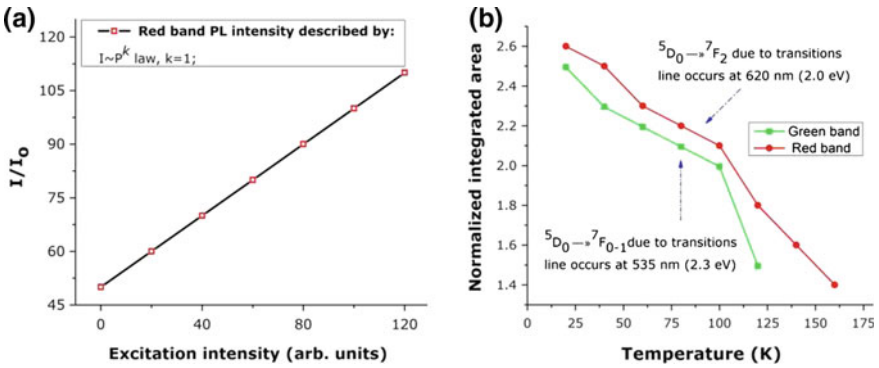

Fig. 6 **a**, **b** Luminescence studies of Cs:SnO_2 nanofibers calcinated at 700 °C

the intention of additional survey the optical fringe centers of the pure SnO_2 nanocrystals (green and red emission bands) the PL proportions were acknowledged next to remarkable excitation energies realized at RT. Figure 6a, shows a log (I/Io)-log(P/Po) arrange of the further than mentioned emission wherever 'I' corresponds to the included concentration and 'P' is the excitation ascendancy [39]. During declining the excitation absorption beyond no changes in the indistinct outline and the peak positions were predictable. These consequences in cooperation by means of the angle obtained proposed for the power law, $I \sim P^k$, suggest through the intention of a gear relating to donar-acceptor pairs transitions strength be surplus even as recombination illustration planned for the red PL bands. For that reason a unitary incline suggests an exciton-like transition regarding a thoughtful stage defect. At RT temperatures the untried information is trustworthy during one optical node peak at $\sim$660 nm which is responsible in good turn of the red luminescence overlapped among high energy creation assembly which accounts on behalf of the position empirical in the green spectral region as in Fig. 6b. As a result of thought-provoking the SnO_2 nanostructures in the insertion edge with 3.8 eV (325 nm) energy photons the luminescence of the undoped samples is conquered by a extensive shapeless secretion band extending beginning the ultraviolet to the near infrared due to the overlapped emitting centers.

3.5 Cyclic Voltammogram Measurements

The electrochemical responses of SnO_2:Cs/GCE were deliberate using cyclic voltammogram (CV) in 0.1 M Phosphate Buffer (PBS) as electrolyte (pH $\sim$ 7) at scan rate, 50 mV/s, in the eventual range of −1.0–1.0 V, In Fig. 7, three redox responses and one irreversible peak from the anodic region are shown in the multi scan sweep distribution. The anodic oxidation transition of Sn(I)/Sn(II) and Sn(II)/Sn(III) be attributed to the four dissimilar tin oxide transition so as to occur on the electrode

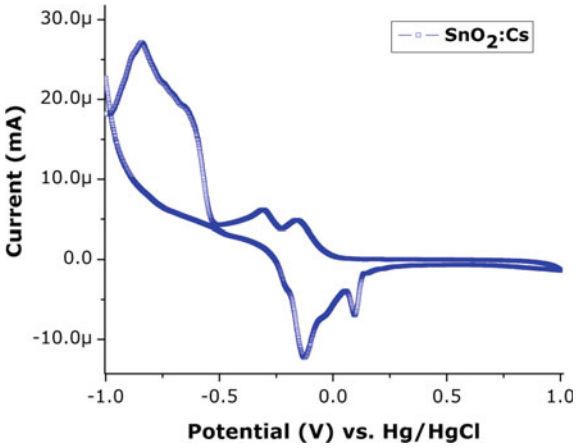

Fig. 7 Electrochemical behavior of Cs:SnO_2 nanofibers calcinated at 700 °C

frontage ($Sn(O)_2$, SnO–OH and SnO_2) and the cathodic responses become known in the consequential turn down [40, 41]. The unchangeable anodic retort observed at −0.99 V; proves that nano-tin has high functionality due to higher electrochemical bustle lacking any modification. As of the second sweep segments the current was decreased by the adsorption of Na^+/K^+ ion on the facade of the electrode from the firm interfacial deposit on the SnO_2:Cs/GCE.

3.6 I–V Characterization Studies

The optoelectronic retort of pure SnO_2 and SnO_2:Cs nanocrystals was investigated in air by means of UV light with a wavelength of 254 nm. Figure 8, shows two *I–V* curves for the pure SnO_2 and Cs:SnO_2 nanocrystals with and without disclosure

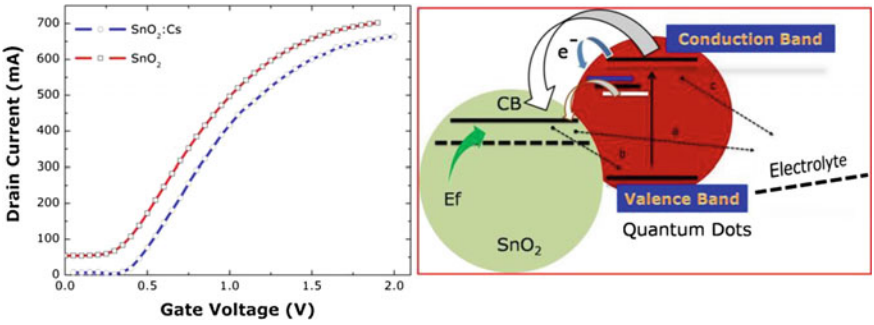

Fig. 8 I-V characterization studies of Cs:SnO_2 nanofibers calcinated at 700 °C

to the UV light, respectively. At the same time as performance to UV light, the nanorods conductance inflated on typical by 33 times (N = 6 devices, ranging from 26 to 36 times). Two large amount significant mechanisms are to be predictable occupied in the conductance scale. First, electrons were directly energized from the valence band (VB) into the conduction band (CB) by the UV light of 254 nm in wavelength which communicates to 4.9 eV. This lead to the increase of the integer of gratis carriers within the nanorods and therefore, the conduction augmentation. Second, the UV light triggered the photo desorption of oxygen and damp on the nanofibers surface, which resulted in the decline of the size of the electron depletion layer close to the surface.

3.7 SEM and HRTEM Measurements

The morphology and microstructure were considered by SEM and HRTEM, and the outcomes are depicted in Fig. 9a–f. As shown in Fig. 9a–c, the result is comprised of micron-sized fibers-like structures constructed by rod-like nanofibers [42–45]. The elevated-magnification SEM image in Fig. 9b reveals to facilitate they are of smooth surfaces and rectangular cross section with a diameter of 25 nm and a span up to several hundred nanometers. The rod-like shape of the nanofibers can be inveterate unambiguously in the low-magnification SEM image displayed in Fig. 9a. To study the complete lattice structure, the SEM image and its EDS image are approved out. Uniform and regular lattice fringes can be seen evidently, which confirms that the SnO_2:Cs nanofibers without any other phases such as SnO_2 nanofibers. The interplanar distances of the two groups of crystallographic planes noticeable in the picture have been intentional to be 0.47 and 0.31 nm, respectively,

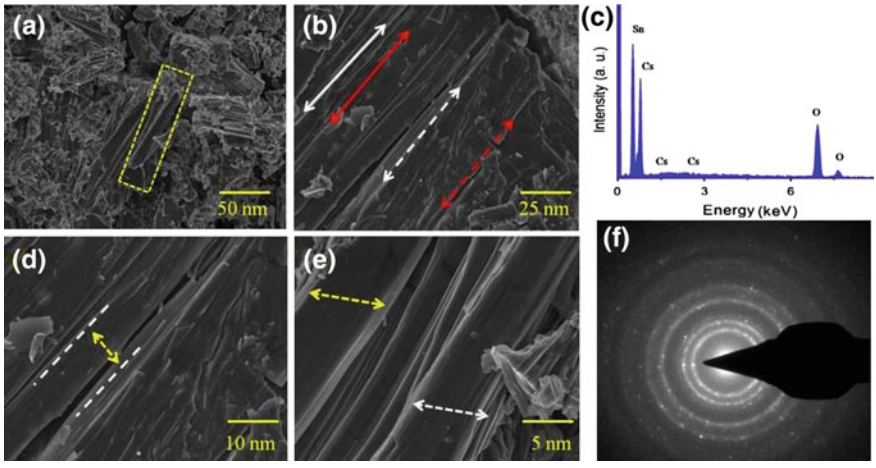

Fig. 9 **a–f** SEM and HRTEM images of Cs:SnO_2 nanofibers calcinated at 700 °C

indistinguishable well with the (110) and (101) planes of rutile SnO_2, and representative so as to the extension direction is [112]. Figure 9d–f shows HRTEM images of SnO_2:Cs nanofibers displaying opaque growth of homogeneous nanofibers that are extended with lengths ranging from 5 to 50 nm and additional. The SnO_2:Cs nanofibers can develop to such comprehensive lengths since a intensification time of 2 h was worn and nanofibers with lengths of a few microns can be synthesized by sinking the growth time to less than 1 hr. Figure 9d, e shows a high-exaggeration picture of the SnO_2:Cs nanofibers which draw closer into vision in a straight line and stretchy with smooth surfaces; the diameters of these nanofibers assortment frequently between 5 and 10 nm. The nanofibers at the fiber apexes in wide-ranging emerge dappled and have high distinction compared with the trunk of the nanofibers. Figure 9f shows the selected area electron diffraction (SAED) pattern of SnO_2:Cs nanofibers calcinated at room temperature (RT). SAED pattern recorded perpendicular to the axis of this nanofibers can be indexed for the (220) region of the cubic phase of SnO_2:Cs which reveals the single crystalline scenery of these nanofibers [46]. Subsequently, HRTEM is occupied to view the arrangement of the nanofibers [47]. In addition, the angle between the (002) plane and the comprehensive axis are parallel to the (111) crystalline direction of the cubic of SnO_2:Cs. The SAED pattern has moreover recognized that the nanofibers quite grow next to (112) in agreement with the HRTEM investigations, the SnO_2:Cs nanofibers is conceivably due to the highly crystalline nature of SnO_2.

3.8 Conductivity Measurements

The conductivity of the material can be detected through illustration the graph between resistivity and temperature. In the Fig. 10, shows the resistivity retort of the SnO_2:Cs aligned with temperature. The graph shows the non linear concert of

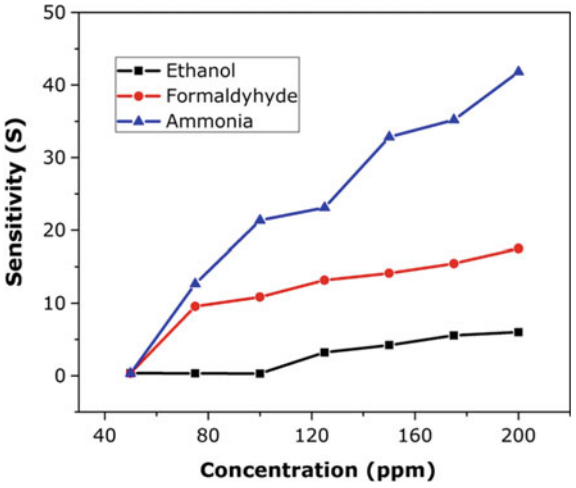

Fig. 10 Conductivity images of Cs:SnO_2 nanofibers calcinated at 700 °C

the conducting assets of the composite. From the Fig. 10, showed the proportional graph of SnO_2:Cs nanofibers. The blue spectral line of the graph displays the resistance uniqueness of SnO_2:Cs. Initially, the resistance is directly proportional to the temperature [48]. It is stable between 200–220 °C and after that; the resistance is inversely proportional to the temperature. From the graph, it is originating that; the conductivity of the material can be tuned by the controlling of the temperature.

3.9 Sensor Analysis

In Fig. 11 shows the sensitivity variations of SnO_2:Cs of nanosamples for methanol concentration of 75 ppm for different temperatures. The graph shows the linear performance of the sensing assets of the composite. The projection of blue spectral line up in the graph reflects the sensing competence of the present materials [49, 50]. The sensitivity of the SnO_2:Cs material is deliberate up to 220 °C and it is observed that, the sensitivity is more at 200 °C. From the analysis, it is concluded that, the sensitivity of the present compound is more than pure SnO_2 and Cs. The sensitivity of the SnO_2 is added with sensing ability of the Cs compound and if this material used as sensor, the device efficiency will be more.

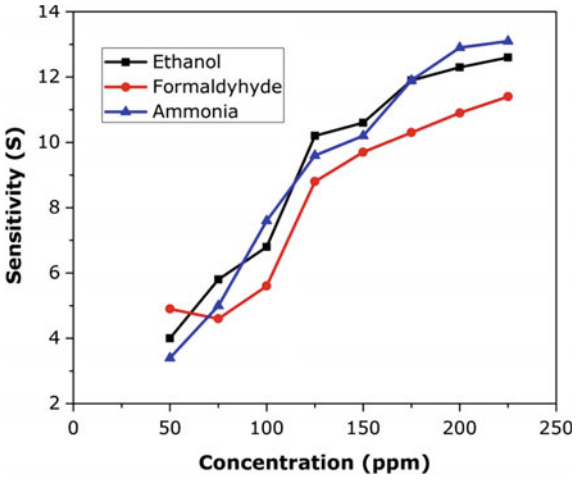

Fig. 11 Gas sensing images of Cs:SnO_2 nanofibers calcinated at 700 °C

4 Conclusions

The structural and surface morphological investigations from XRD, SEM, TEM and UV absorption are concordant and optical PL spectrum reveals the formation of highly pure SnO_2 and SnO_2:Cs nanofibers. This approach offers a great deal of control of the size and the size distribution of the particles and facilities their production at relatively low temperatures under ambient conditions, have the ability of self-assembling into ordered arrays on a large scale. The sharpness of the emission peak observed in the pure SnO_2 and SnO_2:Cs nanocrystals for PL spectra ascertains that they have desirable uniformity and good emission properties. The reaction medium is harmless, and simple, and can be used as a hydrothermal route to synthesize high quality SnO_2:Cs nanofibers. The crystallization temperature is initiate to play an important role in the morphological variation of SnO_2:Cs nanofibers. This technique may provide a new route to 1D semiconductor from the same kind of materials that are usually of regular shape with large sized aggregations on its surface.

Acknowledgments The authors gratefully acknowledge research funding from UNESCO-UNISA Africa Chair in Nanosciences/Nanotechnology Laboratories, College of Graduate Studies, University of South Africa (UNISA), Muckleneuk Ridge, Pretoria, South Africa, (Research Grant Fellowship of framework Post-Doctoral Fellowship program under contract number Research Fund: 139000). One of the authors (***Dr. K. Kaviyarasu***) is grateful ***Prof. M. Maaza***, Nanosciences African network (NANOAFNET), Materials Research Department (MSD), iThemba LABS-National Research Foundation (NRF), Somerset West, South Africa. Support Program and the Basic Science Research Program through the National Research Foundation of South Africa for his constant support, help and encouragement generously.

References

1. Liu, Y., Liu, M.: Growth of aligned square-shaped SnO_2 tube arrays. Adv. Fun. Mater. **15**(1), 57–62 (2005). doi:10.1002/adfm.200400001
2. Wang, H., Rogach, A.L.: Hierarchical SnO_2 nanostructures: recent advances in design, synthesis, and applications. Chem. Mater. **26**(1), 123–133 (2014). doi:10.1021/cm4018248
3. Kid, T., Doi, T., Shimanoe, K.: Synthesis of monodispersed SnO_2 nanocrystals and their remarkably high sensitivity to volatile organic compounds. Chem. Mater. **22**(8), 2662–2667 (2010). doi:10.1021/cm100228d
4. Ding, L., He, S., Miao, S., Jorgensen, M.R., Leubner, S., Yan, C., Hickey, S.G., Eychmüller, A., Xu, J., Schmidt, O.G.: Ultrasmall SnO_2 nanocrystals: hot-bubbling synthesis, encapsulation in carbon layers and applications in high capacity Li-ion storage. Sci. Rep. **4**, (2014). doi:10.1038/srep04647
5. Kravchyk, K., Protesescu, L., Bodnarchuk, M.I., Krumeich, F., Yarema, M., Walter, M., Guntlin, C.: Monodisperse and inorganically capped Sn and Sn/SnO_2 nanocrystals for high-performance Li-ion battery anodes. J. Am. Chem. Soc. **135**(11), 4199–4202 (2013). doi:10.1021/ja312604r
6. Talapin, D.V., Lee, J.S., Kovalenko, M.V., Shevchenko, E.V.: Prospects of colloidal nanocrystals for electronic and optoelectronic applications. Chem. Rev. **110**(1), 389–458 (2009). doi:10.1021/cr900137k

7. Cho, K.S., Talapin, D.V., Gaschler, W., Murray, C.B.: Designing PbSe nanowires and nanorings through oriented attachment of nanoparticles. J. Am. Chem. Soc. **127**(19), 7140–7147 (2005). doi:10.1021/ja050107s
8. Talapin, D.V., Rogach, A.L., Shevchenko, E.V., Kornowski, A., Haase, M.: Dynamic distribution of growth rates within the ensembles of colloidal II-VI and III-V semiconductor nanocrystals as a factor governing their photoluminescence efficiency. J. Am. Chem. Soc. **124** (20), 5782–5790 (2002). doi:10.1021/ja0123599
9. Hyeon, T.: Chemical synthesis of magnetic nanoparticles. Chem Comm. **21**(8), 927–934 (2003). doi:10.1039/b207789b
10. Talapin, D.V., Nelson, J.H., Shevchenko, E.V., Aloni, S., Sadtler, B., Alivisatos, A.P.: Seeded growth of highly luminescent CdSe/CdS nanoheterostructures with rod and tetrapod morphologies. Nano letters **7**(10), 2951–2959 (2007). doi:10.1021/nl072003g
11. Ansari, S.G., Boroojerdian, P., Sainkar, S.R., Karekar, R.N., Aiyer, R.C., Kulkarni, S.K.: Grain size effects on H_2 gas sensitivity of thick film resistor using SnO_2 nanoparticles. Thin Solid Films **295**(1), 271–276 (1997). doi:10.1016/S0040-6090(96)09152-3
12. Arnold, M.S., Avouris, P., Pan, Z., Wang, Z.L.: Field-effect transistors based on single semiconducting oxide nanobelts. J. Phys. Chem. B. **107**, 659–663 (2003). doi:10.1021/jp0271054
13. Kaviyarasu, K., Prem Anand, D. Stanly John Xavier, S., Augustine Thomas, S., Selvakumar, S.: One pot synthesis and characterization of cesium doped SnO_2 nanocrystals via a hydrothermal process. J. Mater. Sci. Technol. **28**(1), 15–20 (2012). doi:10.1016/S1005-0302(12)60017-6
14. Sun, S.H., Meng, G.W., Zhang, M.G., An, X.H., Wu, G.S., Zhang, L.D.: Synthesis of SnO_2 nanostructures by carbothermal reduction of SnO_2 powder. J. Phys. D: Appl. Phys. **37**(3), 409 (2004). doi:10.1088/0022-3727/37/3/017
15. Dai, Z.R., Pan, Z.W., Wang, Z.L.: Ultra-long single crystalline nanoribbons of tin oxide. Sol. St. Comm. **118**(7), 351–354 (2001). doi:10.1016/S0038-1098(01)00122-3
16. Yan, S.H., Ma, S.Y., Xu, X.L., Li, W.Q., Luo, J., Jin, W.X., Wang, T.T., Jiang, X.H., Lu, Y., Song, H.S.: Preparation of SnO_2–ZnO hetero-nanofibers and their application in acetone sensing performance. Mat. Lett. **159**(15), 447–450 (2015). doi:10.1016/j.matlet.2015.07.051
17. Li, W., Yoon, D., Hwang, J., Chang, W., Kim, J.: One-pot route to synthesize SnO_2-reduced graphene oxide composites and their enhanced electrochemical performance as anodes in lithium-ion batteries. J. Pow. Sour. **293**(20), 1024–1031 (2015). doi:10.1016/j.jpowsour.2015.06.025
18. Kanjwal, M.A., Barakat, A.M., Park, S.J., Kim, H.Y.: Effects of silver content and morphology on the catalytic activity of silver-grafted titanium oxide nanostructure. Fib. Poly. **11**(5), 700–709 (2010). doi:10.1007/s12221-010-0700-x
19. Schrier, J., Demchenko, D.O., Wang, L.W.: Optical properties of ZnO/ZnS and ZnO/ZnTe heterostructures for photovoltaic applications. Nano Lett **7**(8), 2377–2382 (2007). doi:10.1021/nl071027k
20. Arico, A.S., Cret, P., Antonucci, P.L., Cho, J., Kim, H., Antonucci, V.: Optimization of operating parameters of a direct methanol fuel cell and physico-chemical investigation of catalyst–electrolyte interface. Electrochimica Acta. **43**(24), 3719–3729 (1998). doi:10.1016/S0013-4686(98)00130-3
21. Wei, F., Zhang, H., Nguyen, M., Ying, M., Jiao, Z.: Template-free synthesis of flower-like SnO_2 hierarchical nanostructures with improved gas sensing performance. Sen. Act. B: Chem. **215**, 15–23 (2015). doi:10.1016/j.snb.2015.03.042
22. Kaviyarasu, K., Manikandan, E., Kennedy, J., Jayachandran, M.: Quantum confinement and photoluminescence of well-aligned CdO nanofibers by a solvothermal route. Mat. Lett **120**(1), 243–245 (2014). doi:10.1016/j.matlet.2014.01.048
23. Weber, I.T., Valentini, A., Probst, L.F.D., Longo, E., Leit, E.R.: Influence of noble metals on the structural and catalytic properties of Ce-doped SnO_2 systems. Sen. Actu. B **97**, 31–38 (2004) doi: 10.1016/S0925-4005(03)00577-X

24. Wang, J., Xu, Y., Xu, W., Zhang, M., Chen, X.: Simplified preparation of SnO_2 inverse opal for methanol gas sensing performance. Microp. Mesop. Mat. **208**(15), 93–97 (2015). doi:10.1016/j.micromeso.2015.01.038
25. Kaviyarasu, K., Manikandan, E., Mohamed, S.B., Kennedy, J.: One dimensional well-aligned CdO nanocrystal by solvothermal method. J. Alloy. Compd. **593**(25), 67–70 (2014). doi:10.1016/j.jallcom.2014.01.071
26. Zhang, P., Wang, L., Zhang, X., Shao, C., Hu, J., Shao, G.: SnO_2-core carbon-shell composite nanotubes with enhanced photocurrent and photocatalytic performance. Appl. Catal. B: Environ. **166**(167), 193–201 (2015). doi:10.1016/j.apcatb.2014.11.031
27. Villamagua, L., Stashans, A., Lee, P.M., Liu, Y.S., Liu, C.Y., Carini, M.: Change in the electrical conductivity of SnO_2 crystal from n-type to p-type conductivity. Chem. Phy. **452**(1), 71–77 (2015). doi:10.1016/j.chemphys.2015.03.002
28. Chetri, P., Choudhury, A.: Investigation of structural and magnetic properties of nanoscale Cu doped SnO_2: An experimental and density functional study. J. Alloy. Compd. **627**(5), 261–267 (2015). doi:10.1016/j.jallcom.2014.11.204
29. Pavelko, R.G., Yuasa, M., Kida, T., Shimanoe, K., Yamazoe, N.: Impurity level in SnO_2 materials and its impact on gas sensing properties. Sens. Actuators B: Chem. **210**, 719–725 (2015). doi:10.1016/j.snb.2015.01.038
30. Kaviyarasu,K., Sajan, D., Selvakumar, M. S., Thomas, S. A., Prem Anand, D.: A facile hydrothermal route to synthesize novel PbI_2 nanorods. J. Phy. Chem. Sol. **73**(11), 1396–1400 (2012). doi: 10.1016/j.jpcs.2012.06.005
31. Hou, L.R., Lian, L., Zhou, L., Zhang, L.H., Yuan, C.Z.: Interfacial hydrothermal synthesis of SnO_2 nanorods towards photocatalytic degradation of methyl orange. Mat. Res. Bull. **60**, 1–4 (2014). doi:10.1016/j.materresbull.2014.08.006
32. Rieu, M., Camara, M., Tournier, G., Viricelle, J.P., Pijolat, C., de Rooij, N.F., Briand, D.: Inkjet printed SnO_2 gas sensor on plastic substrate. Procedia Eng. **120**, 75–78 (2015). doi:10.1016/j.proeng.2015.08.569
33. Shalan, A.E., Rasly, M., Osama, I., Rashad, M.M., Ibrahim, I.A.: Photocurrent enhancement by Ni^{2+} and Zn^{2+} ion doped in SnO_2 nanoparticles in highly porous dye-sensitized solar cells. Cer. Int. **40**(8), 11619–11626 (2014). doi:10.1016/j.ceramint.2014.03.152
34. Kaviyarasu, K., Kennedy, J., Manikandan, E.: Synthesis of Mg doped TiO_2 nanocrystals prepared by wet-chemical method: optical and microscopic studies. Int. J. Nanosci. **12**(5), 1350033 (2013). doi:10.1142/S0219581X13500336
35. Robina, A., German, E., Pronsato, M.E., Juan, A., Matolinova, I., Matolin, V.: Electronic structure and bonding of small Pd clusters on stoichiometric and reduced SnO_2 (110) surfaces. Vacuum **106**, 86–93 (2014). doi:10.1016/j.vacuum.2014.03.016
36. Gaiduk, P.I., Chevallier, J. Prokopyev, S.L., Larsen, A.N.: Plasmonic-based SnO_2 gas sensor with in-void segregated silver nanoparticles. Microelec. Eng. **125**(1), 68–72 (2014). doi: 10.1016/j.mee.2013.11.005
37. Ziat, Y., Benyoussef, A., El Kenz, A.: Magnetic and electronic properties of Cr- and Mn-doped SnO_2: ab initio calculations. J. Phy. Chem. Sol. **75**(6), 701–709 (2014). doi:10.1016/j.jpcs.2014.01.018
38. Fernandes, A., Santos, D., Pacheco, M.J., Ciríaco, L., Lopes, A.: Nitrogen and organic load removal from sanitary landfill leachates by anodic oxidation at Ti/Pt/PbO_2, Ti/Pt/SnO_2-Sb_2O_4 and Si/BDD. App. Cataly. B: Envir. **148**(27), 288–294 (2014). doi:10.1016/j.apcatb.2013.10.060
39. Barkade, S.S., Pinjari, D.V., Nakate, U.T., Singh, A.K., Gogate, P.R., Naik, J.B., Son, S.H.: Ultrasound assisted synthesis of polythiophene/SnO_2 hybrid nanolatex particles for LPG sensing. Chem. Eng. Proc: Process Intensif. **74**, 115–123 (2013). doi:10.1016/j.cep.2013.09.005
40. Kusior, A., Klich-Kafel, J., Trenczek-Zajac, A., Swierczek, K., Radecka, M., Zakrzewska, K.: TiO_2–SnO_2 nanomaterials for gas sensing and photocatalysis. J. Eur. Cer. Soc. **33**(12), 2285–2290 (2013). doi:10.1016/j.jeurceramsoc.2013.01.022

41. Boumeddiene, A., Bouamra, F., Rérat, M., Belkhir, H.: Structural and electronic properties of Sb-doped SnO_2 (110) surface: a first principles study. App. Sur. Sci. **284**(1), 581–587 (2013). doi:10.1016/j.apsusc.2013.07.137
42. Zhou, G.X., Xiong, S.J., Wu, X.L., Liu, L.Z., Li, T.H., Chu, P.K.: N-doped SnO_2 nanocrystals with green emission dependent upon mutual effects of nitrogen dopant and oxygen vacancy. Acta Materialia. **61**(19), 7342–7347 (2013). doi:10.1016/j.actamat.2013.08.040
43. Kaviyarasu, K., Magdalane, C.M., Anand, K., Manikandan, E., Maaza, M.: Synthesis and characterization studies of MgO:CuO nanocrystals by wet-chemical method. Spectrochimica Acta Part A: Mol. Biomol. Spect. **142**(5), 405–409 (2015). doi: 10.1016/j.saa.2015.01.111
44. Kaviyarasu, K., Raja, A., Devarajan, P.A.: Structural elucidation and spectral characterizations of Co_3O_4 nanoflakes. Spectrochimica Acta Part A: Mol. Biomol. Spect. **11**(5), 586–591 (2013). doi: 10.1016/j.saa.2013.04.126
45. Kaviyarasu, K., Sajan, D., Devarajan, P.A.: A rapid and versatile method for solvothermal synthesis of Sb_2O_3 nanocrystals under mild conditions. Appl. Nanosci. **3**, 529 (2013). doi:10.1007/s13204-012-0156-y
46. Kaviyarasu, K., Devarajan, P.A.: A versatile route to synthesize MgO nanocrystals by combustion technique. Der Pharma Chemica, **3**(5), 248–254 (2011). ISSN: 0975-413X
47. Kaviyarasu, K., Devarajan, P.A.: Synthesis and characterization studies of cadmium doped MgO nanocrystals for optoelectronics application. Adv. Appl. Sci. Res. **2**(6), 131–138 (2011). ISSN: 0976-861
48. Kaviyarasu, K., Devarajan, P.A.: A convenient route to synthesize hexagonal pillar shaped ZnO nanoneedles via CTAB surfactant. Adv. Mat. Lett. **4**(7), 582–585 (2013). doi: 10.5185/amlett.2012.10443
49. Kaviyarasu, K., Manikandan, E., Maaza, M.: Quantum confinement of lead titanate nanocrystals by wet chemical method. J. Alloy. Compd. **649**(15), 50–53 (2015). doi:10.1016/j.jallcom.2015.07.099
50. Kaviyarasu, K., Manikandan, E., Nuru, Z.Y., Maaza, M.: Investigation on the structural properties of CeO_2 nanofibers via CTAB surfactant. Mat. Lett. **160**(1), 61–63 (2015). doi:10.1016/j.matlet.2015.07.099

Microscopy Study of Amorphous/Nanocrystalline Coatings Thermally Sprayed

Nacer E. Bacha

Abstract A commercial NiCrBSi and FeCrPC amorphous–nanocrystalline coatings were fabricated on a carbon steel substrate by plasma thermal spraying in a controlled atmosphere vessel. A cold helium gas stream can be blown directly onto freshly deposited layers to form amorphous coating or suppressed to allow formation of crystalline coating. Microstructural studies are investigated by means of X-ray diffraction (XRD), optical microscopy, scanning (SEM) and transmission (TEM) electron microscopy. Hand fracture surfaces in the fully amorphous coatings specimens exhibited a vein like morphology typical of many metallic glasses. When coatings are aged at 300 °C for 15 min, the vein like morphology is still present. If the coating is heated to 500 °C for 15 min, the vein pattern, characteristic of amorphous materials, disappears completely and nanocrystalline structure appeared. TEM was made to give more detailed information on the nanocrystallized structure. Fine nanocrystalline particles were grown on the amorphous matrix in the aged coatings having grain size ranged between 50 and 100 nm. From XRD, full amorphous coatings seem to be obtained but meticulous TEM examination has revealed the presence of crystallites of approximately 100 nm within size in the amorphous matrix. The thermal plasma technology is well adapted to the manufacture amorphous coatings on a substrate of any shape. However, the numerous operating parameters that govern the deposition of a coating render difficult the preparation of fully amorphous coatings. X-rays diffraction is not sufficient to assert that the crystallization is totally suppressed. Careful observation by the TEM microscope is necessary.

N.E. Bacha (✉)
Lab. of Surface Treatment and Materials, University of Blida 1,
Blida, 09000 Blida, Algeria
e-mail: bacnacer@gmail.com

A.Y. Oral and Z.B. Bahsi Oral (eds.), *3rd International Multidisciplinary Microscopy and Microanalysis Congress (InterM)*, Springer Proceedings in Physics 186,
DOI 10.1007/978-3-319-46601-9_15

1 Introduction

The first amorphous metal alloy was obtained by rapid solidification there are already five decades [1]. The alloy Au–Si consisted of a metal and a metalloid, the composition was close to a eutectic. Both semi empirical conditions were subsequently used to guide the development of a large number of amorphous alloys. The properties of an alloy in the amorphous state are different from those of the alloy in the crystalline state with the same chemical composition, because of the lack of periodicity in the atomic structure. Studies on the kinetics of the crystallization of metallic glasses were moderately developed to date. The results obtained are however encouraging. For example, an amorphous $Fe_{80}B_{20}$ alloy, heated to a few degrees per minute, almost instantly crystallizes around 400 °C and would take over 500 years to initiate crystallization to 200 °C [2].

When a liquid is cooled slowly, so that it can, at each instant, be considered to thermodynamic equilibrium, there is a liquid-solid transition at a characteristic temperature T_M. During cooling, all crystalline structural rearrangements have time to develop, thus obtaining a crystal. Below T_M, there is a T_g for which the degree of mobility of the atoms becomes smaller than their size. All structural rearrangement becomes impossible for a reasonable time scale. If the metal liquid taken to a temperature just above T_M, is suddenly frozen to a temperature below or equal to T_g, resulting in a solid off-balance that has kept the atomic structure of so-called liquid glass structure. For alloys capable of forming amorphous solids, the crystalline state is reached within a few milliseconds, which requires a cooling rate of the order of 10^5–10^6 °C/s [3].

Amorphous alloys in ribbon, wire and powder forms have been produced and used as commercialized materials. The ordinary critical sizes of these amorphous alloys are about 20–30 μm in thickness for ribbon, about 100–200 μm in diameter for wire and less than 25 μm in thickness for powder, respectively [4–6]. The development of amorphous alloys by thermal spraying currently looks more and more researchers across the world because of the enormous potential of this technology. The purpose of this work is to prepare amorphous coatings using thermal plasma and study the physical characteristics of the deposits obtained.

2 Experimental Details

Two powder compositions were used to make amorphous metal coatings: an AMDRY-915 NiCrBSi based powder and FeCrPC Special AMDRY-based powder. Both powders provided by Alloys Metals Inc. were prepared by atomization in liquid phase. For both powders, the percentage of chromium by atomic weight, is over 10 %. Examination by X-ray diffraction of powders confirmed that both received powders have a crystalline structure. The atomized particles for both powders are in the 20–90 μm size range with an average diameter of 75 μm for the

Ni based alloy and 45 μm for Fe based alloy. The coating is sprayed onto mild steel samples. The surface to be sprayed is sand blasted immediately before plasma spraying with Al_2O_3 abrasive. The powder to be deposited is injected into the plasma stream through stainless steel tube screwed externally to the gun just before the inlet of the nozzle. A cold gas stream can be blown directly onto freshly deposited layers to form amorphous coating or suppressed to allow formation of crystalline coating. All specimens are maintained on a rotating water-cooled holder during the deposition stage. The amorphous coatings obtained are about 250 μm thickness. The coatings obtained are examined by optical microscope, transmission and scanning electron microscope with EDX, X-ray diffraction with CuKα radiation.

3 Results

The degree of fusion of the powder particles FeCrPC was evaluated based torch power, plasma gas flow, the flow rate of carrier gas and the mass flow of the particles. In the first experiments, we found that a detrimental reaction occurs to the quality of the coating produced with the plasma gas Ar-N_2 as shown in Fig. 1a. Figure 1b reveals unmelted particles and excessive porosity. Accordingly, the nitrogen was removed and argon was used alone as a primary gas.

Figure 2 shows respectively the amorphous coatings NiCrBSi (Fig. 2a) and FeCrPC (Fig. 2b) fractured by hand. Venous pattern, characteristic of an amorphous state is highlighted. The structure of the coating FeCrPC reveals a good compactness and low porosity. For the coating based on NiCrBSi, the coating structure is lamellar.

The quenching action of a jet of helium on freshly deposited liquid particles on the substrate results in formation of an amorphous structure. Thin blades of the amorphous coating FeCrPC observed in a transmission electron microscope

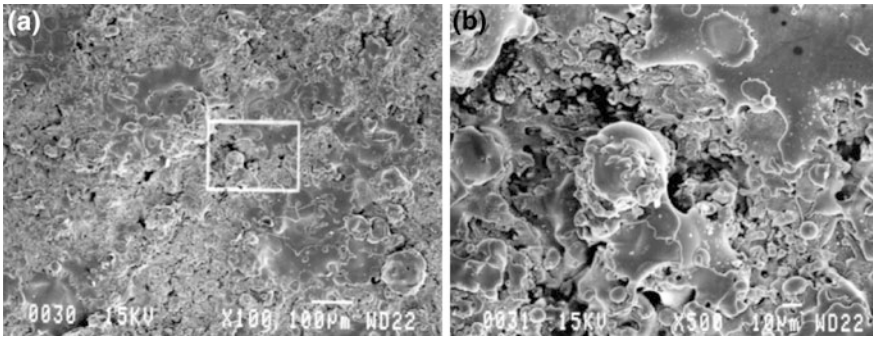

Fig. 1 Surface appearance of **a** coating deposited by a gas plasma with Ar-N_2, **b** magnification of the inset area

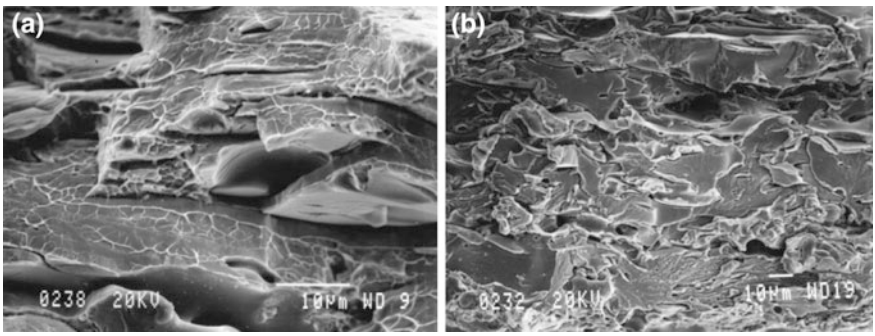

Fig. 2 Cross sections of **a** NiCrBSi coating, **b** FeCrPC coating

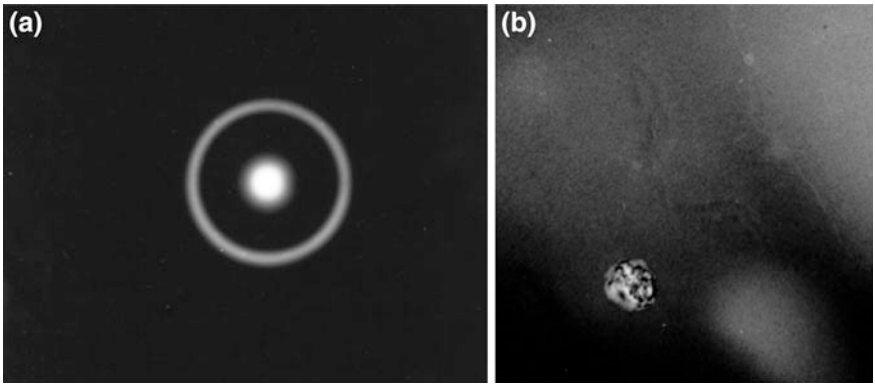

Fig. 3 TEM pattern of an amorphous FeCrPC coating of **a** completely amorphous region, **b** crystallites in the amorphous phase

(TEM) confirmed the amorphous state of the coating as shown in Fig. 3a. However, meticulous microscopic examination reveals the presence of crystallites in the amorphous matrix of approximately 100 nm in size as is shown in Fig. 3b.

The idea of using metallic glasses as precursors for crystallization has been long in coming. The exploitation of crystallization only began in the early 80's. Special interest of crystallized metallic glasses is that they offer the possibility of micro-cristallinity (grain diameter < 1 μm) combines high resistance to grain grow during the heat treatment. Figure 4 shows TEM pattern of cristallized FeCrPC coating helium gas is suppressed during thermal spraying.

When Fe based coating is heat treated at 800 °C during 15 min, secondary phases is highlighted as shown in Fig. 5a. Figure 5b shows the magnification of the second phase. The second phase is rich in phosphorous element due to its segregation at the surface.

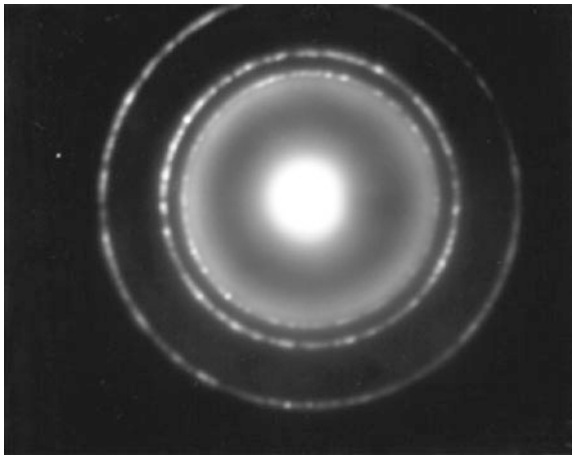

Fig. 4 TEM pattern of crystallized FeCrPC coating

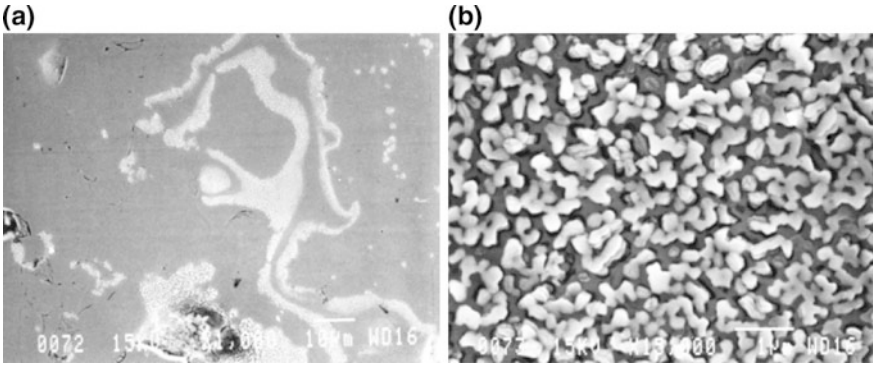

Fig. 5 Microstructure of **a** an amorphous FeCrPC aged at 800 °C during 15 min, **b** magnification of the second phase

4 Conclusion

The thermal plasma technology is well adapted to the manufacture amorphous coatings on a substrate of any shape. However, the numerous operating parameters that govern the deposition of a coating render difficult the preparation of fully amorphous coatings. X-rays diffraction is not sufficient to assert that the crystallization is totally suppressed. Careful observation by the TEM microscope is necessary.

References

1. Klement, W., Willens, R.H., Duwez, P.: Non-crystalline structure in solidified Gold-Silicon alloys. Nature **187**, 869–870 (1960)
2. Gilman, J.J.: Mechanical behavior of metallic glasses. J. Appl. Phys. **46**(4), 1625–1633 (1975)
3. Cahn, R.W.: Recent developments in rapidly Melt-Quenched crystalline alloys. Annu. Rev. Mater. Sci. **12**, 51–63 (1982)
4. Cheng, J.B., Liang, X.B., Wang, Z.H., Xu, B.S.: Microstructure and mechanical properties of FeBSiNb metallic glass coatings by twin wire arc spraying. J. Therm. Spray Technol. **22**(4), 471–477 (2013)
5. Zhang, C., Guoa, R.Q., Yang, Y., Wua, Y., Liu, L.: Influence of the size of spraying powders on the microstructure and corrosion resistance of Fe-based amorphous coating. Electrochim. Acta **56**, 6380–6388 (2011)
6. Guo, W., Wu, Y., Zhang, J., Hong, S., Li, G., Ying, G., Guo, J., Qin, Y.: Fabrication and characterization of Thermal-Sprayed Fe-based amorphous/nanocrystalline composite coatings: an overview. J. Therm. Spray Technol. **23**(7), 1157–1180 (2014)

Phenotypic Plasticity in Desert Rodents Harderian Glands Under Seasonal Steroids Control

O. Saadi-Brenkia and N. Haniche

Abstract Sex hormones activate reproductive behaviors throughout the Harderian glands (HG) in desert rodents. It appears that gonadal hormones have both organizational and activational effects on epithelial cells. This study, thus represents a significant advance in our understanding of the steroid actions that regulate cellular differentiation and thereby pheromones production. Our results reveal that HG of two desert rodents having an opposite lifestyle, *Psammomys obesus* (diurne) and *Gerbillus tarabuli* (nocturne) are capable of undergoing significant morphological changes from season to season. In both species, during the mating season, HG exhibit remarkable phenotypic responsiveness in order to produce chemical cues that promote sexual interaction. Small specimens from the HG were processed for light and transmission electron microscopic study. Obvious structural differences were observed between diurnal and nocturnal species. The gland is compound tubulo-alveolar, being characterized by a single layer of vacuolated columnar cells in *Psammomys obeus,* whereas two cells types were found in *Gerbillus tarabuli*, vacuolated columnar cells and pyramidal basal cells. In breeding season, a new cellular type (the same for both species) appears characterized by large lipid vacuoles. Porphyrins and cellular debris were observed in the glandular lumens indicating that important cellular remodelling occurs in the HG of desert rodents. The possible functional significance of this new cellular type was discussed. These results suggest, that phenotypic plasticity is an important means by which HG cope with environmental lighting.

O. Saadi-Brenkia (✉) · N. Haniche
Laboratoire de Biologie et Physiologie Des Organismes Equipe de Neurobiologie, USTHB, Bab Ezzouar, Algérie
e-mail: saadianissa@yahoo.fr

O. Saadi-Brenkia
Departement de Biologie, Université M'hamed Bougara Boumerdes, Avenue de l'indépendance, Boumerdes 35000 Algérie

A.Y. Oral and Z.B. Bahsi Oral (eds.), *3rd International Multidisciplinary Microscopy and Microanalysis Congress (InterM)*, Springer Proceedings in Physics 186,
DOI 10.1007/978-3-319-46601-9_16

1 Introduction

The Harderian gland (HG) is a large orbital gland which occurs in most terrestrial vertebrates and which opens by a duct onto the surface of the nictitating membrane [1]. The main role of the HG in many species is to provide a source of lubrication for the third eyelid (nictitating membrane), and contribute to the lipid phase of the tear film, however, other secondarily functions have been assigned to this gland. These consist of being a potential site of immune response [2–5] part of the retinal-pineal axis [6, 7] and a source of pheromones [8–10]. Previous data have indicated that, HG activity is under endogenous control such hormones and environmental factors such light and temperature [11–13].

Previous studies on HG morphology in Saharan rodents have been conducted by [14, 15]. But, there has been no seasonal work on their structural aspect related to gonadal status. As is commonly known steroid hormones mediate pleiotropic cellular processes involved in metabolism, cellular proliferation, and differentiation. In addition [16] have reported that, androgens are recognized to affect HG morphology and secretory activity. Thus, the current study aims to investigate, whether the secretory cells in HG undergo seasonal differentiation under steroids control. This might provide some knowledge on the phenotypic plasticity in HG at the intraspecific level in these seasonal breeders which inhabits desert.

2 Experimental

Animals: Desert rodents are seasonal breeders, we used in this study *Gerbillus tarabuli* (strictly nocturnal) and *Psammomys obesus* (strictly diurnal) species, both from Gerbillidae family. The breeding season for sand rat extends from September to March and from December to April for gerbil [17, 18]. Ten adult's male from both species were captured during May (resting season) and December (breeding season). They were caught in desert of Béni-Abbès, Wilaya of Béchar, Algeria: 30° 7'N; 2°10'W. The animals were cared for in accordance with the criteria outlined in the "Guide for the Care and Use of Experimental Animals" prepared by the National Academy of Sciences and published by the National Institute of Health.

Light microscopic analysis: HG samples were fixed in 10 % buffered formalin, paraffin-embedded, and sectioned at 5 μm. For standard histology, sections were stained by different procedures.

Transmission electron microscopic analysis: Following glutaraldehyde fixation, samples were washed in phosphate buffer and then post-fixed in 1 % osmium tetroxide in phosphate buffer. Tissue pieces were then dehydrated through an ascending ethanol gradient, and embedded in Epon 812 resin. Semithin sections were cut, stained with 1 % Toluidine Blue and examined under light microscope. The ultrathin sections placed on copper grids and double-stained with uranyl acetate and lead citrate were observed by an electron Zeiss EM-109.

3 Results and Discussion

Our morphological observations demonstrate that HG of each species varied in accordance with the reproductive state. The gland is enclosed in a fine capsule, made up of connective tissue rich in vessels and nerves, in addition to melanocytes (Fig. 1a, b). This capsule sent septa which divide the secretory portion into lobules.

Secretory cells are organized into tubulo-alveolar units. In sand rat, the glandular epithelium is uniform lined by only one cellular type. Columnar in shape, containing acidophilic cytoplasm, richly vacuolated (Fig. 2a).

In pseudostratified epithelium of gerbil, two cell types can be distinguished. Columnar principal, cells similar to those observed in sand rat and pyramidal basal with highly basophilic cytoplasm (Fig. 3). In the glandular lumens, porphyrin accretions and cellular debris are observed in both species.

A remarkable effect of sex steroids in our study concerned the induction of new cellular phenotype revealed by structural and ultrastructural studies. Indeed, in both species, in reproductive season some principal cells undergo significant morphological changes which are regarded as an indicative of cell differentiation. In breeding season the secretory epithelium contains two cellular types in *P obesus* and three in *G tarabuli.* This new cellular phenotype is characterized by numerous and large lipid droplets occupying the whole cytoplasm (Figs. 4, 5).

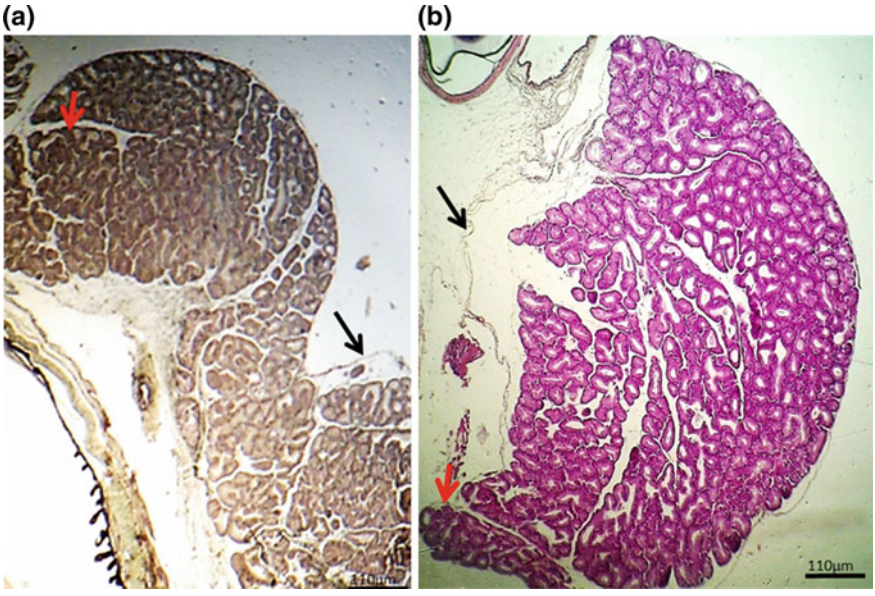

Fig. 1 Histological sections showing the general view of HG in desert rodents **a** in *Psammomys obesus*. Van Gieson stain **b** in *Gerbillus tarabuli*. Hemalun/eosin stain. Capsule (*black arrow*), lobule (*red arrow*)

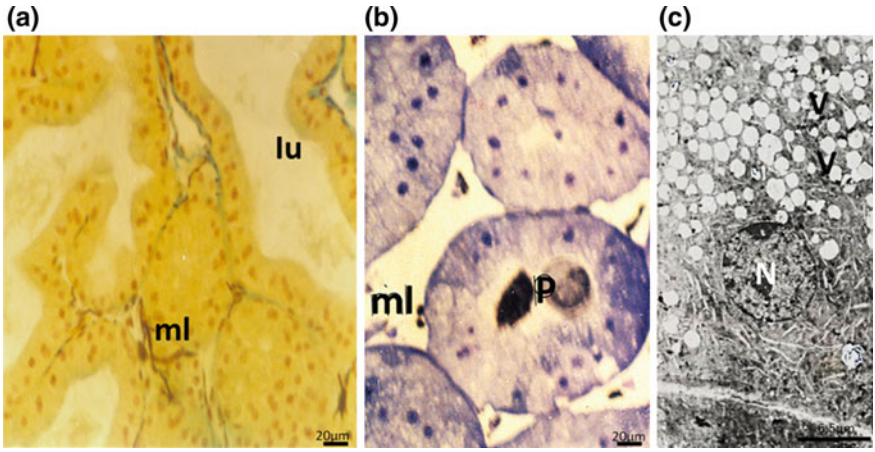

Fig. 2 *Psammomys obesus* HG, showing the large lumen (lu) of tubules lined by prismatic homogeneous cells. **a** Hemalun/picroindigocarmin staining of the tubuloalveoli. Note the abundance of melanin (ml) in connective tissue septa. **b** Semithin section Toluidine blue stain. A porphyrin accretion (P) in a gland tubule lumen. **c** Low magnification electron micrograph of prismatic epithelial cell. Note numerous small lipid vacuoles (V) and nucleus (N) located at basal portion of cell

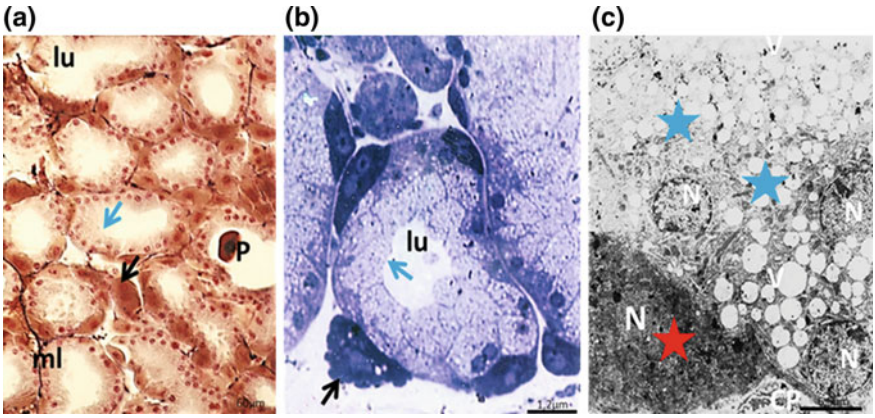

Fig. 3 Morphological features of *Gerbillus tarabuli* HG. **a** Photomicrograph of a paraffin section illustrating The lining epithelium of the glandular units consists on two cellular types are clearly distinguishable. Prismatic cells (*blue arrow*) and pyramidal shaped cells (*black arrow*). Note the presence of porphyrin (P) in the lumen and melanin in the interstices. Azan Stain. **b** Semithin section stained with Toluidine blue, showed that the secretory end-pieces were lined with principal columnar cells (*blue arrow*) and basal pyramidal cells (*black arrow*). **c** Low magnification electron micrograph displaying prismatic cell with acidophilic vacuolated cytoplasm (*blue star*) and basophilic pyramidal cells (*red star*). Nuclei (N),Vacuoles (V) and capillary (CP). Often epithelial cells are binucleated

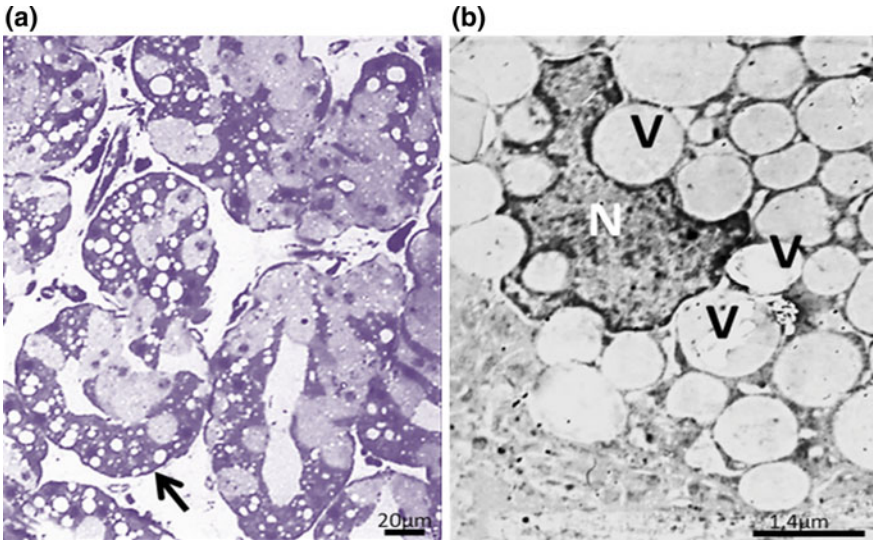

Fig. 4 The glandular epithelium of sand rat in reproductive season. **a** Semithin section stained with *Toluidine blue*. Appearance of new cellular phenotype containing large lipids vacuoles (*black arrow*). **b** Electron micrograph at high magnification of new differentiated cell showing numerous large lipids vacuoles (V) invading the cytoplasm and deforming the nucleus (N)

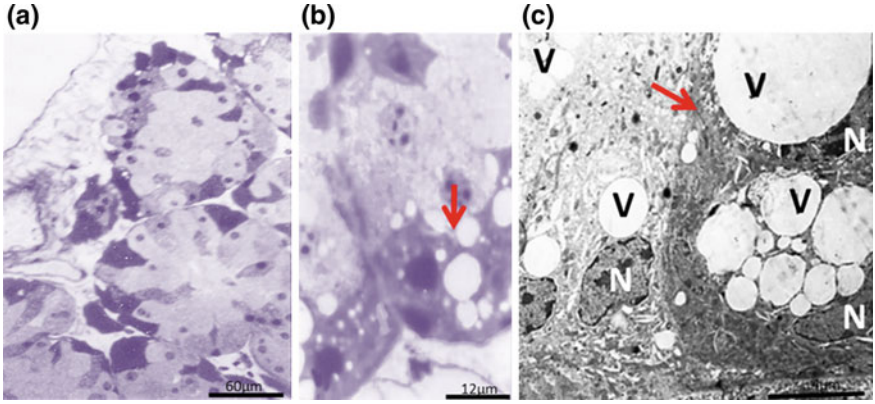

Fig. 5 The tubuloalveoli with secretory cells types from gerbil's HG in reproductive season. **a** Semithin section of general view, showing three cellular types. Toluidine blue stain. **b** Semithin section at high magnification displaying the newly cellular type (*red arrow*). Toluidine blue stain. **c** ultrastructural appearance of secretory prismatic cells. Note the newly differentiated (*red arrow*) charged with large lipids vacuoles (V), nuclei (N) are completely deformed

4 Discussion

The results of the present study underline that, desert rodent's HG is capable of undergoing significant morphological changes from season to season. And it's considered as a target for steroid hormones. Indeed, as revealed by [19] the gland has receptors for the steroids hormones. Earlier reports by [20] have indicated that, androgenic hormones exert a variety of effects upon mammalian tissues. Including of gene expression and control of cellular growth and differentiation. In addition, [21, 22] have reported that, androgens are the principal determinants of the regulation and the differentiation of the Harderian glands in Syrian hamster. According to [23], to convert information from the environment to the appropriate behavioral responses, animals use a combination of somatosensory, visual, auditory, chemical, and mechanical inputs to acquire information about their surroundings [24] have stated that, pheromones released from HG act through olfactory pathways to exert powerful effects on sexual behavior in rodents. Then, it appears that in both species, target cell groups within HG that mediate mating by pheromones released displayed a significant morphological plasticity during seasons. Steroid hormones induce cytological differentiation involved in metabolism of the steroidal pheromones. There seems that, some principal prismatic cells under steroids control exhibit an epithelial phenotype resulting in intracellular changes. In fact, numerous large lipids vacuoles deforming the nucleus are observed. According to [25], the size and appearance of lipid droplets were controlled by androgens [24] have proposed that, the lipids from the Harderian gland of golden hamster serve as a pheromone to declare their territory and to seek the mate with good congeniality. We suggest that, the new cellular phenotype plenty of numerous and large lipid droplets encountered only in mating season in these desert species is related to pheromones production. Hence, cellular death and tissue remodeling are evidenced by the presence of cellular debris in the glandular lumens. Despite to the voluminous literature on the hamster's HG, we cannot take it as a reference. Since, according to [26–28], the hamster's HG shows a remarkable anatomical and biochemical sexual dimorphism. But in desert species, no morphological differences in HGs between male and female have been detected by [14, 15].

5 Conclusions

The current data suggest that in desert rodents:

- The glandular morphology is related to the habits of the species, uniform epithelium (one cell type) in diurnal species and pseudostratified (two cells types) in nocturnal species.
- Steroids are essential for appropriate cytological differentiations, which are probably linked to pheromones production in breeding season.

– Steroids act as a morphogenic signal and indirectly regulate social behavior in these species.
– Beside cellular differentiation in HG steroids hormones control tissue homeostasis.

Further studies are necessary to identify the expression of androgen receptors according to seasons for a clear understanding.

References

1. Sakai, T.: The mammalian Harderian gland: morphology, biochemistry, function and phylogeny. Arch. Histologicum Japonicum **44**, 299–333 (1981)
2. Mueller, A.P., Sato, K., Glick, B.: The chicken lacrimal gland, gland of Harder, caecal tonsil and accessory spleens as sources of antibody-producing cells. Cell. Immunol. **2**, 140 (1971)
3. Albini, B., Wick, G., Rose, M.Elaine, Orlans, Eva: Immunoglobulin production in chicken Harderian glands. Int. Arch. Allergy Appl. Immunol. **47**, 23–34 (1974)
4. Burns, R.B., Maxwell, M.H.: The structure of the Harderian and lacrimal gland ducts of the Turkey, fowl and duck. A light microscope study. J. Anat. **128**, 285–292 (1979)
5. Schramm, U.: Lymphoid cells in the Harderian gland of birds. An electron microscopical study. Cell Tissue Res. **205**, 85–94 (1980)
6. Wetterberg, L., Geller, E., Yuwiler, A.: Harderian gland: An extraretinal photoreceptor influencing the pineal gland in neonatal rats? Science. **167**, 884–885 (1970)
7. Reiter, R.J., Klein, D.C.: Observations on the pineal gland, the Harderian glands, the retina and the reproductive organs of adult female rats exposed to continuous light. J. Endocrinol. **51**, 117–125 (1974)
8. Thiessen, D.D., Clancy, A., Goodwin, M.: Harderian gland pheromones in the Mongolian gerbil, Meriones unguiculatus. J. Chem. Ecol. **2**, 231–238 (1976)
9. Payne, A.P.: Pheromonal effects of Harderian gland homogenates on aggressive behaviour in the hamster. J. Endocrinol. **73**, 191–192 (1977)
10. Thiessen, D.D., Kittrell, M.W.: The Harderian gland and thermoregulation in the gerbil (Meriones unguiculatus). Physiol. Behav. **24**, 417–424 (1980)
11. Reiter, R.J., Richardson, B., Hurlbert, E.C.: Pineal, retinal and Harderian gland melatonin in a diurnal species, Richardson's ground squirrel (*Spermophilus richardsoni*). Neurosci. Lett. **22**, 285–288 (1981)
12. Buzzell, G.R., Menendez-Pelaez, A.: The interrelationship between theharderian glands and the neuroendocrine-thyroid axis in rodents. In: Webb, S.M., Hoffman, R.A., Puig-Domingo, M.L., Reiter, R.J. (eds.) Harderian glands: Porphyrin, metabolism, behavioral and endocrine effects, pp. 255–270. Springer-Verlag, Berlin (1992)
13. Tomas-Zapico, C., Coto-Montes, A., Martinez-Fraga, J., et al.: Effects of continuous light exposure on antioxidant enzymes, porphyric enzymes and cellular damage in the Harderian gland of the Syrian hamster. J. Pineal Res. **34**, 60–68 (2003)
14. Djeridane, Y.: The Harderian gland of desert rodents: a histological and ultrastructural study. J. Anat. **180**, 465 ± 480 (1992)
15. Saadi-Brenkia, O., Haniche, N., Bendjelloul, M.: Light and electron microscopic studies of the Gerbillus tarabuli (Thomas, 1902) Harderian gland. Zoolog. Sci. **30**(1), 53–59 (2013)
16. Chieffi Baccari, G., Monteforte, R., de Lange, P., Raucci, F., Farina, P., Lanni, A.: Thyroid hormone affects secretory activity and uncoupling protein-3 expression in rat harderian gland. Endocrinology **145**, 3338–3345 (2004)

17. Khammar, F., Brudieux, R.: Seasonal changes in testicular contents and plasma concentrations of androgens in the desert gerbil (Gerbillus gerbillus). J. Reprod. Fertil. **80**, 589–594 (1987)
18. Amirat, Z., Khammar, F., Brudieux, R.: Variations saisonnières comparées de l'activité sexuelle (données pondérales) chez deux espèces de Rongeurs(Psammomys obesus et Gerbillus gerbillus) du Sahara occidental algérien. Mammalia **41**, 341–356 (1977)
19. Vilchis, F., Pérez-Palacios, G.: Steroid hormone receptors and the sexual phenotype of the Harderian gland in hamster. J. Endocrinol. **112**, 3–8 (1989)
20. Berger, FG., Watson G.: Androgen-regulated gene expression. Annu. Rev. Physiol. **51**, 51–65 (1989)
21. Rodriguez, C., Menendez-Pelaez, A., Nonaka, K.O., Vaughan, M.K., Reiter, R.J.: Effects of LH manipulations on the castration-induced prophyrin rise in Syrian hamster Harderian glands. Endocrinologia **38**(9), 270–272 (1991)
22. Rodriguez-Colunga, M.J., Rodriguez, C., Antolin, I., Uria, H., Tolivia, D., Vaughan, M.K., Menendez-Pelaez, A.: Development and androgen regulation of the secretory cell types of the Syrian hamster (Mesocricetus auratus) Harderian gland. Cell Tissue Res. **274**, 186–197 (1993)
23. Huston, S.J., Jayaaman, V.: Studying sensorimotor integration in insects. Curr. Opin. Neurobiol. **21**, 527–534 (2011)
24. Seyama, Y., Uchijima, Y.: Novel function of lipids as a pheromone from the Harderian gland of golden hamster. Proc. Jpn. Acad. Ser. B Phys. Biol. Sci. **83**(3), 77–96 (2007)
25. Buzzell, G.R., Blank, J.L., Vaughan, M.K., Reiter, R.J.: Control of secretory lipid droplets in the Harderian gland by testosterone and the photoperiod: comparison of two species of hamsters. General Comp. Endocrinol. **99**, 230–238 (1995)
26. Hoffman, R.A.: Influence of some endocrine glands, hormones and blinding of the histology of the Harderian glands of golden hamsters. Am. J. Anat. **132**, 463–478 (1971)
27. Payne, A.P.: The Harderian gland: A tercentennial review. J. Anat. **185**, 1–49 (1994)
28. Menendez-Pelaez, A., Reiter, R.J., Guerrero, J.M., Puig-Domingo, M.: Sexual dimorphism in N-acetyl-transferase activity, hydroxyindole-O-methyltransferase activity, and melatonin content in the Harderian gland of syrian hamsters: changes following gonadectomy. Proc. Soc. Exp. Biol. Med. **187**, 287–291 (1988)

TEM Investigation of Nanostructures with a High Aspect Ratio

A.V. Myasoedov, A.E. Kalmykov, D.A. Kirilenko and L.M. Sorokin

Abstract In this work, we intend to demonstrate an essential role that can play a TEM investigation of cross-sections of HAR nanostructures for a characterization of their internal structure and surface morphology. For illustrative purposes we briefly present some results of the TEM investigation of CuO, GaAs, GaN whiskers as well the comparative study of mineral and synthetic chrysotile nanotubes. In particular, the investigation of CuO nanowires (NWs) revealed that they do not have a proper crystal habit and in a majority of cases the nanowhiskers have a bi-crystalline structure, but rarely come across ones consisting of more than two crystals. And it is also interesting, that a boundary of a junction of two crystals can be not planar. As a result of the analysis of diffraction patterns of cross-sections of different nanowhiskers the growth direction was determined as [110]. Concerning the GaAs and GaN whiskers, their cross-sections have the shape close to a regular hexagon, as was expected. In addition, the observed GaN whisker has the faceted nanopipe, also with a hexagon shape. The average diameter of nanotubes in a chrysotile fibre was estimated and compared with the diameters of the given synthetic chrysotile nanotubes.

1 Introduction

One of the main objectives of high-resolution TEM studies is a characterization of novel materials. A significant part of these materials constitute high-aspect-ratio (HAR) micro- and nanostructures. Examples of HAR micro- and nanostructures are carbon nanotubes, semiconductor nanowires, mineral and synthetic chrysotile nanotubes, such structures usually have a diameter in the nanoscale range (<100 nm) and a high length to diameter ratio.

HAR nanostructures may have unique mechanical, chemical and electrical properties, that can strongly differ from properties of the same bulk material [1]. For

A.V. Myasoedov (✉) · A.E. Kalmykov · D.A. Kirilenko · L.M. Sorokin
Ioffe Institute, 26 Polytekhnicheskaya, St. Petersburg 194021, Russia
e-mail: amyasoedov88@gmail.com

A.Y. Oral and Z.B. Bahsi Oral (eds.), *3rd International Multidisciplinary Microscopy and Microanalysis Congress (InterM)*, Springer Proceedings in Physics 186,
DOI 10.1007/978-3-319-46601-9_17

example, it is known, that nanowhiskers can have dislocation-free structure. The absence of dislocations excludes the conventional plastic strain mechanisms, as a result nanowhiskers demonstrate considerable strength, flexibility [2] and resistance to corrosion.

Since the middle of the 20th century the whiskers became the subject of the thoroughly studies [3]. Initially, the interest in whiskers was related with their negative influence on a work of electrical equipment [4], namely, a spontaneous growth of whiskers on the surface of a metal solder may result in a short circuit. The problem was overcome by the use of new solder brands including those not containing the lead.

Over the years of the whiskers research, it was proposed numerous ways of their growth, such as vapour phase epitaxy, electrocrystallization, thermal oxidation and others [5]. At the present time, whiskers find wide application in various fields of science and industry, especially as gas detectors [6], heterogeneous catalysts [7], accumulator electrodes [8], probes [9], emitters [10] and etc. Semiconductor whiskers, for example, CuO and TiO_2 whiskers may be used as a high efficient photocatalysts [9, 11], at that tenorite whiskers (CuO) are more preferable because they have the narrow band gap (band gap 1.2 eV) and have a conductivity of p-type, what makes their application possible in photocatalysis in the visible range.

Natural chrysotile fibre is a soft, fibrous silicate mineral more known as asbestos. The material widely is used in building materials, but could be very toxic for humans. The multi-walled hollow chrysotile nanotubes are perspective material for creation of nanowires. Using both high-pressure techniques and metal-organic chemical vapor deposition (MOCVD) inner nanoscale channels can be filled with the metals or with semiconductor materials [12].

The conventional sample preparation technique of HAR nanostructures for the high-resolution TEM study includes the use of fine mesh grids covered with formvar film. Specimens are placed on the supporting film either by casting of one drop of colloid solution prepared by sonication or by mechanical scrape of sample surface. In order to eliminate a contribution of supporting film in signal usually use a holey film. Nanostructures on the supporting films lie in the plane that is perpendicular to the electron beam and such technique does not allow to observe internal structure and surface morphology of a nanostructure.

The aim of this work is to demonstrate an essential role that can play a TEM investigation of cross-sections of HAR nanostructures for a characterization of their internal structure and surface morphology.

2 Experimental

For illustrative purposes we briefly present the results of the TEM investigation of CuO, GaAs, GaN whiskers as well the comparative study of mineral and synthetic chrysotile nanotubes. The special sample preparation technique for TEM/HREM observation of cross-sections was used. The initial stage of the technique depended

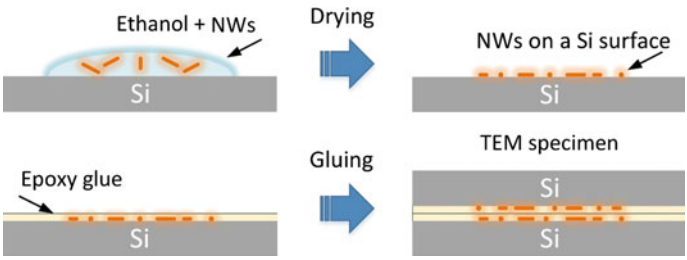

Fig. 1 The schematic illustration of the specimen preparation

on an initial state of samples, but the final aim of this stage was to obtain the randomly or particular way oriented nanotubes embedded in an epoxy resin between two silicon plates. The obtained bars have been used for a conventional cross-section TEM specimen preparation consisting of a mechanical preparation and an ion milling. The schematic illustration of the specimen preparation is shown on Fig. 1. In the [13] is described by authors the similar technique, which was applied for preparation of $SrTiO_3$ nanotubes cross-sections. It is the first description of the technique that we had found.

The investigation was performed with Philips EM420 and JEM 2100F microscopes operated at 100 and 200 kV, respectively.

CuO NWs were formed by a thermal annealing of a thin steel grid coated by copper at the elevated temperatures [14]. The grid was embedded in an epoxy resin and sandwiched between two silicon plates.

GaAs nanowhiskers were grown by an epitaxy on a silicon substrate. A conventional TEM specimen has been prepared with additional compression and lapping in the particular direction at the stage of the gluing. This provided more suitable orientation of the nanowhiskers in the specimen instead of side-back views.

GaN nanowhiskers were grown by an epitaxy on a sapphire substrate. In order to embed nanowhiskers in an epoxy resin they were carefully scraped onto a silicon plate coated by an epoxy resin.

In the case of the natural chrysotile, a bunch of chrysotile fibres was embedded in an epoxy resin and sandwiched in the particular way between two silicon plates. The synthetic chrysotile was supplied as the powder. The powder was dispersed in ethanol and sonicated in an ultrasonic bath. Then, a one drop of the solution was poured and dried on a silicon surface. After that, a conventional cross-section TEM specimen has been prepared for the obtained thin film structure.

3 Results and Discussion

The investigation of CuO NWs revealed that they do not have a proper crystal habit. We connect it with the low symmetry of the monoclinic crystal system. In a majority of cases the nanowhiskers have a bi-crystalline structure, but rarely come

across ones consisting of more than two crystals. And it is also interesting, that a boundary of a junction of two crystals can be not planar. As a result of the analysis of diffraction patterns of cross-sections of different nanowhiskers the growth direction was determined as [110] (Fig. 2).

The average diameter of nanotubes in a natural chrysotile fibre was estimated and compared with the diameters of the given synthetic chrysotile nanotubes (Fig. 3). The average diameter of nanotubes in a chrysotile fibre and synthetic chrysotile nanotubes is about 20 and 70 nm, respectively. The HREM investigation of the synthetic chrysotile detected that nanotubes have the shell different from the core. When the nanotubes lie in the plane that is perpendicular to the electron beam, it is more difficult to reveal this shell or impossible at all.

The GaAs and GaN whiskers cross-sections have the crystal habit close to a regular hexagon, as was expected. Such orientation of a nanowhisker could allow to obtain the HREM image of interface between core and shell (Fig. 4).

The GaN whiskers were not enough thin to be transparent to electrons (the diameter of the whiskers was about 2 mkm), that is why the preparation their cross-section was the most suitable way to the TEM observation.

The investigation of the GaN whisker revealed the presence of a faceted nanopipe in the core of the 2 μm thick whisker (Fig. 5). As shown in Fig. 5, b the nanopipe has the shape similar to hexagon.

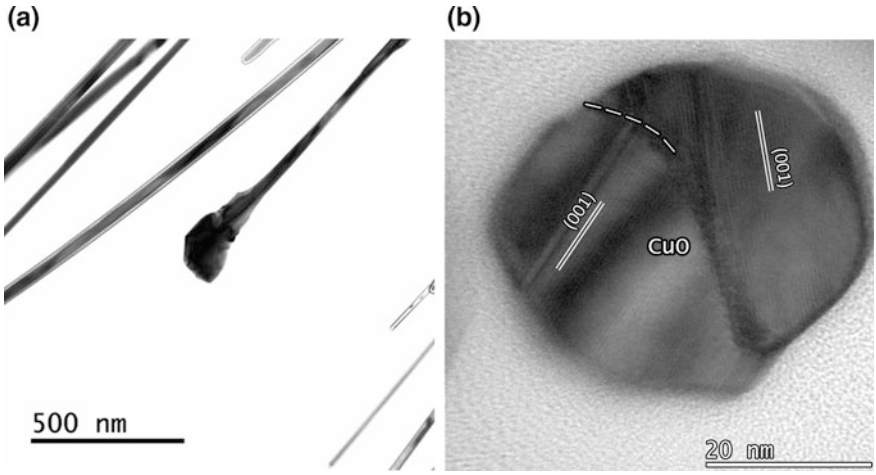

Fig. 2 **a** TEM image of CuO nanowires; **b** cross-section HREM image of a nanowire 'trunk'

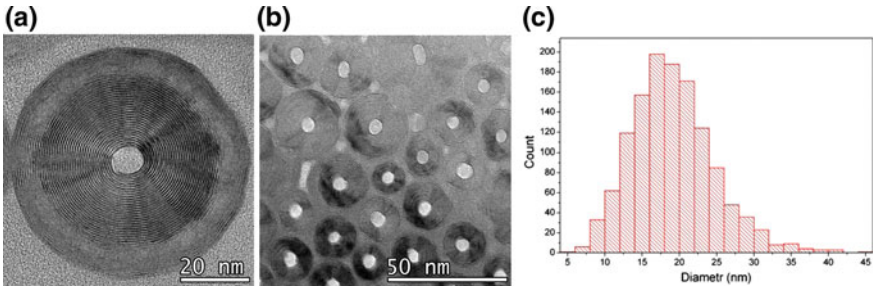

Fig. 3 HREM images of chrysotile nanotubes. **a** cross-section HREM image of a synthetic chrysotile nanotube; **b** cross-section HREM image of a natural chrysotile fibre; **c** diameter distribution of natural chrysotile nanotubes in a fibre

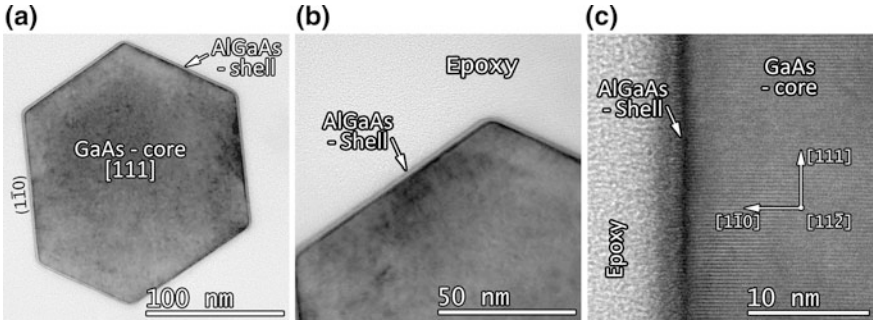

Fig. 4 TEM images of the GaAs nanowhisker. **a**, **b** cross-section TEM images of a GaAs nanowhisker, the image was taken with the incident electrom beam parallel to the [111] zone axis; **c** cross-section HREM image of a GaAs nanowhisker, the image was taken with the incident electrom beam parallel to the [11-2] zone axis

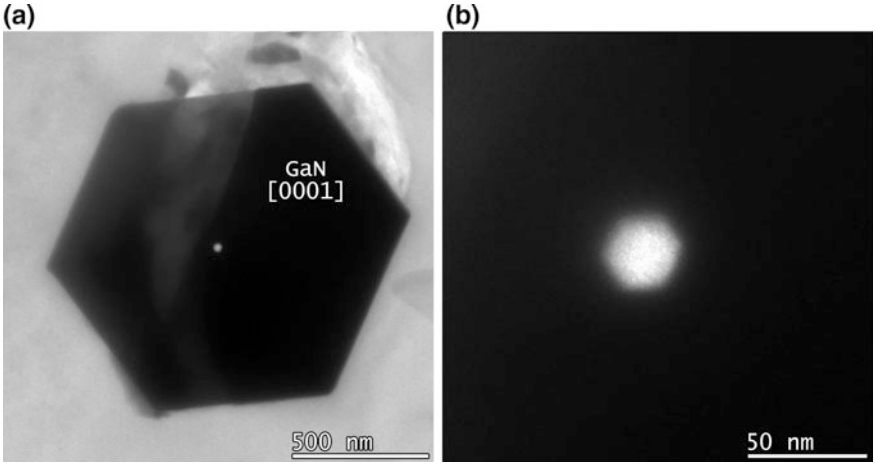

Fig. 5 TEM images of a GaN whisker. **a** cross-section TEM image a GaN whisker, the image was taken with the incident electron beam parallel to the [0001] zone axis, **b** an enlarged portion of the **a** image showing a faceted nanopore in the GaN whisker

4 Conclusion

The essential role of a TEM investigation of cross-sections of HRA nanostructures for a characterization of their internal structure and surface morphology was demonstrated. It is worth noting that the most part of the shown data could not be get without a preparation of the cross-sections.

Acknowledgments Work was made at Joint Research Center "Material science and characterization in advanced technology" Saint-Petersburg, Russia. This study was supported by the program of Presidium of the Russian Academy of Sciences "Actual Problems of Low-Temperature Physics".

References

1. Abramova, A.N., Dorogov, M.V., Vlassov, S., Kink, I., Dorogin, L.M., Lõhmus, R., Romanov, A.E., Vikarchuk, A.A.: Nanowhisker of copper oxide: fabrication technique, structural features and mechanical properties. Mater. Phys. Mechanics **19**, 88–95 (2014)
2. Herring, C., Galt, J.K.: Elastic and plastic properties of very small metal specimens. Phys. Rev. **85**(6), 1060–1061 (1952)
3. Cobb, H.L.: Cadmium whiskers. Mon. Rev. Am. Electroplaters Soc. **33**(28), 28–30 (1946)
4. Compton, K.G., Mendizza, A., Arnold, S.M.: Filamentary growths on metal surfaces—whiskers. Corrosion **7**(10), 327–334 (1951)
5. Tiwari, J.N., Tiwari, R.N., Kim, K.S.: Zero-dimensional, one-dimensional, two-dimensional and three-dimensional nanostructured materials for advanced electrochemical energy devices. Prog. Mater Sci. **57**, 724–823 (2012)
6. Wang, C., Fu, X.Q., Xue, X.Y., Wang, Y.G., Wang, T.H.: Surface accumulation conduction controlled sensing characteristic of p-type CuO nanorods induced by oxygen adsorption. Nanotechnology **18**(14), 145506–145516 (2007)
7. Switzer, J.A., Kothari, H.M., Poizot, P., Nakanishi, S., Bohannan, E.W.: Enantiospecific electrodeposition of a chiral catalyst. Nature **425**(6957), 490–493 (2003)
8. Gao, X.P., Bao, J.L., Pan, G.L., Zhu, H.Y., Huang, P.X., Wu, F., Song, D.Y.: Preparation and electrochemical performance of polycrystalline and single crystalline CuO nanorods as anode materials for li ion battery. J. Phys. Chem. B **108**(18), 5547–5551 (2004)
9. Zhang, Q., Zhang, K., Xu, D., Yang, G., Huang, H., Nie, F., Liu, C., Yang, S.: CuO nanostructures: synthesis, characterization, growth mechanisms, fundamental properties, and applications. Prog. Mater Sci. **60**, 208–337 (2014)
10. Zhu, Y.W., Yu, T., Cheong, F.C., Xu, X.J., Lim, C.T., Tan, V.B.C., Thong, J.T.L., Sow, C. H.: Large-scale synthesis and field emission properties of vertically oriented CuO nanowire films. Nanotechnology **16**(1), 88–92 (2005)
11. Chen, X., Mao, S.S.: Titanium dioxide nanomaterials: Synthesis, properties, modifications and applications. Chem. Rev. **107**(7), 2891–2959 (2007)
12. Roveri, N., Falini, G., Foresti, E., Fracasso, G., Lesci, I.G., Sabatino, P.: Geoinspired synthetic chrysotile nanotubes. J. Mater. Res. **21**(11), 2711–2725 (2006)
13. Gec, M., Zagar, K., Bussmann, B., van Aken, P.A., Ceh, M.: Preparation of nanotubes for cross-sectional TEM/STEM observations MC 2009 Proceedings, pp. 245–246 (2009)
14. Dorogov, M.V., Kozlov, A.Y., Gryzunova, N.N., Vikarchuk, A.A., Romanov, A.E.: Structure, formation mechanism and properties of copper oxide nanowhiskers. In: Sustainable Industrial Processing Summit 2015, vol. 1, pp. 259–268 (2015)

Morphology, Chemical Composition, and Magnetic Properties of Arc Discharge Fe–C Soot

Sergey A. Novopashin, Marina A. Serebryakova and Alexey V. Zaikovskii

Abstract The present research aims of elaborating a new manufacturing technology of magnetic nanoparticles for ferrofluid applications. Composite Fe–C anode sputtering in a low-pressure arc discharge has been used to produce Fe-containing nanoparticles on a carbon matrix. The chemical composition and size distribution function of iron containing nanoparticles have been measured. The sizes of Fe-containing nanoparticles are of 3–12 nm: chemical composition includes iron and iron carbide. It was shown that the powder is a superparamagnetic material. The stable ferrofluid, based on synthesised magnetic nanoparticles on a carbon matrix in water with nonoxynol-9 as surfactant, has been manufactured. The value of saturation magnetization on the level of 30 KA/m has been obtained.

1 Introduction

The studies of the plasma-arc method for the synthesis of magnetic nanoparticles, encapsulated into the carbon coating, started from the paper [1] on the fullerene synthesis. The discovery of a possibility to encapsulate the atoms and nanocrystals by the fullerene structures [2] allowed the start of a study on the magnetic properties of encapsulated atoms at the example of gadolinium carbide [3]. The plasma-arc synthesis and systematic studies of the magnetic properties of nanoparticles obtained by spraying the composite "graphite-transition metal" electrodes, were performed in the work of [4]. The works on the synthesis of magnetic nanoparticles in a carbon coating by the electric arc method are continued. This method uses the DC electric carbon arc with a hot cathode in the atmosphere of inert gas of the reduced pressure. Metal precursors are usually put into a cavity drilled in a graphite electrode, and then they are sprayed together with graphite. Under these conditions, the discharge is maintained by thermal emission of electrons from the cathode. The high temperatures in the zone of arc glow lead to thermal spraying of the anode

S.A. Novopashin (✉) · M.A. Serebryakova · A.V. Zaikovskii
Kutateladze Institute of Thermophysics, Novosibirsk, Russia
e-mail: sanov@itp.nsc.ru

A.Y. Oral and Z.B. Bahsi Oral (eds.), *3rd International Multidisciplinary Microscopy and Microanalysis Congress (InterM)*, Springer Proceedings in Physics 186,
DOI 10.1007/978-3-319-46601-9_18

material. The flow of high-temperature atomic spray products into the buffer gas medium occurs. Diffusion and turbulent mixing of outflowing products with the buffer gas results in cooling, processes of heterogeneous condensation and chemical reactions of the spray products. As a result, the metal particles "packed" into the carbon material are formed. The determining parameters of the synthesis are the pressure and type of the buffer gas, current and discharge voltage, electrode geometry and composition, molar content of the precursor in the sprayed electrode. Varying these parameters, we can control the morphology and chemical composition of the synthesized particles. The pressure of the buffer gas is one of the most important parameters that determine the rate of cooling and kinetics of condensation processes and chemical reactions, which allows the control of an average size of nanoparticles [5]. Usually, the synthesis of nanoparticles is implemented in the inert gas atmosphere. The presence of oxygen in the reactor leads to undesirable oxidation of the graphite electrode. Therefore, the synthesis of metal oxide nanoparticles is performed in two stages. At the first stage, the metal nanoparticles are synthesized on the carbon matrix and at the second stage; synthesized material is annealed in the oxygen atmosphere. The second stage allows oxidation of the metal particles and removal of the carbon material in the form of carbon oxides [6]. The disadvantages of this method are low productivity, broad function of nanoparticles distribution by sizes, and heterogeneity of the carbon coating thickness. Moreover, as usual, the mixture various forms of carbon is synthesized and it is difficult to separate the product from the impurities [7]. Typically, the composite material consisting of graphite and pure metal is used as the sprayed anode, but the plasma-arc method synthesizes nanoparticles from the complex chemical compounds at their spraying and pyrolysis. This ability is demonstrated in experiments [8] on the synthesis of bimetallic magnetic nanoparticles with the use of double salts as the precursors.

The interest in preparation and study of magnetic nanoparticles covered by an inert shell [9, 10] is connected with both the possibility of preventing the coagulation and oxidation of magnetic nanoparticles and the need to ensure biocompatibility in medical applications [11, 12], as well as during their storage and transport in the form of a powder for ferrofluid application. Moreover, at laboratory investigations the presence of magnetic powder can quickly change the magnitude of magnetic properties of fluid and the base fluid itself at application of corresponding surfactants. The magnetic nanoparticles in the coatings of silica dioxide [13], polymers [14], and carbon [3, 4] are the most studied for the synthesis. In this paper we present results of morphology, chemical composition, and magnetic properties of arc discharge Fe–C soot for ferrofluid applications.

2 Experimental

The arc plasma reactor (Fig. 1) is vacuum chamber 1, which can be evacuated to the pressure of 10^{-2} torr and then filled with inert gas to the pressure of 3–500 torr. There are two electrodes in the reactor, and the arc glows between these electrodes in the inert gas atmosphere. Mobile electrode 2 is a graphite pellet with the diameter of 20 mm, immobile electrode (anode) 3 is a rod of 7-mm diameter and 70-mm length. This construction allows variation of a distance between the electrodes and maintenance of the conditions of arc glow. The electrode is moved by bellows unit of translation transfer 4. To introduce the current into the reactor, high-current metal-ceramic hermetic input 5 is used. Around the electrodes, there is copper water-cooled circuit 6. Inside, there is removable stainless steel screen 7 for collecting the synthesized products.

The source of DC current (80–140 A) was used for the arc discharge. Depending on the distance between the electrodes, the voltage obtained on the arc is 20–30 V. The anode is the graphite rod with an axial hole (diameter of 4.2 mm), filled with the iron-graphite powder in a weight ratio of 2:1. Anode spraying leads to the formation of the atomic components of carbon and iron in the arc. Diffusion and convection of atomic components in the buffer gas lead to cooling, heterogeneous condensation and chemical reactions. Then, the products of condensation are deposited on the cooled screen. The synthesized material consists of the nanoparticles of iron and iron carbide on the carbon matrix. The determining parameters of synthesis are geometric and composition of electrodes, buffer gas and its pressure, and electric characteristics of discharge.

All experiments were carried out at a discharge current of 100 A in helium at pressure of 50 torr.

TEM, XRD and magnetic measurements were used to test the material properties. High-resolution TEM images were obtained using a JEM-2010 electron microscope (JEOL, Japan) with lattice-fringe resolution of 0.14 nm and accelerating voltage of 200 kV. The high-resolution images of periodic structures were analyzed by the Fourier method. Local energy-dispersive X-ray analysis (EDXA) was carried out using an EDX spectrometer (EDAX Co.), fitted with a Si

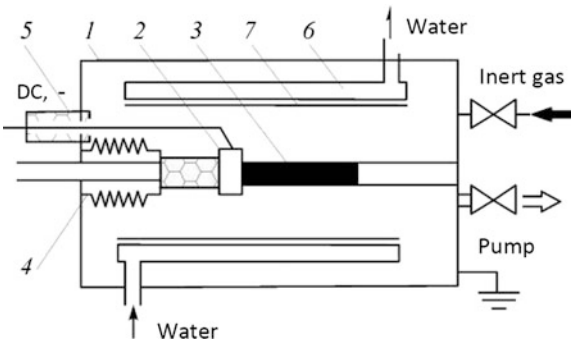

Fig. 1 Experimental setup

(Li) detector, at a resolution of 130 eV. The samples for the HRTEM study were prepared on a perforated carbon film mounted on a copper grid. XRD analysis was carried out using a Bruker D8 Advance diffractometer, equipped with a Lynxeye (1D) linear detector, over the angular range of 10–75° at $2\Theta = 0.05°$ with the storage time of 1 s for each point. Monochromatic CuK-radiation (1.5418 °A) was applied in these experiments. Magnetic susceptibility was measured by an MS2 susceptibility/temperature system (Bartington, Great Britain) and SQUID magnetometer MPMSXL (Quantum Design).

3 Results

Transmission electron microscopy of the synthesized material indicated that it consisted of the iron-containing nanoparticles (see Fig. 2) embedded into the amorphous carbon matrix. The function of size distribution of nanoparticles is shown in Fig. 3. The solid line is the logarithmically normal approximation. The average size of particles is 7 nm.

XRD spectroscopy shows that Fe–C soot consists of graphite, iron, and iron carbide (see Fig. 4).

Magnetic susceptibility was measured in wide range of frequencies (63 Hz–16 kHz). Figure 5 shows logarithmic decreasing of magnetic susceptibility with frequency. Magnetization curve is shown on Fig. 6. Saturation value of about 50 G cm^3/g is reached at magnetic field of about 10^4 Oersted. No hysteresis has been observed at room temperature. Analysis of the magnetization curve near the zero external magnetic field shows that the residual magnetization is zero, i.e., the synthesized material is a superparamagnetic.

To synthesize ferrofluids, we used ultrasonic dispersion synthesized material in water during an hour. Stable ferrofluid was manufactured with the use of nonoxynol-9 as surfactant. For mass fraction of magnetic material of 30 %, the value of saturation magnetization on the level of 30 KA/m has been obtained.

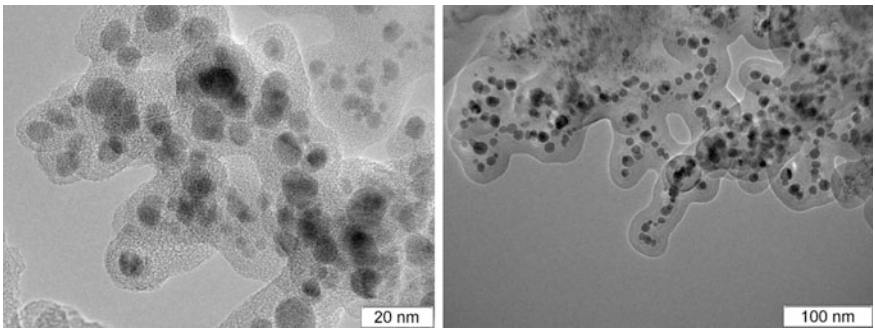

Fig. 2 The morphology of the synthesized material

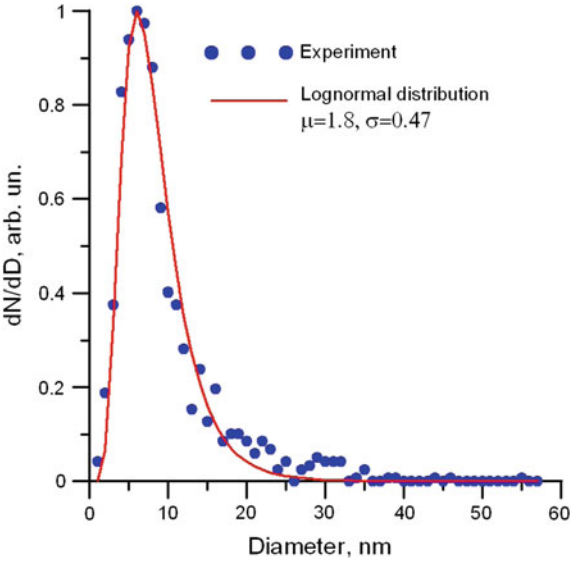

Fig. 3 Size distribution function

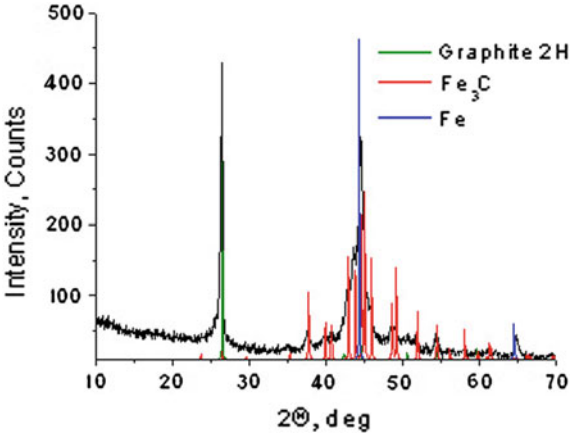

Fig. 4 XRD spectrum of synthesized material

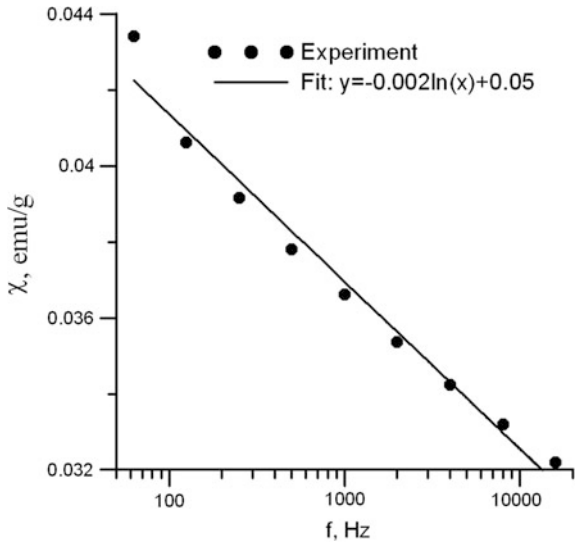

Fig. 5 Magnetic susceptibility at different frequencies

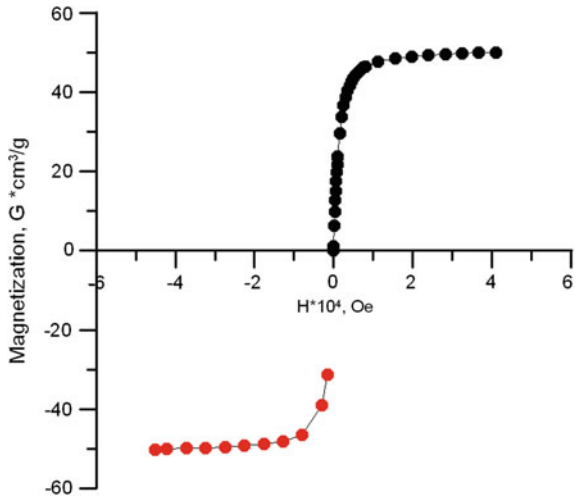

Fig. 6 Magnetization of Fe-C soot

4 Conclusion

Composite Fe–C anode sputtering in a low pressure arc discharge has been used to produce Fe-containing nanoparticles on a carbon matrix. The chemical composition of the synthesized material consists of carbon soot, graphite, iron, and iron carbide. Size distribution function of iron containing nanoparticles is lognormal with maximum at about 7 nm. Relaxation processes of magnetization resulted in logarithmic decreasing of magnetic susceptibility with frequency. The dependency of

magnetization on magnetic field showed no hysteresis. It means that synthesized material is superparamagnetic. The stable ferrofluid, based on synthesised magnetic nanoparticles on a carbon matrix in water with nonoxynol-9 as surfactant, has been manufactured. The value of saturation magnetization on the level of 30 KA/m has been obtained.

Acknowledgments This research was funded by Russian Scientific Foundation, Project No №14-19-01379

References

1. Kratschmer, W., Lamb, L.D., Fostiopoulos, K., Hoffman, D.R.: Solid C-60—a new form of carbon. Nature **348**, 354–358 (1990)
2. Yannoni, C.S., Hoinkis, M., de Vries, M.S., et al.: Scandium clusters in fullerene cages. Science **256**, 1191–1192 (1992)
3. Majetich, S.A., Artman, J.O., McHenry, M.E., et al.: Preparation and properties of carbon coated magnetic nanoparticles. Phys. Rev. B. **48**, 16845–16848 (1993)
4. Brunsman, E.M., Sutton, R., Bortz, E., et al.: Magnetic properties of carbon coated, ferromagnetic nanoparticles produced by carbon-arc method. J. Appl. Phys. **75**, 5882–5884 (1994)
5. Maltsev, V.A., Novopashin, S.A., Nerushev, O.A., Cakhapov, C.Z., Smovzh, D.V.: Synthesis of metal nanoparticles on a carbon matrix. Nanotechnol. Russ. **2**(5, 6), 85–89 (2007)
6. Gulyaev, R.V., Slavinskaya, E.M., Novopashin, S.A., Smovzh, D.V., Zaikovskii, A.V., Osadchii, DYu., Bulavchenko, O.A., Korenev, S.V., Boronin, A.I.: Highly active PdCeOx composite catalysts for low-temperature CO oxidation, prepared by plasma-arc synthesis. Appl. Catal. B **147**, 132–143 (2014)
7. Faraji, Y.Y., Rezaee, M.: Magnetic nanoparticles: synthesis, stabilization, functionalization, characterization, and applications. J. Iran. Chem. Soc. 7(1), 1–37 (2010)
8. Filatov, EYu., Novopashin, S.A., Korenev, S.V.: Co–Pt and Fe–Pt bimetallic nanoparticles in a carbon matrix are prepared by a plasma arc process. Russ. J. Inorg. Chem. **58**(1), 78–83 (2013)
9. Gegechkori, T., Mamniashvili, G., Kutelia, E., et al.: Technology for production of magnetic carbon nanopowders doped with iron and cobalt nanoclusters. J. Magn. Magn. Mater. **373**, 200–206 (2015)
10. Chaitoglou, S., Reza Sanaee, M., Aguiló-Aguayo, N., Bertran, E.: Arc-discharge synthesis of iron encapsulated in carbon nanoparticles for biomedical applications. J. Nanomater. Article ID 178524, 8 p (2014)
11. Macková, H., Horák, D., Donchenko, G.V., et al.: Colloidally stable surface-modified iron oxide nanoparticles: Preparation, characterization and anti-tumor activity. J. Magn. Magn. Mater. **380**, 125–131 (2015)
12. Sharifi, I., Shokrollahi, H., Amiri, S.: Ferrite-based magnetic nanofluids used in hyperthermia applications. J. Magn. Magn. Mater. **373**, 903–915 (2012)
13. Odenbach, S.: Colloidal Magnetic Fluids. Springer, Berlin (2009)
14. Cornell, R.M., Schertmann, U.: The Iron Oxides: Structure, Properties, Reactions, Occurrence and Uses. VCH, Weinheim (1996)

Exploration of Carbon Based Solid Acid Catalyst Derived from Corn Starch for Conversion of Non-edible Oil into Biodiesel

Judy R.B. Witono, Ken Hashigata, Herry Santoso and Inge W. Noordergraaf

Abstract To avoid the problems caused by free fatty acids in the conversion of low cost vegetable oils to biodiesel, the use of solid acid catalyst for (trans-) esterification reaction is considered. Such a catalyst could be produced eco-friendly by using renewable raw materials such as biomass. The use of starch for this purpose it still very limited. In this paper, various methods were explored to produce a solid acid catalyst from corn starch. We investigated two different carbonization methods: complete pyrolysis in an oxygen-free environment and hydrothermal carbonization at milder conditions. Starch was used either in the native form or as pregelatinized starch. After the carbonization, acidic sites were introduced by sulfonating the materials. To characterize the catalysts, Scanning Electron Microscopy (SEM) was applied while the sulfonic content was determined by Energy Dispersive X-ray Spectroscopy (EDS). To test the performance of the catalysts, the conversion of free fatty acids was determined using oleic acid as a representative component of biodiesel feedstock. By both of the carbonization methods, a catalyst can be obtained that shows up to 84 % conversion of oleic acid. The hydrothermal treatment may then be preferred since it can be done at milder conditions. Differences between the performances of the respective catalyst samples could be well explained by structural features seen in the SEM-pictures. These also have

J.R.B. Witono (✉) · K. Hashigata · H. Santoso
Chemical Engineering Department, Parahyangan Catholic University, Bandung, Indonesia
e-mail: judy@unpar.ac.id

K. Hashigata
e-mail: hgt_ken@yahoo.com

H. Santoso
e-mail: hsantoso@unpar.ac.id

I.W. Noordergraaf
Chemical Engineering Department, University of Groningen, Groningen, The Netherlands
e-mail: i.w.noordergraaf@rug.nl

A.Y. Oral and Z.B. Bahsi Oral (eds.), *3rd International Multidisciplinary Microscopy and Microanalysis Congress (InterM)*, Springer Proceedings in Physics 186,
DOI 10.1007/978-3-319-46601-9_19

their effect on the amount of sulfonic groups that was found (from EDS). The general trend is logical: the catalysts with a higher sulfonic load give a higher conversion of oleic acid.

1 Introduction

In this era, the amount of oil reserves in the world is no longer abundant. Also there is ever increasing concern about the climate and the environment. Consequently, there is a need to look for renewable alternatives for the diesel fuels derived from mineral oil. One of the promising substitutes is called *biodiesel*. Biodiesel is a diesel that is derived from triglycerides that are present in many vegetable oils. Apart from the renewable aspect, biodiesel also has several advantages when used as a fuel compared with the conventional diesel. It has lower CO emission, better lubricating effect, it is free of sulfur and also shows much lower dust emissions [1–3].

However, there is a problem in producing biodiesel. Using clean oil with high quality is expensive to produce. Moreover, such clean oil used in biodiesel production is in severe competition with human's other daily needs, food in particular. For this reason, non-edible oils are being used instead of clean oil as raw materials. But using non-edible oil has its own issues. The high free fatty acids (FFA) content in such oils causes saponification with base catalyst during the transesterification reaction [3, 4]. Therefore expensive feed treatment (e.g. esterification of the FFA) is required to remove these fatty acids or to provide anhydrous reaction conditions. However, the alternative to use strong acid catalyst is attractive since by performing esterification in situ, such catalysts are less sensitive to FFA. Although they need more reaction time and perhaps higher temperature, acid catalysts can produce biodiesel from low-cost feedstocks [5].

Earlier, homogenous acid catalysts like sulfuric acid were used as acid catalyst to process feedstocks with high FFA content. But using homogenous catalyst caused several problems, such as corrosion [4, 6] and difficult separation of the product from the acid. In order to eliminate this problem, heterogeneous acid catalysts are being developed [5]. Carbon based acid catalyst is one of the promising candidates for a heterogeneous acid catalyst, because of its eco-friendly properties and effectiveness in the esterification reaction. Many kind of the biomasses have been used as raw materials in synthesizing the carbon based acid catalyst such as D-glucose, sucrose, cellulose and (limited) starch [3, 6] through carbonization [7–10] and hydrothermal carbonization (HTC) [11, 12]. But to obtain the simple process with low energy applied and catalyst that can be reused many times, the research should be developed more.

In this paper, the use of corn starch in its native and pre-gelatinized condition is explored as a raw material in synthesizing carbon based solid acid catalyst. For carbonization, two methods that were used, pyrolysis and hydrothermal

carbonization (HTC) with milder conditions. After the carbonization process, the product was then sulfonated with sulfuric acid solution (98 %) to add SO_3H groups, the active site of the catalyst, to the carbon chain. The resulting catalysts were tested with esterification of oleic acid, to determine their performance in a realistic biodiesel-feedstock reaction system. The application of Scanning Electron Microscopy (SEM) allowed for a visual impression of the carbonaceous materials thus produced. Energy Dispersive X-ray Spectroscopy (EDS) was used to analyze the content of sulfonic groups obtained in the final catalyst.

2 Experimental

2.1 Gelatinization of Corn Starch

50 g of corn starch was added to 500 mL water. The mixture was then heated to 75 °C for 25 min to achieve complete gelatinization. The resulting mixture was then dried overnight with at 80 °C.

2.2 Carbonization of the Starch

For pyrolysis, 45 g of native (PN400) or pre-gelatinized (PG400) starch was heated at 400 °C for 15 h under nitrogen flow. The product was a carbonaceous powder with a black color. For hydrothermal carbonization, 100 gr of starch was added into 200 mL water. The mixture was heated to 75 °C for 25 min (gelatinization). The resulting mixture was added to a pressurized reactor and heated for 24 h at 180 °C. The resulting product was then filtered and washed with ethanol and then water. The product was then dried overnight at 80 °C (HTCG). As an alternative, 100 gr of starch with 200 mL of water added directly to the pressurized reactor without gelatinization (HTCN).

2.3 Sulfonation

For all carbonized samples the same sulfonation procedure was applied. 12 g of the carbonaceous powder was added to 100 mL of 97 % concentrated sulfuric acid and heated to 150 °C. The resulting catalyst was filtered and washed with water. The cleaned catalysts were then dried overnight in the oven at 80 °C.

2.4 Esterification of Oleic Acid

In each case, 1.5 g of the resulting catalyst was reacted with 28.5 g of oleic acid and 32.3 g of methanol at 60 °C for 5 h. Oleic acid has been used for testing the catalyst

in this work since it a good example of the free fatty acids (FFA) that can occur in vegetable oil used as a feedstock for biodiesel. Conditions were chosen such that the molar oleic acid to methanol ratio is 1:10 while catalyst mass is 5 % of the oleic acid mass. The resulting mixture was then separated from the catalyst with a centrifuge. After that, the liquid phase was separated from the remaining methanol in a separatory funnel. The resulting oil-like liquid was then washed with warm water to ensure complete removal of residual methanol.

2.5 FFA Contents Analysis

1 mL of the resulting oil from the esterification reaction was mixed with 10 mL isopropyl alcohol and some drops of phenolphthalein indicator. The mixture was then titrated with KOH solution and the content of free fatty acids (FFA) can be calculated.

2.6 SEM and EDS Analysis

The structural aspects of the produced catalyst samples were examined with Scanning Electron Microscopy (SEM). Energy Dispersive X-ray Spectroscopy (EDS) was used to determine the sulfur content of the materials. Since there is no other source of sulfur in the material, the amount of sulfonic groups can immediately be calculated from the sulfur content. The instrumental analyses were done in commission at Institut Teknologi Bandung (ITB).

3 Results and Discussion

3.1 Conversion FFA for the Different Catalysts

Pure oleic acid is used, so the conversion can directly be calculated from titration analysis after the esterification reaction. Table 1 shows the conversion and the FFA content left in the product, for each of the solid acid catalysts.

Table 1 %-Conversion of FFA by the catalyst

Sample code	FFA remaining (%)	Conversion (%)
PN400	16.5	83.5
PG400	58.6	41.4
HTCN	21.3	78.7
HTCG	15.2	84.7

From Table 1, it can be seen that the best results are obtained with catalysts obtained from hydrothermal treatment of gelatinized starch (HTCG) and the product of pyrolysis of native starch (PN400). Both of these products manage to reach well over 80 % conversion while the catalyst from hydrothermal treatment of native starch (HTCN) can only reach 78 % conversion. On the other hand, PG400, the catalyst obtained from pyrolyzed pre-gelatinized starch, cannot produce more than 42 % conversion.

For further understanding of these results, the information on the properties of the catalyst from the SEM and EDS analyses could be used. Figure 1 is the result of SEM analysis for catalyst PN400 and PG400, the catalyst carriers before sulfonation: the pyrolyzed starches. Figure 2 shows the SEM pictures of the hydrothermally treated materials. In all pictures, magnification is the same (500×).

Between the pyrolyzed starches, in Fig. 1 a clear difference can be seen in the carbonaceous structure that has developed. The sample derived from native starch has a fine morphology while the product from gelatinized starch tends to form an aggregate. This is in parallel with the behavior of gelatinized starch [13].

In Fig. 2, the catalyst carriers produced with hydrothermal treatment show even finer particle dispersion. Peculiarly, the result from gelatinized starch looks better here, in terms of an even finer morphology.

In Table 2 EDS results and calculated sulfonic group contents, and for comparison also the FFA-conversion are shown.

There appears to be at least a qualitative correlation between the visual appearance of the catalysts carriers and the amount of sulfonic groups that could be attached to the material. The PG400 sample, showing the tendency to form aggregates, has the lowest amount of sulfonic groups. The most finely dispersed materials shows the highest level of sulfonation. From Table 2, it can also be seen that the result of EDS analysis agrees with the result of the conversion of oleic acid: catalysts with higher amounts active sites produce a higher conversion percentage. That the correlation is not complete or quantitative, indicates that other factors will also affect the maximum conversion that can be obtained. For example pore size

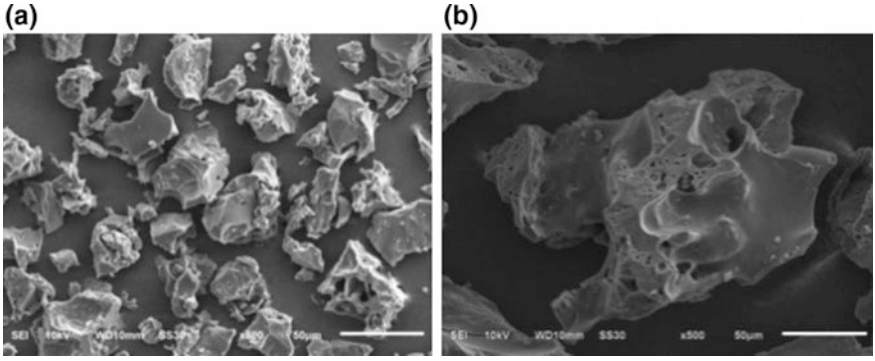

Fig. 1 SEM analysis **a** PN400 **b** PG400

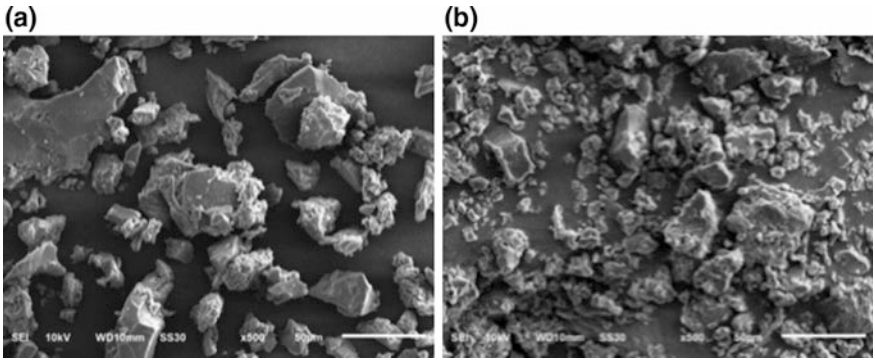

Fig. 2 SEM analysis **a** HTCN **b** HTCG

Table 2 Result of EDS analysis compared to conversion of FFA

Sample	%-wt. S	%-wt. SO_3H	%-Conversion of FFA
PN400	1.35	3.42	83.5
PG400	0.49	1.24	41.4
HTCN	0.69	1.75	78.7
HTCG	2.12	5.36	84.8

and -distribution will be important, as this can interfere with perhaps some steric hindrance effects towards oleic acid molecules. Such factors will need further investigation, in order to obtain the knowledge to develop the optimal catalyst carrier for this reaction. In a follow up project, for example BET-measurements could be included to study this aspect further. Still, almost 85 % conversion of oleic acid, as a benchmark for free fatty acids in biodiesel feed oil, is a promising result already from this first exploration of solid acid catalysts derived from starch.

3.2 Re-Use of the Catalyst

To check the stability of the catalyst, 'spent 'catalysts, that have been used already in an esterification reaction were recovered and tested again with at the same reaction conditions. The most promising materials HTCN and PN400 were recycled, which also allows for a comparison of the stability of catalyst produced from the hydrothermal carbonization and from pyrolysis. Table 3 below shows the results of the second reaction run.

Table 3 %-Conversion of oleid acid by fresh (1) and recycled (2) catalyst

Sample	Number of use	Conversion (%)
HTCN	1	78.7
	2	78.1
PN400	1	83.5
	2	83.5

It can be seen that both of the catalysts retain their conversion capacity in the second cycle. Therefore, it can be concluded that both of the catalysts are stable and there has been almost no leaching of active sites during the first esterification reaction. Of course, more cycles will be needed to test stability also in the longer term. But from these preliminary test results, it can be concluded already that both hydrothermal and pyrolysis carbonization can be used to synthesize a stable carbon based acid catalyst from renewable raw materials. Since the hydrothermal reaction can be conducted at milder conditions, this method is preferable for the production of solid acid catalyst from biomass. With hydrothermal treatment, starting with gelatinized starch gives the catalyst that shows the best FFA conversion.

4 Conclusions

A catalyst could be produced from both pyrolysis and hydrothermal carbonization of starches followed by sulfonation. It was demonstrated by using oleic acid as a test component that these catalysts can decrease the content of free fatty acids significantly by an esterification reaction. Both methods can produce catalysts that have high stability and show high conversion of oleic acid, up to 84 %. Since the performance is almost similar, the material that requires the mildest synthetic conditions should be preferred, which is the product from hydrothermal treatment. Then, starting with gelatinized starch gives a catalyst with slightly better performance. Differences between the conversion results of the respective catalyst samples could be correlated with the structural features that could be seen in SEM-pictures. The same factors, mainly the level of fine dispersion of the carbonized particles, also determine the amount of sulfonic groups that could be attached to the carbonized material. In turn, the sulfonic load has a direct and positive relation with the esterification performance.

References

1. Deshmane, C.A., Wright, M.W., Lachgar, A., Rohlfing, M., Liu, Z., Le, J., Hanson, B.E.: A comparative study of solid carbon acid catalyst for the esterification of free fatty acids for biodiesel production. Evidence for the leaching of colloidal carbon. Biosource Technol. **147**, 597–604 (2013)
2. Marchetti, J.M., Errazu, A.F.: Esterification of free fatty acids using sulfuric acid as catalyst in the presence of triglycerides. Biomass Bioenergy **32**, 892–895 (2008)
3. Lou, W.-Y., Zong, M.-H., Duan, Z.-Q.: Efficient production of biodiesel from high free fatty acid-containing waste oils using various carbohydrate-derived solid acid catalyst. Biosource Technol. **99**, 8752–8758 (2008)
4. Kang, S., Ye, J., Chang, J.: Recent Advances in Carbon-Based Sulfonated Catalyst: Preparation and Application, International Review of Chemical Engineering (I.RE.CH.E.), **5** (2) (2013)

5. Lotero, E., Liu, Y., Lopez, D.E., Suwannakarn, K., Bruce, D.A., Goodwin Jr., J.G.: Synthesis of biodiesel via acid catalysis. Ind. Eng. Chem. Res. **44**(14), 5353–5363 (2005)
6. Zhang, B., Ren, J., Liu, X., Guo, Y., Guo, Y., Guanzhong, L., Wang, Y.: Novel sulfonated carbonaceous materials from p-toluenesulfonic acid/glucose as a high-performance solid-acid catalyst. Catal. Commun. **11**, 629–632 (2010)
7. Liang Geng, Yu., Wang, Gang Yu., Zhu, Y.: Efficient carbon-based solid acid catalysts for the esterification of oleic acid. Catal. Commun. **13**, 26–30 (2011)
8. Xiao, H., Guo, Y., Liang, X., Qi, C.: One step synthesis of novel biacidic carbon via hydrothermal carbonization. J. Solid State Chem. **183**, 1721–1725 (2010)
9. Mar, W.W., Somsook, E.: Sulfonic—functionalized carbon catalyst for esterification of high free fatty acid. Procedia Eng. **32**, 212–218 (2012)
10. Zhenwu, F., Wan, H., Xiaoshuang, H., Cui, Q., Guan, G.: Preparation and catalytic performance of a carbon-based solid acid catalyst with high specific surface area. React. Kinet. Mech. Catal. **107**, 203–213 (2012)
11. Schneider, D., Escala, M., Supawittayayothin, K., Tippayawong, N.: Characterization of biochar from hydrothermal carbonization of bamboo. Int. J. Energy Environ. **2**(4), 647–652 (2011)
12. Zhang, W., Tao, H., Zhang, B., Ren, J., Guanzhong, L., Wang, Y.: One-pot synthesis of carbonaceous monolith with surface sulfonic groups and its carbonization/activation. Carbon **41**, 1811–1820 (2011)
13. Ratnayake, W.S., Jackson, D.S.: Gelatinization and Solubility of Corn Starch during Heating in Excess Water: New Insights, Faculty Publications in Food Science and Technology, paper 118 (2006)

Responses of Dendritic Cells to Different Coatings of Titanium

Natalia G. Plekhova, Irina N. Lyapun, Valentin B. Shumatov, Sergey V. Gnedenkov, Sergey L. Sinebryukhov, Artem V. Puz' and Evgenii V. Pustovalov

Abstract Significant inflammation of the tissues surrounding a fixed implant is associated with activation of dendritic cells (DC). In this work, the effect of surface modification of the titanium implants on the maturation of DC was examined. The method of formation of bioactive calcium-phosphate coating on commercially pure titanium VT1-0 by plasma electrolytic oxidation (PEO) has been developed. Plates without coating (Ti), with calcium phosphate coating formed by PEO (PEO Ti) and with hydroxyapatite coating obtained by boiling of the PEO coated samples in 20 % NaOH aqueous solution (HA PEO Ti) were used as samples. It was snowed that CD86 level on both PEO Ti and HA PEO Ti samples is higher than on the Ti sample. Furthermore, the method of Scanning Electron Microscopy showed that in the cells contacting with PEO Ti or HA PEO Ti samples the maturation processes of DCs were more rapid than on Ti sample. After a 24 h exposure to the Ti the percent DC recovery (recovered DCs/plated DCs) was not different ($p < 0.01$) from the other samples of Ti. Cells growing on Ti were small, round, flattened and lobulated, whereas those on PEO Ti and PEO HA Ti were larger with numerous microvilli and dendritic pseudopodia. These features of morphology cells pointed on the process

N.G. Plekhova (✉) · V.B. Shumatov
Central Scientific Research Laboratory, Pacific State Medical University, Vladivostok, Russia
e-mail: pl_nat@hotmail.com

I.N. Lyapun
Cell Biology and Histopathology Laboratory, Somov Institute of Epidemiology and Microbiology, Vladivostok, Russia
e-mail: irina-lyapun@list.ru

S.V. Gnedenkov · S.L. Sinebryukhov · A.V. Puz'
Institute of Chemistry Far-Eastern Branch Russian Academy of Sciences, Vladivostok, Russia
e-mail: referent@ich.dvo.ru

N.G. Plekhova · E.V. Pustovalov
School of Natural Sciences, School of Biomedical, Far Eastern Federal University, Vladivostok, Russia
e-mail: rectorat@dvfu.ru

A.Y. Oral and Z.B. Bahsi Oral (eds.), *3rd International Multidisciplinary Microscopy and Microanalysis Congress (InterM)*, Springer Proceedings in Physics 186,
DOI 10.1007/978-3-319-46601-9_20

of DCs maturation. Thus, it was demonstrated that the surface modification of Ti influences on the rate of DC maturation, and PEO HA Ti is less immunoreactive as compared to other samples.

1 Introduction

Titanium and its alloys are extensively applied for manufacturing dental and orthopedic implants and artificial joints, plates, and screws used in fracture fixation due to a unique combination of their physical, electrochemical, and mechanical properties (high ultimate strength limit, excellent corrosion resistance, wear resistance, high hardness, and low density) [1]. Numerous studies indicated that incorporation of hydroxyapatite in coating composition improves the biological performance of implants [2]. Plasma electrolytic oxidation (PEO) has been extensively used to form porous coatings on titanium alloys to enhance their bioactivity [3]. Bioactive layers containing hydroxyapatite can be formed [4, 5].

The critical role of innate immunity cells in inflammation induced osteoclastogenesis and subsequent bone loss were studied, thereby establishing a new paradigm of osteoimmunology [6–8]. The initial injury to the tissue surrounding the implant also induces an inflammatory response mediated by the cells of innate immunity, such as neutrophils, macrophages, and dendritic cells (DC). Cells adhered to the implant walls release reactive radicals, enzymes, and chemokines, which triggers a cascade of inflammatory responses [9]. DCs are the most potent antigen-presenting cells responsible for activation of native T cells and orchestration of the immune response, become critically situated at the osteo-immune interface [10]. DCs don't play a role in bone homeostasis at non-pathological conditions, but some data suggest that DCs could act as osteoclasts precursors in an inflammatory milieu through transformation into DC-derived-osteoclasts, according to phenotypic and functional characterization studies [11, 12].

A surface modification of titanium implant would enable to ensure better biocompatibility with the tissue and reduce inflammation and negative side effects at using metal implants without coating. Among the available electrochemical methods of coatings deposition on the metal implant surface, the most significant advantages are concerned with the method of plasma electrolytic oxidation [13, 14]. The PEO process yields the electrochemical synthesis of coatings containing both the oxidized metal and the electrolyte components on the metal surface.

Here, examined the effect of titanium with and without coating on the maturation of DCs.

2 Experimental

Rectangular plates (8 mm × 8 mm × 1 mm) of commercially pure titanium VT1-0 were used as the samples. For standardization, plates were ground with sandpaper until the roughness parameter R_a = 0.12 μm. After mechanical treatment, samples were thoroughly washed with deionized water and ethanol and dried in the air flow.

The electrolyte was prepared in 2 L of deionized water by adding the following components: 30 g/l of calcium glycerophosphate dehydrate $(C_3H_7CaO_6P)\cdot 2H_2O$ and 40 g/l of calcium acetate monohydrate $(Ca(CH_3COOO)_2\cdot H_2O)$. The electrolyte pH was adjusted to 10.9–11.3 by adding 20 % NaOH solution [14]. Plasma electrolytic oxidation was carried out using a reversible thyristor rectifier as power supply equipped with an automated control system with appropriate software. All the samples were treated in the unipolar PEO-mode at a current density of 0.67 A/cm$^{2.}$ The treatment time was 300 s and the final voltage was equal to 540 V.

The phase analysis was carried out using a D8 ADVANCE automatic X-ray diffractometer (BRUKER, Germany) with CuK_α radiation. Conventional Bragg–Brentano geometry was used for the scans within the 2θ range at an increment of 0.02° and 1 s time per step. The relative content of the phases in the coating was estimated as the ratio of the lines with the strongest intensity. X-ray patterns were analyzed with the EVA search program using the PDF-2 powder diffraction database.

Experimental series were carried out with the 2 sample coatings, which included calcium phosphate and hydroxyapatite $Ca_{10}(PO_4)_6(OH)_2$ on titanium substrate. The titanium samples were denoted in the text as: uncoated titanium—Ti; titanium with calcium-phosphate coating (Ca/P = 1.1)—PEO Ti, and titanium with the PEO-coating additionally treated by boiling in 20 % NaOH solution for 2 h and containing hydroxyapatite (Ca/P = 1.6) – HA PEO Ti. The samples were punched in the 6-well tissue culture polystyrene (TCPS) plates (Termo Fisher Scientific, Germany). The samples were sterilized in a laboratory oven (Thermo Scientific, Denmark) at 180 °C for 15 min (with controlling of surface properties), in accordance with the rules for sterilization of medical devices.

Bone marrow (BM) derived DCs were generated, as previously described, by Masoud et al. [15] with some modifications. Briefly, BM cells were removed from a male of guinea pig and cultured in 24-well-culture plates, at a concentration of 5×10^6 cells per well, in 800 μl of RPMI-1640 (Lonza, Belgium) supplemented with heat-inactivated 10 % fetal calf serum (FCS), 100 μg/ml of penicillin, 100 μg/ml of streptomycin, 5×10^{-5} m 2-mercaptoethanol (Lonza, Belgium) plus GM-CSF (50 ng/ml) and IL-4 (10 ng/ml). On days 3, 6, and 9 the supernatant was gently removed and replaced with the same volume of the supplemented medium. On day 9 of culture, ≈ 80 % of the cells were $CD11c^+$ DC.

For the differentiation assays, BM-derived DC were cultured as described above, in the presence of lipopolysaccharide of Escherichia coli (control, LPS, Sigma-Aldrich, USA) and modified coatings and titanium samples. The differentiated cells were harvested on days 3, 6, and 9 of culture, labelled with specific

antibodies (CD34 PE, CD14 FITC, CD80 PE, CD86 FITC, BioLegend, USA) and analyzed. For the maturation assays, the cells were differentiated, as was described earlier, but in the absence of titanium samples. On day 9, the cells were activated by the addition of LPS (1 μg/ml). Cells cultured with supplemented medium plus the recombinant cytokines were considered immature DC (controls). After 48 h of incubation, the cells were recovered and labeled with specific monoclonal antibodies, supernatants from all cell cultures (differentiation and maturation assays) were also collected and stored at −20 °C for cytokines assay. The mean fluorescence intensity (MFI) value for the $CD11^+$ cells expressing CD34, CD80 and CD86 was analyzed using a confocal scanning laser microscope (Zeiss, Germany) and an MACSQuant (Miltenyi Biotec, Germany) 3 lasers flow cytometer equipped with an argon laser (15 mV) source operating at 488 nm. The emission of fluorochromes was recorded through specific band-pass fluorescence filters: FITC, 525 nm (FL1); PE, 575 nm (FL2). Data were analysed using MACSQuantify™ Software 2.6 (Miltenyi Biotec GmbH). For immunophenotyping, gating was done on side scatter (SSC; ordinate). Nonviable (7-AAD-positive) cells were excluded from analysis. An average of 20 000 cells were collected per sample.

Cell viability was estimated at 24, 48, and 72 h using a mitochondrial colorimetric assay (MTT assay) by the percent of total lactate dehydrogenase (LDH) released. Briefly, in each well, 600 μL of culture medium was aspirated, leaving 400 μL, to which 40 μL of MTT solution (3-(4.5-dimethylthiazol 2-yl)-2.5-diphenyltetrazoliumbromide, Sigma) was added. The cells were incubated for 4 h. The upper medium was removed carefully, and the intracellular formazan was solubilized by adding 400 μL of dimethylsulfoxide to each well (Sigma-Aldrich, USA). The absorbance was measured at 570 nm. The results expressed as optical density (OD) were obtained for three different experiments from each surface modification.

The qualitative analysis of cell adhesion was determined at 1, 3, 6, and 9 days using the scanning electron microscope observation. Specimens were fixed using 2 % glutaraldehyde, dehydrated using a standard ethanol dehydration series, freeze-dried, and coated with gold using an ion coater. After the cells were cultured, the material surface was observed and photographed using scanning electron microscopy (SEM) was observed and photographed using scanning electron microscopy (Zeiss, ULTRA PLUS-40-50, Germany) after spraying, in accelerating voltage 5 kV.

3 Results and Discussion

For providing of sufficient progress in direction of formation coating formation on titanium implant, it is required to develop new economically sound methods of synthesis and deposition of hydroxyapatite on its. It is also considered as a promising biomaterial in its porous form improving mechanical compatibility of the implant to the bone tissue [16]. A passive oxide layer on the alloy surface ensures good biocompatibility and protects the metal substrate from an aggressive biological medium. The following methods are applied for the coatings formation:

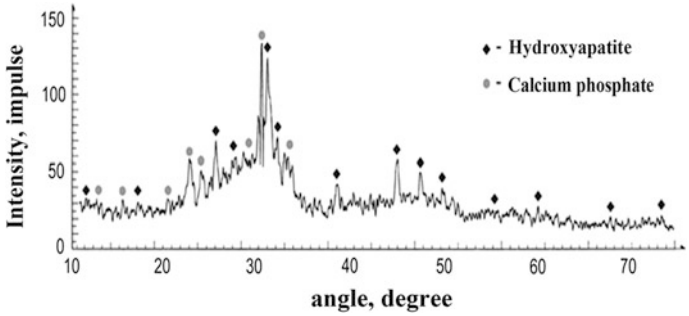

Fig. 1 Diffractogram of the sample VBT1-0 with hydroxyapatite coating obtained by boiling of PEO coated samples in 20 % solution (HA PEO Ti)

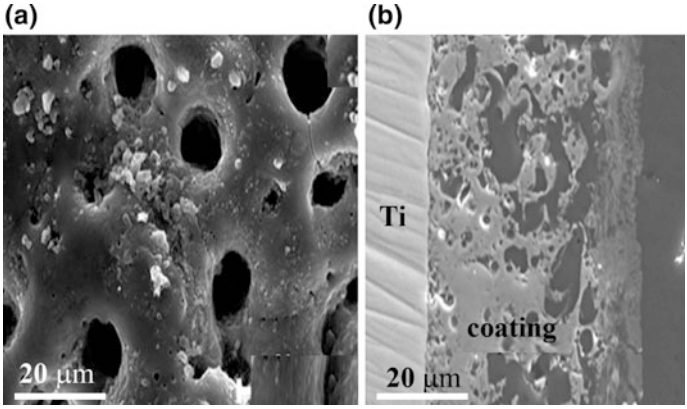

Fig. 2 SEM images of surface (**a**) and a cross-section (**b**) of the sample titanium VT1-0 with hydroxyapatite coating obtained by boiling of PEO coated samples in 20 % NaOH aqueous solution (HA PEO Ti)

sparc anodization, plasma spraying, thermal processing, pulse laser sintering, electrophoretic deposition, biomimetic deposition [17–20] etc. The developed method of the coatings formation using the method of PEO allows formation of bioactive calcium-phosphate coatings on titanium substrate. According to our experiments the coatings on titanium contained calcium and phosphorus at a ratio of (Ca/P = 1.6), which is comparable to that in the bone tissue (1.67). According to X-ray diffraction data, hydroxyapatite and calcium phosphates are present in the coating's chemical composition (Fig. 1). Based on the analysis of the data on the morphology of coatings obtained by means of atomic force, electronic, and optical microscopies, it can be concluded that the surface is developed and has pores, the presence of which is favorable for the ingrowth of bone into them and formation of a stronger implant-bone junction (Fig. 2a, b).

Innate immunity is the nonspecific and first line of the body's defense system, which relies on pattern recognition receptors (PRPs) to recognize broad and conserved molecular patterns found on pathogens (pathogen-associated molecular patterns, PAMPs) [21]. Therefore, the innate immune system plays an essential role in the early recognition and subsequent proinflammatory response. Different physical and chemical properties of coated titanium induce different cellular responses, such as cellular uptake and intracellular biodistribution, leading to the different immune responses [22, 23]. The morphology of DC after contact with Ti sample examined by SEM showed a spherical shape with an estimated size of 20 μm in diameter (Fig. 3a). In contact with PEO Ti and HA PEO Ti DCs were larger and have a long dendrite like pseudopodia, rough cell surface with many folds and different types of protrusions (Fig. 3b, c).

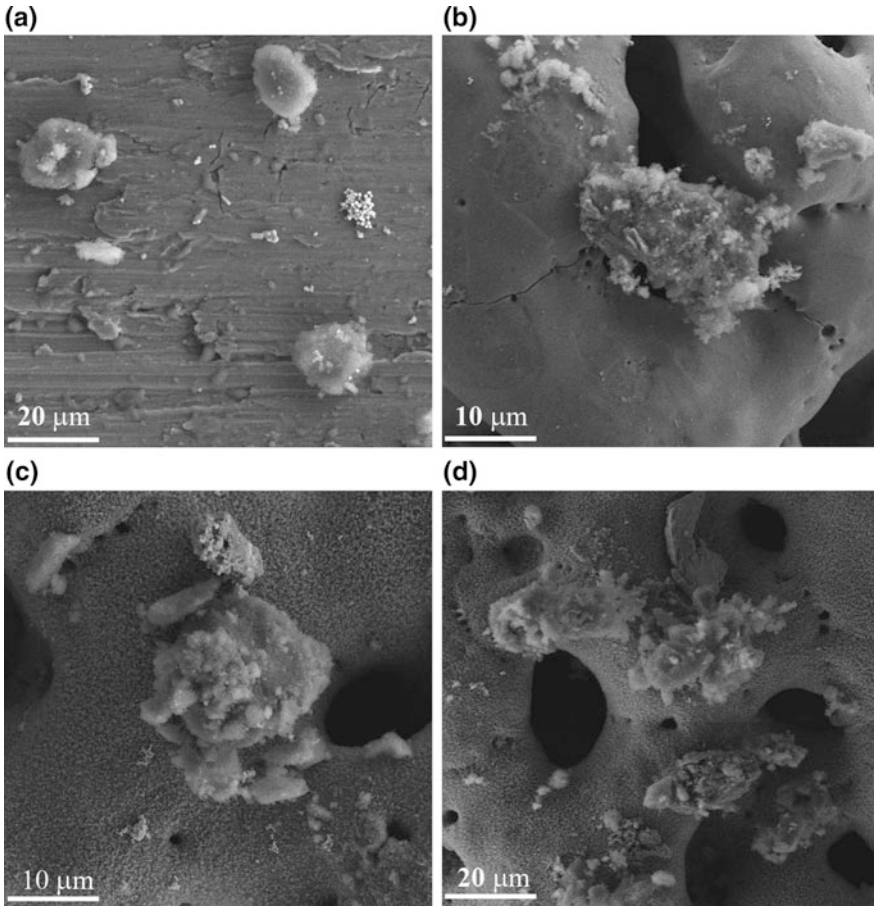

Fig. 3 SEM images of the cells on the surface of the Ti (**a**), PEO Ti (**b**) upon 3 days incubation and HA PEO Ti samples upon 3 days (**c**) and 6 days incubation (**d**)

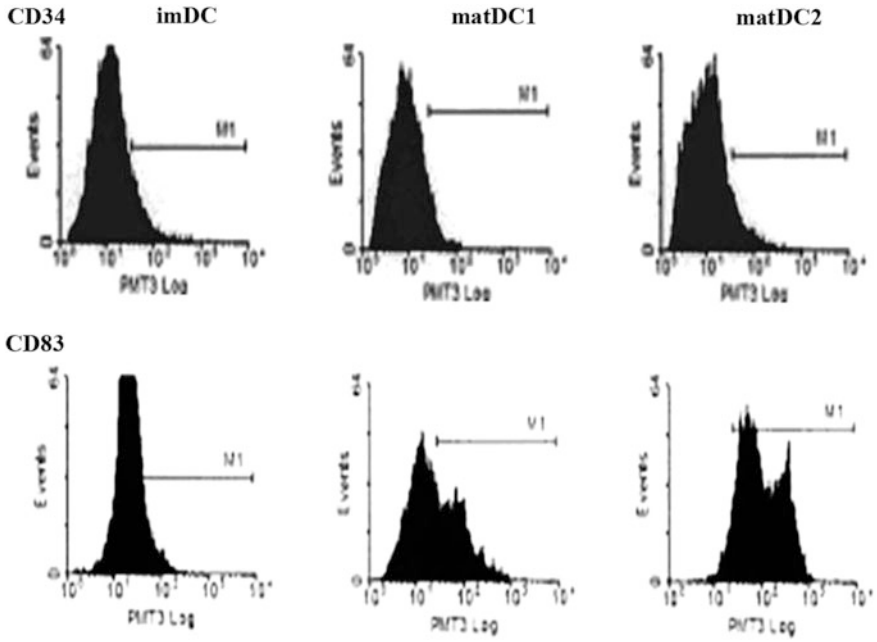

Fig. 4 The phenotype of DCs at different stages of maturation in vitro. BM-derived DCs were tested by flow cytometry and cultured with GM-CSF and IL-4 (1000 IU\l) for 6 days. Immature DC cultured in presence of IL-4 and another 3 days with either LPS, either HA PEO Ti to induce their maturation to matDC1 and matDC2 respectively. At the end of the population were collected and cells stained by fluorochrome. The analysis was performed by flow cytometry. Data of imDC and DC phenotype typical for more than five cellular cultures were presented

The expression of CD34, CD38 indicates the degree of differentiation and maturity of the DC. The $CD34^+$ cells in bone marrow are precursors of both the DC and granulocytes, and such cells are of the "intermediate" type. On the 6 day, under effect of the inductor, these cells capable in differentiation into DCs or leukocytes. In order to study the role of implants as inducers, the receptor phenotype of DC was analyzed. $CD34^+$ DC on 1 day of co-incubation with LPS was 72 ± 5.8 %, thereafter, their number by decreased 8.6 ± 0, 8 % (9 days). Under effect of samples implants, $CD34^+$ DC was lower as compared to the control (Fig. 4).

For the Ti samples it was 56 ± 4.8 % (1 day), while for the samples with PEO coated titanium PEO Ti it was 42 ± 4.6 % (Fig. 5). The minimum number of $CD34^+$ cells was found at the end of the observation period (21 days), and it is equal to 3.8 ± 0.2 % and 8.4 ± 0.6 % respectively. Under effect of LPS on the degrees of expression receptors on day 9, the indicator of $CD14^+$ DC was minimal against the maximum of $CD83^+$ (2.4 ± 0.2 % and 62.4 ± 0.6 %, Fig. 5a). In contact with titanium Ti sample, the number of $CD14^+$ cells in this period was 32 ± 2.1 % and $CD83^+$ 48 ± 2.6 % (Fig. 5), with coated titanium PEO Ti sample—26.4 ± 2.1 % and 52.6 ± 4.6 % and HA PEO Ti sample—21.3 ± 2.3 %

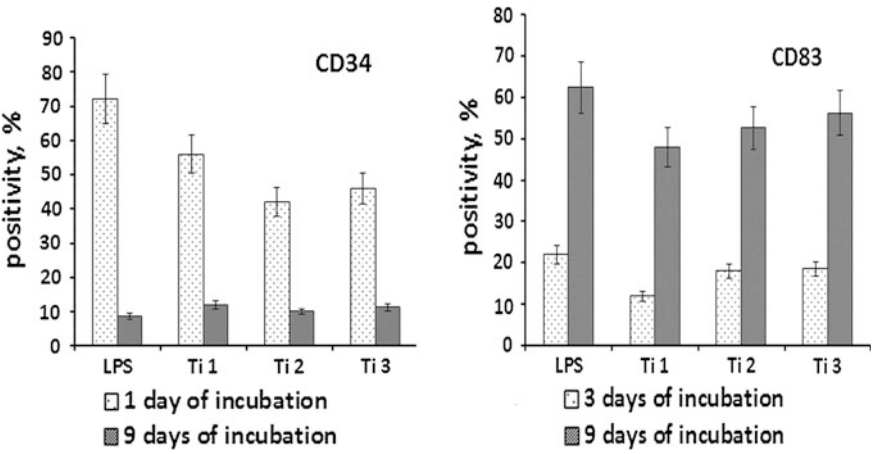

Fig. 5 The effect of LPS and Ti sample, on the expression of differentiation/maturation antigens on DC subsets. The surface expression of CD34, CD144 and DC maturation marker CD83 was examined by flow cytometry. The percentage of cell positivity is shown and is representative of three independent experiments

and 56.2 ± 4.2 %, respectively. These data indicate to the effect of coatings on titanium as inductors of DC differentiation.

The increased indicators of enzyme activity were detected in the initial period of DCs contact with samples. During this period, the difference was observed between indicators of enzymes depending on the sample type: the highest one was detected in cells contacted with Ti 2 and Ti 3 (2 and 3 days). Further these parameters decreased, thus showing the cells stabilization. Such a change in cell metabolism was associated with the components contained in coatings on titanium.

4 Conclusion

The DCs are considered the most potent antigens presentation cells and are essential in the understanding of regulatory mechanisms of immune system. They are the only cells to prime native T cells and initiate primary immune responses [24]. There exists an increasing interest in understanding the DC biology as they have the ability to modulate the immune response towards either specific effector functions or tolerance. Changing after contact with the implants of DCs functional state can be regarded as trigger factors of the inflammatory process that usually accompanied the introduction of a foreign material. In the present study, we explored the effects of uncoated titanium VT1-0; titanium with calcium-phosphate PEO-coating and with the coating comprising hydroxyapatite on the morphology and functional activity of innate immunity cells. A more expressed stimulation of adhesion and enzymes activity cells was detected in contact with hydroxyapatite containing

coating on titanium. Thus, the optimization of the enzyme reaction innate immune cells via the subsistence of titanium of bioactive osteogenesis coating is a prerequisite for a strong, long-term, and lasting fixation of implants in bone tissue. Products of cells released into the extracellular environment mediators, namely, pro- and anti-inflammatory cytokines, might contribute to intercellular signaling biochemical environment for the formation of the bone tissue on implant. Finally, coatings on titanium affect the functional state of cellular processes accompanying bone mineralization, especially in contact with calcium phosphate coating formed by the method of PEO.

Acknowledgments The work was financially supported by the Russian Science Foundation (project no. 14-33-00009) and the Government of Russian Federation (Federal Agency for Scientific Organizations).

References

1. Majeed, A., He, J., Jiao, L., Zhong, X., Sheng, Z.: Surface properties and biocompatibility of nanostructured TiO2 film deposited by RF magnetron sputtering. Nanoscale Res. Lett. **10**, 56 (2015) http://doi.org/10.1186/s11671-015-0732-7
2. Surmenev, R.A., Surmeneva, M.A., Ivanova, A.A.: Significance of calcium phosphate coatings for the enhancement of new bone osteogenesis—a review. Acta Biomater. **10**, 557 (2014). doi:10.1016/j.actbio.2013.10.036
3. Matykina, E., Arrabal, R., Skeldon, P., Thompson, G.E.: Transmission electron microscopy of coatings formed by plasma electrolytic oxidation of titanium. Acta Biomater., **5**, 1356 (2009) doi:10.1016/j.actbio.2008.10.007Ozeki, K., Goto, T., Aoki, H. Masuzawa, T.: Fabrication of hydroxyapatite thin films on zirconia using a sputtering technique. Biomed. Mater. Eng. **24**, 1793–802 (2014) doi:10.3233/BME-140990
4. Ozeki, K., Goto, T., Aoki, H., Masuzawa, T.: Influence of the crystallinity of a sputtered hydroxyapatite film on its osteocompatibility. Biomed. Mater. Eng. **26**, 139–147 (2015). doi:10.3233/BME-151560
5. Wilensky, A., Segev, H., Mizraji, G., Shaul, Y., Capucha, T., Shacham, M., Hovav, A.H.: Dendritic cells and their role in periodontal disease. Oral Dis. **20**(2), 119–126 (2014). doi:10.1111/odi.12122
6. Schlundt, C., Schell, H., Goodman, S.B., Vunjak-Novakovic, G., Duda, G.N., Schmidt-Bleek, K.: Immune modulation as a therapeutic strategy in bone regeneration. J. Exp. Orthop. **2**(1), 1 (2015). doi:10.1186/s40634-014-0017-6
7. Hienz, S.A., Paliwal, S., Ivanovski, S.: Mechanisms of bone resorption in periodontitis. J. Immunol. Res. 615486 (2015) doi:10.1155/2015/615486
8. Stanford, C.M.: Surface modification of biomedical and dental implants and the processes of inflammation, wound healing and bone formation. Int. J. Mol. Sci. **11**(1), 354–369 (2010) doi:10.3390/ijms11010354
9. D'Amelio, P., Fornelli, G., Roato, I., Isaia, G.C.: Interactions between the immune system and bone. World J. Orthop. **2**(3), 25–30 (2011) doi:10.5312/wjo.v2.i3.25
10. Venkatesan, G., Uppoor, A., Naik, D.G.: Redefining the role of dendritic cells in periodontics. J. Indian Soc. Periodontol. **6**, 700–705 (2013). doi:10.4103/0972-124X.124467
11. Dalal, A., Pawar, V., McAllister, K., Weaver, C., Hallab, N.J.: Orthopedic implant cobalt-alloy particles produce greater toxicity and inflammatory cytokines than titanium alloy and zirconium alloy-based particles in vitro, in human osteoblasts, fibroblasts, and macrophages. J. Biomed. Mater. Res. A **100**, 2147–2158 (2012). doi:10.1002/jbm.a.34122

12. Legostaeva, E.V., Egorkin, V.S., Sinebryukhov, S.L., Eroshenko, AYu., Lyamina, G.V., Komarova, E.G.: Nanostructred titanium: structure, mechanical and electrochemical properties. Inorg. Mater. **5**, 44 (2014)
13. Gnedenkov, S.V., Sinebryukhov, S.L., Zavidnaya, A.G., Egorkin, V.S., Puz', A.V., Mashtalyar, D.V.: Composite hydroxyapatite-PTFE coatings on Mg-Mn-Ce alloy for resorbable implant applications via a plasma electrolytic oxidation-based route. J. Taiwan. Inst. Chem. Eng. **45**, 3104 (2014)
14. Masoud, R., Bizouarn, T., Trepout, S., Wien, F., Baciou, L., Marco, S., Houée Levin, C.: Titanium dioxide nanoparticles increase superoxide anion production by acting on NADPH oxidase. PLoS ONE **10**(12), e0144829 (2015). doi:10.1371/journal.pone.0144829
15. Li, F., Li, J., Kou, H., Huang, T., Zhou, L.: Compressive mechanical compatibility of anisotropic porous Ti6Al4 V alloys in the range of physiological strain rate for cortical bone implant applications. J. Mater. Sci.: Mater. Med. **26**, 233 (2015) doi:10.1007/s10856-015-5565-5
16. Sharma, A., McQuillan. A.J., Sharma, L.A., Waddell, J.N., Shibata, Y., Duncan, W.J.: Spark anodization of titanium–zirconium alloy: surface characterization and bioactivity assessment. J. Mater. Sci.: Mater. Med. **26**, 221 (2015) doi:10.1007/s10856-015-5555-7
17. Vahabzadeh, S., Roy, M., Bandyopadhyay, A., Bose, S.: Phase stability and biological property evaluation of plasma sprayed hydroxyapatite coatings for orthopedic and dental applications. Acta Biomaterialia. **17**, 47–55 (2015) http://doi.org/10.1016/j.actbio.2015.01.022
18. Cleries, L., Martınez, E., Fernandez-Pradas, J., Sardin, G., Esteve, J., Morenza, J.: Mechanical properties of calcium phosphate coatings deposited by laser ablation. Biomaterials **21**, 967–971 (2000)
19. Ciobanu, G., Ciobanu, O.: Investigation on the effect of collagen and vitamins on biomimetic hydroxyapatite coatingformation on titanium surfaces. Mater. Sci. Eng. C Mater. Biol. Appl. **33**(3), 1683–1688 (2013) doi:10.1016/j.msec.2012.12.080
20. Luo, Y.-H., Chang, L.W., Lin, P.: Metal-based nanoparticles and the immune system: activation, inflammation, and potential applications. BioMed Research International. 143720 (2015) doi:10.1155/2015/143720
21. Goodman, S., Konttinen, Y.T., Takagi, M.: Joint replacement surgery and the innate immune system. J. Long Term Eff. Med. Implants **24**(4), 253–257 (2014)
22. Nich, C., Takakubo, Y., Pajarinen, J., Ainola, M., Salem, A., Sillat, T., Rao, A.J., Raska, M., Tamaki, Y., Takagi, M., Konttinen, Y.T., Goodman, S.B., Gallo, J.: Macrophages—key cells in the response to wear debris from joint replacements. J. Biomed. Mater. Res. A. **101**(10), 3033–3045 (2013). doi:10.1002/jbm.a.34599
23. Landgraeber, S., Jäger, M., Jacobs, J.J., Hallab N.J.: The pathology of orthopedic implant failure is mediated by innate immune system cytokines. Mediators Inflamm. 185150 (2014) doi:10.1155/2014/185150
24. Iwasaki, A., Medzhitov, R.: Control of adaptive immunity by the innate immune system. Nature Immunology. **16**(4), 343–353 (2015) http://doi.org/10.1038/ni.3123

Microscopy of a Goatskin Bag Cheese "Bouhezza"

O. Aissaoui Zitoun, S. Carpino, N. Fucà, M.L. Mansour, H. Attia and M.N. Zidoune

Abstract Scanning electron microscopy and confocal laser scanning microscopy (CLSM) were used to visualize changes in the microstructure of a goatskin bag cheese "Bouhezza" during manufacturing and ripening. The exceptional cheese-making process is based on the successive addition of salted fermented milk "Lben" in the goatskin bag for few weeks and then adding raw milk at the end of ripening. The SEM observation shows a proteinic aggregates organised in an open space matrix in which lipids and whey are entrapped in the proteinic mass. We observe the limits of micelles where caseins are not completely fused between them. During the manufacturing the semi-liquid structure of the Lben change to a gel structure and the formed cheese grows rich out of proteins and its structure becomes denser, specially marked enter the first and the third week of manufacturing. Then and to 6 weeks, the structure of cheese does not changed and the proteinic network became just more dense. This structure allows the continuous draining of the whey through the perforations of the goatskin. The CLSM shows the same observation.

O. Aissaoui Zitoun (✉) · M.N. Zidoune
INATAA, Laboratory of Nutrition and Food S Technologies,
University Frères Mentouri Constantine 1, Route Ain El Bey, Constantine, Algeria
e-mail: azouarda@yahoo.fr

M.N. Zidoune
e-mail: zidounem@yahoo.fr

S. Carpino · N. Fucà
CoRFiLaC, Regione Siciliana, s.p. 25 km 5, Ragusa Mare, Italy
e-mail: carpino@corfilac.it

N. Fucà
e-mail: fuca@corfilac.it

M.L. Mansour
Faculté des Sciences de la Nature et de la Vie, Université Ferhat Abbas, Setif, Algeria
e-mail: mlyndamaya@yahoo.fr

H. Attia
Unité d'Analyses Alimentaires - École Nationale d'Ingénieurs, Sfax, Tunisie
e-mail: Hamadi.Attia@enis.rnu.tn

A.Y. Oral and Z.B. Bahsi Oral (eds.), *3rd International Multidisciplinary Microscopy and Microanalysis Congress (InterM)*, Springer Proceedings in Physics 186,
DOI 10.1007/978-3-319-46601-9_21

Fat globules were less in the first weeks of manufacturing and at the end their distribution appears to be homogenous in the protein matrix and are in form of visible small and large globules.

1 Introduction

The microstructure of cheeses compiles information from surface observation of the product structure and visualizing the different macromolecules arrangement that principally proteins (appearance, size, arrangement of caseins) and lipids (size and dispersion). Several studies have been conducted on cheeses or lactic acid gels microstructure using different types of microscopes [1–3]. For cheese, the microstructure differs depending on the type of cheese and the manufacturing technology. It has been proven that cheese's microstructure can be influenced by various factors related to the milk and to cheese-making processes (the pressure and temperature treatment of the milk, rennet, ripening bacteria action …) [4, 5].

The goatskin bag is a container, traditionally used for foods preparation or conservation in some African and Asian countries. In dairy products its used for churning the fermented milk to obtain "Lben" beverage and for ripening in few cheese-making process like Tulum cheese (Turky), Darfeyeh (Lebanon) and Bouhezza cheese in Algeria. Bouhezza is a traditional cheese made from goat, ewe or cow's raw and/or fermented milk "Lben". The cheese is obtained by spontaneous coagulation in the goatskin bag container locally named "chekoua" for draining and ripening during at least one month. First results showed that the Bouhezza is a soft and mid-fat cheese and described with a slightly spicy taste, a rather pronounced acidity and a medium salty flavor [6].

Considering the limited information available concerning Bouhezza cheese characteristics, the aim of this work was to study the microstructure of the formed cheese in the goatskin "chekoua" and its changes during ripening using the Scanning electron microscopy (SEM) the and confocal laser scanning microscopy (CLSM).

2 Experimental

Chees making of Bouhezza was undergone as cited by Aissaoui Zitoun et al. [6]. Figure 1 show all stapes of manufacturing.

Tow manufacturing experiments were carried out in our laboratory via the traditional diagram and for a ten weeks' time. During the first six weeks, the tow goatskin bags received each three day only salted Lben, this time to ensure the ripening mechanisms. At the last weeks of manufacturing-ripening and to adjust organolepic characteristics of the bouhezza pasta (salt and acidity intensity), additions of whole raw milk were done. In this study the additions of fresh whole

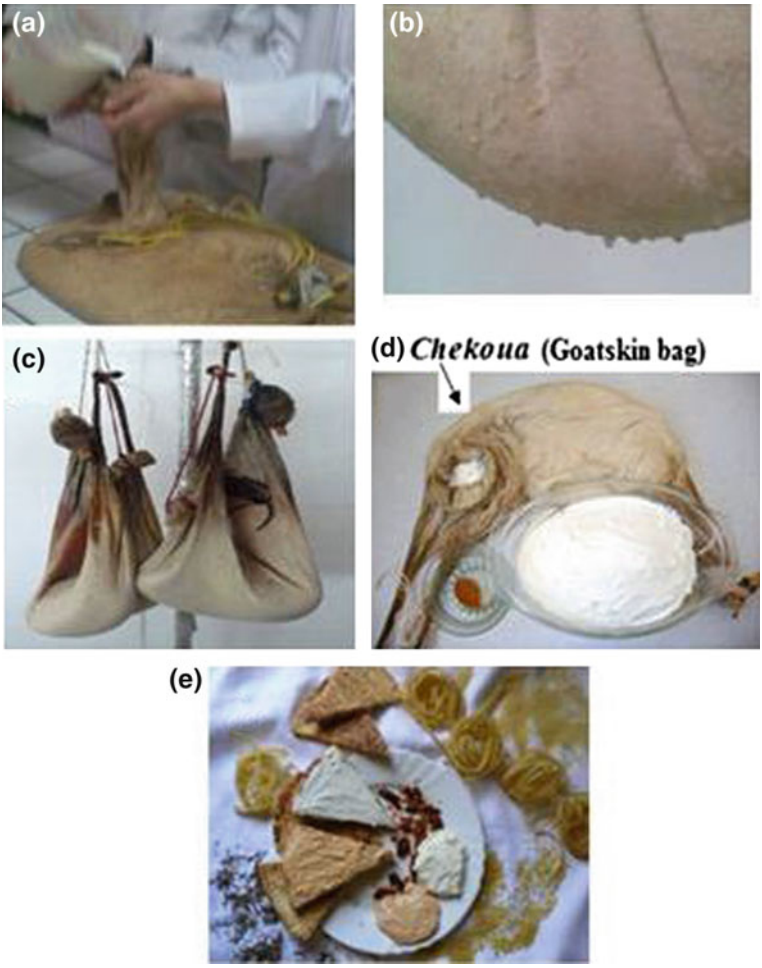

Fig. 1 Adopted procedure for traditional Bouhezza cheesemaking in permeable goat skin [7]. **a** The process was started with salted lben (6 L to start at day 0, salt: 25 g L-1), and repeated additions of lben are made until day 42 (3 L at day 1, and then 1.5 L every three days); **b** continual draining; **c** additions of fresh whole raw milk are made between day 42 and 70 (1.5 L every three days); **d** recovery of the Bouhezza cheese from the chekoua and spicing with red hot pepper; **e** Bouhezza cheese spread on traditional bread

milk was perused until the tenth week to observe eventual evolutions in this case. In all cheesmakin process, the goatskin "chekoua" was suspended in an aerated room and daily washed and scraped on the external face.

Cheese sampling was performed at different manufacturing and ripening stages. Samples were at 2, 4, 6, 8 and 9 weeks.

Cheese samples of Scanning Electron microscopy (SEM) analysis were prepared according to Attia et al. [8]. A fine layer of Bouhezza sample was spread on a

sluggish surface and dried on air for one hour and in a saturated atmosphere with glutaraldehyde for a night. Next samples were deshydrated in graded ethanol series and observed under a scanning electron microscope Philips XL30 (Philips, France) after drying to CO2 critical point using a Baltec CPD 030 apparatus and coating with gold using a Baltec MED 20 apparatus (Balzers Union, Balzers, Germany).

For Confocal Microscopy, samples at different ripening time were mounted on a microscope slide and directly stained with 10 µL of Nile Red 0.0025 % diluted in acetone to detect lipids and 10 µL of fluorescein isothiocyanate (FITC) 0.002 % in acetone to distinguish proteins. After 15 min of dark incubation, the samples were observed with a C1si Spectral Confocal system on a Nikon TE2000E inverted otorized microscope using 10× and 20× objective lenses [9]. Protein and lipid fluorescence excitation was produced with the 488 nm line from a 40 mW Argon Ion Melles Griot Laser and the 543 nm line from a He/Ne 2.0 mW Melles Griot Laser, respectively. Their emission wavelengths were 520 nm and 640 nm, respectively. Images were obtained with a multi-anode PMT and controlled with Nikon EZ-C1 3.0 version software.

3 Results and Discussion

SEM and confocal microscopy observations are presented in Figs. 2 and 3 respectively.

The SEM observation shows a proteinic aggregates organized in an open space matrix (Fig. 2) in which lipids and whey are entrapped in the proteinic mass. In protein mass we see the limits of micelles which caseins are not completely fused together. The cheese structure was open at the beginning than but more compact at the end of ripening. During the manufacture the cheese is enriched in protein and its structure becomes denser it is marked enter the first weeks where the appearance of the cheese that forms changes completely.

After the 4th week, the cheese structure does not appear changed and the protein network is visualized with the presence of various microorganisms within. In our opinion it is this structure that allows continuous draining of whey through the goatskin perforations; this is again a feature of making cheese Bouhezza. This microstructure is consistent with remarks of TUCKEY (1964) [1] where he states that the proteins in granule form as an active, sensitive surface which, under normal conditions, acts as a semi-permeable membrane, allowing the passage of whey.

Figure 3 of CLSM results shows the same observation as SEM and complete first Bouhezza cheese results [7] Fat globules were less in the first weeks of manufacturing and at the end their distribution appears to be homogenous in the protein matrix and are in form of visible small and large globules. Native fat globules were completely spherical and usually small-sized, which proposes that appear after whole raw milk additions starting at 6 weeks manufacturing. Fat pools are probably generated from Lben fat, which is in the form of small lipid grains.

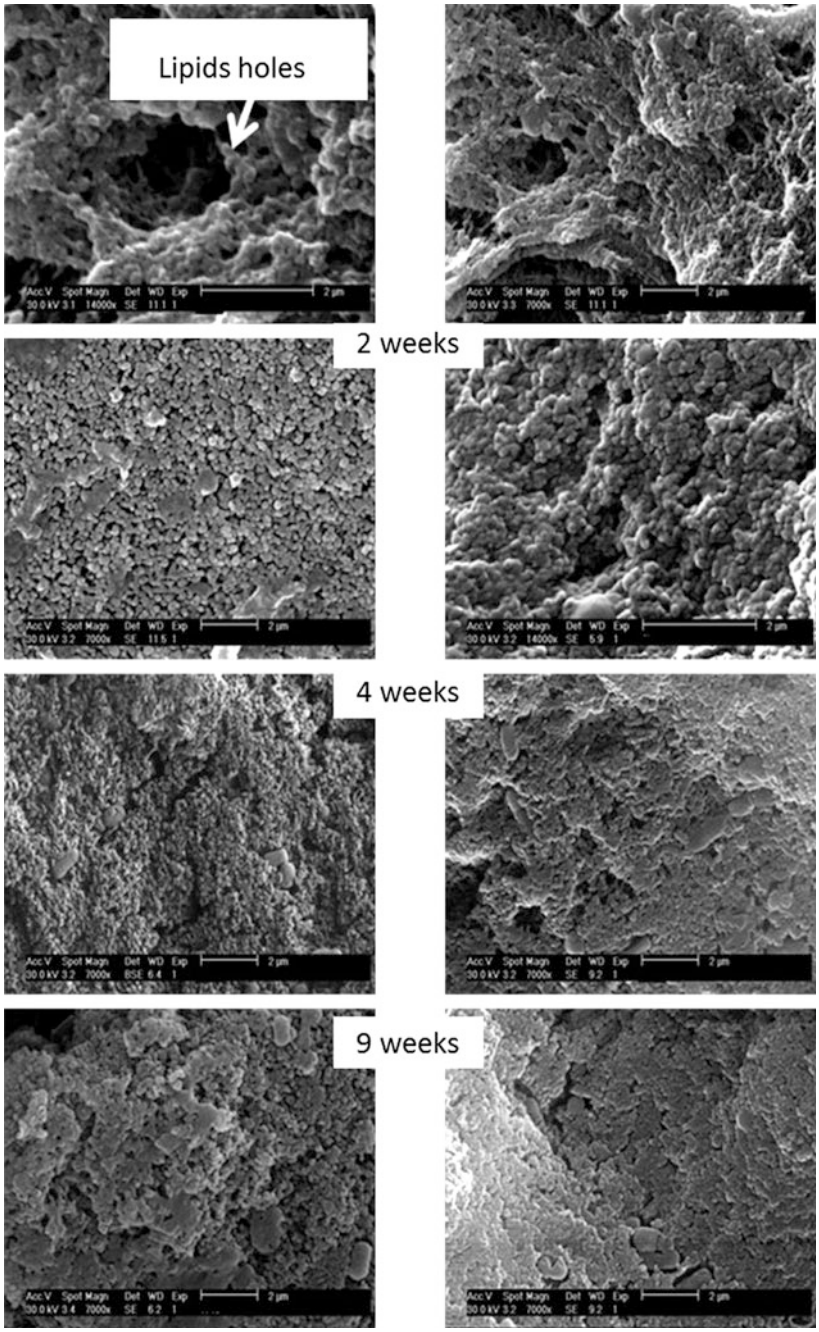

Fig. 2 SEM observations on Bouhezza cheese during manufacturing-ripening

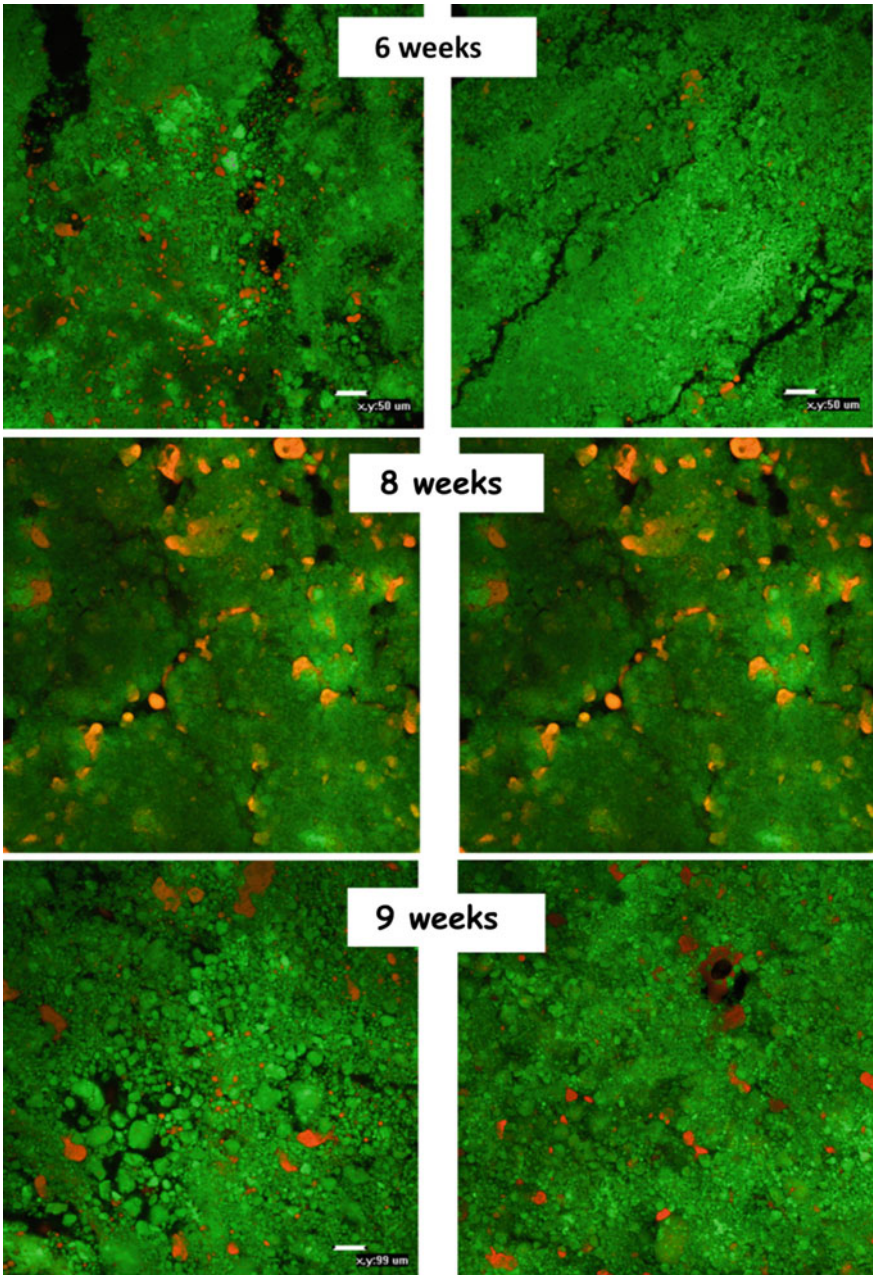

Fig. 3 CLSM observations of Bouhezza cheese during manufacturing-ripening

4 Conclusion

During the manufacturing of the Bouhezza cheese, the semi-liquid structure of the fermented Lben change to a gel structure and the formed cheese grows rich out of proteins and its structure becomes denser. The SEM and CLSM shows similar observations where proteins are organized in an open space matrix in which lipids and whey are entrapped. The Bouhezza microstructure is similar to the microstructure of other soft and creamy cheeses.

References

1. Kalab, M.: Microstructure of dairy foods. 1. Milk products based on protein. symposium: physical properties and structure of dairy foods. J. Dairy Sci. **62**, 1352–1364 (1979)
2. Marchesseau, S., Gastaldi, E., Lagaude, A., Cuq, J.: Influence of pH on protein interactions and microstructure of process cheese. J. Dairy Sci. **80**, 1483–1489 (1997)
3. Ong, L., Dagastine, R.R., Kentish, E.S., Gras, S.L.: Microstructure of milk gel and cheese curd observed using cryo scanning electron microscopy and confocal microscopy. LWT - Food Sci. Technol. **44**, 1291–1302 (2011)
4. Pereira, C.I., Gomes, A.M.P., Malcata, F.X.: Microstructure of cheese: processing, technological and microbiological considerations. Trends Food Sci. Technol. **20**, 213–219 (2009)
5. Auty, M.: Microscopy (Microstructure of milk constituents and products). Analytical Methods, 226–234 (2011)
6. Aissaoui Zitoun, O., Benatallah, L., Ghennam E.H., Zidoune, M.N.: Manufacture and characteristics of the traditional Algerian ripened Bouhezza cheese. J. Food Agri. Envir. **9**, 96–100 (2011)
7. Aissaoui Zitoun, O., Pediliggieri, C., Benatallah, L., Lortal, S., Licitra, G., Zidoune M.N.: Bouhezza, a traditional Algerian raw milk cheese, made and ripened in goatskin bags. J. Food Agri. Envir. **10**(2), 289–295 (2012)
8. Attia, H., Bennasar, M., De La Fuente, B.T.: Study of the fouling of inorganic membranes by acidified milks using scanning electron microscopy and electrophoresis: i. Membrane with pore diameter 0.2 μm. J. Dairy Res. **5**, 39–50 (1991)
9. Auty, M.A.E., Towmey, M., Guinee, T.P., Mulvihill, D.M.: Development and application of confocal scanning laser microscopy methods dor studing the distribution of fat and protein in selected dairy products. J. Dairy Res. **68**, 417–427 (2001)

N-Hexane Isomerization on Pt-Containing Ti-Pillared Tagan's Montmorillonite

N.A. Zakarina, A.K. Akurpekova, D.A. Zhumadulaev and O. Dalelkhanuly

Abstract Ti–pillared interlayered clays have been synthesized by the exchange reaction between acid modified Tagan montmorillonite in Na-form with an aqueous solutions of $TiCl_4$ and characterized by XRD, N_2–adsorption/desorption analyses, temperature-programmed desorption of ammonia (TPD NH_3), transmission electron microscopy (TEM). The maximum conversion of n–hexane equal to 64.1 % was found on 0.35 %Pt/Ti (5,0) NaHMM + M-catalyst thus the yield of isohexanes makes 45.0 %. At the decrease of platinum amount to 0.1 %, the conversion of n-hexane decreases slightly it makes 61.7 %, and the yield of isohexanes increases by 1.4 %. According to TEM separate dense particles mainly with a sizes of 50–100 Å are shown. Morelarger particles have the sizes within 200 Å. These particles can be related to the mixture of the phases Pt, PtTi, Pt_3Ti, TiO, TiO_2 that testify about strong interaction of the supported metal Pt with the support with formation of intermetallids (PtTi, Pt_3Ti) and oxides.

1 Introduction

Reactions of a catalytic isomerization of light normal alkanes are widely widespread in oil processing for production of isomerizats—a high-octane component of commodity gasolines. The isomerization changes raw materials—light C_4–C_6 alkanes—into isoparafins with a high octane numbers. There are processes of an isomerization of n-butane to isobutane, which is raw material for alkylation; n-pentane to isopentans; n-hexane to isohexans; a pentane-hexane fraction to mixture of isopentans and isohexans which have high octane numbers. The isomerization of C_5–C_6 fractions appeared in the most economically effective way for achievement of new requirements to commodity gasolines and now the isomerization is the most large-capacity industrial process [1].

N.A. Zakarina (✉) · A.K. Akurpekova · D.A. Zhumadulaev · O. Dalelkhanuly
D.V.Sokolsky Institute of Organic Catalysis and Electrochemistry, 142, Kunaev St., Almaty 480100, Kazakhstan
e-mail: nelly_zakarina@rambler.ru

A.Y. Oral and Z.B. Bahsi Oral (eds.), *3rd International Multidisciplinary Microscopy and Microanalysis Congress (InterM)*, Springer Proceedings in Physics 186,
DOI 10.1007/978-3-319-46601-9_22

Materials on the basis of clay minerals can serve as effective and rather cheap sorbents and catalysts in various processes. Development of technologies of production the modified clays and research of their adsorptive and catalytic properties is an actual task. Pillaring of the montmorillonite (MM) clays is the modification method allowing to improve porous structure of clays, to change its structure and acid properties [2–5].

The purpose of this work is to synthesize and investigate the catalytic activity of Pt-catalysts on pillared Ti- montmorillonite (TiNaHMM), modified by mordenite (M) with the silica modulus 20 in a hydroisomerization of n-hexane and the definition of physical and chemical characteristics of catalysts.

2 Experimental

Synthesis of Ti-pillared NaHMM on the basis of Tagan MM is described earlier [6]. Textural characteristics of samples determined by the BET method by low-temperature adsorption of nitrogen on the ACCUSORB device.

Dispersion of metal particles was determined electron microscopically (EMV-125) by method of replicas with the extraction and the application of microdiffraction method. Catalysts were tested in the course of a hydroisomerization of model hydrocarbon—n-hexane, a component of industrial a pentane-hexane straight-run gasoline oil with the aim of receiving a high-octane component of gasoline. Process was carried out in the range of temperatures of 250–400 °C with an atmospheric pressure of hydrogen, the molar ratio H_2:C_6H_{14} = 3.5 and volume feed rate of 0.82 h^{-1}. Catalyst volume—5 cm^3. The analysis of products of reaction was carried out by gas chromatography on the chromatograph 3700 with application of the capillary column (50 m) filled by skwalane.

Pt (0.05–0.35 % mass.)—catalysts prepared via the impregnation of Ti-pillared montmorillonite with H_2PtCl_6 solutions followed by thermal decomposition (500 °C) to the oxides and their subsequent reduction in hydrogen current at 450 °C. The catalysts were modified by mordenite (15 %).

3 Results and Discussion

Data on textural characteristics of initial NaMM, the acid activated NaHMM and Ti-pillared montmorillonite modified by mordenite TiNaHMM + M are provided in Table 1.

It was seen that a pillaring increases the specific surface of a sample from 90.3 to 190.5 m^2/g (Table 1). The increase in concentration of the pillaring agent from 5.0 mmol of Ti/g NaHMM to 7.5 mmol of Ti/g NaHMM leads to growth of a specific surface area from 115.1 to 190.5 m^2/g, the total volume of a pores passes through a maximum for Ti (5.0) NaHMM + M. According to the standard

Table 1 Comparative structural and adsorption characteristics of the initial NaMM, activated NaHMM and Ti-pillared MM (TiNaHMM + M) with various ratio of Ti^{4+}/NaHMM

Sample	S (m^2/g)	Total volume of a pores (cm^3/g)	R (Å)	Relative quantity (%)	
				Micropores (0–20 Å)	Mesopores (20–80 Å)
NaMM	76.9	0.176	12.0-70.0	22.9	77.1
NaHMM	90.3	0.070	12.5-70.0	38.7	61.3
Ti(5.0) NaHMM + M	115.1	0.223	12.5-70.0	11.8	88.2
Ti(7.5) NaHMM + M	190.5	0.172	12.0-70.0	36.0	64.0

classification of a pores, a pores with a width <20 Å are a micropores, with a width 20–80 Å-intermediate mesopores, a pores with a width >200 Å—a macropores. It should be noted the absence of a macropores (>200 Å) at the synthesized samples. The calculation (Table 1) shows that in comparison with NaMM and NaHMM for which the share of a mesopores equal to 77.1 and 61.3 %, respectively, at the pillared TiNaHMM from the H-form at the ratio Ti^{4+}/NaHMM = 5.0 mmol/g the quantity of a mesopores is 88.2 %, a share of micropores—11.8 %.

Data on the hydroconversion of n-hexane over 0.35 % of Pt/TiNaHMM-catalyst with an additive of a mordenit are given in Table 2 at various temperatures and ratios of Ti in TiNaHMM.

As it seen from Table 2, conversion of n-hexane increases as the process temperature increases from 250 to 400 °C. Selectivity to all formed isomers remains very high (90.6–100 %). The maximum yields of isohexanes were observed at 350 °C on catalysts with ratios 5.0, 2.5 and 7.5 mmol Ti^{4+}/g NaHMM which accordingly equal to 46.8, 36.8.0 and 37.6 %. Existence of C_7 isomers testifies probably about parallel proceeding processes of disproportionation in the course of n-hexane isomerization.

Figure 1 presents the data on the activity and selectivity of Pt/TiNaHMM + M-catalyst in reaction of a hydroisomerization of n-hexane depending on the ratio of Ti^{4+}/NaHMM. The optimal activity shows the catalyst with a ratio of 5.0 mmol Ti^{4+}/g NaHMM. Conversion of a n-hexane on Pt/Ti(5.0) NaHMM + M-catalyst reaches 64.1 %at 400 °C. On this catalyst at 350 °C about 25 % of a 2,2-dimethylbutan (2.2-DMB) and 21.8 % of a 2-methylpentan(2-MP) are formed. Also Pt/Ti(2,5) NaHMM with conversion of n-hexane 50.1 % and high selectivity of process is rather active. On this catalyst the yield of disubstituted isomers equal to 22.5 %.

The acid properties of the catalysts prepared from Ti-pillared NaHMM are presented in Table 3 according to the modern acid centers classification.

From data of Table 3 it is visible that for 0.35 % of Pt/Ti(2,5) NaHMM-catalyst the total amount of acid centers is 206,3 μmol of NH_3/g. From them the amount of

Table 2 An isomerization of n-hexane over 0.35 %Pt/TiNaHMM + M—the composite catalyst at the ratio Ti/NaHMM = 2.5; 5.0 and 7.5 mmol/g

Ratio Ti^4/ NaHMM	T (°C)	α (%)	S_{C6} (%)	S_{C6+} (%)	Yield of products of reaction (%)											
					{C_1–C_4	i-B	2 MB	2,2DMB	2MP	2,2 DMP	2,4DMP	2,2,3TMB	2MH	3MH	3EP	H-Hept
2.5	250	11.0	50.0	100	–		–	2.4	3.1	–	–	5.5	–	–	–	–
	300	24.7	80.9	99.1	0.03		0.2	11.4	8.6	–	–	4.2	0.2	0.1	–	–
	350	42.6	86.3	96.5	0.5		1.0	21.6	15.2	–	–	3.3	0.9	0.04	0.04	0.05
	400	50.1	81.9	95.3	0.7		1.6	22.5	18.5	0.1	0.2	4.1	2.2	0.03	0.06	0.07
5.0	250	16.0	61.3	100	–	–	–	4.5	5.3	–	–	6.0	–	0.2	–	–
	300	42.2	86.5	97.9	0.1	0.2	0.6	21.1	15.4	–	–	4.0	0.5	0.3		–
	350	58.7	79.7	91.0	0.8	0.6	3.8	25.0	21.8	0.2	–	3.6	2.6	0.1	0.1	0.1
	400	64.1	70.2	90.6	0.6	0.6	4.6	24.0	21.0	0.4	–	5.9	6.6	0.1	0.1	0.2
7.5	250	16.0	57.5	100	–	–	–	3.9	5.3	–	–	6.7	–	0.1	–	–
	300	31.5	81.0	98.4	0.2	–	0.3	14.8	10.7	–	–	5.1	0.3	0.1	–	–
	350	46.1	81.6	92.4	1.4	–	2.0	21.2	16.4	0.1		3.9	0.8	0.1	0.1	0.1
	400	48.6	80.0	93.8	1.6	–	1.3	20.6	18.3	0.1	0.5	4.3	1.6	0.1	0.1	0.1

α conversion, *S* selectivity, *T* temperature

i-B isobutan; *MB* methylbutan; *DMB* dimethylbutan; *MP* methylpentan; *DMP* dimethylpentan; *TMB* trimethylbutane; *MH* methylhexane; *EP* ethylpentan; *n-Hept* n-Heptan

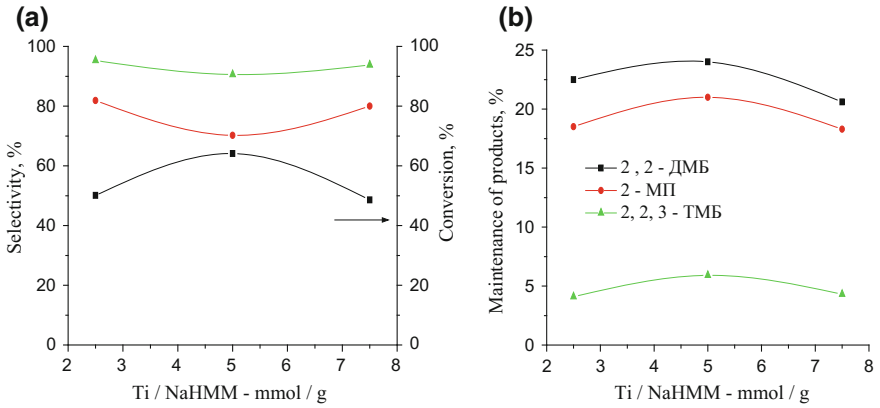

Fig. 1 Change of conversion and selectivity of 0.35mass%Pt/TiNaHMM + M-catalyst with various ratio of Ti^{4+}/NaHMM in the isomerization of n-hexane at 400 °C, and the structure of the main formed products

Table 3 Acidity of 0.35 %Pt/Ti(2.5)NaHMM and 0.35 %Pt/Ti(2,5)NaHMM + M – catalysts

Sample	Amount of acid centers (a.c)	Acid centers			
		Weak <200 °C	Medium 200–300 °C	Strong >300 °C	Total acidity
(0.35 %) Pt/Ti(2,5) NaHMM	%	15.0	15.0	70.0	100
	μmol NH_3/г	30.9	30.9	144.4	206.3
(0.35 %) Pt/Ti(2.5) NaHMM + M	%	22.2	25.9	51.9	100
	μmol NH_3/г	52.0	60.7	121.7	234.4

weak acid sites (50 < T< 200 °C) is 15.0 %, amount of the medium a.c. (200 < T < 300 °C)—15.0 % and on a share of the strong a.c. (T > 300 °C)—70 %. The introduction of a mordenite grows the total acidity of the catalyst, it makes 234.4 μmol of NH_3/g. From them on a share weak (50 < T < 200 °C) a.c. have 22.2 %, on a share of the medium a.c. (200 < T < 300 °C)—25.9 % and on a share of the strong a.c. (T > 300 °C)—51.9 %, i.e. at the introduction of a mordenit occurs reduction of the relative contents strong a.c. from 70 to 51.9 %, while the amount of medium and weak a.c. grows that is followed by increase of isomerization activity of the studied catalysts.

We conducted electron—microscopic examination of the dispersion and structure of platinum particles after their preliminary reduction in a hydrogen flow at 450 °C and experiments at 250–400 °C.

The electron microphotographs of the 0.35 %Pt/Ti(2.5)NaHMM + M-catalyst are given in Fig. 2.

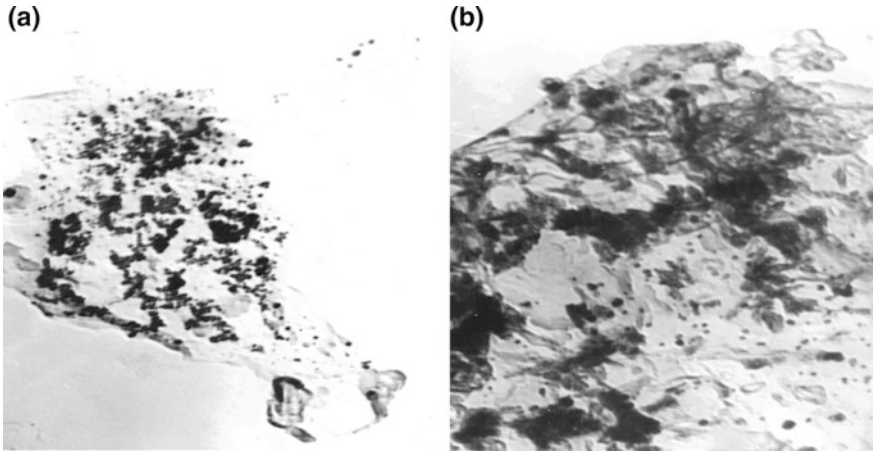

Fig. 2 Elektron microphotographs of the 0.35 %Pt/Ti (2.5) NaHMM + M-catalyst (magnification 50,000)

Figure 2a taken for Pt/TiNaHMM-catalyst show small dense particles of Pt which the size fluctuates within 30–50 Å. They alternate with the dense particles of the TiO_2 carrier with a size of 100–200 Å (Fig. 2b).

Data on isomerization activity of Pt/Ti (2,5) NaHMM, modified by mordenite depending on the content of metal are presented in Table 4 and in Fig. 3.

The conversion of n-hexane grows with temperature increase and reaches 61.7 % for 0.1 %Pt/Ti(5,0)NaHMM + M-catalyst and 55.4 % for 0.05 % Pt/Ti (5,0) NaHMM + M-catalyst. Selectivity on all formed isomers remains the very high—93.0–100 %. The yield of S_6-disubstituted isomers at 400 °C for 0.1 %Pt/Ti (5,0) NaHMM-catalyst makes 24.4 %. At decreasing of the quantity of platinum to 0.05 % yields of C_6-disubstituted isomers changes a little and makes 23.5 %. At increase in the concentration of the pillaring agent the isomerization activity of the catalyst is falled. The quantity of products of hydrocracking fluctuates from 0.1 to 1.4 % depending on the structure of the catalyst and the temperature.

The maximum yield of isohexanes was received on 0.1 % Pt/Ti (5,0) NaHMM + M-catalyst at 400 °C that makes 46.4 %. Formation 9.7 % of C_7 isomers (2,2,3 TMB, 2 MG, 3MG, 3 EP) on this catalyst testifies probably about is collateral the proceeding processes at an isomerization of n-hexane.

The electron microscopy picture of the catalyst at the reduction of the content of platinum to 0.1 % is given in Fig. 4.

In Fig. 4a separate dense particles of the TiO_2 carrier are shown which size fluctuates within 50–70 Å. In the Fig. 4b separate dense particles mainly with a size of 50–100 Å are shown. More larger particles have the sizes within 200 Å. These particles can be related to the mixture of the phases PtTi, Pt_3Ti, TiO, TiO_2 and Pt that testify about strong interaction of the supported metal with the support with formation of intermetallids (PtTi, Pt_3Ti) and oxides.

Table 4 Influence of quantity of Pt in composite Pt/TiNaHMM + M catalysts on an isomerization of n-hexane

Catalyst Pt/Ti NaHMM	T (°C)	α (%)	S_{C6} (%)	S_{C6+} (%)	Yield of products of reaction (%)											
					{C_1–C_4	i-B	2 MB	2,2DMB	2MP	2,2 DMP	2,4DMP	2,2,3TMB	2MH	3MH	3EP	H-Hept
(0.1 %)* 2.5**	250	11.6	50.0	100	–		–	2.0	3.8	–	–	5.8	–	–	–	–
	300	19.1	71.4	99.5	0.1		–	7.1	6.5	–	–	5.2	0.1	0.06	–	–
	350	40.6	85.2	96.7	0.5		0.8	20.4	14.2	0.1	–	3.8	0.7	0.06	0.05	0.05
	400	44.2	82.9	96.0	0.7		1.0	21.2	15.5	0.1	0.4	3.9	1.2	0.07	0.1	0.07
(0.1 %)* 5.0**	250	15.2	54.6	100	–	–	–	3.4	4.9	–	–	6.8	–	0.1	–	–
	300	39.3	84.7	98.7	0.1	0.1	0.3	19.2	14.1	–	–	4.9	0.4	0.2	–	–
	350	54.8	84.1	94.0	0.6	0.3	2.3	23.7	22.4	–	–	3.6	1.6	0.1	0.1	0.1
	400	61.7	75.2	91.9	0.7	0.4	3.7	24.4	22.0	0.1	0.5	4.8	4.7	0.1	0.1	0.2
(0.05 %)* 5.0**	250	15.0	57.3	100	–	–	–	3.7	4.9	–	–	6.3	–	0.1	–	–
	300	33.8	82.5	98.5	0.1	0.1	0.3	16.1	11.8	–	–	4.9	0.3	0.2	–	–
	350	50.9	86.4	95.3	0.6	0.3	1.4	22.7	21.3	–	–	3.3	1.0	0.1	0.1	0.1
	400	55.4	81.9	93.0	1.0	0.6	2.2	23.5	21.9	0.1	0.4	3.4	2.0	0.1	0.1	0.1
(0.1 %)* 7.5**	250	13.6	52.2	100	–	–	–	2.7	4.4	–	–	6.5	–	–	–	–
	300	21.4	71.0	98.6	0.1	–	0.2	8.1	7.1		–	5.7	0.1	0.1	–	–
	350	32.2	79.2	95.7	0.9	–	0.5	14.7	10.8	0.1	–	4.6	0.4	0.2	–	–
	400	36.2	76.2	93.9	1.4	–	0.7	15.9	11.7	0.6	–	4.8	0.9	0.1	–	0.1

* In *brackets* the content of metal is specified

** Ratio of Ti:NaHMM, mmol/g

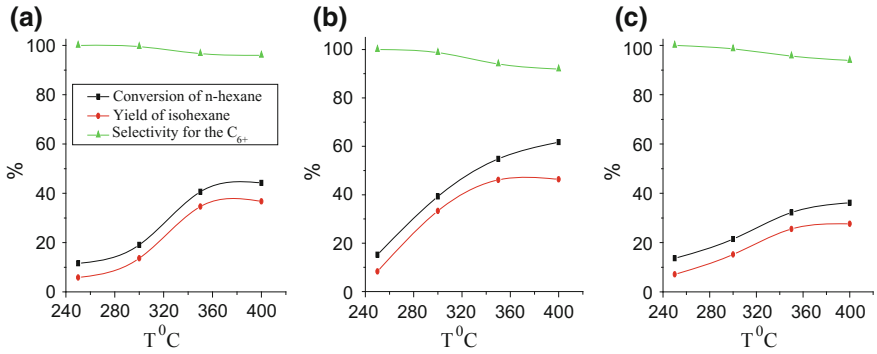

Fig. 3 An yield of isohexane, selectivity and conversion of n-hexane over 0.1 %Pt/Ti (2.5) NaHMM + M (**a**); 0.1 %Pt/Ti (5,0) NaHMM + M (**b**); 0.1 %Pt/Ti (7,5) NaHMM + M (**c**)—catalysts depending on process temperature

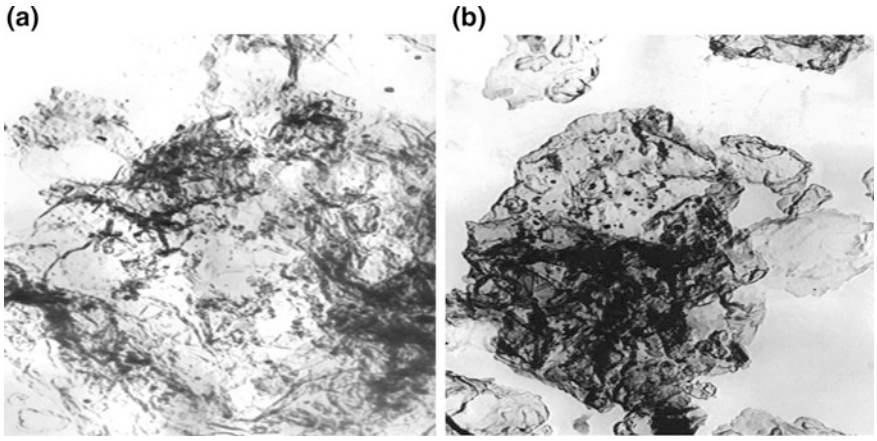

Fig. 4 Electron microphotographs of the 0.1 % Pt/Ti (2.5) NaHMM + M-catalyst (magnification 50,000)

The comparison of the electron microscopy photographs of Pt-catalysts with the quantity of Pt 0.35 and 0.1 % (Figs. 2 and 4) shows that with the decreasing of Pt quantity in the catalyst the interaction of Pt with Ti from the support intensified while it isn't possible to do a conclusion about the dispersion of Pt particles on the basis of the received results.

4 Conclusion

Ti–pillared interlayered clays have been synthesized by the exchange reaction between acid modified Tagan montmorillonite in Na-form with an aqueous solutions of $TiCl_4$ and characterized by XRD, N_2–adsorption/desorption analyses, temperature-programmed desorption of ammonia (TPD NH_3), transmission electron microscopy (TEM).

Pt-catalysts, supported on TiNaHMM, were tested in the isomerisation n-hexane depending from amounts of Pt, Ti and reaction temperature. The maximum conversion of n-hexane equal to 64.1 % was found on 0.35 %Pt/Ti (5,0) NaHMM + M-catalyst at 400 °C. In these conditions the yield of isohexanes was 45.0 %, the yield of 2,2-dimethylbutan was 24.0 %. The decrease of platinum amount to 0.1 %, the conversion of n-hexane decreases slightly it makes 61.7 %, and the yield of isohexanes increases to 46.4 %.

According to TEM separate dense particles mainly with a size of 50–100 Å were revealed. More larger particles have the sizes within 200 Å. These particles can be related to the mixture of the phases Pt, PtTi, Pt_3Ti, TiO, TiO_2 that testify about strong interaction of the supported metal with the support with formation of intermetallids (PtTi, Pt_3Ti) and oxides.

Thus, Ti-pillared Tagan montmorillonite containing as the metal phase Pt, and as acid component TiNaHMM + M can be used in reaction of a skeletal isomerization of linear alkanes to isomers with high octane number at the atmospheric pressure.

References

1. Vu, T.N., van Gestel, J., Gilson, J.P., et al.: Platinum-tungstated zirconia isomerization catalysts Part II. Effect of platinum and tungsten loading on the mechanism of isomerization of n-hexane: a kinetic study. J. Catal. **231**, 468–479 (2005). doi:10.1016/jcat2005.02.003
2. Gil, A., Korili, S.A., Vicente, M.A.: Recent advances in the control and characterization of the porous structure of pillared clay catalysts. J. Catal. Rev. **50**, 153–221 (2008). doi:10.1080/101614940802019383
3. De Stefanis, A., Tomlinson, A.A.G.: Towards designing pillared clays for catalysis. J. Catal. Today **114**, 126–141 (2006). doi:10.1016/jcattod.2006.01.019
4. Timofeeva, M.N., Panchenko, V.N., Gil, A., et al.: Synthesis of propylene glycol methyl ether from methanol and propylene oxide over alumina-pillared clays. J. Appl. Catal. B Environ. **102**, 433–440 (2011). doi:10.1016/j.apcatb2010.12.020
5. Zakarina, N.A., Volkova, L.D., Akurpekova, A.K., et al.: Isomerization of n-hexane on platinum, palladium, and nickel catalysts deposited on columnar montmorillonite. J. Pet. Chem. **48**, 186–192 (2008). doi:10.1134/S0965544108030031
6. Kawabata, T., Kato, M., Mizugaki, T., et al.: Highly efficient deprotection of acetals by titanium cation-exchanged monmorillonite as a strong solid acid catalyst. J. Chem. Lett. **32**, 648–649 (2003). doi:10.1246/cl2003.648

Part III
Advances in Instrumentation and Techniques

Analysis of Historical Monuments Through the Lens and Electrons: Case Study: The Monastery Hurezi

Ioana Gomoiu, Dan Mohanu, Ileana Mohanu, Mădălin Enache and Roxana Cojoc

Abstract The Horezu Monastery is dating from the seventeenth century, but the refectory was built in the western side of its axis and painted in the early eighteenth centuries. The main objective of the work is to perform a deep analysis of pink and black pigmentation from the refectory and the cellar. It started from the pink coloration observed by the naked eye followed by photographic registration and analysis by mobile optical microscope. Then micro samples have been taken for analysis at optical and electronic microscope and resin embedding to obtain cross-sections. Photographic registration is a useful method to map pink pigmentation but microscopy and microbiological analysis are essential for finding its biological origin. Spherical cells like *Rubrobacter* grouped in chains or tetrads developing a pink biofilm and filamentous branching bacteria like actinomyces were identified on the surface of mortar, mural painting and bricks. Many groups of bacteria have been found in cracks and pores. This observation explains the ability of pink bacteria to travel through pores and clog them impairing water evaporation. Black pigmentation is the result of mortar colonization by fungi which developed both mycelium and conidiophores with conidia. Examination of the samples by lens and electrons allows scientists and restorers to identify the microbiological origin of the pink and black discoloration and to avoid their misinterpretation as colors which are coming from chemical reactions or deposits from the atmosphere. Based on these results, a strategy for decontamination is elaborated to be applied before restoration work.

I. Gomoiu (✉) · D. Mohanu
Conservation and Restoration Department, National University of Arts,
19, G. Budişteanu, 010773 Bucharest, Romania
e-mail: gomoiu@hotmail.com

I. Mohanu
Binders Materials Research Department, CEPROCIM S.A., 6 Blvd Preciziei,
10146 Bucharest, Romania

M. Enache · R. Cojoc
Microbiology Department, Institute of Biology Bucharest, Romanian Academy,
296, Spl Independentei, 060031 Bucharest, Romania

A.Y. Oral and Z.B. Bahsi Oral (eds.), *3rd International Multidisciplinary Microscopy and Microanalysis Congress (InterM)*, Springer Proceedings in Physics 186,
DOI 10.1007/978-3-319-46601-9_23

1 Introduction

Biodeterioration of mural painting from historical monuments has as result chromatic changes, colored stains appearance, cracks and detachments promoting aesthetical and structural damages. The main biodeteriogens of mural painting are bacteria, algae, yeasts, fungi and lichens. Specific conditions favorable for microbial colonization are as follows: reduced carbon and energy sources, varying moisture levels and low or variable temperatures [1, 2]. The pink color of stains is due to carotenoids produced by archaebacteria (genera *Halobacterium*, *Halococcus*), halophilic bacteria (genus *Rubrobacter*) and yeasts (genus *Rhodotorula*) [3, 4]. White patina appears as an intensive, compact and whitish deposit on the powdered pictorial layer, very similar to salt efflorescence, but in fact is produced by pseudomycelium belonging to *Actinomycetes* [1]. Blue–green biofilm is produced by *Cyanobacteria* and green biofilm by green algae grown on the mural paintings exposed to natural and artificial light [5, 6]. Stains are also a consequence of the presence of secondary colonizers like fungi. Melanized fungi produce black stains (genera *Aspegillus*, *Ulocladium*, *Alternaria*) or dark-brown spots (genus *Cladosporium*) [7–9]. Other fungi like *Trichoderma viride* develop brownish–grey patina [10]. Lichens produce colored crusts on the surface of the external walls and even on the internal ones if there is natural or artificial light [11]. The aim of this research is to identify stains on the surface of pictorial layer and mortar from Hurezi complex monastery and their origin, to elaborate a scientific diagnosis useful for the strategy of restoration. We also investigate the methodology for examination of stains in situ and in laboratory.

2 Materials and Methods

The Hurezi monastic complex dates back to the 17th century (1690–1693), being founded by the ruler Constantin Brancoveanu. In early eighteen century, a refectory was built and decorated with mural painting made in al frescoes techniques in the western side of its axis. Later on, the eastern and western walls of the refectory as well as the inner side of the niches have been covered by massive over paintings on the lower side of the walls. All walls of the refectory in the lower part are stained in yellow-pink and black. Stairs, walls and the ceiling of the cellar are covered with pink-red biofilm.

After visual identification of stains and photographic registration, the examination under Dino-Lite Digital microscope was performed. The walls of the refectory, bricks and stairs were sampled at 30 cm above the ground and observed under optical microscope (Nikon AZ 100) as well as under Scanning Electron Microscope (SEM; JEOL JSPM 5200—Japan), to identify the origin of pigmentation. Samples for microbiological analysis were weighed (g) then the decimal dilutions were inoculated on solid media supplemented with 10 % respectively 20 % NaCl [12] as

well as on the yeast-glucose-chloramphenicol-agar [7] and incubated at 28 °C for 35 days. Pure cultures were obtained using depletion loop technique.

3 Detection of Pink Pigmentation

Visual Examination of the refectory identified pink pigmentation on the infilling mortars of eastern wall on the lower part either as uniform areas with well defined margins (Fig. 1a) or as detached even powdery areas (Fig. 1b). On the northern wall, very clear pink areas were observed both on the infilling mortar and pictorial layer (Fig. 1c). Pink pigmentation from the northern wall passing to the western wall could be remarked only at the level of infilling mortar which was applied up to 60–70 cm high (Fig. 1d). Our research started one year ago but religious persons

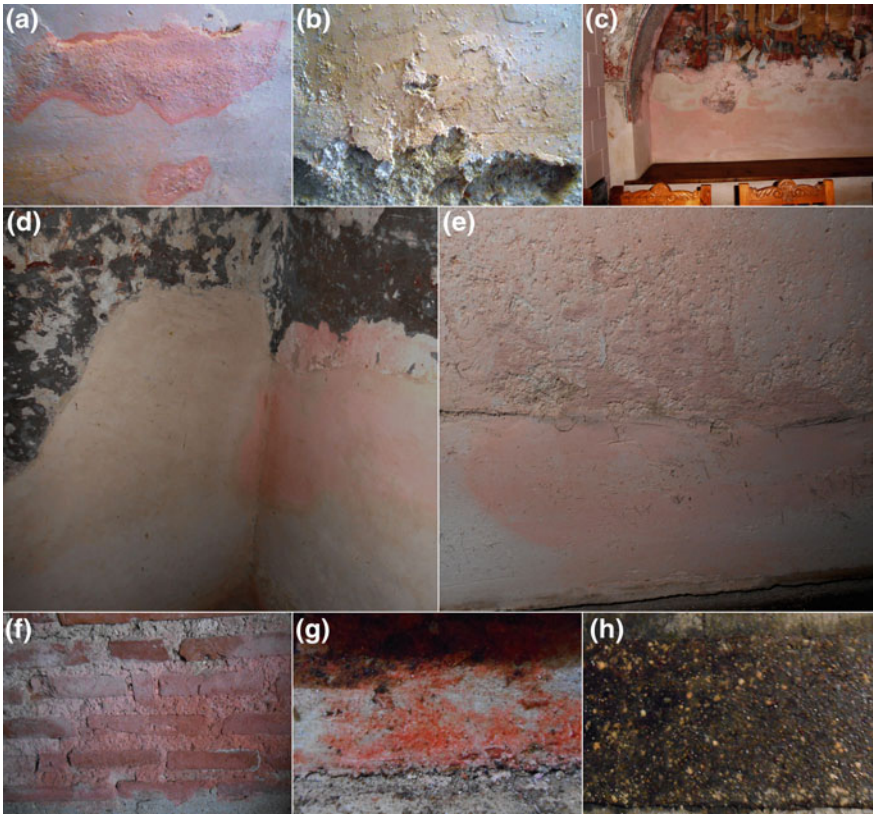

Fig. 1 General view of the distribution of pink discoloration in the refectory and cellar: **a**, **b** the eastern wall; **c** the northern wall; **d** the western wall; **e** the **s**outhern wall; **f** bricks; **g** stairs; **h** some bricks are covered by black deposit and yellow or white colonies

frequenting the place sustained that pink pigmentation on the northern wall has appeared at least 10 years ago. On the southern wall pink pigmentation was observed in the lower part of the wall (up to 30 cm height); it changed color from light yellow six months ago to light pink presently (Fig. 1e).

Mortar and bricks from all walls as well as on the stairs, ceiling and floor are covered by pink pigmentation; mortar became powdery, bricks are covered by pink efflorescences and stairs (Fig. 1f) by the red biofilm (Fig. 1g). Also, there were put in evidence even yellow and pink colonies (Fig. 1h).

Microscopical Examination in laboratory, under Nikon AZ 100, performed both on samples from the refectory and from the cellar revealed large or small pink areas, white and pink efflorescences on the surface of the pictorial layer, infilling and original mortar (Fig. 2a–c). The real color of pictorial layer cannot be seen because of pink biofilm. Also the original mortar is covered by smaller or larger pink areas (Fig. 2a, c). These observations show that contamination covered both refectory and cellar and it could be a possible consequence of migration of water from soil

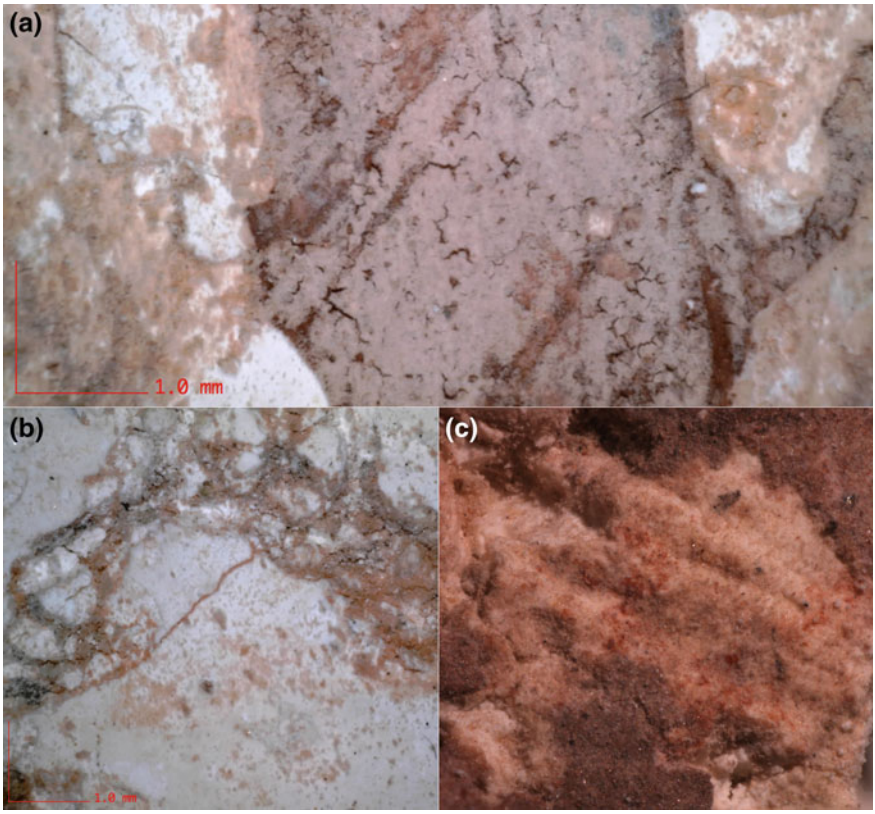

Fig. 2 Pink pigmentation identified in situ and in laboratory under optical microscope: **a**, **c** on the pictorial layer and on the infilling mortar; **b** only on the infilling mortar

into the walls. The process is continuous and takes place in connection with available water into the walls, relative humidity, temperature and biological characteristics of biodeteriogens. White, yellow and pink efflorescences had been observed. Laiz et al. [13] and Imperi et al. [14] found in three different sampling sites with specific environment the bacterial aetiology of rosy discoloration. Our results have been obtained on a monument with different environments: the refectory is situated on the ground and indoor, with the door open during the day where relative humidity and temperature are different during the day and night; the cellar is situated underground with high relative humidity and low temperature. The main sources of bacteria producing pink discoloration are: water, outdoor microbiota and already contaminated areas.

Electron micrographs revealed that samples taken from the refectory and cellar are covered by groups of round shaped bacteria distributed either on the surface (Fig. 3a–c) or in pores (Fig. 3c, e, f). Filamentous branching bacteria together with

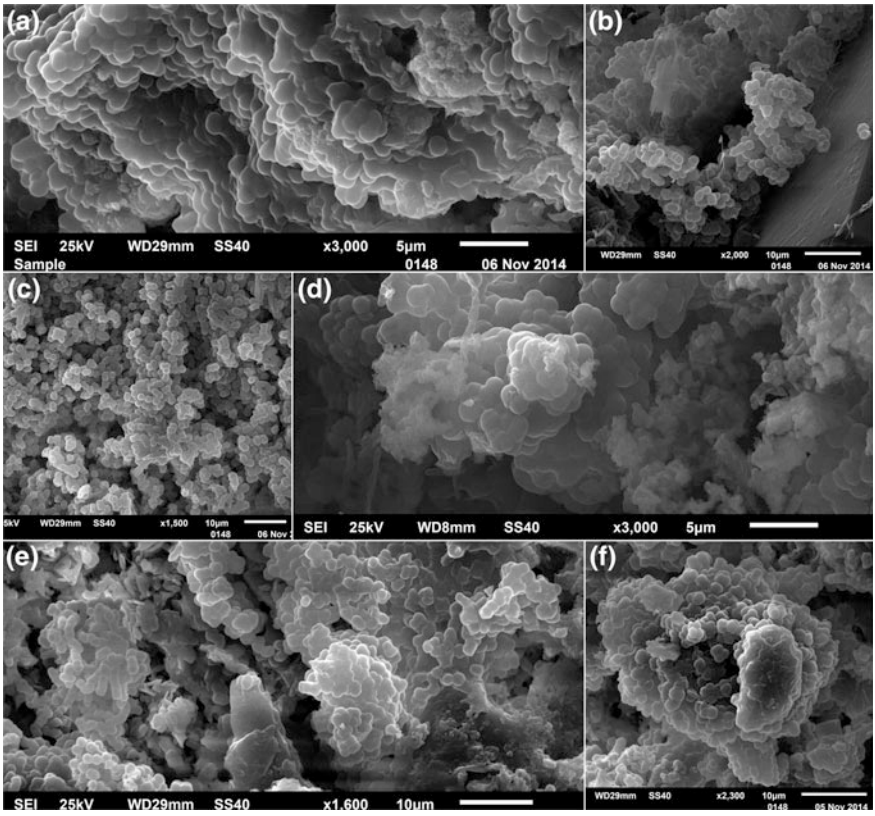

Fig. 3 Round shaped bacteria and filamentous branching bacteria: **a** the eastern wall; **b** the northern wall; **c** the western wall; **d** the southern wall; **e** bricks; **f** stairs

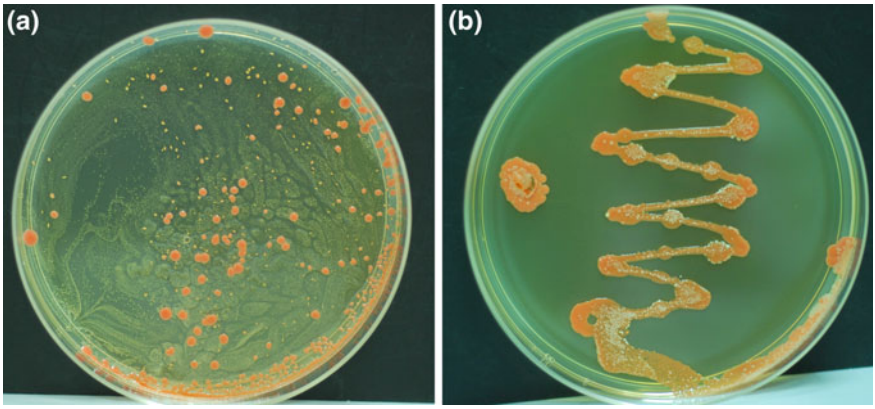

Fig. 4 Microbiological analysis: **a** macroscopic features of predominant isolated strains; **b** pink biofilm includes red, yellow and white colonies

spherical cells had been found on the northern and southern walls, as well as on the bricks (Fig. 3b, d, f).

Microbiological Analysis of samples allowed to isolate the microorganisms associated with damage to the mural painting and infilling mortar which developed pink, yellow, white colonies (Fig. 4a, b). They belong to different species but yellow and pink colonies belong to the same species. All species are halotolerant or moderately halophilic strains.

4 Detection of Black Pigmentation

Visual Examination of the refectory identified brown and black spots on the infilling mortars from the northern wall of the refectory at about 60–70 cm height (Fig. 5a). Some of them are more colored in the center and light colored to the margins. Macroscopically no differences could be observed in consistency of the fungal biofilm.

Microscopical Examination in situ revealed that in dark brown and black areas there is sporulated mycelium and in the light brown and dark areas there are branched hyphae. Their sparsely distribution makes them light colored (Fig. 5b). Electron micrographs have demonstrated that mycelia, hyphae, conidiophores and spores are present both on the surface and in the deeper layers of the infilling mortar. In the dried areas hyphae and conidiophores are collapsed. Individual or chains of spores attached to the mortar suggest the spreading potential of fungi. In the wet areas germinated spores of *Ulocladium* sp. (Fig. 5c), conidiophors of *Penicillium* sp. (Fig. 5d), and hyphae were found. There are some areas where hyphae could be found next to groups of round shape bacteria.

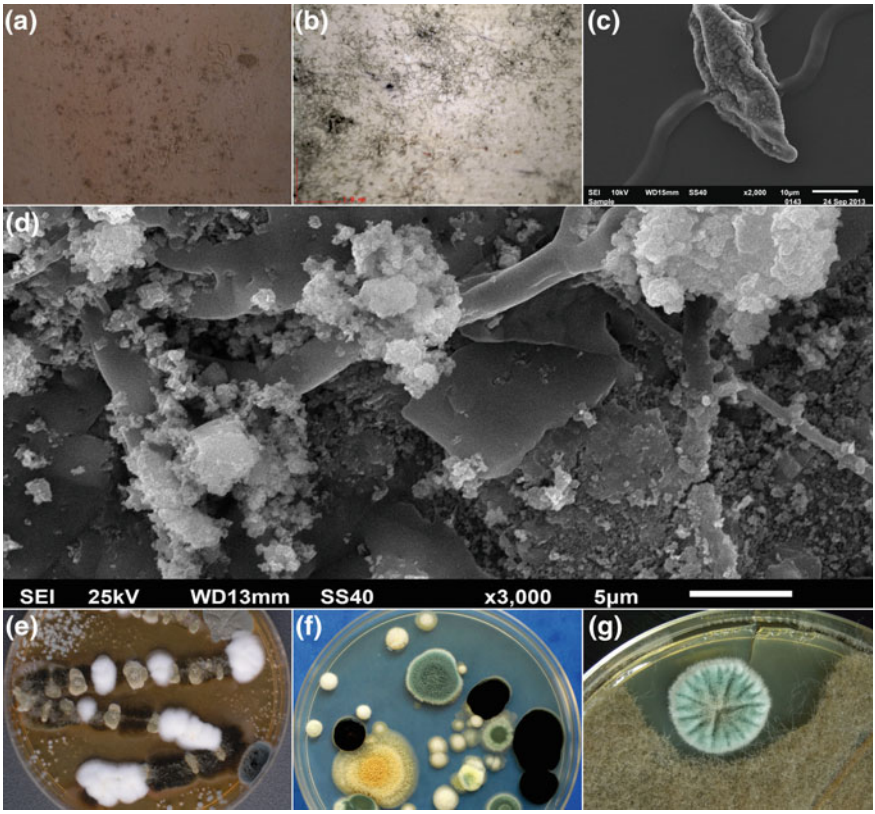

Fig. 5 Black pigmentation identified by different methods: **a** *dark and light spots*—visual observation; **b** mycelia—optical microscopy; **c** germinated spore of *Ulocladium* sp.; **d** conidiophores of *Penicillium* sp.; **e–g** fungal colonies

Microbiological Analysis of samples brought more information about areas colonized by fungi. They belong to different species that develop on the nutrient colonies which have different colors due to the sporulation stage (Fig. 5e–g). The following genera: *Acremonium*, *Aspergillus*, *Penicillium*, *Ulocladium* (Fig. 5e), *Aspergillus*, *Penicillium*, *Aureobasidium* (Fig. 5f) had been identified. Some genera develop antagonistic relationships like *Penicillium* and *Ulocladium* (Fig. 5g). Melanized fungal strains as well as genera *Acremonium* and *Penicillium* had been found as typical inhabitants of frescoes [8, 15, 16].

5 Conclusions

The macroscopical and microscopical analysis of mural painting and mortar demonstrated pink and black pigmentation. In the refectory, pink pigmentation was identified on all walls mostly on the lower part, but in the cellar it was found on the walls, stairs and ceiling. SEM micrographs clearly demonstrated the presence of microorganisms as bacteria and fungi. Individual and grouped cells, hyphae, conidiophores and spores are spread both on the pictorial layer and mortar.

The microbiological analysis confirmed the biological origin of pink and black pigmentation. Pink, yellow, white bacterial colonies had been isolated. Their affinity to salt explains the colonization of mortar and pictorial layer covered by efflorescences. Black pigmentation is produced by melanized fungi like genera *Aspergillus*, *Ulocladium* and *Aureobasidium*. Further investigations are needed for the molecular identification of bacteria and fungi as well as for decontamination.

This work highlights the importance of the analysis of the origin of mural paintings pigmentation in order to establish the scientific diagnosis and the proper treatment as step of restoration process. It suggests also the importance and significance of methods applied in this study: visual analysis, microscopical analysis (LM and SEM) and microbiological analysis.

Acknowledgments This research was carried out with financial support of the National Research Program *Parteneriate în domenii prioritare—PN II*, MEN—UEFISCDI, grant no. PN-II-PT-PCCA-2013-4-0660.

References

1. Karbowska-Berent, J.: Microbiodeterioration of mural paintings: a review. In: Koestler, R.J., Koestler, V.H., Charola, A.E., Nieto-Fernandez, F.E. (eds.) Art Biology, and Conservation: Biodeterioration of Works of Art, pp. 267–296 (2002)
2. Pepe, O., Palomba, S., Sannino, L., Blaiotta, G., Ventorino, V., Moschetti, G., Villani, F.: Characterization in the archaeological excavation site of heterotrophic bacteria and fungi of deteriorated wall painting of Herculaneum in Italy. J. Environ. Biol. **32**, 241–250 (2011)
3. Ettenauer, J.D., Jurado, V., Pinãr, G., Miller, A.Z., Santner, M., Saiz-Jimenez, C., Sterflinger, K.: Halophilic microorganisms are responsible for the rosy discolouration of saline environments in three historical buildings with mural paintings. PLoS ONE **9**(8) (2014). doi:10.1371/s0103844
4. Rosado, T., Mirão, J., Candeias, A., Caldeira, A.T.: Microbial communities analysis assessed by pyrosequencing—a new approach applied to conservation state studies of mural paintings. Anal. Bioanal. Chem. **406**, 887–895 (2014)
5. Raimondi, V., Palombi, L., Longoli, D., Cecchi, G., Gomoiu, I.: A lidar experiment for the characterization of phototrophic and heterotrophic biodeteriogens by means of remote sensed fluorescence spectra. In: Taylor & Francis Group London (eds.) Laser in the Conservation of Artworks, pp. 157–162 (2008)
6. Bellezza, S., Albertano, P.: A Chroococcalean species from Roman hypogean sites: characterization of Gloeothece membranacea (Cyanobacteria, Synechoccaceae). Arch. Hidrobiol. Suppl. b Algol. Stud. **109**, 103–112 (2003)

7. Gomoiu, I., Chatzitheodoridis, E., Vadrucci, S., Walther, I.: The effect of spaceflight on growth of *Ulocladium chartarum* colonies on the International Space Station. PLoS ONE **8** (4), (2013). doi:10.1371/s0062130
8. Gorbushina, A.A., Heyrman, J., Dornieden, T., Gonzalez-Delvalle, M., Krumbein, W.E., Laiz, L., Petersen, K., Saiz-Jimenez, C., Swings, J.: Bacterial and fungal diversity and biodeterioration problems in mural painting environments of St. Martins church (Greene–Kreiensen, Germany). Int. Biodeter. Biodegr. **53**, 13–24 (2004)
9. Garg, K.L., Jain, K.K., Mishra, A.K.: Role of fungi in the deterioration of wall paintings. Sci. Total Environ. **167**, 255–271 (1995)
10. Aira, M.J., Jato, V., Stchigel, A.M., Rodríguez-Rajo, F.J., Piontelli, E.: Aeromycological study in the Cathedral of Santiago de Compostela (Spain). Int. Biodeterior. Biodegrad. **60**, 231–237 (2007)
11. Schiavon, N., De Caro, T., Kiros, A., Caldeira, A.T., Parisi, I.E., Riccucci, C., Gigante, G.E.: A multianalytical approach to investigate stone biodeterioration at a UNESCO world heritage site: the volcanic rock hewn churches of Lalibela. Northern Ethiopia. Appl. Phys. A **113**, 843–854 (2013)
12. Ventosa, A., Gutierrez, M.C., García, M.T., Ruiz-Berraquero, F.: Classification of *Chromobacterium marismortui* in a new genus, *Chromohalobacter* gen. nov., as *Chromohalobacter marismortui* comb. nov. nom. rev. Int. J. Syst. Bacteriol. **39**, 382–386 (1989)
13. Laiz, L., Miller, A.Z., Jurado, V., Akatova, E., Sanchez-Moral, S., Gonzalez, J.M., Dionísio, A., Macedo, M.F., Saiz-Jimenez, C.: Isolation of five *Rubrobacter* strains from biodeteriorated monuments. Naturwissenschaften **96**, 71–79 (2009)
14. Imperi, F., Caneva, G., Cancellieri, L., Ricci, M.A., Sodo, A., Visca, P.: The bacterial aetiology of rosy discoloration of ancient wall paintings. Environ. Microbiol. **9**, 2894–2902 (2007)
15. Milanesi, C., Baldi, F., Vignani, R., Ciampolini, F., Faleri, C., Cresti, M.: Fungal deterioration of medieval wall fresco determined by analyzing small fragments containing copper. Int. Biodeter. Biodegr. **57**, 7–13 (2006)
16. Jroundi, F., Gonzalez-Muñoz, M.T., Sterflinger, K., Piñar, G.: Molecular tools for monitoring the ecological sustainability of a stone bio-consolidation treatment at the Royal Chapel, Granada. PLoS ONE. (2015). doi:10.1371/s0132465

Investigation on Switching Operation in Resistive RAM Using In-Situ TEM

Masashi Arita and Yasuo Takahashi

Abstract Our recent works on resistive RAMs (ReRAMs) are reviewed, where in-situ transmission electron microscopy (TEM) realizing simultaneous electric measurements and TEM observations was applied to investigate resistive switching operation of some conductive bridging RAMs (CBRAMs). In multiple switching cycles, the Cu conductive filament was experimentally confirmed to appear in the *Set* process giving the low resistance state (LRS, on-state) and to disappear in the *Reset* process giving the high resistance state (HRS, off-state). No drastic change in the geometry of the conductive filament was seen when the switching current was small. With increasing the current, the filament became thick, but its position was unstable, and too much Cu moved into the switching layer in a wide area. This may induce the device degradation and failure.

1 Introduction

Large resistance change with voltage application was widely known in Perovskite type complex oxides, binary oxides such as NiO, TiO_2, HfO_2 and Ta_2O_5, and solid electrolyte (e.g. Ge-S) with Cu or Ag. In recent years, many works have been reported to apply this phenomenon on non-volatile resistive RAMs (ReRAMs) and on neuromorphic devices [1–4]. To guarantee the operation of these devices, clarification of the switching mechanism is strongly required. Based on the electrochemical discussion of their electric properties, it is a common knowledge that the resistance switching in binary oxides and solid electrolytes is caused by formation and rupture of the conductive filament [1, 2]. However, details of its operation mechanism are still ambiguous and difficult to be clarified only using electric properties. Dynamical observations in real space using in-situ transmission electron microscopy (TEM) are a method to overcome this difficulty, where the

M. Arita (✉) · Y. Takahashi
Graduate School of Information Science and Technology, Hokkaido University,
Kita-14, Nishi-9, Kita-ku, Sapporo 060-0814, Japan
e-mail: arita@nano.ist.hokudai.ac.jp

A.Y. Oral and Z.B. Bahsi Oral (eds.), *3rd International Multidisciplinary Microscopy and Microanalysis Congress (InterM)*, Springer Proceedings in Physics 186,
DOI 10.1007/978-3-319-46601-9_24

electric measurements and TEM observations can be performed synchronously [5–10]. Several types of in-situ TEM holders became commercially available in recent years, and the number of reports in this category has increased. However, works on realistic switching operations such as the current-voltage (*I-V*) switching cycle, the switching repetition and the pulse endurance are rare [11, 12].

In this report, our recent works on ReRAMs using the in-situ TEM are reviewed, which are categorized as the conductive bridging RAM (CBRAM) such as GeS-Cu [13, 14], Cu/MoO_x [11, 15, 16] and Cu/WO_x [17, 18]. In all of these CBRAM systems, the Cu conductive filament was experimentally confirmed to appear in the *Set* process giving the low resistance state (LRS, on-state) and to disappear in the *Reset* process giving the high resistance state (HRS, off-state). No drastic change in the geometry of the conductive filament was seen at the *Set*/*Reset* switching moment, and the filament growth/erasure was seen during continuation of the current flow.

2 Experimental Procedure

Three types of ReRAMs were used for investigation, which were composite GeS-$Cu_{(8–60\ nm)}$ deposited on a wedge-shaped PtIr, $Pt_{(100\ nm)}/Cu_{(30\ nm)}/MoO_{x(50nm)}$ or $Pt_{(100nm)}/Cu_{(30nm)}/WO_{x(20nm)}$ trilayer films on a TiN/Si wafer chip. For all samples, the film deposition was done using conventional RF sputtering (Ar) or reactive sputtering (Ar-20 %O_2) of metal targets at room temperature (RT). In the latter two samples, the Cu and the TiN layers worked as the top electrode (TE) and the bottom electrode (BE), respectively. The GeS-Cu sample was used for in-situ TEM without any further processing, because the tip of the PtIr wedge was thin enough for TEM observations. On the other hand, the ReRAM samples of MoO_x and WO_x were processed using the ion-shadow method [19] which is a kind of the ion-milling method.

In-situ TEM experiments were carried out using the system shown in Fig. 1 composed of a hand-made piezo-driven TEM holder and a JEM-2010 microscope (C_s = 0.5 mm). A movable Pt-Ir probe was contacted to one of the ReRAM devices formed on the TEM sample, and the *I-V* switching cycles were measured using a commercially available source-measure-unit (SMU, Yokogawa GS610). To prevent eternal device destruction caused by the strong overshoot current in the *Set* process, current limitation (compliance current; I_{comp}) was introduced using this SMU. In the GeS-Cu sample, the wedge-shaped PtIr substrate was biased while the probe was grounded. On the other hand, in MoO_x and WO_x samples, the TiN/Si substrate was grounded while the probe was biased. Geometrical change of the filament was dynamically recorded using a CCD camera (30 ms/frame).

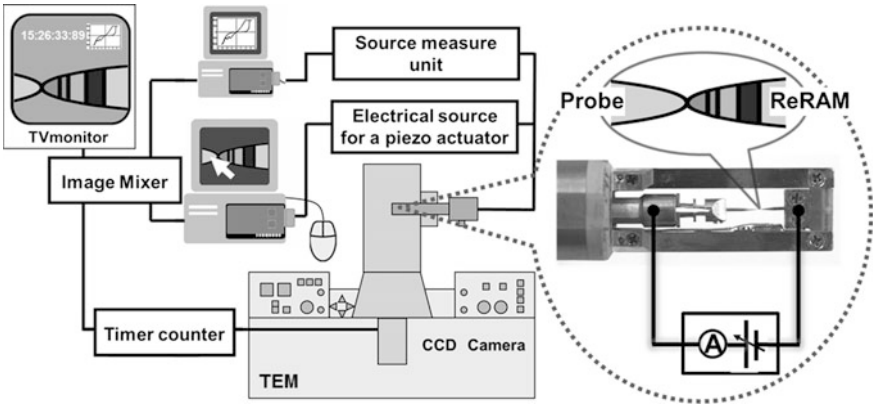

Fig. 1 In-situ TEM system

3 Results and Discussion

3.1 Filament Formation in Cu-GeS

The *I-V* curve measured in TEM is shown in Fig. 2, where the horizontal axis corresponds to the potential of the substrate relative to the probe [13, 14]. The voltage was varied in a sequence of 0 V, +7 V, −2 V and 0 V, and a clear hysteresis curve was obtained. Though the retention time (memory holding time) of the LRS was not long enough for the practical memory application, formation and erasure of the conductive filament was clearly confirmed.

The TEM images extracted from the video are shown in Fig. 3. There are a Cu-GeS amorphous film containing Ge nanocrystals on the Pt-Ir substrate (Fig. 3a). In the first quadrant of the *I-V* graph, where the substrate was positively biased

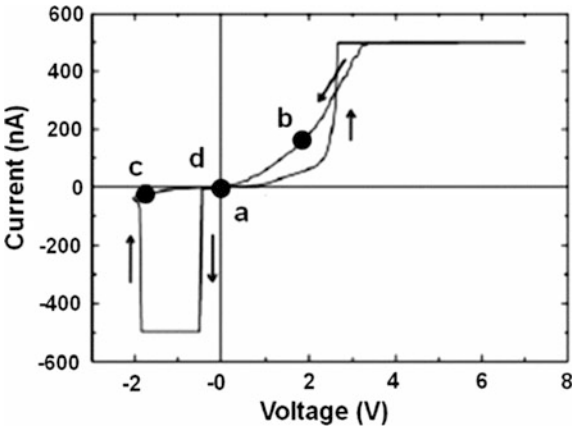

Fig. 2 *I-V* curve of Cu-GeS

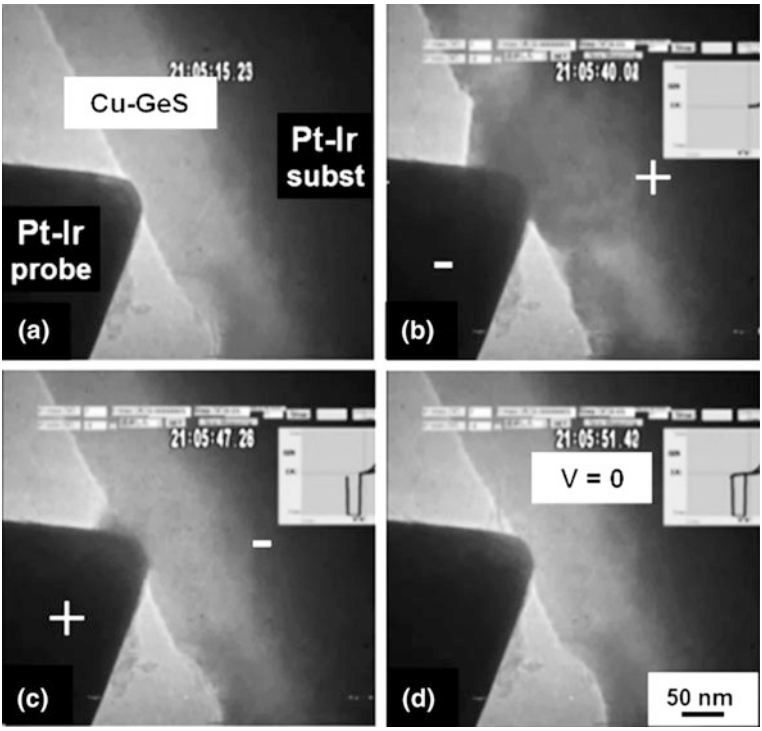

Fig. 3 Microstructure corresponding to Fig. 2. Video **a** in the initial state, **b** and **c** with positive or negative voltage, and **d** after the *I-V* cycle

relative to the probe, the current increased gradually. There was drastic increase at the voltage of +2.6 V, and its resistance was converted to the LRS (*Set* operation). Correspondingly to this change, a filamentary dark contrast appeared (Fig. 3b). In the selected area diffraction (SAD) pattern during the *Set* process, Debye rings of Cu appeared. In addition, the energy dispersive X-ray spectroscopy (EDX) measurements were done during the *Set* process with positive bias voltage to the substrate (but on another filament than that in Fig. 3). In Fig. 4, the EDX spectra before (Fig. 4a) and during (Fig. 4b) the *Set* operation are compared. It was clearly identified that the deposit contained much Cu. Considering these two results, the deposit appeared in the *Set* process was concluded to be made of Cu nanocrystals. Afterwards, a negative voltage sweep was done, and the deposit gradually disappeared and completely erased at about −2.8 V (Fig. 3c, d). The resistance showed a sudden increase at this moment. This is the *Reset* process which converts the LRS to the HRS. The deposit observed here worked as a conductive filament for the CBRAM switching.

Repeating switching cycles, the *Set* voltage (V_{set}) gradually decreased. This indicates that the Cu-GeS layer in the HRS after the *Reset* operation changed from the initial state as confirmed in Fig. 5. First, a filament was formed (Fig. 5a) and

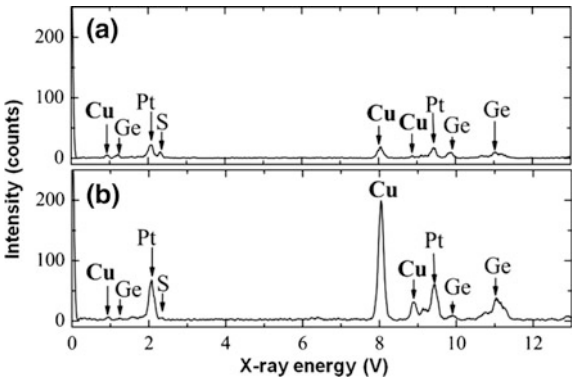

Fig. 4 EDX spectra **a** without and **b** with positive voltage application. The deposit contained much more Cu than other regions

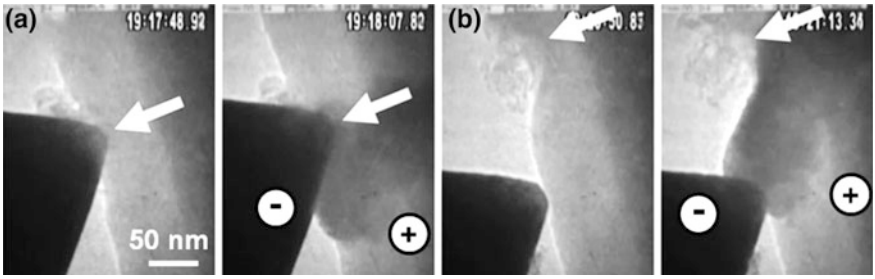

Fig. 5 Filament growth in sequential switching cycles (**a** and **b**), where *arrows* indicate corresponding position. In each figure, the *left panel* is before the switching cycle, and the *right panel* is with positive voltage. The filament appeared almost in same place

erased. Afterwards, the Pt-Ir probe was shifted by 100 nm (Fig. 5b left panel), and a positive voltage was applied to generate a filament again (Fig. 5b right panel). The filament appeared from the probe toward the position of the first filament. It did not reach the nearest position on the substrate. The region in which the filament was formed once must be a priority position for the formation and the growth of a filament. It is expected that there are some residuals such as Cu nanocrystals even after filament erasure, which can behave as filament nuclei. This is thought to make the filament formation easy and to induce reduction of V_{Set}.

The results mentioned above suggest that the Cu filament is formed/erased by application of positive/negative voltage, and the CBRAM operation is achieved. Checking the TEM video, the filament grew from the probe (negative voltage side) with positive voltage, and it was ruptured and erased from the substrate (negative voltage side) with negative voltage. This dynamics fits to the electrochemical model (ECM) reported so far, where the Cu ions drifted along the electric field are reduced to be the metal by receiving electrons on the cathode surface, and the Cu filament is

formed towards the anode [1]. However, the current was small (<1 μA), and the retention property of the LRS was not good enough. The probe used as the BE was mechanically contacted to the solid electrolyte switching layer (Cu-GeS), and this is different from the realistic CBRAM device. To investigate more realistic switching operation, a Cu/MoO_x/TiN trilayer CBRAM will be discussed in the next subsection.

3.2 *Set/Reset Switching of Cu/MoO_x/TiN*

The sample was Pt/Cu/MoO_x/TiN/Si where Cu and TiN were the TE and BE, respectively [11, 15, 16]. The device size was 350 nm in diameter. The electric properties were measured between the Pt cap layer (biased) and the Si substrate (grounded). An example of the *I-V* curve is shown in Fig. 6a, which was the second switching cycle after the initialization process called as *Forming*. A shaper *Set* than in Cu-GeS is seen in the first quadrant. The corresponding TEM images extracted from a video are presented in Fig. 6b. The resistance state was the HRS between the states A and B, and there was no clear change in the image. Just after the *Set* switching (state C), a small dark region (nucleus of the filament) appeared near the TiN BE. Though the current was almost the compliance value (I_{comp}), there was no dark region binding the TE and BE. The ionic current of the Cu anion is thought to contribute to electric conduction. Afterwards, the filament grew from the TiN BE towards the Cu TE. The bridging of the filament between the TE and the BE was completed within 200 ms.

The *Reset* operation was started at 5 min. after the *Set* process was completed. The LRS was kept after this interval, because I_{comp} was large (400 μA). Two small current jumps between −1 and −2 V in Fig. 6a correspond to the *Reset* switching. The *Reset* curve was uneven as frequently observed in conventional CBRAM devices. This may suggest that *Reset* is more complicated process than *Set*. In the corresponding TEM image (Fig. 6b), there is no clear structure change just after *Reset* switching (state F). This switching is thought to occur very locally, and it was

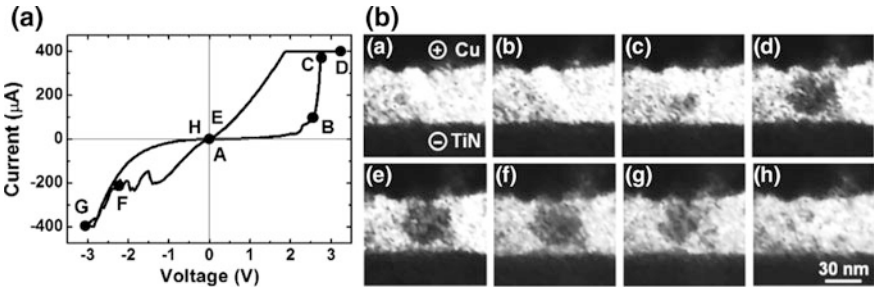

Fig. 6 **a** I-V characteristics of Cu/MoO_x/TiN and **b** TEM images during in-situ observation

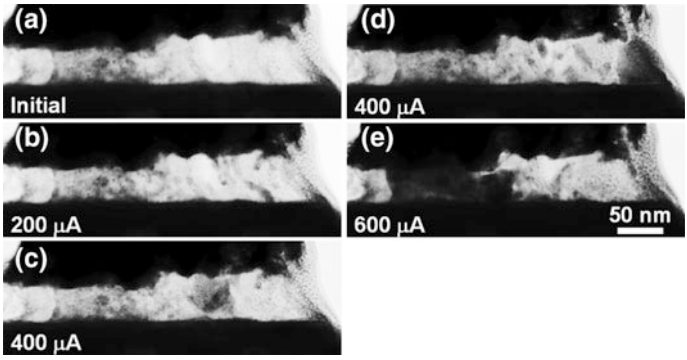

Fig. 7 TEM images of Cu/MoO_x/TiN. **a** Initial state and **b–e** LRS with increasing I_{comp}

not identified in the TEM image. Increasing negative current to about −300 μA (at −2.6 V), the filament was ruptured near the interface between MoO_x and TiN and shrank toward the Cu TE (states G). This process with additional negative current is called the *over-Reset* process in this report. The filament erasure here cannot be explained by the ECM model where the filament shrinks from the Cu TE to the BE. In the present work, the surface of the TiN BE was oxidized. The resistance at this oxidized region is high, and the local temperature must increase by Joule heating. Thus, it is thought that the electrochemical reaction of Cu in this region preferentially occurred, and the Cu filament shrank toward the TE. The current of 100 μA (or more) was used for switching operation in many CBRAM devices reported earlier. While the details are still obscure, it must be sure that the Joule heat influences the *Reset* operation.

In this paragraph, the filament position and size will be discussed. Images after *Set* of five switching cycles are compared in Fig. 7, where I_{comp} was increased stepwise. Here, the filament was almost completely erased by performing *over-Reset*. The initial state was the HRS, and the contrast in Fig. 7a is due to the matters such as the outer shape of the specimen. In the first switch with I_{comp} = 200 μA, a filament having a width of 7 nm was formed (Fig. 7b). By increasing I_{comp}, the filament width increased to 35, 45 and 100 nm in Figs. 7c–e respectively. This increase can be used for the multi-bit memory operation. However, the filament position changed as seen in these figures. This position instability is thought to be caused by almost complete filament erasure during *over-Reset*.

3.3 Device Degradation of Cu/WO_x/TiN

The investigated sample was Pt/Cu/WO_x/TiN/Si [17, 18]. Examples of *I-V* graphs measured during in-situ TEM are shown in Fig. 8a–c where the horizontal axis denotes the potential of the Cu electrode relative to TiN/Si. Figure 8a is the

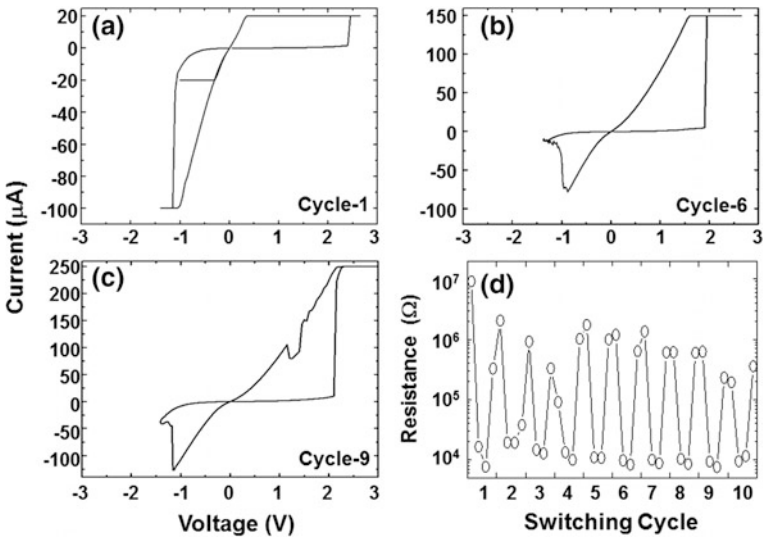

Fig. 8 **a**–**c** *I-V* curves during in-situ TEM of Cu/WO_x/TiN and **d** the cyclic endurance where the resistance was estimated at ±0.3 V

Forming curve. There was a current jump at 2.4 V. This resistance change to the LRS was much quicker than in MoO_x. Correspondingly, a filament was formed between the Cu and TiN electrodes within one video frame (30 ms). The LRS was kept just before the *Reset* operation which was performed at 9.5 min after *Set*, and the retention time was long enough for *in-situ* TEM experiments. By carefully checking the video during the *Reset* operations, clear filament erasure was not identified though sharp switching to the HRS was realized. No strong *over-Reset* was adopted in this switching series as seen in Fig. 8b, c, and thus the filament was not erased (but with switching to the HRS). This result suggests that ReRAM switching occurs in local area of the filament. The resistance change in switching repetition (endurance graph) is shown in Fig. 8d. The resistance ratio of HRS/LRS was kept about 100, and a reasonable CBRAM endurance property is seen. However, as seen in this graph, the resistance in the HRS gradually decreased with the switching cycle. This degradation is known also in realistic ReRAM devices, and it has been reported to induce the endurance failure where the ReRAM switching cannot be achieved [20, 21]. This is believed to be caused by imbalance between *Set* and *Reset*. In Fig. 9, TEM images after *Set*/*Reset* switching cycles are compared. During switching repetition with increasing I_{comp}, Cu moved into the WO_x layer in a wide area, and the effective thickness of the WO_x layer became thin. This is thought to be the origin of the endurance failure.

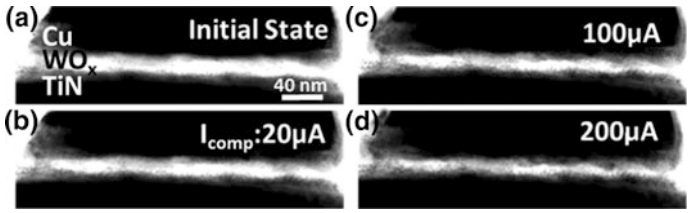

Fig. 9 TEM images of Cu/WO_x/TiN. **a** Initial state and **b–e** LRS after the continuous *Set* operations with increasing compliance current

4 Conclusion

In this work, in-situ TEM was applied on three CBRAMs to investigate the microstructure during the switching operation. It was experimentally confirmed that the Cu filament is formed in *Set*, ruptured in *Reset* and erased in *over-Reset*. The filament becomes thick with increasing the operation current, but its position becomes instable. It was also confirmed that Cu moved into the solid electrolyte and thinned the switching layer. This reduces the resistance of the HRS and finally induces the endurance failure. The retention property must improve by increasing the *Set* current, and large resistance ratio of HRS/LRS is expected by *over-Reset*. However, these treatments induce instability of the filament position and movement of excess Cu in wide area. These can be origins of device failure. Selection of materials and the device structure for easy *Set*/*Reset* balancing must be important for further development of ReRAM devices.

Acknowledgments This work was supported by KAKENHI by JSPS (Nos. 25420279, 26630141, 15H01706) and the Mitsubishi Foundation. Part of this work was collaborated with STARC and Cooperative Research Program of "Network Joint Research Center for Materials and Devices". Support by the Nanotechnology Platform Program is also acknowledged. We are also grateful to our laboratory members for collaboration.

References

1. Waser, R., Aono, M.: Nanoionics-based resistive switching memories. Nat. Mater **6**, 833–840 (2007). doi:10.1038/nmat2023
2. Akinaga, H., Shima, H.: Resistive random access memory (ReRAM) based on metal oxides. Proc. IEEE **98**, 2237–2251 (2010). doi:10.1109/JPROC.2010.2070830
3. Prezioso, M., Merrikh-Bayer, F., Hoskins, B.D., Adam, G.C., Likharev, K.K., Strukov, D.B.: Training and operation of an integrated neuromorphic network based on metal-oxide memristors. Nature **521**, 61–64 (2015). doi:10.1038/nature14441
4. DeSalvo, B., Vianello, E., Garbin, D., Bichler, O., Perniola, L.: From memory in our brain to emerging resistive memories in neuromorphic systems. In: Proceedings of 7th International Memory Workshop (IMW), pp. 9–12. IEEE, Piscataway (2015). doi:10.1109/IMW.2015.7150286

5. Fujii, T., Kaji, H., Kondo, H., Hamada, K., Arita, M., Takahashi, Y.: I-V hysteresis of $Pr_{0.7}Ca_{0.3}MnO_3$ during TEM observation. IOP Conf. Ser. Mater. Sci. Eng. **8**, 012033 (2010). doi:10.1088/1757-899X/8/1/012033
6. Kwon, D.-H., et al.: Atomic structure of conducting nanofilaments in TiO_2 resistive switching memory. Nat. Nanotechnol. **5**, 148–153 (2010). doi:10.1038/NNANO.2009.456
7. Fujii, T., et al.: I-V measurement of NiO nanoregion during observation by transmission-electron microscopy. J. Appl. Phys. **109**, 053702 (2011). doi:10.1063/1.3553868
8. Choi, S.-J., et al.: In situ observation of voltage-induced multilevel resistive switching in solid electrolyte memory. Adv. Mater. **23**(3272–3277), 2011 (2011). doi:10.1002/adma.00507
9. Yang, Y., Gao, P., Gaba, S., Chang, T., Pan, X., Lu, W.: Observation of conducting filament growth in nanoscale resistive memories. Nat. Commun. **3**, 732 (2012). doi:10.1038/ncomms1737
10. Liu, Q., et al.: Real-time observation on dynamic growth/dissolution of conductive filaments in oxide-electrolyte-based ReRAM. Adv. Mater. **24**, 1844–1849 (2012). doi:10.1002/adma.201104104
11. Kudo, M., Arita, M., Ohno, Y., Takahashi, Y.: Filament formation and erasure in molybdenum oxide during resistive switching cycles. Appl. Phys. Lett. **105**, 173504 (2014). doi:10.1063/1.4898773
12. Kudo, M., Arita, M., Takahashi, Y., Ohba, K., Shimuta, M., Fujiwara, I.: Visualization of conductive filament during write and erase cycles on nanometer-scale ReRAM achieved by in-situ TEM. In: Proceedings of 7th International Memory Workshop (IMW), pp. 85–88. IEEE, Piscataway (2015). doi:10.1109/IMW.2015.7150312
13. Fujii, T., Arita, M., Takahashi, Y., Fujiwara, I.: In situ transmission electron microscopy analysis of conductive filament during solid electrolyte resistance switching. Appl. Phys. Lett. **98**, 212104 (2011). doi:10.1063/1.3593494
14. Fujii, T., Arita, M., Takahashi, Y., Fujiwara, I.: Analysis of resistance switching and conductive filaments inside Cu-Ge-S using in situ transmission electron microscopy. J. Mater. Res. **27**, 886–896 (2012). doi:10.1557/jmr.2011.437
15. Kudo, M., Ohno, Y., Hamada, K., Arita, M., Takahashi, Y.: In-situ TEM observation of Cu/MoO_x ReRAM switching. ECS Trans. **58**, 19–25 (2013). doi:10.1149/05805.0019ecst
16. Arita, M., Ohno, Y., Takahashi, Y.: Switching of $Cu/MoO_x/TiN$ CBRAM at MoO_x/TiN interface. Phys. Status Solidi A **213**, 306–310 (2016). doi:10.1002/pssa.201532414
17. Takahashi, A., Ohno, Y., Kudo, M., Nakane, A., Arita, M., Takahashi, Y.: Study on in-situ TEM observation of WO_x ReRAMs with Cu top electrodes. Paper presented at European Material Research Society (EMRS) 2015, Spring Meeting, Congress Center, Lille, 11–15 May 2015
18. Arita, M., Takahashi, A., Ohno, Y., Nakane, A., Tsurumaki-Fukuchi, A., Takahashi, Y.: Switching operation and degradation of resistive random access memory composed of tungsten oxide and copper investigated using in-situ TEM. Sci. Rep. **5**, 17103 (2015). doi:10.1038/srep17103
19. Kudo, M., et al.: Preparation of resistance random access memory samples for in situ transmission electron microscopy experiments. Thin Solid Films **533**, 48–53 (2013). doi:10.1016/j.tsf.2012.10.102
20. Rahama, S.Z., et al.: Excellent resistive memory characteristics and switching mechanism using a Ti nanolayer at the Cu/TaO_x interface. Nano. Res. Lett. **7**, 345 (2012). doi:10.1186/1556-276X-7-345
21. Chen, Y.Y., et al.: Balancing SET/RESET pulse for $>10^{10}$ endurance in HfO_2/Hf 1T1R bipolar RRAM. IEEE Trans. Electr. Dev. **59**, 3243–3249 (2012). doi:10.1109/TED.2012.2218607

Simulation and Verification of Tip-Induced Polarization During Kelvin Probe Force Microscopy Measurements on Film Capacitors

D.A. Nielsen, V.N. Popok and K. Pedersen

Abstract Kelvin probe force microscopy (KPFM) is widely used as characterization tool on functional heterostructures and components but it often suffers from measurement artifacts on such structures because the presence of the biased cantilever tip transforms the actual surface potential. In this work we have developed a physics-based finite element model of KPFM measurements on dielectrics in order to investigate the impact of tip-induced polarization. The model is compared with experiments on film capacitors, where it is found that tip-induced polarization is a significant contributor to the potential profiles obtained by KPFM.

1 Introduction

KPFM is a very powerful tool in the field of materials characterization. It allows to measure electric surface potential distributions with nano-scale resolution [1–3]. It has increasingly being used as a characterization tool in the study of dielectric films, multi-layered systems and interfaces [4–6]. However, the potential distributions measured by KPFM on such structures are often affected by tip-induced polarization of the sample [7]. This effect is rarely considered and the measured surface potentials on, for example, organic field-effect transistors, layered capacitors and solar cells are wrongly interpreted as actual ones [8–10].

The use of KPFM has also entered the field of reliability and failure analysis of active and passive electronic components [11]. In particular, capacitors are of great importance within the field of power electronics but as any other electronic devices they undergo fatigue [12]. For that reason the intention is to use KPFM as a failure analysis tool to investigate metallization corrosion and degradation of the dielectric. This does, however, require a deeper knowledge in how to interpret the measured potential profiles and how to avoid measurement artifacts when using KPFM on metal/dielectric structures.

D.A. Nielsen · V.N. Popok (✉) · K. Pedersen
Department of Physics and Nanotechnology, Aalborg University, Aalborg, Denmark
e-mail: vp@nano.aau.dk

A.Y. Oral and Z.B. Bahsi Oral (eds.), *3rd International Multidisciplinary Microscopy and Microanalysis Congress (InterM)*, Springer Proceedings in Physics 186,
DOI 10.1007/978-3-319-46601-9_25

In this work we have prepared film capacitors for analysis by micro-sectioning. We have measured the surface potential distributions by KPFM and found that they do not correspond to the expected distributions. In order to explain the measured surface potentials we have developed a physics-based model of the measured system that takes into account polarization of the dielectric due to the presence of the cantilever tip.

2 Experimental

The film capacitors used in this work were of the metallized polypropylene (PP) type and they were new, meaning that they have not been exposed to any electrical, thermal or environmental stresses. The samples were prepared using micro-sectioning method as described in [13] with some details mentioned below. The capacitors were initially cast into epoxy for structural support. Next, the surface of interest was exposed using a water-cooled, rotating diamond saw blade. The surface was then grinded using a series of sanding pads. A 2 mm thick slice was cut from the sample and, finally, wires were soldered on to the terminals, enabling application of an external voltage during KPFM measurement. Optical images of a typical capacitor sample and its cross-section at high magnification are shown in Fig. 1.

The AFM and KPFM measurements were carried out using an NTEGRA-Aura nanolaboratory from NT-MDT. The cantilevers used in this study were the platinum-iridium coated NSG01/Pt type, also from NT-MDT, with a tip apex radius of 35 nm according to the manufacturer. The KPFM measurements were performed in two-pass mode. To measure the surface potential the samples were scanned twice: first with both leads connected to the AFM ground and second with 5 V DC applied to one of the terminals while keeping the second one grounded.

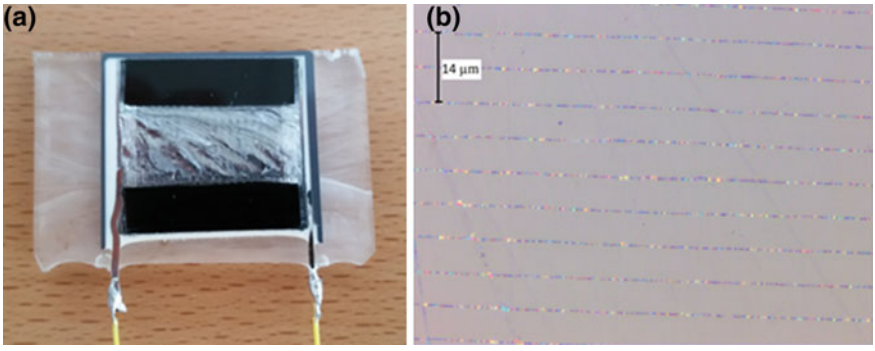

Fig. 1 **a** Cross-section of film capacitor prepared for KPFM analysis and **b** optical microscopy image of it where bright stripes represent the metallization layers

3 Tip/Capacitor System Model

Tip-induced polarization of a dielectric has shown to have a great impact on KPFM measurements, especially at interfaces with metallic layers or contacts [7]. Furthermore, the polarization strongly depends on the position of the tip which moves across the surface during scanning. For that reason, a three-dimensional finite element of a system containing the cantilever tip and layered metal/polymer sample (resembling the cross-sectional structure of the capacitor) is constructed. It serves to predict the surface potential distribution measured by KPFM. It also allows calculation of the "true" potential distribution that exists on the surface of a capacitor structure without presence of the tip.

The simulations are carried out by COMSOL Multiphysics 4.3. The tip is represented by a cone with a hemispherical apex. The film capacitor surface is constructed as a solid PP dielectric with periodic vertical planes of the metallization layers. Geometry and close-up of the tip are shown in Fig. 2.

The model utilizes a stationary simulation tool that solves the Poisson equation using a set of boundary conditions as a starting point. It is assumed that there are no free charges in the system and therefore the charge density term in the Poisson equation is set to zero. The electric potential at the tip surface is fixed at −1.4 V corresponding to the contact potential difference between the aluminum metallization and the platinum iridium coating of the tip. The width (film thickness) of the PP layers is 7 µm and its dielectric constant is set to 2.2. The tip height is set to 5 µm, the tip apex radius to 35 nm and the tip half-aperture angle to 15°. The tip-to-sample distance is 10 nm as was the case for the KPFM measurements.

Simulation sets were carried out for a grounded capacitor and a capacitor with 5 V applied to every second metallization layer. In both simulation sets the spatial potential distribution is calculated for tip positions on a line spanning two metallization layers with 0.5 µm between every tip position. For every tip position the potential profile along the scan line is recorded. A point spread function (PSF) de-rived by COMSOL according to [14] and presented in [7] is then applied in order to simulate the potential as measured by KPFM.

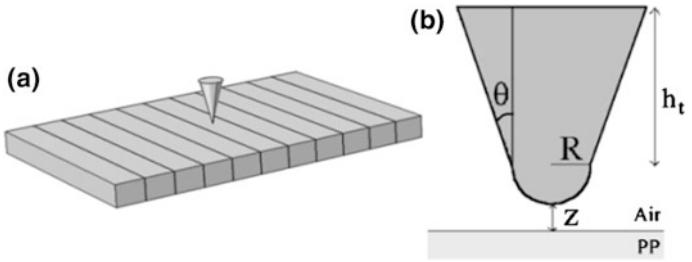

Fig. 2 **a** 3D image of the sample geometry and **b** 2D image of the tip geometry, where h_t is the tip height, R is the tip apex radius, z is the tip-sample distance, and θ the half aperture angle

4 Results and Discussion

Initially, the KPFM measurements are performed on the sample with both connector leads grounded. Hence, there should not be any potential distribution in the component. However, as can be seen in Fig. 3a the KPFM measurement reveals a periodic potential distribution corresponding to periodicity of the PP and metal layers. Then, 5 V DC is applied to one of the terminals, while the power supply ground was connected to the AFM ground. The measured potential profile is given in Fig. 3b which shows a period corresponding to twice the PP film thickness.

From the KPFM measurements presented in Fig. 3 it is clear that the measured potential profiles do not resemble the expected potential distributions in a grounded and biased capacitor, respectively. Furthermore, in Fig. 3b it is seen that the measured potential difference between biased and grounded metallization layers are in the range of 1.5 V but not 5 V applied during the measurement. This phenomenon can be explained by the tip-induced polarization of PP layers as well as by fact that the biased cantilever beam being affected by the electrostatic potentials of metallization layers during the measurement.

The results of the potential simulations for the grounded and biased capacitor are shown in Fig. 4a, b, respectively. This modelling includes the potential distributions after the application of the PSF. The surface potential profiles that would exist without presence of the tip are also shown.

As can be seen for the grounded capacitor in Fig. 4a, the simulated potential distribution including the PSF both qualitatively and quantitatively resembles the measured one (see Fig. 3a). One distinct difference is that the peaks at the

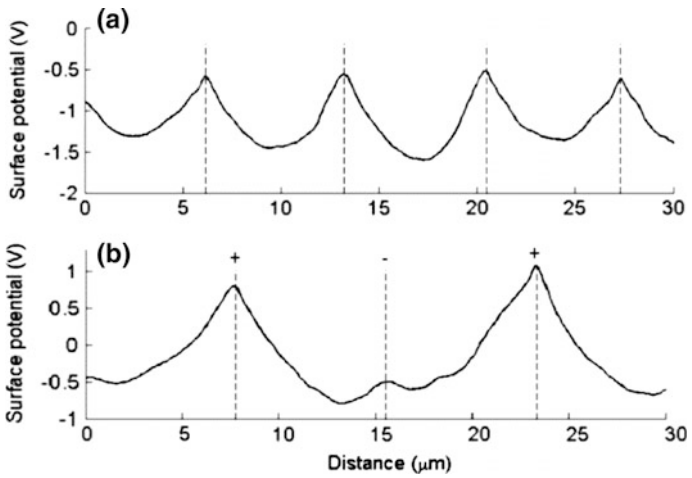

Fig. 3 Line profiles of the KPFM measurements on **a** grounded and **b** biased capacitor, respectively. The *dashed lines* indicate positions of metallization layers. The *plus* and *minus* signs show whether the metallization is connected to bias or ground

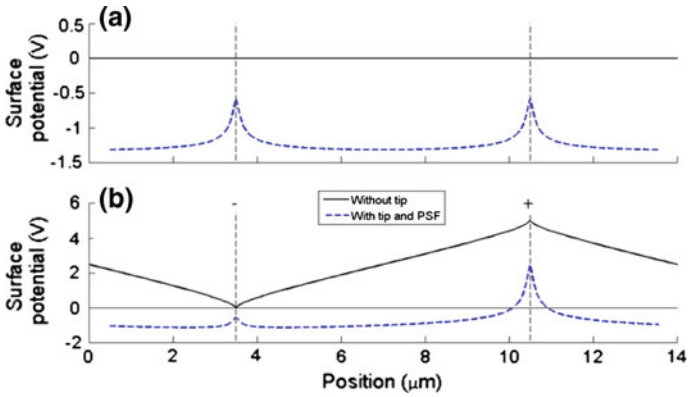

Fig. 4 Simulated surface potential profiles without the tip (*black solid line*) and with the tip (*dashed blue line*) for the **a** grounded and **b** biased capacitor, respectively

metallization layers are broader in the measurements compared to the simulations. It is expected that this is a result of the exclusion of the cantilever beam from the model, which may have an impact during KPFM measurements, as described in [15].

The profile for the biased capacitor, shown in Fig. 4b, is also observed to be in good agreement with the measured one (see Fig. 3b). The potential difference between the biased and grounded metallization layers is larger for the simulated potential profiles compared to the measured ones. Also the width of the peaks is smaller for the simulated potential distributions. Again, it is expected to be caused by the cantilever beam.

From the results presented in Figs. 3 and 4 it is evident that tip-induced polarization during KPFM on layered metal/polymer structures has a great impact on the measured surface potential profiles. It is also clear that the potential measured by KPFM does not resemble the actual surface potential distribution of the sample. Thus, great care and consideration should be taken when applying KPFM to heterostructures. However, if the physical phenomena that occur during KPFM measurements are well investigated and understood, this method is still a powerful tool in the analysis of dielectric components and heterostructures.

5 Conclusion

In this work we have investigated the phenomenon of tip-induced polarization during KPFM on cross-sectional slides of capacitors by comparing potential profiles from measurements and simulations. Samples of standard film capacitors were prepared by micro-sectioning and the surface potential distributions were measured by KPFM. An electrostatic finite element model that calculates the expected surface

potential distributions on the layered metal/polymer structures was developed and the results were compared to the KPFM measurements. Good agreement was found between the model and experiments, where the small differences are assigned to the exclusion of the cantilever beam and general simplicity of the model. Thus, it is concluded that tip-induced polarization during KPFM measurements is one of the significant factors which can lead to misinterpretation of the obtained potential distributions on samples with dielectric materials.

Acknowledgments This work is a part of the research activity within the Center of Reliable Power Electronics (CORPE) funded by the Innovation Fund Denmark.

References

1. Nonnenmacher, M., O'Boyle, M.P., Wickramasinghe, H.K.: Kelvin probe force microscopy. Appl. Phys. Lett. **58**, 2921–2923 (1991). doi:10.1063/1.105227
2. Melitz, W., Shen, J., Kummel, A.C., Lee, S.: Kelvin probe force microscopy and its application. Surf. Sci. Rep. **66**, 1–27 (2011). doi:10.1016/j.surfrep.2010.10.001
3. Kou, L., Ma, Z., Li, Y.J., Naitoh, Y., Komiyama, M., Sugawara, Y.: Surface potential imaging with atomic resolution by frequency-modulation Kelvin probe force microscopy without bias voltage feedback. Nanotechnology **26**, 195701 (2015). doi:10.1088/0957-4484/26/19/195701
4. Barth, C., Henry, C.R.: Surface double layer on (001) surfaces of alkali halide crystals: a scanning force microscopy study. Phys. Rev. Lett. **98**, 136804 (2007). doi:10.1103/PhysRevLett.98.136804
5. Nowak, R., Moraru, D., Mizuno, T., Jablonski, R., Tabe, M.: Potential profile and photovoltaic effect in nanoscale lateral pn junction observed by Kelvin probe force microscop. Thin Solid Films **557**, 249–253 (2014). doi:10.1016/j.tsf.2013.08.115
6. Popok, V.N., Kalabukhov, A., Gunnarsson, R., Lemeshko, S., Claeson, T., Winkler, D.: Kelvin probe force microscopy study of $LaAlO_3/SrTiO_3$ heterointerfaces. J. Adv. Microsc. Res. **5**, 26–30 (2010). doi:10.1166/jamr.2010.1020
7. Nielsen, D.A., Popok, V.N., Pedersen, K.: Modelling and experimental verification of tip-induced polarization in Kelvin probe force microscopy measurements on dielectric surfaces. J. Appl. Phys. **118**, 195301 (2015). doi:10.1063/1.4935811
8. Bürgi, L., Sirringhaus, H., Friend, R.: Noncontact potentiometry of polymer field-effect transistors. Appl. Phys. Lett. **80**, 2913–2915 (2002). doi:10.1063/1.1470702
9. Okamoto, T., Kitagawa, S., Inoue, N., Ando, A.: Electric field concentration in the vicinity of the interface between anode and degraded BaTiO3-based ceramics in multilayer ceramic capacitor. Appl. Phys. Lett. **98**, 072905 (2011). doi:10.1063/1.3555466
10. Jiang, C.-S., Moutinho, H.R., Geisz, J.F., Al-Jassim, M.M.: Measurement of built-in electrical potential in III-V solar cells by scanning Kelvin probe microscopy. J. Appl. Phys. **93**(12), 10035 (2003). doi:10.1063/1.1573736
11. Nielsen, D.A., Popok, V.N., Pedersen, K.: Electric field mapping inside metallized film capacitors. In: Proceedings of the IEEE Annual Reliability and Maintainability Symposium, (2015). doi:10.1109/RAMS.2015.7105153
12. Yang, S., Bryant, A., Mawby, P., Xiang, D., Ran, L., Tavner, P.: An industry-based survey of reliability in power electronic converters. IEEE Trans. Ind. Appl. **47**(3), 1441–1451 (2011). doi:10.1109/TIA.2011.2124436

13. Pedersen, K.B., Kristensen, P.K., Popok, V.N., Pedersen, K.: Micro-sectioning approach for quality and reliability assessment of wire bonding interfaces in IGBT modules. Microelectron. Reliab. **57**, 1422–1426 (2013). doi:10.1016/j.microrel.2013.07.010
14. Palermo, V., Palma, M., Samorì, P.: Electronic characterization of organic thin films by Kelvin probe force microscopy. Adv. Mater. **18**, 145–164 (2006). doi:10.1002/adma.200501394
15. Elias, G., Glatzel, T., Meyer, E., Rosenwaks, Y.: The role of the cantilever in Kelvin probe force microscopy. Beilstein J. Nanotechnol. **2**, 252–260 (2011). doi:10.3762/bjnano.2.29

Estimating 3D Volume of Dirt Particles Using Depth from Shadow

Peter Frühberger, Thomas Stephan, Jan Burke and Jürgen Beyerer

Abstract Measuring the volume of dirt particles within the context of technical cleanliness is a crucial task, because the measured 3D shape yields important information concerning the risks those particles might cause while operating the technical component in the intended application. The production process therefore needs to be optimized to take care, that such particles are not introduced into the final product during fabrication. Measuring 3D volume in the range of a few microns concerning the area of a particle implies expensive microscope measuring devices. In this paper we describe a hardware approach combined with software algorithms using eight LED lights for illuminating the specimen from various known directions. The LEDs are used to produce cast shadows of the specimen to be inspected. The circular layout of the LEDs takes care to illuminate the particles out of different directions to yield shadows surrounding the whole object. The brightness of the LEDs can be manipulated to adapt for various specimen with different reflection properties. Our model driven approach uses a grid, which is aligned to the image data in order to sample the surface for estimating the height at those discrete positions. The model-driven approach incorporates the measurement results given by established state-of-the-art microscopes for initial calibration. The estimated heights are illustrated in a 2.5D pseudo-color representation and evaluated from a quality point of view. The approach described in this paper yields a practical solution for estimating 3D shape and volume with little hardware requirements and therefore low maintenance costs.

P. Frühberger · T. Stephan · J. Burke (✉) · J. Beyerer
Systems for Measurement, Control and Diagnosis (MRD), Fraunhofer Institute of Optronics, System Technologies and Image Exploitation IOSB, Fraunhoferstr. 1, 76131 Karlsruhe, Germany
e-mail: jan.burke@iosb.fraunhofer.de

P. Frühberger · T. Stephan · J. Beyerer
Vision and Fusion Laboratory (IES), Karlsruhe Institute of Technology (KIT), Adenauerring 4, 76131 Karlsruhe, Germany

A.Y. Oral and Z.B. Bahsi Oral (eds.), *3rd International Multidisciplinary Microscopy and Microanalysis Congress (InterM)*, Springer Proceedings in Physics 186,
DOI 10.1007/978-3-319-46601-9_26

1 Introduction

Estimating the volume and the 3D shape of dirt particles in the context of technical cleanliness is a crucial task as it yields important information concerning the risks such particles might cause inside technical components. The fabrication process therefore needs to be adjusted, such that perturbing particles are not introduced into the attachment parts. According to [1] particles within a range of 50–1000 µm diameter are relevant and need to be detected. 3D shape and therefore the volume is not yet a mandatory result demanded by this spec, but given the impact, especially concerning the possible conglomeration, it will most likely be added in the future. This paper at hand describes an image processing approach for detecting and analyzing clotted residuals inside of those components, e.g. motor parts and cylinders that would clog supply lines during operation. A cost-efficient setup, consisting of an industrial camera in combination with a developed LED ring light illumination is used to extract volume information by illuminating the sample from different directions.

2 Hardware and Software Setup

The hardware setup consists of three components, a custom-built double LED ring light in combination with an industrial camera equipped with a bi-telecentric objective. The LEDs used in this setup are fabricated by Nichia company having a color temperature of 5000 K while providing 4.16 W electrical power. The angle of radiation is specified as 120° and therefore suitable for uniform illumination while producing sharp shadows. The lower ring consists of eight LEDs arranged equally spaced to illuminate the specimen from a flat angle as shown in Fig. 1c. The upper ring is used to acquire homogeneous illuminated overview images (Fig. 1b). The second component is an industrial color camera Manta G-419C of ALLIED Vision Technologies with a resolution of 2048 × 2048 pixels. This camera was combined

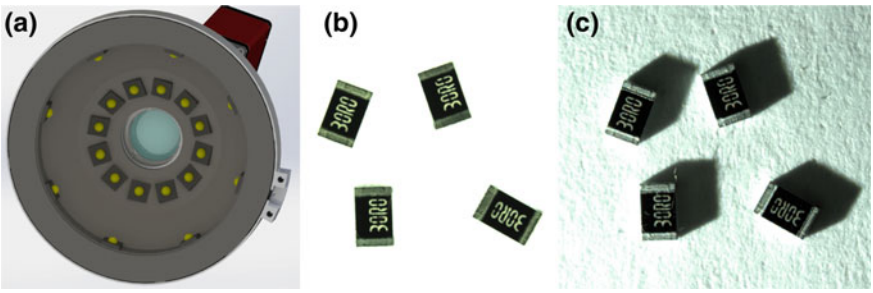

Fig. 1 Illustration of the hardware setup showing the LED ring light (**a**), an overview image using the upper ring (**b**) and resulting shadows using one of the LEDs of the lower ring (**c**)

with the bi-telecentric objective TC 2M HR 016-C manufactured by Opto Engineering. The setup allows a pixel size of 4.5 μm^2 and a depth of view of 2.0 mm. Therefore the field of view is 9.2×9.2 mm^2. In order to scan larger surfaces, this setup can be extended with a motorized stage as shown in [2]. The software implementation was done in C++ using the opencv image processing library [3].

3 Algorithm and Implementation

The initial step of the algorithm is finding a robust calibration to estimate the positions of the lights $\mathbf{L}_i$ in three-dimensional space. The center point $\mathbf{p_c} = (c_x, c_y, z)^T$ of the spanned vector space is set to $\mathbf{0}$ at the center of the projected image scene. The unit of this vector is *pixel* in the x and y dimension. The z dimension is a scalar value mapped to a metric scale by comparing to ground-truth height measurements or a-priori known height of a common specimen. When assuming a punctual light source $\mathbf{L}_i$ with its correspondences $C_i = \{c_{jk}\}$ with $|C_i| \geq 2$, c_{jk} representing a point on the object $\mathbf{o_j}$ and its corresponding shadow contour point $\mathbf{s_k}$, it is possible to construct equations of lines $l(c_{jk})$ with $\mathbf{o_j}$ as support vector and $t \cdot (\mathbf{s_k} - \mathbf{s_j})$ with $t \in \mathbb{R}$ as the direction vector. The light source $\mathbf{L}_i$ can then be estimated by finding the intersection point by pairwise constructing lines $l(c_{jk})$ and $l(c_{j'k'}), j' \neq j, k' \neq k$. Because of deviations when computing the corresponding points a single intersection point does not necessarily exist. Therefore we need to solve this problem by finding a point $\mathbf{p}$ with minimal euclidean distance, denoted as $dist(\mathbf{p}, l)$ to all lines constructed out of C_i, which yields an estimation for $\mathbf{L}_i$.

$$\mathbf{L}_i = \arg\min_{\mathbf{p}} \sum_{\substack{j,k \\ j \neq k}} dist(\mathbf{p}, l(c_{jk})) \tag{1}$$

An example correspondence mapping is shown in Fig. 2a. The calibration needs to be estimated for all LEDs in the given setup. To find the correspondence points, knowledge of the light source's position can be incorporated. It is helpful to choose simple specimens for calibration. In our example the corresponding points could be estimated by using a Harris corner detector as shown in [4, 5]. In combination with the overview image Fig. 1b corner candidates located on the object and others introduced by shadow can be distinguished as those appear in both images. False positives can be eliminated by taking previously known symmetric constraints into account. As the calibration is a crucial part concerning the accuracy of this method a manual calibration, implemented as a wizard in software is highly recommended.

Figure 2b illustrates the algorithm for determining the height value at different positions (red circles) on the image plane. The outer contour of a shadow area S_i introduced by LED $\mathbf{L}_i$ can be estimated by masking the segmented specimen itself

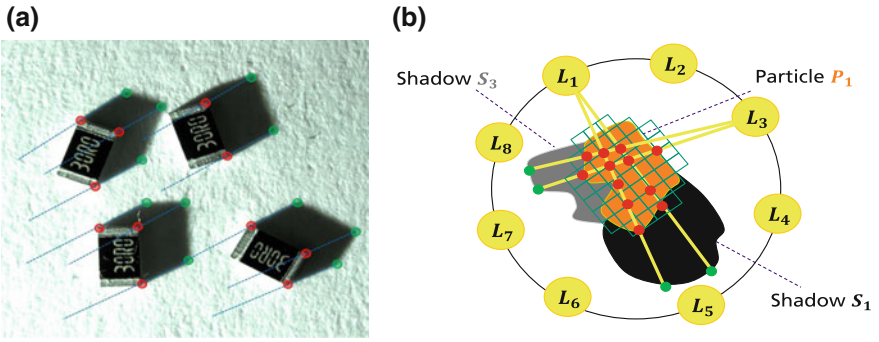

Fig. 2 Lines (*blue dashed*) are constructed out of correspondence points between object (*red*) and surface (*green*) (**a**). The height value of the modeled beam between light source and shadow point is assigned to the corresponding position on the image plane (**b**)

with the post-processed overview image Fig. 3a. After applying a threshold to segment the shadow from the background the contour can be estimated by computing its outline with morphological operators and edge detection. As we are only interested in those parts of the outer boundary, that have at least a minimum distance from the specimen itself in the direction of light position, those non relevant candidates are removed by multiplying the contour image with a slightly enlarged mask. The result can be seen in Fig. 3b. With the position of $\mathbf{L}_i$ and the shadow boundary points B_i, containing all shadow points produced by the light source out of the direction $\mathbf{L}_i$, a height value can be assigned to every pixel position $\mathbf{q} = (x, \quad y, \quad 0)^T$ on the image plane. The height value is computed by an orthogonal projection of the line of sight between the LED $\mathbf{L}_i$ and all corresponding shadow boundary points B_i as shown in Fig. 2b. This procedure is repeated for all

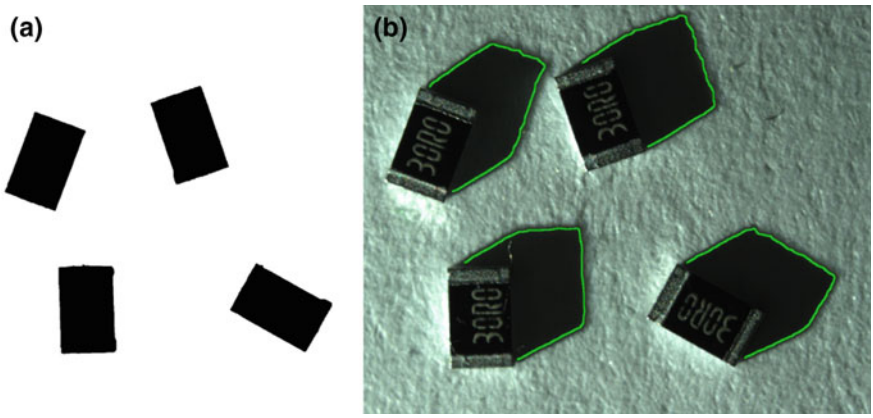

Fig. 3 The mask is generated with morphological operators (**a**) while the outline (*green*) is constructed by using an edge filter and removing inner parts of the boundary (**b**)

calibrated LEDs in this setup. The assignment is done by maintaining a minimum rule, which means, that a height value at position $\mathbf{q}'$ is only updated whenever the new height value would be lower than its current value. After the iteration is finished the mask computed in a prior step is again multiplied by the image to eliminate artifacts located outside the object.

4 Results

When directly comparing the results with measurements acquired by a professional system as illustrated in Fig. 4a one can directly see that the height resolution of the microscope is much higher than the reconstruction seen in Fig. 4b, c. The microscope reconstructs the surface in much greater detail, taking surface properties like roughness into account. As seen in Fig. 4b the initial calibration yields results that fit into the expected range of the before measured values. The chip and its cuboid shape are accurately reconstructed. The height, which is specified at around 6 mm according to the data-sheet is in the same range with the method described here. When looking at Fig. 4c, it becomes clear that the calibration needs to be optimized as currently single outliers in the list of corresponding points result in a displacement of the estimated LED position, which directly influences height estimation. Another point for improvement is the shadow edge detection, as single artifacts worsen the measurement results. This cannot alone be achieved by changing the edge detection algorithms or further post-processing but needs to be incorporated into a model approach which uses sanity checks to remove falsely detected contours.

As shown in Fig. 4 on flat objects, that are known before hand, these calibration errors can be corrected after the reconstruction by averaging the height values. But for rough surfaces, this compensation approach will lower the reproduction granularity of the surface and therefore the height resolution will be further reduced. Hence it is suggested to reduce possible errors in each image processing step. When comparing the given results with the microscope's measurement one can see, that the height dimensions are in a similar range but still way off when micrometer

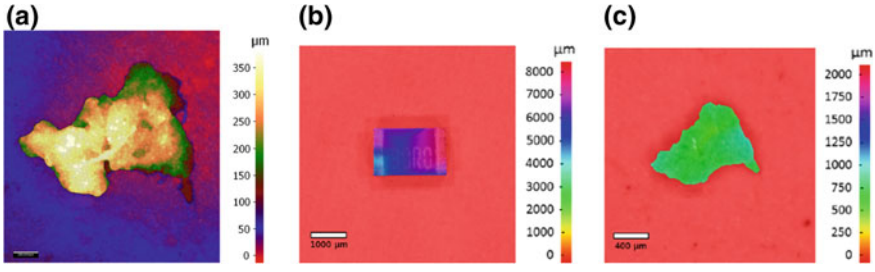

Fig. 4 The measurement of **a** was acquired with an Alicona InfiniteFocus G4 microscope. The results generated from the custom-build sensor are shown in **a** and **c**

accuracy is required. A really big advantage of the donated setup is the large lateral range $1000 \times 1000\ \mu m^2$ that can be measured without stitching partial results together.

5 Summary and Outlook

The approach shown in Sect. 3 was implemented as a software and hardware prototype with the goal to realize a cost-efficient sensor for estimating height and volume information of dirt particles. As demonstrated in Sect. 4 it is possible to estimate this information with a quite simple setup. In the future, these results need to be further compared and benchmarked in detail against ground-truth measurements to determine the accuracy and robustness of this approach. Also the introduced model should be extended by surface properties like roughness or material characteristics to improve the height estimation. The artifacts introduced by assuming a linear relation between shadow contour candidate, the point light position and the resulting height could be post-processed by introducing these surface characteristics.

Estimating height information while maintaining high-throughput measurements in the context of an industrial in-line QA process is still a critical task today. Hence a huge demand exists for measurement systems, that can ensure persistence in industrial environments while also keeping service costs low. The solution shown in this paper yields great potential for those kind of systems in the near future.

References

1. VDA, Band 19 Prüfung der Technischen Sauberkeit - Partikelverunreinigung funktionsrelevanter Automobilteile (2014)
2. Frühberger, P., Stephan, T., Beyerer, J.: Integrating microscopic analysis into existing quality assurance processes. In: 2nd International Multidisciplinary Microscopy and Microanalysis Congress: Proceedings of InterM, 16–19 Oct 2014. Springer International Publishing, Cham, pp. 57–64. doi:10.1007/978-3-319-04639-6
3. Bradski, G.: Dr. Dobb's J. Softw. Tools (2000)
4. Beyerer, J., Puente León, F., Frese, C.: Automatische Sichtprüfung: Grundlagen, Methoden und Praxis der Bildgewinnung und Bildauswertung. Springer Vieweg (2012). doi:10.1007/978-3-642-23966-3
5. Gonzalez, R.C., Woods, R.E.: Digital Image Processing. Pearson Education (2008)

Structural/Functional Analyses of Protein-Nucleic Acid Interactions by AFM

Kunio Takeyasu, Katashi Deguchi and Jamie L. Gilmore

Abstract Here we review 20 years of investigations on the molecular mechanisms of protein-nucleic acid interactions using a combination of molecular biological and biochemical techniques and atomic force microscopy (AFM). AFM can be used for molecular imaging as well as for measurement of interactive forces between molecules. This chapter focuses on the imaging capabilities: (i) imaging abilities of AFM as a tool for biological studies, (ii) action mechanisms of nucleic acid-binding proteins revealed by AFM, and (iii) challenges in shifting from double-stranded to single-stranded nucleic acids.

1 Introduction

Elucidation of the structures of biological macromolecules and subcellular compartments is of great interest to the scientific community. In order to extract useful information, it is desirable to achieve spatial resolutions in the range of nanometers (nm) to micrometers (μm) and sub-second time resolution. The ability of Atomic Force Microscopy (AFM) to directly visualize the nanostructure of the whole genome in a variety of configurations in a single experiment makes it a very useful technique to assess the higher-order structures and dynamics in a variety of conditions. The usefulness of AFM for evaluating the nanometer scale architecture of biological molecules was realized soon after the inception of the technology (1). AFM has been used extensively for imaging of DNA with applications ranging from the study of DNA dynamics, DNA-protein interactions, to DNA ORIGAMI structures (2).

K. Takeyasu (✉) · K. Deguchi · J.L. Gilmore
Laboratory of Plasma Membrane and Nuclear Signaling,
Kyoto University Graduate School of Biostudies, Yoshida-konoe,
Sakyo-ku, Kyoto 606-8501, Japan
e-mail: takeyasu@lif.kyoto-u.ac.jp

A.Y. Oral and Z.B. Bahsi Oral (eds.), *3rd International Multidisciplinary Microscopy and Microanalysis Congress (InterM)*, Springer Proceedings in Physics 186,
DOI 10.1007/978-3-319-46601-9_27

2 AFM as a Tool

Over the last 20 years, the configuration, operation techniques, and sample preparation procedures have developed to a point where AFM has become a powerful tool in the biological sciences [1, 2]. In addition to imaging, AFM can be used for the measurement of forces at the piconewton level between molecules (as a rupture force) or within a molecule (such as the unwinding force of secondary/tertiary structures). This technique has been well documented elsewhere [3].

2.1 Spatial and Time Resolution

AFM experiments can be performed in solution as well as in air. Currently, spatial and time resolutions of a few nm and ~100 ms have been achieved using high-speed AFM systems, respectively. Figure 1 shows a representative image of fluctuating DNA in solution using this technology.

2.2 Double-Stranded RNA and Double-Stranded DNA

Methods of imaging DNA have been well established [4]. Double-stranded RNA can be imaged in a similar way. When the length of DNA is measured from an AFM image, it generally approximates the Watson-Crick Model for B-DNA, with a

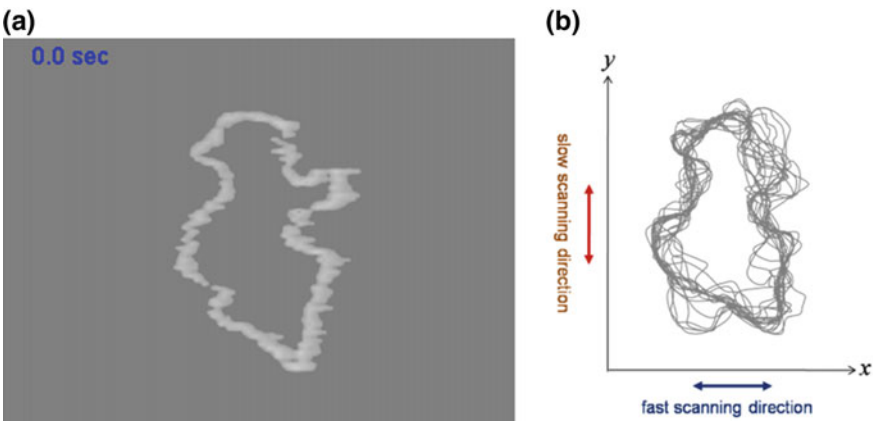

Fig. 1 Dynamic motion of DNA captured by fast-scanning AFM in solution. **a** A snap shot of a 3 kbp DNA plasmid. **b** Consecutive AFM images obtained over 30 s were overlaid. The data illustrate thermodynamic fluctuations

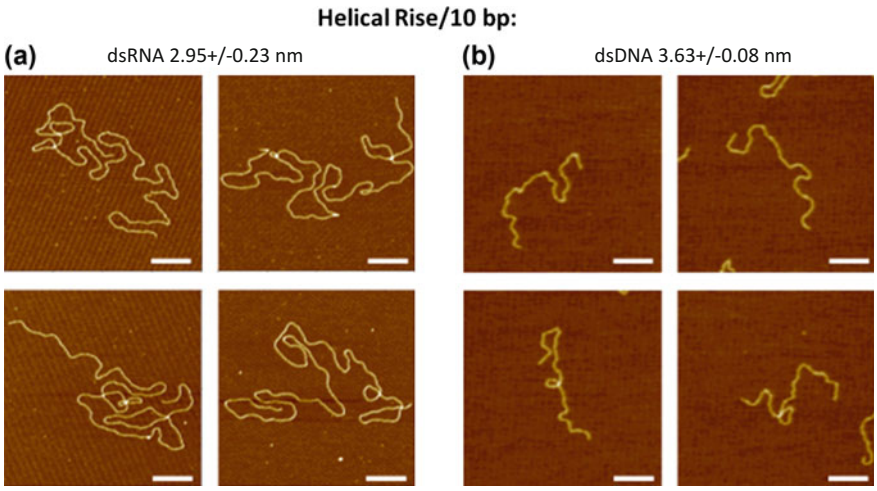

Fig. 2 AFM images of double-stranded RNA (14,728 base pairs of bell pepper endornavirus RNA, n = 11) (**a**) and double-stranded DNA (3412 base pairs of linearized pGEM-T pac, n = 14) (**b**). *Scale bars* 200 nm. The helical rise (mean ± S.D.) were calculated from the measured length of each molecule

measured length of about 3.4 nm per 10 base pairs. On the other hand, the length of double-stranded RNA measures slightly shorter as shown in Fig. 2.

3 Protein-Nucleic Acid Interactions

Various proteins interact with DNA and RNA to elicit various biological functions. Such proteins can directly regulate gene function, promote formation of chromatin structures, and act as signaling molecules. Now AFM can analyze such processes at nanometer and sub-second time resolution.

3.1 Protein Interaction and Action on DNA

It has been reported that DNA-binding proteins can find their site of action on DNA faster than would be expected for interactions relying on random diffusion. Proposed mechanisms to increase the efficiency of the site-search process include binding, sliding, jumping, and hopping. Fast scanning AFM experiments have enabled investigation of these mechanisms [5, 6]. Once proteins have found their site of action, they exert their functions. Figure 3a shows an example of an enzyme (restriction endonuclease SfiI) cutting DNA in solution [5]. This technique has also been used for another restriction enzyme (EcoRII) [6] as well as for RNA polymerase [7].

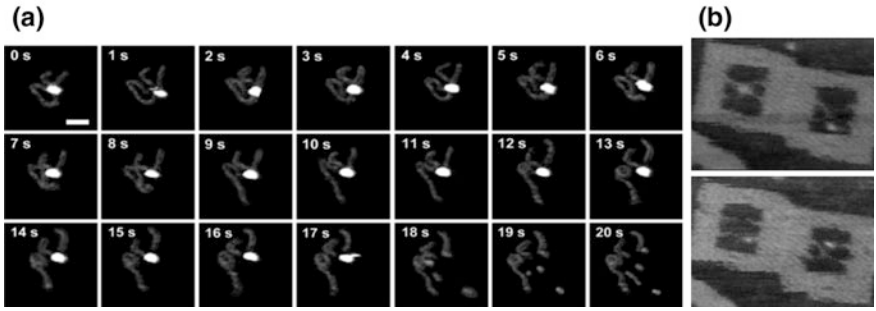

Fig. 3 **a** Dynamic imaging of a restriction enzyme, SfiI, was captured by fast-scanning AFM. The snap shots are shown at 1 s intervals (5). *Scale bar* 50 nm. **b** Resolvase reaction captured by fast-scanning AFM with DNA origami (**7**). Two origami tiles, one has a resolvase (*top*) and the other free. After a second, the Holiday junction was resolved (*bottom*)

For imaging dynamic processes in solution, one complication is that the specimen must be loosely attached to the substrate to observe sample movement. Optimization of imaging conditions usually requires trial-and-error. One method to overcome this issue is the use of a DNA origami tile (Fig. 3b). Here, we investigated the action of resolvase on Holliday junctions. The origami was designed so that the DNA forming a Holiday-junction could be held in the center of the tile [8].

3.2 Chromatin Structural Proteins

The nucleosome is one of the most well studied protein-DNA structures. This structure in comprised of eight histone proteins wrapped around 146 bp of DNA. Using a reconstitution technique, arrays of nucleosomes on DNA (beads-on-a-string) can be visualized [9–12], and the dynamics of nucleosomes on DNA have been analyzed by using fast-scanning AFM [13]. Another structural protein (TK0417) in *Thermococcus kodakarensis* does not wrap around DNA, but instead binds to DNA and forms thick fiber-like structures, resulting in no DNA compaction as visualized by AFM [14].

3.3 Signal Transduction

MDA5 plays a role in natural cellular immunity as a double-stranded RNA sensor. Initial AFM investigation demonstrated that the MDA5 molecule assumes both open and closed conformations [15]. AFM imaging also showed that MDA5 binds double-stranded RNA in a cooperative manner to form a thick fiber-like structure. ATP-binding to MDA5 accelerates this fiber formation, whereas ATP hydrolysis

induces dissociation of MDA5 from RNA, causing a conformational change in the protein (Deguchi et al., manuscript in preparation).

4 Single-Stranded Nucleic Acid

Compared to double-stranded nucleic acids, imaging single-stranded RNA has been difficult due to its complicated internal structures. Most techniques generally study bits and pieces of long single-stranded RNA and hope to eventually arrive at the final global structure over time. We have chosen a different approach taking advantage of the ability AFM to image long single-stranded RNA.

4.1 Single-Stranded RNA Length-Volume Relationship

The contour length of single-stranded RNA is difficult to measure, because many secondary structures are formed within a single RNA molecule. We found that there

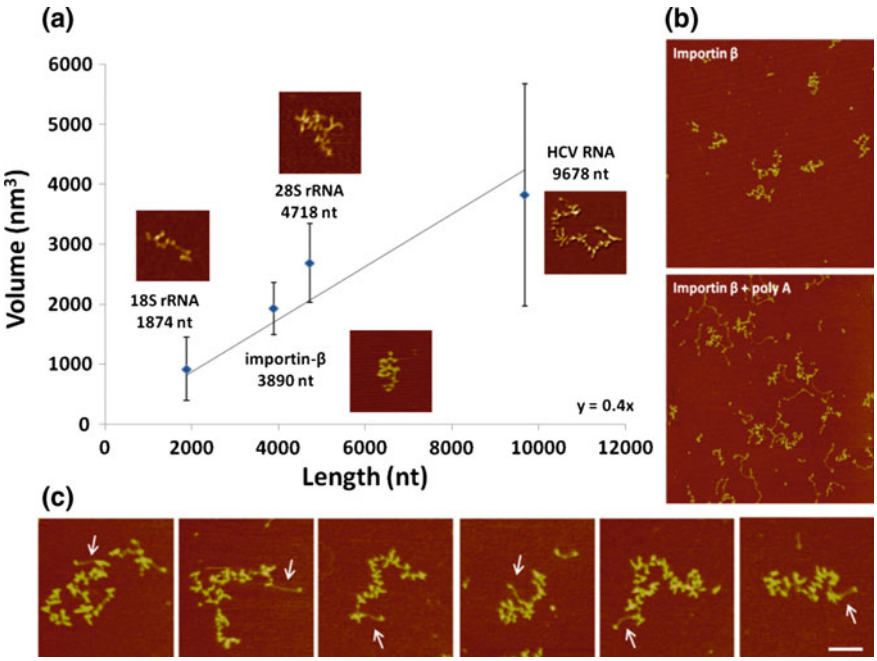

Fig. 4 **a** Length-volume relationship of single-stranded RNA as imaged with AFM and analyzed by Gwyddion grain analysis. **b** 1.5 × 1.5 μm^2 AFM image of importin-β RNA transcript secondary structure with (*top*) and without a poly(A)-tail (*bottom*) (11). **c** Representative 0.4 × 0.4 μm^2 images with a gallery of HCV genomic RNA. *Arrows* show the poly(U) region. *Scale bar* 100 nm

is a linear relationship between the length (number of bases) of RNA and the volume measured by AFM imaging (Fig. 4a) [16]. This relationship is important for further structural studies on the single-stranded RNA.

4.2 Structure of Poly(A)-Tailed RNA

Polynucleotides of a single species can be visualized as, expected, lacking higher-ordered structural domains. Figure 4b shows an AFM image of Poly(A)-tailed single-stranded RNA, where the Poly(A) region can be seen easily.

4.3 Visualization of Long Genomic RNA

To analyze the structure of long single-stranded RNA (>1000 kb) is challenging. We chose the Hepatitis C virus genomic RNA as a target of our AFM studies. AFM imaging depicted the Poly(U) region within the genome (Fig. 4c). We are currently working on the development of analytical methods based on the AFM images, and will describe in detail in the following chapter.

Acknowledgments Our work has been supported by the Grant-in-Aid for Basic Research (A), (B), and for Scientific Research on Priority/Innovative Areas from the JSPS, as well as the JSPS Bilateral Collaboration Grants between Japan-UK and Japan-Spain. We also thank the support from the HFSP. We especially thank our previous lab members (Drs. Y. Suzuki, S.H. Yoshimura, H. Maruyama, K. Hizume, and H. Takahashi) and collaborators, Drs. R.M. Henderson (Cambridge) and J.C. Alonso (Madrid).

References

1. Takeyasu, K., et al.: Modern atomic force microscopy and its application to the study of genome architecture. In: Bhushan, B. (ed.) Scanning Probe Microscopy in Nanoscience and Nanotechnology, vol. 14, pp. 723–756. Springer, Heidelberg (2009)
2. Takeyasu, K. (ed.): Atomic Force Microscopy in Nano-Biology. Pan-Stanford Press, Singapore (2015)
3. Takahashi, H., et al.: Force spectroscopy addresses fundamental problems in cell physiology. In: Méndez-Vilas, A., Díaz, J. (eds.) Microscopy: Science, Technology, Applications and Education, pp. 478–488. Badajoz, Spain (2010)
4. Gilmore, J.L., et al.: Analyses of nuclear proteins and nucleic acid structures using atomic force microscopy. Methods Mol. Biol. **1262**, 119–153 (2015). doi:10.1007/978-1-4939-2253-6_8
5. Suzuki, Y., et al.: Visual analysis of concerted cleavage by type IIF restriction enzyme SfiI in subsecond time region. Biophys. J. **101**(12), 2992–2998 (2011). doi:10.1016/j.bpj.2011.09.064

6. Gilmore, J.L., et al.: Single-molecule dynamics of the DNA-EcoRII protein complexes revealed with high-speed atomic force microscopy. Biochemistry **48**(44), 10492–10498 (2009). doi:10.1021/bi9010368
7. Suzuki, Y., et al.: Fast microscopical dissection of action scenes played by Escherichia coli RNA polymerase. FEBS Lett. **586**(19), 3187–3192 (2012). doi:10.1016/j.febslet.2012.06.033
8. Suzuki, Y., et al.: Direct analysis of Holliday junction resolving enzyme in a DNA origami nanostructure. Nucleic Acids Res. **42**(11), 7421–7428 (2014). doi:10.1016/j.febslet.2012.06.033
9. Sato, M.H., et al.: Atomic force microscopy sees nucleosome positioning and histone H1-induced compaction in reconstituted chromatin. FEBS Lett. **452**, 267–271 (1999). doi:10.1016/S0014-5793(99)00644-4
10. Hizume, K., et al.: Atomic force microscopy demonstrates a critical role of DNA superhelicity in the nucleosome dynamics. Cell Biochem. Biophy. **40**, 249–262 (2004). doi:10.1016/S0014-5793(99)00644-4
11. Hizume, K., et al.: Linker histone H1 per se can induce three-dimensional folding of chromatin fiber. Biochemistry **44**, 12978–12989 (2005). doi:10.1021/bi050623v
12. Hizume, K., et al.: Topoisomerase II, a scaffold component, promotes chromatin-compaction in vitro in a linker-histone H1-dependent manner. Nucleic Acid Res. **35**, 2787–2799 (2007). doi:10.1093/nar/gkm116
13. Suzuki, Y., et al.: Molecular dynamics of dna and nucleosomes in solution studied by fast-scanning atomic force microscopy. Ultramicroscopy **110**(6), 682–688 (2010). doi:10.1016/j.ultramic.2010.02.032
14. Maruyama, H., et al.: Histone and TK0471/TrmBL2 form a novel heterogeneous genome architecture in the hyperthermophilic archaeon Thermococcus kodakarensis. Mol. Biol. Cell **22**(3), 386–398 (2011). doi:10.1091/mbc.E10-08-0668
15. Funabiki, M., et al.: Autoimmune disorders associated with gain of function of the intracellular sensor MDA5. Immunity **40**(2), 199–212 (2014). doi:10.1016/j.immuni.2013.12.014
16. Gilmore, J.L., et al.: Nanoimaging of ssRNA: genome architecture of the Hepatitis C virus revealed by atomic force microscopy. J. Nanomed. Nanotechol. **S5**, 010 (2014). doi:10.4172/2157-7439.S5-010

Dual Energy Microtomography Applied to Oil and Gas Assessments

A.P. Teles, R.T. Lopes and I. Lima

Abstract Dual energy X-ray Microtomography (DE-MicroCT) has proven to be a valuable method in oil and gas industry because it provides non-destructive investigation of the mineral composition of internal structures, characteristic of reservoir core materials. In order to distinguish among different rock materials, a dual energy scanning is carried out to determine both the density and effective atomic number of the minerals of interest. Accurate and reliable quantitative measurements can be achieved with an appropriate calibration within the range of measured attenuation values. However, image quality is the key of an accurate measurement and image signal to noise ratio (SNR), which is related to the ability to define the ratio of the signal intensity to the ambient noise level, is primary determinant. This study provides an investigation of the inner mineralogy phases and microstructural characteristics of a reservoir rock sample by DE-MicroCT. For that purpose a carbonate with different ranges of total porosity and consequently permeability was used. Image analysis process is crucial for an accurate differentiation between calcite (matrix density = 2.71 g/cm^3) and dolomite (matrix density = 2.87 g/cm^3) minerals because they are very similar, although the last mineral is denser than the first one. The results show that small differences are enough to obtain measurements of different mineral phases in Brazilian reservoir rock samples. The results also illustrate that important morphometric parameters to petrophysics investigation may be obtained in this approach.

A.P. Teles · R.T. Lopes · I. Lima (✉)
Nuclear Instrumentation Laboratory, PEN/COPPE/UFRJ, P.O. Box 68.509
21941-972 Rio de Janeiro, RJ, Brazil
e-mail: inaya@lin.ufrj.br

A.P. Teles
e-mail: atila@lin.ufrj.br

R.T. Lopes
e-mail: ricardo@lin.ufrj.br

A.Y. Oral and Z.B. Bahsi Oral (eds.), *3rd International Multidisciplinary Microscopy and Microanalysis Congress (InterM)*, Springer Proceedings in Physics 186,
DOI 10.1007/978-3-319-46601-9_28

1 Introduction

X-ray computed microtomography (microCT) is a sophisticated method used to investigate the inner part of an object. With a mathematical approach it is possible to access all the coronal, axial and sagittal planes and perform a comprehensive three-dimensional (3D) microanalysis procedure. The basis of CT lies in how radiation interacts with matter according to the energy range, which is related with the experiment objectives. For a particular material with homogeneous attenuation coefficient a linear relationship should be found between X-ray intensity and material thickness. For a monoenergetic X-ray beam the linear attenuation coefficient is energy dependent [1]. However, in practice X-ray sources such as the usual X-rays tubes are naturally polychromatic, impairing the determination of those coefficients. Furthermore, most investigations are related to heterogeneous materials and single microCT becomes very limited.

Dual-Energy X-ray microtomography (DE-MicroCT) refers to microCT that uses two photon spectra, which usually in practice consists in setting two different X-ray tube voltages in order to obtain absorption information by using a sophisticated flat panel detector. Because of its non-destructive nature, microCT can inspect with excellent spatial resolution the inner part of almost any kind of material, such as carbonate rock samples playing an increasingly important role in the gas and oil field where the mineralogy of those samples has to be evaluated. Dolomite is a common mineral found in carbonates often coexisting with calcite. These two minerals share a lot of similarities with very close chemical properties. The first one has matrix density of 2.87 g/cm^3 while the second one presents a value of 2.71 g/cm^3. Such extremely close quantities are very complicated to be solved by conventional microCT with a single energy value, because the similarity of the attenuation coefficients is a challenge for material differentiation. However, DE-microCT evaluates the density of rocks by two different X-ray spectra and uses the energy dependence of mineral attenuation coefficients to provide more accurate quantitative measurements [2]. Another issue is that beam hardening effect causes a shift in the X-ray spectral distribution and consequently, mathematical or physical corrections should be performed in order not to propagate this error [3, 4].

One of the main concerns of Humanity refers to global warming. A good alternative to mitigate the greenhouse effect is carbon geological sequestration, which consists in storing a major cause of global warming under sedimentary layers. Fossil fuels and accumulation of sedimentary basins are associated [5] to each other. About 80 % of fossil carbon is fixed in oxidized state as geochemically stable carbonate minerals in limestone and dolomite deposits [6], while the remaining 20 % consists of the altered remains of organisms. The great interest in carbonates is justified by the fact that these rocks store the largest portion of the Earth's remaining conventional petroleum resources [7]. Mineral phase investigation is crucial to understand the complexity of carbonate reservoirs and

consequently their relationship with well porosity potential. In this context, this possibility has significantly increased the relevance of microscopic elemental 3D distribution in geochemical sciences.

2 Imaging Strategy

The capability of the X-rays to distinguish objects depends on theirs linear attenuation coefficients. In this sense, DE-MicroCT is useful to improve the visualization of certain regions of the materials, such as dolomite and calcite, which are key factors in carbonate reservoir quality. From X-rays produced at different energy levels, continuous rock scans were calibrated in order to supply attenuation coefficient dependent images at the micrometer order. Yet, photoelectric effect and Compton scattering are dominant effects in the diagnosis using this energy range. At an (x, y) position the attenuation coefficient can be written as a linear combination of those two effects [8]. According to Eq. 2.1, κ_1, κ_2 and f_p are constants, ρ is the mass density, Z is the atomic number, A is the atomic weight and $f_{\kappa N}$ refers to Klein-Nishima formula contribution. κ_1 and κ_2 are constants that need to be determined by calibration procedure.

$$\mu(x, y, E) \approx \kappa_1 \frac{\rho Z}{A}(x, y) f_{\kappa N}(E) + \kappa_2 \frac{\rho Z^4}{A}(x, y) f_p(E) \tag{2.1}$$

The calibration procedure method uses phantom materials with known properties in order to obtain electron density based on the relationship between μ for a mixture of elements together with tabulated cross-section values [9]. When the constants are determined it is possib to predict any other electron density of an unknown material. In this study geochemical minerals were used to generate the DE-microCT calibrated curve [9].

The lowest and highest experimental tube voltages (bench-top microCT scanner) were 80 and 130 kV respectively, with extra 0.5 mm copper filtration, aimed at physically correcting the beam hardening effect due to the use of the polychromatic X-ray spectrum. This procedure considers a pre-processing routine acting on the projection data. In order to optimize image quality and consequently obtaining very good signal-to-noise ratio (SNR), the following setup conditions were used: 720 projections obtained by regular steps of 0.5°, each projection averaged from 5 frames and pixel size of 24 μm. SNR is strongly influenced by the number of frames by projection, in general the noise level decreases with the number of frames, however total time acquisition that is product of exposure time, number of incremental movements and frames by projection increases [10]. Thus, it is impractical to increase this parameter indiscriminately. In this se, the solution is adopting a value for this parameter that provides worthwhile sample scan results.

The X-ray source and the flat panel detector remain stationary while the rock sample rotates along the minor z axis (conventionally x and y directions are within the plane of the slice whereas z direction is along the axis of the material). Figure 1

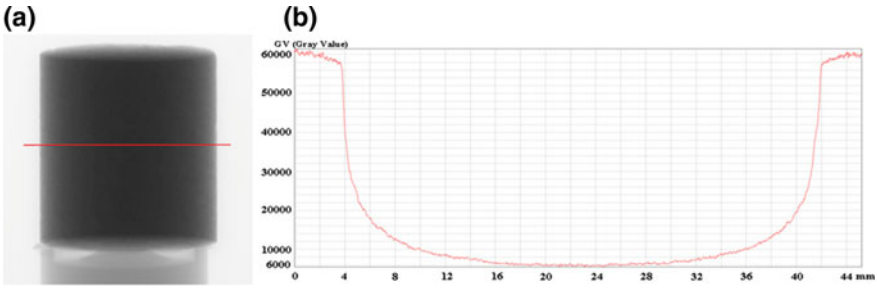

Fig. 1 MicroCT scout view of a carbonate rock sample (**a**) and a profile line (**b**)

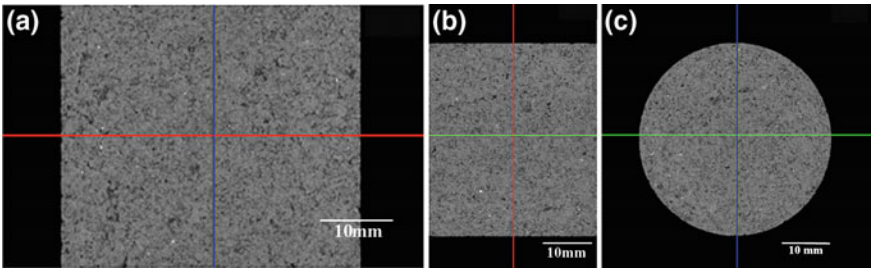

Fig. 2 MicroCT carbonate reconstruction. **a** Coronal, **b** sagittal and **c** axial

shows a scout view (a) and an example of a profile line (b), which sometimes helps to clarify, in real time, image quality in terms of contrast and noise.

3D reconstruction can be achieved either by iterative or analytical methods. The most popular routine belongs to the last group and it is the so-called filtered back-projection based on Feldkamp paper [11], which applies a filter in the spatial domain before back-projecting the projection images. Figure 2 shows an example of microCT reconstructed slices of a carbonate rock sample used in this study acquired at 130 kV: (a) coronal and (b) sagittal and (c) axial.

The major experimental quantitative concern in microCT is the segmentation procedure, which generates one of the highest uncertainty sources for dimensional measurements. Threshold operations are used for separating objects of interest from the rest of the image. There is no standard method and a reliable choice may profoundly impact final data analysis. Some practices still use manual segmentation in some cases. However, is time consuming and impractical for large data sets. Among different approaches it is possible to choose a single value, which is applied to the entire image and can be classified as a global method. Other possibility is to choose an adapting value, which depends on local image characteristics. Some interface areas are difficult to label correctly by thresholding. As a result, a pre-processing filter was used in order to enhance boundaries. Followed by this procedure, the watershed method was applied, which is based on the mathematical morphology theory [12].

3 Results and Discussion

The goal of DE-microCT imaging was properly and clearly modeling 3D density range in a non-destructive way in order to understand reservoir heterogeneity. The stack of images was rendered by using AVIZO package. Figure 3a shows the resulting density calibrated images; in this image, three phases may be observed. The main phases of the matrix (around 2.0–3.25 g/cm^3) correspond to density values of materials expected in this carbonate example. The denser phases (approximately 4.0–4.5 g/cm^3) are particles of other materials that need to be analyzed. Although it is possible to identify different phases in the sample, a more accurate methodology needs to be developed, since materials that compose carbonate rocks, such as calcite and dolomite, have very close density values [13].

In Fig. 3b the 3D porous space model is showed, which was produced at 40 µm spatial resolution and these high resolution images were used to obtain porosity results. Total porosity is the volume of all open plus closed pores as a percent of the total volume. Porosity value obtained in this study was 10.49 %.

Together with porosity, geometry and connectivity influence the petrophysical properties, and their study helps assessing the potential of a petroleum and gas reservoir. Porous space images obtained by dual energy methodology provide other important information on rock characteristics. Porous space 3D thickness may be obtained by Skeletonization [14]; a 3D skeletonization result of a cubic region extracted of the sample is presented in Fig. 4. This approach is based on the distance map of pixels, where, starting from the object edge, inner pixel values are increased recursively by one, and finally, one region formed by higher value pixels defines the image skeleton. The 3D mean separation among pores (sr.Sp), that may be interpreted as the rock matrix thickness among the pores of the studied sample

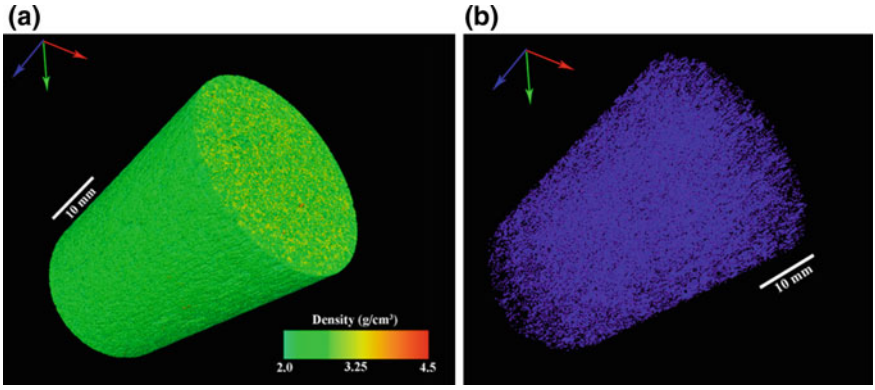

Fig. 3 3D rendering of DE-microCT density calibrated images of a carbonate rock sample: matrix (**a**); porous space (**b**)

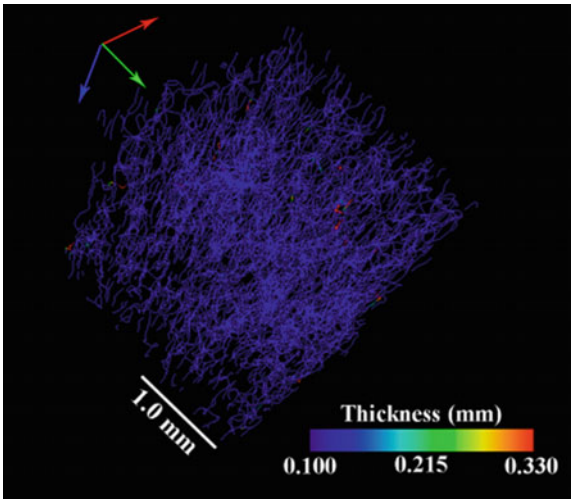

Fig. 4 Porous space skeletonization model

was obtained by its binarization within the image assuming average value of 0.63 mm. Connectivity of porous space may be investigated by the fragmentation index (Fr.I), which can be calculated taking into account the solid perimeter and area before and after the dilatation procedure of a binary image. The idea of Fr.I is the fact that all structures can be described by their relation between concave and convex surfaces, where concavities indicate connectivity and convexities indicate disconnected structures [15]. The fragmentation index obtained analyzing the sample images was Fr.I = 5.8 mm^{-1}. If this result is analyzed with others rock samples, connectivity may be compared.

4 Conclusions

Images obtained by dual energy methodology provided value information about density distribution into a rock sample. The material composition of a sample is important to help defining the best strategy for oil and gas exploration. In addition, the 3D porous space model obtained by dual energy images showed potential to provide information on petrophysical parameters, such as, pore thickness and connectivity.

Acknowledgments The authors would like to thank CAPES, CNPQ and ANP for financial support. We would like to thank CENPES/PETROBRAS for financial and technical support and for furnishing the rock sample.

References

1. Van Geet, M., et al.: Porosity measurement of sedimentary rocks by means of microfocus Xray computed tomography (μCT). In: Mees, F., et al. (eds.) Applications of X-ray Computed Tomography in the Geosciences (Special Publication, Geological Society, London), vol 215, pp. 51–60 (2003)
2. Banks, L.M., Stevenson, J.C.: Modified method of spinal computed tomography for trabecular bone mineral measurement. J. Comput. Assist. Tomogr. **10**(3), 463–467 (1986)
3. Flannery, B.P., et al.: Three-dimensional X-ray microtomography. Science **237**, 1439–1444 (1987). doi:10.1126/science.237.4821.1439
4. Gao, H., et al.: Beam hardening correction for middle-energy industrial computerized tomography. IEEE Trans. Nucl. Sci. **53**, 2796–2807 (2006). doi:10.1109/TNS.2006.879825
5. Hitchon, B., et al.: Sedimentary basins and greenhouse gases: a serendipitous association. Energy Convers. Manag. **40**, 825–843 (1999). doi:10.1016/S0196-8904(98)00146-0
6. Dunsmore, H.E.: A geological perspective on global warming and the possibility of carbon dioxide removal as calcium carbonate mineral. Energy Convers. Manag. **33**, 565–572 (1992). doi:10.1016/0196-8904(92)90057-4
7. Burchette, T.P.: Carbonate rocks and petroleum reservoir: a geological perspective from the industry. Geol. Soc. Spec. Publ. **370**, 17–37 (2012). doi:10.1144/SP370.14
8. Alvarez, R.E., Macovcki. A.: Energy-selective reconstructions in x-ray computerized tomography. Phys. Med. Biol. **21**, 733–744 (1976)
9. Alves, H., et al.: Mineralogy evaluation and segmentation using dual-energy microtomography. X-Ray Spectrom. **44**, 99–104 (2015). doi:10.1002/xrs.2582
10. Van Geet, M., et al.: Towards 3-D petrophysical: application of microfocus computer tomography in geological science. Comput. Geosci. **27**, 1091–1099 (2001). doi:10.1016/S0098-3004(00)00154-0
11. Feldkamp, L.A., et al.: Practical cone-beam algorithm. J. Opt. Soc. Am. **1**, 612–619 (1984). doi:10.1364/JOSAA.1.000612
12. Beucher, S.: The watershed transformation applied to image segmentation. Scanning Microsc. Int. Suppl. **6**, 299–314 (1992)
13. Remeysen, K., Swennen, R.: Application of microfocus computed tomography in carbonate reservoir characterization: possibilities and limitations. Mar. Pet. Geol. **25**, 486–499 (2008). doi:10.1016/j.marpetgeo.2007.07.008
14. Brun, F., et al.: Pore 3D; a software library for quantitative analysis of porous media. Nucl. Instrum. Methods Phys. Res. A. **615**, 326–332 (2010). doi:10.1016/j.nima.2010.02.063
15. Hahn, M., et al.: Trabecular bone pattern factor—a new parameter for simple quantification bone microarchitecture. Bone **13**, 327–330 (1992). doi:10.1016/8756-3282(92)90078-B

Contribution of X-Ray Imaging Microscopy in Metal Bioaccumulation Studies

S. Pennafirme, R.G. Leitão, R.T. Lopes, I. Lima and M.A.C. Crapez

Abstract Industrialization, urbanization, agriculture and natural resource exploration activities are the main sources of release of pollutants, which contaminate both the aqueous compartment and the sediment. In general, metals are the major pollutant, and 90 % approximately of the heavy metals bind to mineral particles, organic matter and to microbial biofilm. The sufficient bioavailability of contaminants can result in bioaccumulation and, depending on the contaminant level, most marine sedimentary ecosystems can become toxic and/or presumably extinct. The knowledge of the physiological mechanisms and the investigation of how these organisms deal with the bioaccumulation of heavy metals are the key in order to unlock adaptive processes, which contribute to the evolutionary fitness and permanence of the species in the environment. In this context, X-ray fluorescence microscopy with Synchrotron radiation with tomography assessment (3D images) was used in order to mapping the body heavy metal distribution of a high abundant marine worm from Guanabara Bay, which is a chronic heavy metal polluted area located at Rio de Janeiro, Brazil. Cadmium, nickel, chromo and cooper were investigated and the results showed a bioaccumulation in the inner parts and especially at the anterior region of the organism. Therefore, X-ray imaging techniques can be a useful tool in order to investigate bioaccumulation in marine benthic invertebrates.

S. Pennafirme (✉) · M.A.C. Crapez
Marine Biology Postgraduate Program, Federal Fluminense University,
Angra dos Reis, Brazil
e-mail: spennafirme@id.uff.br

R.G. Leitão · R.T. Lopes · I. Lima
Nuclear Instrumentation Laboratory, PEN/COPPE/UFRJ, Rio de Janeiro, Brazil

A.Y. Oral and Z.B. Bahsi Oral (eds.), *3rd International Multidisciplinary Microscopy and Microanalysis Congress (InterM)*, Springer Proceedings in Physics 186,
DOI 10.1007/978-3-319-46601-9_29

1 Introduction

The X-ray imaging microscopy with fluorescence through synchrotron light can be used to investigate biological samples, with the benefits of to reveal the elemental distribution of the sample in a non-destructive way [1]. This is because a chemical element can be stimulated to X-ray fluorescence by exposure X-rays whose energy is greater than or equal to the binding energy of the electrons in the shell [2]. The elemental mapping of a given organisms can highlight the first clues regarding its physiologic and metabolic adaptations [3–5].

Marine benthic organisms can bioaccumulate heavy metals in their body structures. Metals are the major pollutants of marine ecosystems and 90 % approximately of the heavy metals bind to the mineral particles, organic matter and to the microbial biofilm [5–8]. Once marine benthic organisms feed on these materials, concentrations of heavy metals can be found accumulated in their bodies, especially in those that inhabit polluted areas [9–12].

The investigation of how these marine organisms deal with the bioaccumulation of heavy metals is the key in order to unlock adaptive processes, which contribute to the evolutionary fitness and permanence of the species in the environment [13–15].

In this context, arises the need for a method which allows both identifying the metal which is being bioaccumulated and its location inside the organism. The present work aimed to investigate the support of X-ray imaging microscopy in metal bioaccumulation studies of marine worms.

2 Material and Methods

Individuals of *Laeonereis acuta* (Nereididae: Polichaeta) were collected from the mangrove of Guanabara Bay, Rio de Janeiro, Brazil, a highly heavy metals polluted area [16]. The organisms were fixed with formalin 4 % and dehydrated through alcohol series. One adult individual was sectioned under stereoscopic microscopy and the region from prostomium to third setiger was analyzed (Fig. 1).

The images acquisitions were realized through synchrotron X-ray fluorescence microscopy (μSXRF) at the Synchrotron Light National Laboratory (LNLS), São Paulo State, Brazil. The sample was positioned at 90° relative to the detector and the incident beam. The sampling scheme is demonstrated on Fig. 2 and the acquisition parameters on Table 1. The sample was kept under the cryojet flux during the images acquisition.

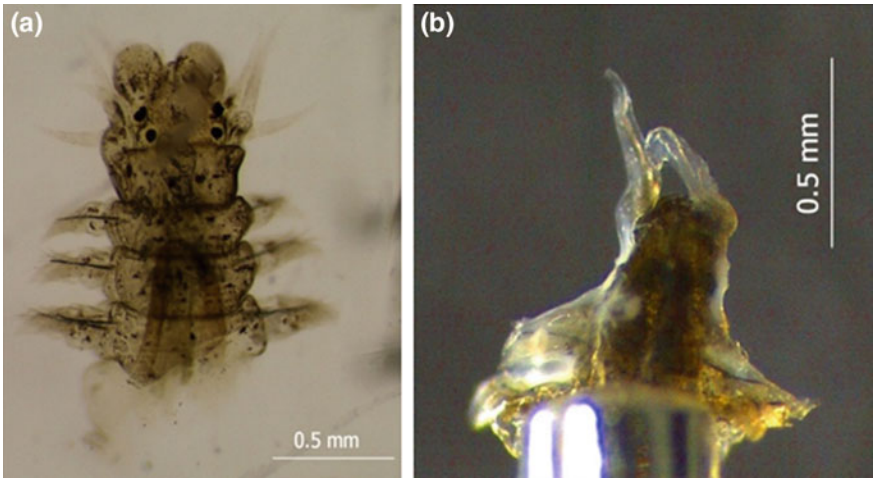

Fig. 1 Analyzed region of *L. acuta* **a** under stereoscopy microscopy before image acquisition and **b** on sampler holder after image acquisition

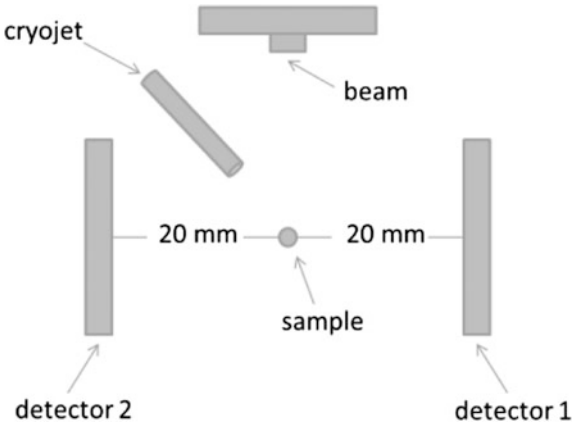

Fig. 2 Sampling scheme of X-ray fluorescence microscopy with Synchrotron radiation with tomography assessment for *L. acuta*

The metals analyzed were cadmium, nickel, chromo and cooper, since they are found at the mangrove sediment of Guanabara Bay [16]. The images reconstruction followed [17, 18].

Table 1 Sampling parameters of X-ray fluorescence microscopy with Synchrotron radiation with tomography assessment for *L. acuta*

X-ray synchrotron experimental parameters	
Sample distance from detector	20 mm
Aluminum filter thickness	165 µm
Collimator thickness of detector 1	3 mm
Collimator thickness of detector 2	2 mm
Dual energy	Yes
Sample rotation	180°
Pixel size	20 µm
Time/pixel	0.2 s
Angle	6°
Cryojet temperature	−30.4 °C
Average temperature on sample	−20 °C
Sample distance from cryojet	74 mm

3 Results and Discussion

The X-ray fluorescence microscopy with Synchrotron radiation and tomography assessment (µSXRF-CT) allowed the generation of 3D images of metal bioaccumulation in marine worms (Fig. 3). It was also possible to investigate the metal distribution inside the organism in a non-destructive way, which may amplify the possibilities of toxicology and physiological studies.

Further, the comparison of the metal distribution at the same organism slice through µSXRF allowed important biologic consideration. For example, it was possible to observe that the metals do not have the same distribution within the organism and different tissues/organs might have different roles on metal bioaccumulation (Fig. 4).

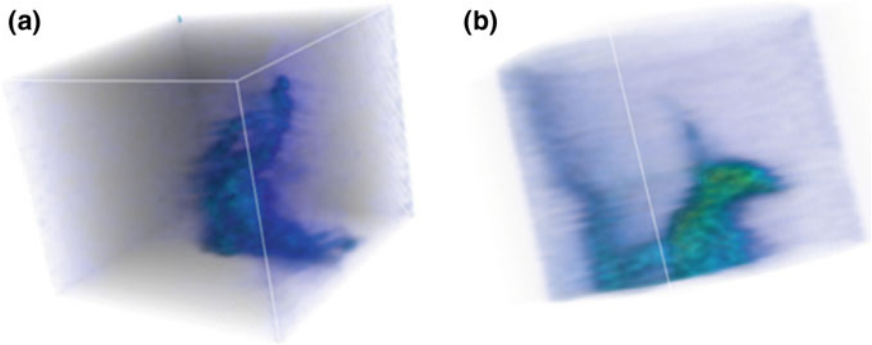

Fig. 3 3D view of **a** cadmium and **b** cooper bioaccumulation of *L. acuta*

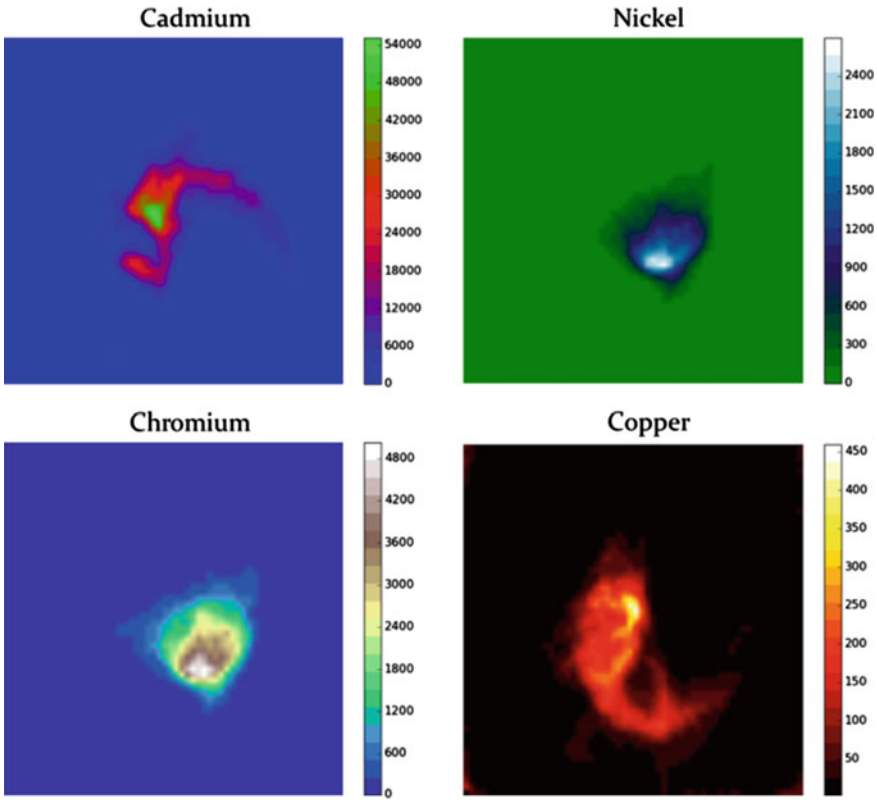

Fig. 4 Metal bioaccumulation mapping (X-ray fluorescence intensity scale) of *L. acuta*

4 Conclusions

X-ray fluorescence microscopy with Synchrotron radiation and tomography assessment (μSXRF-CT) can be a useful tool to investigated metal bioaccumulation in marine worms.

This technic allowed visualizing the heterogeneous metal spatial distribution inside the organism, suggesting that different tissues/organs might have different roles on metal bioaccumulation.

Acknowledgments To LNLS for research grant for this project (XAFS1-17053), to Dr. Perez and Dr. Miqueles for beamline and image reconstruction supports and to Dr. Soares-Gomes for laboratory support.

References

1. Lopes, R.T., Lima, I., Pereira, G.R., Perez, C.A.: Synchrotron radiation X-ray microfluorescence techniques and biological applications. PRAMANA J. Phys. **76**(2), 271–279 (2011)
2. Bousmans, P., Klockenkämper, R.: Total reflection X-ray fluorescence spectrometry. Spectrochim. Acta, Part B **44**, 433–549 (1989)
3. Majumdara, S., Peralta-Videaa, J.R., Castillo-Michelc, H., Hongb, J., Ricoa, C.M., Gardea-Torresdeya, J.L.: Applications of synchrotron μ-XRF to study the distribution of biologically important elements in different environmental matrices: a review. Anal. Chim. Acta **755**, 1–16 (2012). doi:10.1016/j.aca.2012.09.050
4. Leitao, R.G., Santos, C.A.N., Palumbo, A., Souza, P.A.V.R., Pereira, G.R., Anjos, M.J., Nasciutti, L.E., Lopes, R.T.: Distribution of Fe, Cu and Zn in cellular spheroid derived human prostate tumor cells by synchrotron X-Ray fluorescence. IEEE T Nucl. Sci. **60**(2), 758–762 (2013). doi:10.1109/TNS.2012.2231095
5. Pennafirme, S., Lima, I., Bitencourt, J.A., Crapez, M.A.C., Lopes, R.T.: Microbial biofilm study by synchrotron X-ray microscopy. Rad. Phys. Chem. **116**, 116–119 (2015). doi:10.1016/j.radphyschem.2015.05.040
6. Bayen, S.: Occurrence, bioavailability and toxic effects of trace metals and organic contaminants in mangrove ecosystems: a review. Environ. Int. **48**, 84–101 (2012). doi:10.1016/j.envint.2012.07.008
7. Chakraborty, R., Zaman, S., Mukhopadhyay, N., Banerjee, K., Mitra, A.: Seasonal variation of Zn, Cu and Pb in estuarine stretch of West Bengal. Ind. J. Mar. Sci. **38**, 104–109 (2009)
8. Chen, C.W., Kao, C.M., Chen, C.F., Dong, C.D.: Distribution and accumulation of heavy metals in the sediments of Kaohsiung Harbor, Taiwan. Chemosphere **66**, 431–1440 (2007). doi:10.1016/j.chemosphere.2006.09.030
9. Casado-Martinez, M.C., Smith, B.D., Rainbow, P.S.: Assessing metal bioaccumulation from estuarine sediments: comparative experimental results for the polychaete *Arenicola marina*. J. Soil Sed. **13**(2), 429–440 (2013). doi:10.1007/s11368-012-0611-0
10. Goodyeara, K.L., McNeillb, S.: Bioaccumulation of heavy metals by aquatic macro-invertebrates of different feeding guilds: a review. Sci. Total Environ. **229**, 1–19 (1999). doi:10.1016/S0048-9697(99)00051-0
11. Gray, J.S.: Biomagnification in marine systems: the perspective of an ecologist. Mar. Pollut. Bull. **45**, 46–52 (2002). doi:10.1016/S0025-326X(01)00323-X
12. Sakellari, A., Karavoltsos, S., Theodorou, D., Dassenakis, M., Scoullos, M.: Bioaccumulation of metals (Cd, Cu, Zn) by the marine bivalves *M. galloprovincialis, P. radiata, V. verrucosa and C. chione in* Mediterranean coastal microenvironments: association with metal bioavailability. Environ. Monit. Assess. **185**(4), 3383–3395 (2012). doi:10.1007/s10661-012-2799-2
13. Bertin, G., Averbeck, D.: Cadmium: cellular effects, modifications of biomolecules, modulation of DNA repair and genotoxic consequences (a review). Biochimie **88**, 1549–1559 (2006). doi:10.1016/j.biochi.2006.10.001
14. Janssens, T.K.S., Roelofs, D., Van Straalen, N.M.: Molecular mechanisms of heavy metal tolerance and evolution in invertebrates. Insect Sci. **16**(1), 3–18 (2009). doi:10.1111/j.1744-7917.2009.00249.x
15. Morgan, A.J., Kille, P., Stürzenbaum, S.R.: Microevolution and ecotoxicology of metals in invertebrates. Environ. Sci. Technol. **41**(4), 1085–1096 (2007). doi:10.1021/es061992x
16. Neto, J.A.B., Gingele, F.X., Leipe, T., Brehme, I.: Spatial distribution of heavy metals in surficial sediments from Guanabara Bay: Rio de Janeiro, Brazil. Environ Geol. **49**(7), 1051–1063 (2006). doi:10.1007/s00254-005-0149-1

17. Miqueles, E., Pierro, A.R.: Iterative reconstruction in X-ray fluorescence tomography based on radon inversion. IEEE Trans. Med. Imaging **30**, 438–450 (2011). doi:10.1109/TMI.2010.2085011
18. Miqueles, E.X., De Pierro, A.R.: C-library raft: reconstruction algorithms for tomography. Applications to X-ray fluorescence tomography. Comput. Phys. Commun. **182**, 2661–2673 (2011). doi:10.1016/j.cpc.2011.07.020

Index

A.Y. Oral and Z.B. Bahsi Oral (eds.), *3rd International Multidisciplinary Microscopy and Microanalysis Congress (InterM)*, Springer Proceedings in Physics 186,
DOI 10.1007/978-3-319-46601-9